Numerical Simulations of ICRF Heated Tokamak Plasmas

D.T. Blackfield

May 1980

UWFDM-353

Ph.D. thesis.

FUSION TECHNOLOGY INSTITUTE

UNIVERSITY OF WISCONSIN

MADISON WISCONSIN

Numerical Simulations of ICRF Heated Tokamak Plasmas

D.T. Blackfield

Fusion Technology Institute
University of Wisconsin
1500 Engineering Drive
Madison, WI 53706

http://fti.neep.wisc.edu

May 1980

UWFDM-353

Ph.D. thesis.

NUMERICAL SIMULATIONS OF ICRF HEATED TOKAMAK PLASMAS

by

DONALD THOMAS BLACKFIELD

A thesis submitted in partial fulfillment of the
requirements for the degree of

DOCTOR OF PHILOSOPHY
(Nuclear Engineering)

at the

UNIVERSITY OF WISCONSIN-MADISON

1980

ABSTRACT

NUMERICAL SIMULATIONS OF ICRF HEATED TOKAMAK PLASMAS

Donald Thomas Blackfield

Under the supervision of Professor J.E. Scharer

Several computer models are used to examine ICRF heating in PLT and the conceptual tokamak reactor NUWMAK. A 0-D transport code which uses trapped particle scaling finds that $\sim$240 MJ of RF energy is required to ignite the 660 MW_e NUWMAK reactor.

The complete multi-species 3 x 3 hot plasma dispersion tensor, accurate for any temperature, for ion cyclotron harmonics up to five is derived. The dispersion relation which is obtained is then coupled to a Fokker-Planck code and a 1-D transport code.

Using a 2-D in velocity space, time-dependent Fokker-Planck code, in which charge exchange, radial losses, radiation and Ohmic heating are included, we find that over 90% of the RF power is absorbed through fundamental minority damping by the protons ($n_H/n_e \sim 0.1$) . The spatially-averaged deuterium temperature doubles while the protons become nonMaxwellian with a high energy tail of 18 keV. In NUWMAK, both deuterium and tritium remain Maxwellian with $T_D \simeq T_T \simeq T_e$. There is little ICRF Q enhancement when fundamental or second harmonic damping is the dominant heating process.

A WKB slab model is coupled to a 1-D time-dependent transport code to investigate the spatial aspects of ICRF heating. In PLT, over 90% of the RF power is absorbed near the center by the protons, over a heating width of 12-14 cm. In both PLT and NUWMAK, a plane fast wave launched from the low field side is almost completely absorbed before the mode conversion layer is reached. The occurrence of mode conversion, near the ion cyclotron resonance layer, does not alter the density and temperature profiles. Due to the high reactor densities and temperatures, the dominant heating processes in the ICRF startup of NUWMAK are electron Landau and transit time damping when the RF frequency $f = nf_{cD}$ near the plasma center with $n = 1,2,3$. Using "PLT empirical" scaling, 150-300 MJ of RF energy is needed to ignite NUWMAK.

For PLT, both the Fokker-Planck and space-time simulations agree with the experiment. For NUWMAK, direct electron heating dominates and no high energy ion tails are produced. In both devices the RF power is deposited close to the plasma core. Therefore, ICRF heating appears to be an attractive auxiliary heating scheme for tokamaks.

ACKNOWLEDGEMENTS

A thesis of this length reflects the large amount of assistance needed. I would first like to thank my parents, whose guidance lead me to this accomplishment. I would also like to thank Prof. Meyer of the Mathematics Department who steered me from Applied Math to plasma physics and to Prof. Conn who initially guided me in my studies.

This thesis could not have been written without the innumerable discussions I conducted with Drs. Kesner, McVey, Gordinier, Houlberg, and Mense. A special expression of gratitude goes to Dr. T. K. Mau who helped with much of the problem formulation and to Prof. Scharer who provided invaluable assistance. In addition, K. Fong at LLL provided me with several essential mathematical subroutines.

The typing of this thesis was heroically performed by Diana, Gail and Connie.

Finally, I would like to acknowledge the tremendous amount of support provided by my wife Kathy. Her patience and understanding really made this paper possible.

TABLE OF CONTENTS

CHAPTER 1

INTRODUCTION

1.A. Overview

Auxiliary heating should be required in a tokamak reactor since Ohmic heating alone cannot supply enough energy for a plasma to reach ignition. Auxiliary heating is now used to investigate the effects of a higher plasma temperature than that provided by Ohmic heating alone on plasma transport and confinement properties.

There are two general types of auxiliary heating currently being investigated, neutral beams and RF heating. Studies comparing the advantages and disadvantages of these two types of heating have been done by Stix(1-2), Scharer, Conn, and Blackfield(3), and others(4-6).

Under the category of RF heating, several frequency regimes have been proposed(4-10). From the standpoint of both experimental results and the availability of power sources, the Ion Cyclotron Range of Frequencies (ICRF) heating seems most promising. In this thesis, we investigate fundamental minority, second harmonic, and higher ion harmonic fast wave heating.

We shall briefly review recent experimental results in the next section. In Chapter 2, we review the 0-D, or point model fluid description of second and third harmonic heating in a reactor. In Chapter 3, we derive the complete 3 x 3 hot plasma dispersion tensor which forms the basis of the Fokker-Planck and 1-D slab model calculations. In Chapter 4, we examine both PLT and NUWMAK(11-12) for anisotropy and high energy tail formation due to the presence of RF. Chapter 5 focuses on ICRF heating using a WKB slab model in connection with a 1-D multi-species transport code. We look at fundamental minority heating in PLT and NUWMAK and second and third harmonic heating in NUWMAK. Results obtained from the three codes, 0-D and 1-D fluid and 2-D velocity space models, are compared in Chapter 6. Finally, in Chapter 7 we discuss the areas of theory and computational analysis which need more development.

1.B. Recent ICRF Experimental Results

Some of the earliest experiments involving ICRF heating in a tokamak were carried out on the ST machine at Princeton(13-17) from 1972-1974. Further experiments were performed on the ATC(10-21) and PLT(22-25) tokamaks, also at Princeton. ICRF heating is currently being studied on MICROTOR and MACROTOR(26) at UCLA and on a tokamak at Cal Tech(27).

In France, extensive investigation of ICRF heating is being done on TFR(28-31). The Russians have studied ICRF in TO-1, TM-Vch, and T-4(32-40). The ERASMUS tokamak(41) in Belgium also uses ICRF. Finally, the DIVA tokamak(42-43) in Japan has ICRF heating.
A review of ICRF heating experiments prior to 1979 on these tokamaks may be found in several sources(4-6,44).

Since 1978, significant experimental results have been obtained on DIVA, T-4, TFR and PLT. In DIVA(43), second harmonic

($f = 2f_{cD}$) ICRF heating experiments have been performed on a deuterium plasma with a variable proton minority concentration ($5\% \leq n_H/n_D \leq 40\%$). The plasma in this machine is quite clean, having $Z \simeq 1$.

Without electrostatic shielding and a balanced drive antenna, the overall ion heating efficiency was 40% at most. The remaining power was coupled to the plasma edge. When the antenna was electrostatically shielded from the plasma by a Faraday shield and driven in a balanced RF mode, the ion heating efficiency approached 100%. Net RF power up to 100 kW was coupled to the plasma, increasing the ion temperature from 160 eV to 450 eV. The dominant ion energy loss mechanisms appeared to be through neoclassical thermal conduction and electron-ion Coulomb collisions. An RF power density up to 1.4 W/cm^3 was achieved without adversely affecting plasma confinement.

On T-4(40), good agreement has been obtained between the experimentally measured hydrogen minority velocity distribution and Stix's quasilinear theory(45). In addition, with $B_o = 15$ kG, $\bar{n}_e = 1.5 \times 10^{13}$ cm^{-3} and $P_{RF} = 72$ kW, the deuterium or majority species' temperature rose from 150 eV to 260 eV. The $m = 0$ mode was excited with RF frequency, $f = 23$ MHz. Since the minority concentration was low ($n_H/n_D \sim 2.3\%$), the dominant heating mechanism appeared to be fundamental minority heating of the protons. The deuterons were heated through Coulomb collisions with the high energy proton tail. Using Stix's notation, $Z = 2.2$, $\zeta = 12.8$ and $\langle p \rangle \sim 3.5 \times 10^{-2}$ W/cm^3 appeared to match the measured proton distribution $f(v)$. Since $<p>$ is low, this implies that there may be substantial energy losses by RF heated protons escaping through loss cones.

In TFR$^{(31)}$, the hydrogen concentration in the deuterium plasma was varied from 3% to 45% to investigate the effect of varying minority concentrations on second harmonic ICRF heating. High density ($n_e(0) = 1.2 - 1.4 \times 10^{14}$ cm^3) and low density ($n_e(0) = 5 \times 10^{13}$ cm^3) experiments were performed for RF power levels up to 250 kW with pulse durations from 30 to 60 ms and $f \sim 60$-61 MHz ($B_o = 41$ kG - 42 kG).

In the high density experiments, $\sim 85\%$ of the RF power delivered by the generator was coupled to the plasma. Using different power levels, the peak deuterium temperature increased linearly with power

$$\frac{\Delta T_D(0)}{P_{RF}} = 0.7 \text{ eV/kW} \quad \text{or} \quad \Delta T_D(0) = \frac{5P_{RF}(\text{kW})}{<n_e> \; (10^{13} \text{ cm}^{-3})} \qquad (1\text{-}1)$$

where P_{RF} is the amount of RF power absorbed in the plasma. A high energy proton tail ($T_{eff} \sim 2$ keV) was observed. No energy tail was seen in the deuterium distribution.

In the high density case, no significant heating efficiency difference was observed between the $m = 0$ and $m = -1$ modes. In the low density experiments ($m=0$) the heating efficiency was halved

$$\Delta T_D(0) \approx \frac{2.5 \; P_{RF}(\text{kW})}{<n_e> \; (10^{13} \text{ cm}^{-3})} \; . \qquad (1\text{-}2)$$

For high density operation $\tau_E \sim 20$ ms, while the low density τ_E is 8-10 ms. The shorter confinement time leads to greater energy transport losses, thereby reducing the overall heating efficiency.

In the above experiments, $n_H/n_D < 5\%$. In these cases, fundamental minority heating of the hydrogen species appears to be the dominant heating mechanism. By varying both the magnetic field and proton concentration it was shown that the radial position of the ion-ion hybrid layer determines, to a large extent, the radial position of the RF heating. Consequently, this influences the overall heating efficiency. An analysis of the heating mechanisms is currently underway.

For low hydrogen concentrations, the ion-ion hybrid resonance layer(46)

$$\omega^2 = \frac{\chi_H f_D + \chi_D f_H}{\chi_D f_D + \chi_H f_H} \omega_{CD} \omega_{CH} \tag{1-3}$$

where $\chi_D \equiv n_D/n_e$, $f_D = m_e/M_D$

$\chi_H \equiv n_H/n_e$, $f_H = m_e/M_H$

lies near the cyclotron layer, both being near the plasma center. In low proton concentration experiments the RF power was deposited in the center, resulting in high heating efficiencies. As the proton concentration is increased ($n_H/n_D \sim 15\%$), the ion-ion hybrid layer moves near the plasma edge, while the cyclotron layer stays near the center. In this case the heating efficiency became comparable to the best result, when both resonance layers were near the center.

The TFR experiments have shown that power levels up to 250 kW can be coupled to a predominantly deuterium plasma using an all metal loop. The average ion temperature was raised 150 eV. Finally, the position of the ion-ion hybrid resonance layer seems to play an important role in determining the overall heating efficiency.

Recent PLT experiments(24-25), which will be analyzed in detail in Chapters 4-6, will now be briefly summarized. Initial low density, low power ($\bar{n}_e \sim 1\text{-}1.5 \times 10^{13}$ cm^{-3}, $P_{RF} = 30\text{-}35$ kW) resulted in stronger than expected damping of the fast magnetosonic wave with $\Delta T_D(0) \sim 80$ eV. Though the deuterium spectra showed no apparent energetic tail, hydrogen charge exchange measurements showed strong proton ($n_H/n_D \sim 3\%$) heating. The strong wave damping and hydrogen heating can again be explained from the presence of fundamental minority heating of the fast wave.

Within the past year, PLT has upgraded the amount of power coupled to 350 kW for an RF pulse length of 100 ms(25). For higher densities ($\bar{n}_e \sim 3 \times 10^{13}$ cm^{-3}), the average ion temperature at the center increased 600 eV from 600 eV to 1200 eV. Although no deuteron high energy tail was seen, a high energy ($T_{eff} \sim 15$ keV) proton tail was. The heating approached saturation to within 10% during the RF pulse indicating a τ_{RF} of ~ 40 ms.

When a minority concentration of ^{3}He was released into the deuterium plasma, the overall heating efficiency doubled

($\Delta T_D(0) \sim 500$ eV for $P_{RF} \sim 150$ kW with $n_e \sim 2.1 \times 10^{13}$ cm^{-3}). By heating at the fundamental resonance frequency of ^{3}He, the magnetic field could be raised from 16.4 kG to 24.6 kG. Therefore, the plasma current could be raised from 400 kA to 500 kA, increasing the Ohmic power. The increased magnetic field leads to better plasma confinement, while the increased Ohmic heating and lowered charge exchange loss improves the overall heating efficiency. Therefore, the energetic ^{3}He ions are confined better and can deposit more of their energy in the rest of the plasma.

Our goal is to develop a realistic model of ICRF heating using the fast magnetosonic wave which will predict the plasma behavior during the ICRF startup of a fusion reactor. To have confidence in the model, we should be able to simulate present day experiments. In Chapters 4-6, computer simulated PLT results will be compared with the most recent experimental findings. The next chapter contains a review of the initial NUWMAK reactor studies(11-12) which used the 0-D fluid time-dependent code, POint Radiofrequency Transport (PORT).

CHAPTER 1 REFERENCES

1. T.H. Stix, Princeton Univ. Report MATT-1089 (Nov., 1974).
2. T.H. Stix, Princeton Univ. Report MATT-862 (Sug., 1971).
3. J.E. Scharer, R.W. Conn, D.T. Blackfield, EPRI Report ER-268 (1976).
4. D.L. Jassby, et al., Princeton Univ. Report PPPL-1610 (Nov., 1979); INTOR Internal Report #5 (May, 1979).
5. L.D. Smullin, et al, ERDA Report 76/115 (Nov., 1979).
6. J.M. Rawls, et al, DOE Report DOE/ER-0034 (Oct., 1979).
7. F.W. Perkins, in Radio Frequency Plasma Heating (Proc. 3rd Topical Conf. Pasadena, 1978) Paper C1.
8. J.C. Hosea, in Radio Frequency Plasma Heating (Proc. 3rd Topical Conf. Pasadena, 1978) Paper C2.
9. J. Jacquinot and A. Messian, Annex5 to INTOR Meeting (May 10-11, 1979).
10. H. Takahasi, Journal de Physique 38, Supp. C-6 (Dec., 1977) 171.
11. B. Badger, et al, Univ. of Wisconsin Report UWFDM-330 (March, 1979).
12. J.E. Scharer, D.T. Blackfield, J.B. Beyer, T.K. Mau, Nuc. Fusion 19 (1979) 1171.
13. W.M. Hooke, J.C. Hosea, MATT-940 (Nov., 1972).
14. J.C. Hosea, W.M. Hooke, Phys. Rev. Lett. 31 (1973) 150.
15. J. Adam, et al, in Plasma Heating and Controlled Nuclear Fusion (Proc. 5th Int'l. Conf. Tokyo, 1974) Paper IAEA-CN-33/A 3-2.
16. J.C. Hosea, MATT-1129 (May, 1975).
17. H. Takahasi, MATT-1140 (Oct.,1975).
18. H. Takahasi, et al, Phys. Rev. Lett. 39 (1977) 31.
19. H. Takahasi, MATT-1374 (Oct., 1977).

20. H. Hsuan, et al, in Radio Frequency Plasma Heating (Proc. 3rd Topical Conf. Pasadena, 1978) Paper C8.

21. H. Takahasi, PPL-1545 (April, 1979).

22. P.L. Colestock, et al, in Heating in Toroidal Plasmas (Proc. Joint Varenna-Grenoble Int'l. Symp. Grenoble, 1978) Vol. II, 217.

23. P.L. Colestock, et al, in Radio Frequency Plasma Heating (Proc. 3rd Topical Conf., Pasadena, 1978) Paper C7.

24. J. Hosea, et al, PPL-1554 (July, 1979).

25. J. Hosea, et al. PPPL-1558 (Oct., 1979).

26. G.J. Morales, R.J. Taylor, in Heating in Toroidal Plasmas (Proc. Joint Varenna-Grenoble Int'l. Symp. Grenoble, 1978) Vol. II, 241.

27. D.Q. Hwang, R.W. Gould, in Radio Frequency Heating in Toroidal Plasmas (Proc. 3rd Topical Conf. Pasadena, 1978) Paper C6.

28. TFR Group, in Theoretical and Experimental Aspects of Heating Toroidal Plasmas (Proc. 3rd Int'l. Meeting CEA, Grenoble, 1976) Vol. I, 87.

29. TFR Group in Heating Toroidal Plasmas (Proc. Joint Varenna-Grenoble Int'l. Symp. Grenoble, 1978) Vol. II, 207.

30. TFR Group, in Plasma Physics and Nuclear Fusion Research (Proc. 6th Conf. Berchtesgaden, 1976) Paper IAEA-CN-35/G8 IAEA (Vienna, 1977) Vol. III, 39.

31. TFR Group, in Controlled Fusion and Plasma Physics Research (Proc. 9th European Conf. Oxford, Sept., 1979).

32. N.V. Ivanov, I.A. Kovan, E.V. Los´, JETP Lett. 14 (1971) 138.

33. N.V. Lovan, I.A. Kovan, E.V. Los´, translated from Atomaya Eneriqiya 32 (1971) 138.

34. N.V. Lovan, et al, JETP Lett. 16 (1972) 60.

35. N.V. Ivanov, et al, JETP Lett. 20 (1972) 39.

36. V.L. Vadovin, et al, JETP Lett. 14, (1971) 49.

37. V.L. Vadovin, et al, JETP Lett. 17 (1973) 2.

38. V.L. Vadovin, N.V. Shapotkovskii, V.D. Rusanov, in Theoretical and Experimental Aspects of Toroidal Plasmas (Proc. 3rd Int'l. Meeting Grenoble, 1976) Vol II, 347.

39. V.V. Buzakin, et al, in Plasma Physics and Controlled Fusion Research (Proc. 6th Int'l. Conf. Berchtesgaden, 1976) Paper IAEA CN35/G10 IAEA.

40. N.V. Ivanov, et al, Sov. J. Plasma Phys. 4(6) (Nov.-Dec., 1978) 675.

41. V.P. Bhatnager, et al, in Heating Toroidal Plasmas (Proc. Joint Varenna-Grenoble Int'l. Symp. Grenoble, 1978) Vol. III, 133.

42. DIVA Group, in Heating Toroidal Plasmas (Proc. Joint Varenna-Grenoble Int'l. Symp. Grenoble, 1978).

43. Haruyuki Kimura, et al, Japan Atomic Energy Research Institute Report JAERI-M 8429 (Sept.,1979).

44. D.T. Blackfield, UWFDM-278 (Jan., 1979).

45. T.H. Stix, Nuc. Fusion 15 (1975) 737.

46. D.G. Swanson Phys. Rev. Lett. 36 (1976) 316.

CHAPTER 2

REVIEW OF 0-D FLUID MODEL NUWMAK RESULTS

2.A. 0-D Model

There have been several reactor studies where neutral beams have been the main auxiliary heating system$^{(1-7)}$. Recently RF heating, particularly ICRF, has become more attractive. The overall heating efficiencies of both systems are comparable. At Wisconsin, we have begun to examine reactor systems where the dominant heating source is ICRF$^{(8-10)}$. The potential advantages of ICRF are utilized in the reactor designs while potential problems are brought out.

To design an RF heating system, an estimate of the amount of power and wave frequency is necessary. For the NUWMAK reactor study$^{(9-10)}$ the POint Radiofrequency heating Transport code, PORT, provided this. Using the computer code PORT, based on a spatially averaged, time dependent model$^{(8-13)}$, the following electron and ion energy balance equations are solved

$$\frac{\partial n_e}{\partial t} = \frac{4.28 \times 10^{-11}\, n_e n_i (T_i - T_e)}{T_e^{3/2}} + \frac{1}{1.5r}\frac{\partial}{\partial r}\left(r n_e \chi_e \frac{\partial T_e}{\partial r}\right)$$

$$- \frac{1}{r}\frac{\partial}{\partial r}\left(r n_e V_e T_e\right) + 4.17 \times 10^{15}\left\{ n_D n_T \langle \sigma v \rangle\, U_{\alpha e} \right\} \qquad (2\text{-}1)$$

$$+ \bar{E} \cdot \bar{J} - P_B - P_S + P^e_{RF} \qquad \text{(2-1 continued).}$$

$$\frac{\partial n_i}{\partial t} = -4.28 \times 10^{-11} \frac{n_e n_i (T_i - T_e)}{T_e^{3/2}} + \frac{1}{1.5r} \frac{\partial}{\partial r} \left(r n_i \chi_i \frac{\partial T_i}{\partial r}\right)$$

$$- \frac{1}{r} \frac{\partial}{\partial r} (r n_i V_i T_i) + 4.17 \times 10^{15} \left\{ n_D n_T <\sigma V> U_{\alpha i} \right\} + P^i_{RF} \qquad \text{(2-2)}$$

where $T_{e(i)}$ is the electron (ion) temperature (eV) ($T_D = T_T = T_i$ due to the short ion-ion equilibration time); $n_{e(i)}$ is the electron (ion) density (cm^{-3}) ($n_i = n_D + n_T$); $V_{e(i)}$ is the electron (ion) fluid velocity (cm/ms); r is the plasma radius (cm); t is time (ms); $\chi_{e(i)}$ is the electron (ion) thermal diffusivity (cm^2/sec); $U_{\alpha e(i)}$ is the fraction of alpha energy deposited in the electrons (ions); $\bar{E}$ is the toroidal electric field ($V \cdot cm^{-1}$); $\bar{J}$ is the toroidal current density ($A \cdot cm^{-2}$); P_B is the Bremsstrahlung loss term (W); P_S is the synchrotron radiation loss term (W); $P^{e(i)}_{RF}$ is the electron (ion) RF heating term (W).

Equations (2-1 and 2-2) are obtained from the second moment of the Boltzmann equation(14-16) averaged over a magnetic flux surface (see Chapter 5). The heating terms due to the RF and the slowing down of alphas are added. The radiation loss terms are also added. Since $Z_{eff} = 1$ is assumed, there are no charge exchange or impact ionization loss terms. The ion-electron equilibration is calculated from classical theory while the Ohmic heating term uses neoclassical theory.

The Bremsstrahlung radiation term may be written as(14,17)

$$P_B = 4.8 \times 10^{-31} Z_{eff}\, n_e^2\, T_e^{1/2} \quad (W/cm^3) \qquad (2\text{-}3)$$

with T_e in keV. The synchrotron term is(18)

$$P_S = 1.55 \times 10^{-14}(1 - r_w)^{\frac{1}{2}}\, [5. + .17(5\text{-}A)]^3\, \frac{n_e^{\frac{1}{2}}\, B_o^{5/2}}{a^{\frac{1}{2}}}\, T_e^{2.1} (W/cm^3) \qquad (2\text{-}4)$$

where A is the aspect ratio; r_w is the wall reflectivity; T_e is in keV; B_o is the toroidal B field in Tesla; a is the minor radius in cm.

PORT assumes that a density feedback control exists which keeps the total ion density constant, though the ratio n_D/n_T may vary in time. The electron density is solved from the charge neutrality condition.

The fusion alphas, produced at 3.52 MeV, are assumed to slow down instantaneously. The amount of energy deposited to each species as the alphas slow down is calculated using classical theory(14,19).

Since PORT is spatially independent, the conduction and convection gradients are eliminated by assuming that

$$\frac{2}{3}\frac{\partial}{\partial r}\left(rn\, V\, \chi\, \frac{\partial T}{\partial r}\right) \rightarrow \frac{nT}{\tau_c} \qquad (2\text{-}5)$$

where $\tau_c \equiv a^2/\chi$, and that

$$\frac{1}{r}\frac{\partial}{\partial r}(rnVT) \rightarrow \frac{nT}{\tau_D} \qquad (2\text{-}6)$$

where $\tau_D \equiv a^2/D$.

τ_c is a "characteristic" thermal diffusion time and τ_D is a "characteristic" particle diffusion time. For the NUWMAK calculations, χ and D were calculated using trapped particle scaling$^{(14,20)}$.

To eliminate the spatial dependency in density and temperature, the following expressions for the average density and temperature are used

$$\overline{n} = \frac{2\int_0^a n(r)\ r\ dr}{a^2} \qquad (2\text{-}7)$$

and

$$\overline{T} = \frac{\int_0^a n(r)\ T(r)\ rdr}{\int_0^a n(r)\ rdr} \qquad (2\text{-}8)$$

where

$$n(r) = 2n_o\ (1 - \frac{r^2}{a^2}) + 0.01\ n_o$$

and $\qquad (2\text{-}9)$

$$T(r) = 2\ T_o(1- \frac{r^2}{a^2}) + 0.01\ T_o .$$

The dispersion relation used in PORT in the calculation of the RF heating terms is somewhat limited. Only $\omega = 2\ \omega_{CD} = 3\omega_{CT}$ or $\omega = 2\ \omega_{CT}$ heating for the ions could be calculated. Landau and transit time damping are the assumed heating processes for the electrons.

For the $\omega = 2\,\omega_{CD} = 3\,\omega_{CT}$ case, the ion RF heating term is$^{(9-10,21)}$

$$P^{i}_{RF} = \sum_{\ell=2}^{3} \frac{|E_+|^2}{2\,\ell\omega_{cio}a^2}\,\varepsilon_o\,R \int_o^a \omega^2_{pi}(r) \left[\frac{\langle k_\perp^2\rangle\, V^2_{thi}(r)}{2\,\omega^2_{ci}(r)}\right]^{\ell-1} dr \qquad (2\text{-}10)$$

where $\ell = 2$ for deuterium and 3 for tritium.

The electron RF heating term is $^{(9-10,21)}$

$$P^{e}_{RF} = \frac{\langle k_\perp^2\rangle\, |E_+|^2 \varepsilon_o \pi^{\frac{1}{2}}}{2\,k_{\parallel}\,a^2} \int_o^a \frac{\omega^2_{pe}(r)}{\omega^2_{ce}(r)}\, V_{the}(r)\,\left(1 + x^2(r)\right) e^{-[\ell^2\omega^2_{cio}/k^2_{\parallel}\, V^2_{the}]}\, rdr \qquad (2\text{-}11)$$

where

$$x^2(r) = \frac{3\,\pi^{\frac{1}{2}}\,\langle k_\perp^2\rangle\, V_{the}(r)}{8\,k_{\parallel}\,\omega_{ci}(r)} \qquad (2\text{-}12)$$

and $\langle k_\perp^2\rangle$ is $k_\perp^2$ (r) spatially averaged over the heating zone. For the ions, this heating width is over the cyclotron resonant layer$^{(9-10,21)}$

$$\Delta R = \frac{2k_{\parallel}\, V_{thi}\, R}{\ell\omega_{cio}}\,. \qquad (2\text{-}13)$$

For electron Landau and transit time damping, the heating zone is over the entire plasma cross section.

Assuming a spatially averaged RF electric field E_+

$$P^i_{RF} = PRFI' \, |E_+|^2$$

$$P^e_{RF} = PRFE' \, |E_+|^2 \quad . \qquad (2\text{-}14)$$

The normalization for $|E_+|$ is obtained by assuming that all of the RF power is coupled to the plasma. This assumption yields a minimum RF heating system requirement. $|E_+|$ is normalized so that

$$|E_+|^2 = \frac{\text{Total RF Power assumed coupled to Plasma}}{PRFI' + PRFE'} \, . \qquad (2\text{-}15)$$

By assuming a spatially averaged value for $|E_+|$ and $k_\perp^2(r)$, we are implicitly assuming that the RF energy is deposited near the plasma center where $\omega \sim 2\omega_{CD} \sim 3\omega_{CT}$. Although this may be a good assumption in present day ICRF heating experiments, Chapter 5 shows that for reactors, this may not occur.

2.B. Numerical Results

To ignite the NUWMAK conceptual reactor (parameters given in Table 2-1), 175 MW of RF power for 1 sec. must be provided. The ion and electron time dependent temperature curves are shown in Fig. (2-1). Also plotted in Fig. (2-1) is the amount of alpha fusion power deposited in the electrons. The ignition point is reached on the steep rise in the curves. Once ignition is achieved, both the temperatures and alpha power production continue to increase after the RF is turned off. An equilibrium between the alpha power and the energy transport is obtained near t = 1.5 sec, indicated by the levelling of the temperature curves.

The electron and ion energy balance terms are plotted in Figs. (2-2-3). Early in the startup phase $T_i > T_e$ since most of the RF power heats the ions directly. Therefore, the ion-electron equilibration term is positive (heating) for the electrons and negative (cooling) for the ions. However, since a majority of the alpha power is deposited in the electrons, T_e becomes greater than T_i and the ion-electron equilibration term cools the electrons and heats the ions. This interchange in the dominant heating role between the RF and alpha power determines which temperature is higher ($T_i \gtrless T_e$ when $P_{RF} \gtrless P_\alpha$).

In Fig. (2-4) we see that over 98% of the RF power is deposited in the ions through second and third harmonic damping with second harmonic damping on the deuterons being dominant. Since the electron absorption term is small, only a small amount of power is deposited outside of the cyclotron resonance layer.

As the plasma temperature increases, slightly more electron Landau and transit-time damping occurs. In the small gyroradius expansion, the power deposited to the ions goes as

$$P^i_{RF} \sim (k_\perp^2 V_\perp^2)^{\ell-1} \sim \lambda_i^{\ell-1}. \qquad (2\text{-}16)$$

Consequently, as T_i increases, more power flows to the tritium.

In Fig. (2-5) the magnitude of the spatially-averaged $|E_+|$ field is shown. As the plasma temperature increases, the conductivity increases. To keep the RF power constant, the electric field magnitude must drop. In Fig. (2-6), the deuterium and tritium resonance widths are plotted. Since $\Delta R \propto T_i^{1/2}$, the widths increase in time. Finally, the magnitudes of $\langle k_\perp \rangle \equiv (|\langle k_\perp^2 \rangle|)^{1/2}$ are shown in Fig. (2-7). Since ΔR for the deuterons does not equal ΔR for the tritons, $\langle k_\perp \rangle_D \neq \langle k_\perp \rangle_T$.

PORT is limited to two different ICRF harmonics, n=2 or 3. The effects of resonant alphas and impurities being present in the plasmas are not included. In addition, the small λ or gyroradius expansion used may begin to break down as the plasma reaches ignition. The 3.52 MeV alphas cannot be included in a small gyroradius expansion since $\lambda_\alpha \sim O(1)$. For these reasons, a general dispersion relation is derived in the next chapter. With this dispersion relation, the spatial effects which had been neglected will be examined in Chapter 5.

Table 2-1

NUWMAK REACTOR PARAMETERS

$a = 125 \text{ cm}$

$R = 500 \text{ cm}$

$A = 4$

$S = 1.33$

$I = 6.48 \text{ MA}$

$B_o = 60 \text{ kG}$

$P_{\text{Thermal}} \approx 2300 \text{ MW}$

$\bar{n}_e = 1.95 \times 10^{14} \text{ cm}^{-3}$

$\bar{n}_e = \bar{n}_T = 0.975 \times 10^{14} \text{ cm}^{-3}$

$\frac{n_{\text{edge}}}{n_{\text{max}}} = \frac{T_{\text{edge}}}{T_{\text{max}}} = .01$

$T_i = T_e = 1.0 \text{ keV}$

$f = 92 \text{ MHz}$

$k_{\parallel} = 0.1 \text{ cm}^{-1}$

$k_{\perp} \sim 1.6 \text{ cm}^{-1}$

LIST OF FIGURES

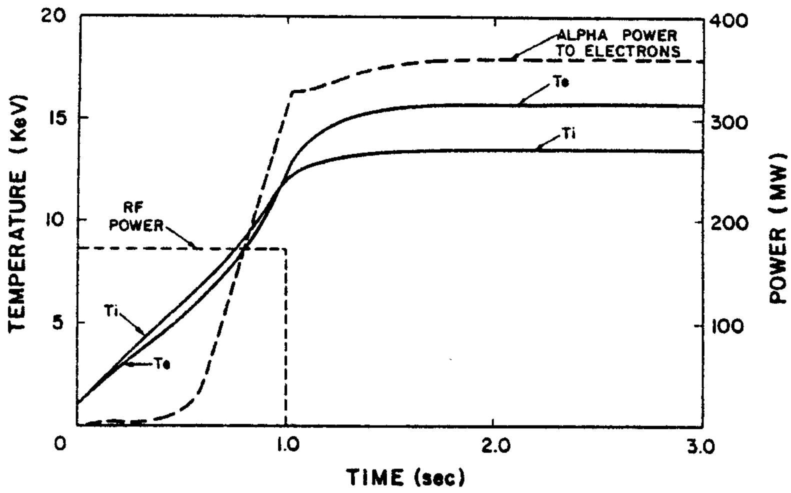

Fig.(2-1)

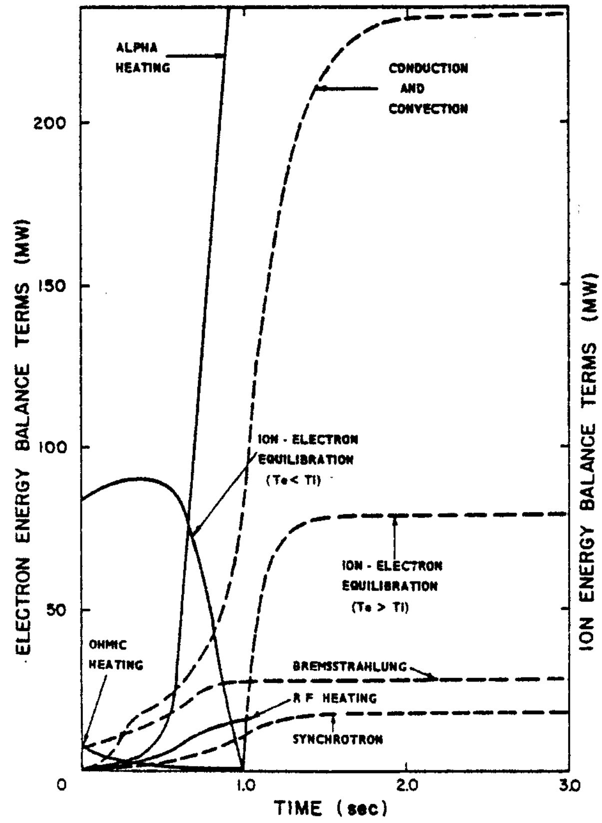

Fig.(2-2)

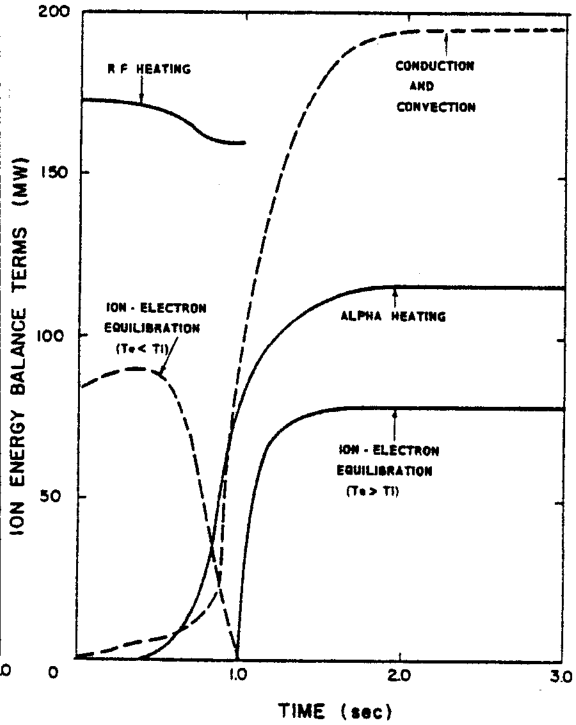

Fig.(2-3)

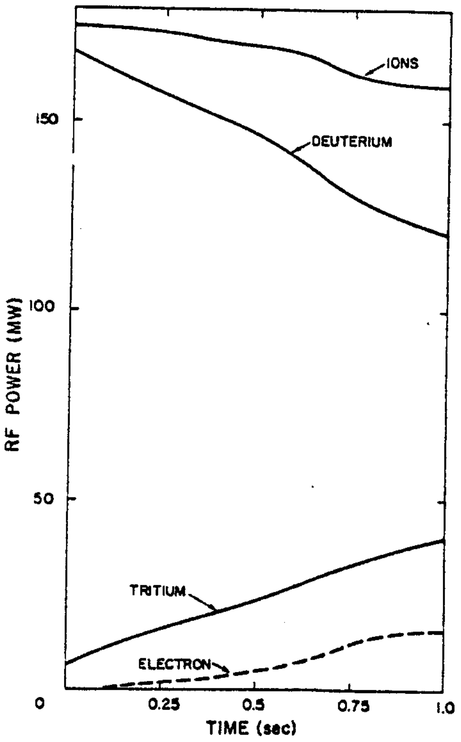

Fig.(2-4)

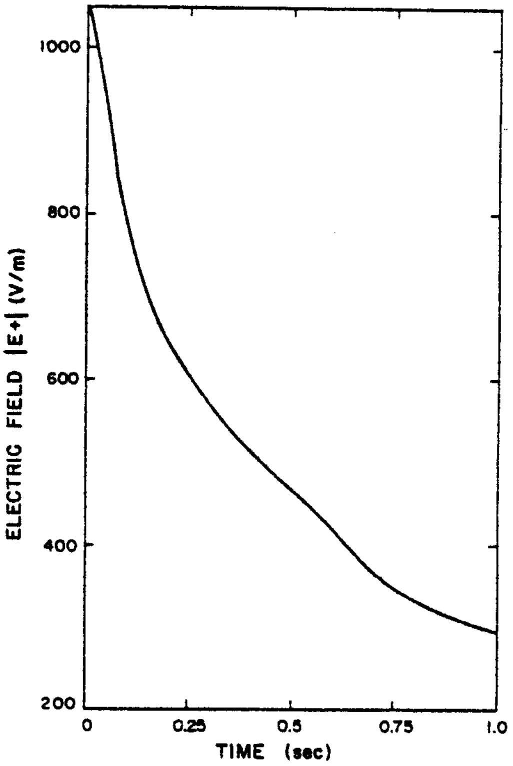

Fig.(2-5)

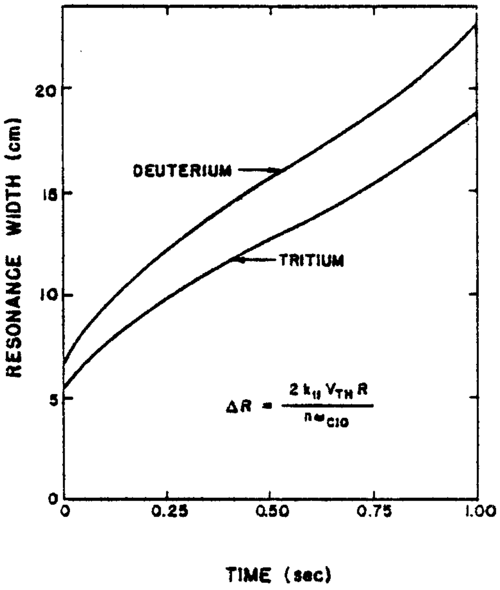

Fig.(2-6)

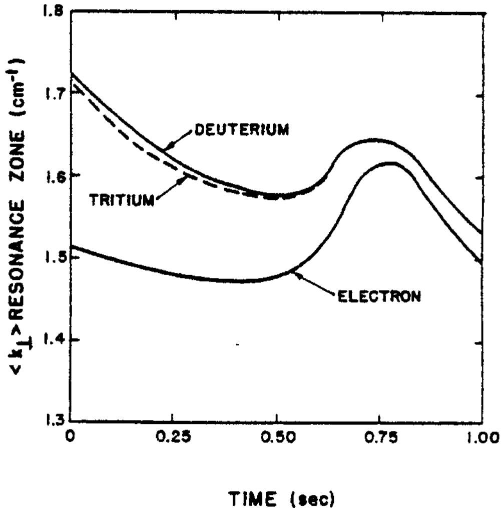

Fig.(2-7)

CHAPTER 2 REFERENCES

1. B. Badger, UWFDM-68 (March, 1974).
2. P.N. Haubenreich, M. Roberts, eds., Oak Ridge National Laboratory Report ORNL-TM-4634 (June, 1974).
3. R.G. Mills, et al, MATT-1050 (Aug., 1974).
4. W.M. Stacy, Jr., et al, Argonne National Laboratory Report ANL/CTR-75-2 (June, 1975).
5. B. Badger, et al, UWFDM-112 (Oct., 1975).
6. B. Badger, et al, UWFDM-191 (Dec., 1977).
7. D.R. Cohn, et al, MIT Fusion Center Research Report R-77-2 (Jan., 1979).
8. B. Badger, et al, EPRI-ER-368 (July, 1976).
9. B. Badger, et al, UWFDM-330 (March, 1979).
10. J.E. Scharer, D.T. Blackfield, J.B. Beyer, T.K. Mau, Nuc. Fusion 19 (1979) 1171.
11. J.E. Scharer, R.W. Conn, D.T. Blackfield, EPRI ER-268 (1976).
12. R.W. Conn, J. Kesner, Nuc. Fusion 15 (1975) 775.
13. J. Kesner, R.W. Conn, Nuc. Fusion 16 (1976) 397.
14. W. Houldberg, Ph.D. Thesis Univ. of Wisconsin-Madison (1977).
15. S.I. Braginskii, Review of Plasma Physics, Plenum Publishing Co., N.Y. (1965) Vol. I, 205.
16. N.A. Krall and A.W. Trivelpiece, Principles of Plasma Physics, McGraw-Hill Book Co., N.Y. (1973).
17. R.W. Conn, UWFDM-16 (July, 1972).
18. T.F. Yang, et al, UWFDM-49 (1973).
19. W.A. Houlberg, UWFDM-103 (1974).

20. S.O. Dean, et al, U.S. Atomic Energy Commission Report WASH-1295 UC-20.

21. D.T. Blackfield, UWFDM-278 (Jan., 1979).

CHAPTER 3

HOT PLASMA FAST WAVE DISPERSION RELATION

3.A. Hot Plasma Dispersion Tensor

In cold plasma theory, both the fast and slow ion cyclotron waves may propagate parallel to an externally applied magnetic field. From space and access considerations of the RF launching structure, the wave should be launched from the low field edge of the plasma (see Fig. (3-1)). Any wave generated in a tokamak must propagate across magnetic field lines and up a density gradient. In a tokamak a slow wave, when propagating from the high field edge towards the plasma center, must travel up a density gradient. Near the inside plasma edge, the perpendicular cyclotron resonance is reached. Here the slow wave mode may convert to an electrostatic ion cyclotron or Ion Bernstein wave which propagates back towards the high field edge(1). The electrostatic wave is strongly damped by electron Landau and transit time processes. The resulting surface heating may lead to enhanced radiation and particle losses. A slow wave launched from the low field side is evanescent and cannot penetrate into the plasma. Therefore, the slow wave does not appear to be an attractive mode for core heating in a tokamak.

The fast wave can propagate across magnetic field lines. In a cold plasma with a single ion species, the fast wave near the ion

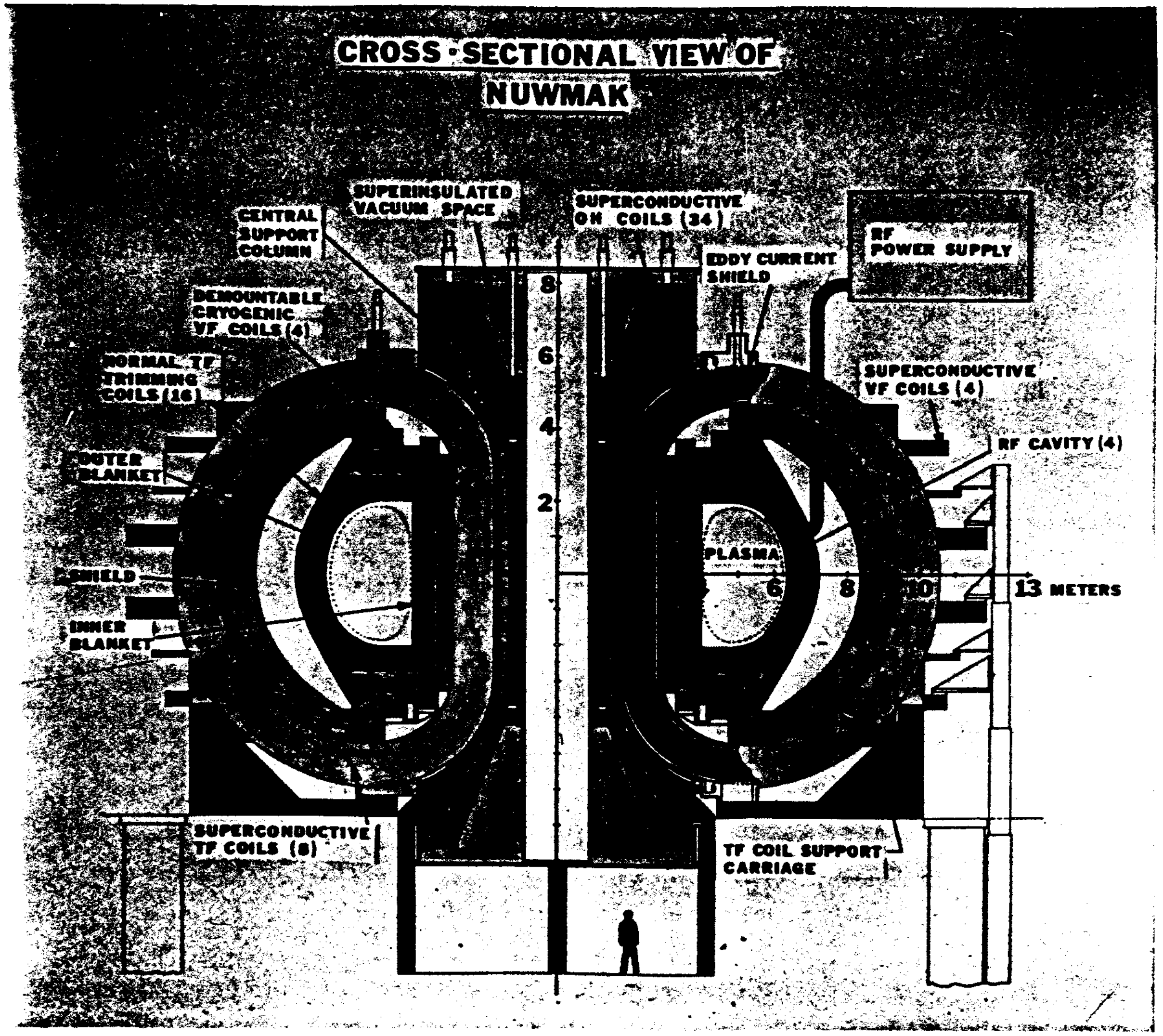

Fig.(3-1) Cross-sectional view of the conceptual NUWMAK reactor.

cyclotron resonance layer is right-hand circularly polarized. Since the ions rotate about field lines in the opposite sense, little ion heating would be expected to occur. However, the presence of two ion species, together with hot plasma effects, produces an enhancement of the left-hand component of the RF electric field. For fundamental and second ion harmonic heating with several ion species, $|E_+|/|E_-| \sim O(1)$ (see Chapters 4-5).

The dispersion relation determines the region of wave propagation, evanescence, mode coupling and ultimately the RF power deposition. To calculate a general, multi-species, hot plasma dispersion relation, a local approximation is used. This implies that each point in the plasma receives no information from adjacent spatial regions. Density, temperature and magnetic field gradients are ignored. The effects of density and temperature gradients have been examined by Mau(2) and found to be small. Therefore, we assume that each point represents an isotropic unbounded plasma with density $n(r_o)$, temperature $T(r_o)$, and magnetic field $B(r_o)$. We also assume a slab model geometry with plane RF electric fields of the form

$$E = E_o \, e^{i(k_\perp \cdot \hat{x} + k_\parallel \cdot \hat{z} - \omega t)} \qquad (3\text{-}1)$$

with $k_y = 0$; $\hat{z}$ is the direction along B_o; $\hat{x}$ is along the minor radius at the mid-plane.

Using the Vlasov-Maxwell equations and integration along unperturbed particle orbits, we obtain the following 3 x 3 generalized hot plasma dispersion tensor for slab geometry(2-5)

$$\begin{vmatrix} K_{xx} - n_{\parallel}^2 & K_{xy} & K_{xz} + n_{\parallel} n_{\perp} \\ K_{yx} & K_{yy} - n^2 & K_{yz} \\ K_{zx} + n_{\parallel} n_{\perp} & K_{zy} & K_{zz} - n_{\perp}^2 \end{vmatrix} \bullet \left[E_1 \right] = 0 \qquad (3\text{-}2)$$

where $\overline{\overline{K}} = \frac{c^2 \overline{\overline{\varepsilon}}}{\omega^2}$; $\overline{n} = \frac{c\overline{k}}{\omega}$; and $\overline{\overline{\varepsilon}}$ is the dielectric tensor for a uniform, unbounded plasma

$$\frac{c^2}{\omega^2} (\overline{k} \times (\overline{k} \times \overline{E}) + \overline{\overline{\varepsilon}} \cdot \overline{E}) = 0 \qquad (3\text{-}3)$$

and

$$K_{xx} = 1 + \sum_{\alpha} \frac{\omega_{p\alpha}^2}{2\omega k_{\parallel}} e^{-\lambda_\alpha} \sum_n \frac{n^2 I_n}{\lambda_\alpha} \theta_n^\alpha$$

$$K_{yy} = 1 + \sum_{\alpha} \frac{\omega_{p\alpha}^2}{2\omega k_{\parallel}} e^{-\lambda_\alpha} \sum_n \frac{n^2 I_n}{\lambda_\alpha} \theta_n^\alpha - \frac{2k_x^3}{k_{\perp}^2} \lambda_\alpha (I_n' - I_n) \theta_n^2$$

$$K_{zz} = 1 - \sum_{\alpha} \frac{\omega_{p\alpha}^{2}}{\omega k_{\parallel} V_{th\alpha}} e^{-\lambda_{\alpha}} \sum_{n} I_{n} \zeta_{n}^{\alpha} \Phi_{n}^{\alpha}$$

$$K_{xy} = -K_{yx} = -i \sum_{\alpha} \frac{\omega_{p\alpha}^{2}}{2\omega k_{\parallel}} e^{-\lambda_{\alpha}} \sum_{n} n(I_{n}' - I_{n})\, \theta_{n}^{\alpha}$$

$$K_{xz} = \sum_{\alpha} \frac{\omega_{p\alpha}^{2}}{2\omega k_{\parallel} \omega_{c\alpha}} e^{-\lambda_{\alpha}} \sum_{n} k_{x} \frac{nI_{n}}{\lambda_{\alpha}} \Phi_{n}^{\alpha} = K_{zx}$$

$$K_{yz} = -K_{zy} = \sum_{\alpha} i \frac{\omega_{p\alpha}^{2}}{2\omega k_{\parallel} \omega_{c\alpha}} e^{-\lambda_{\alpha}} \sum_{n} k_{x}(I_{n}' - I_{n})\, \Phi_{n}^{\alpha} \tag{3-4}$$

where $\theta_{n}^{\alpha} = \frac{2}{V_{th\alpha}} Z(\zeta_{n}^{\alpha})$

$$\Phi_{n}^{\alpha} = Z'(\zeta_{n}^{\alpha})$$

$$\zeta_{n}^{\alpha} = \frac{\omega - n\omega_{c\alpha}}{k_{\parallel} V_{th\alpha}}, \quad \lambda_{\alpha} = \frac{1}{2} \frac{k_{\perp}^{2} V_{th\alpha}^{2}}{\omega_{c\alpha}^{2}} = \frac{1}{2} k_{\perp}^{2} \rho_{\alpha}^{2}$$

$$I_{n}^{\alpha} = I_{n}^{\alpha}(\lambda_{\alpha}).$$

3.B. Fast Wave Dispersion Relation

Previously, a small argument expansion in $\lambda \ll 1$ was used to obtain the fast wave dispersion relation. In Eqs. (3-4), both the Bessel functions and the exponentials involving λ are expanded in a power series. For example

$$K_{xx} \rightarrow A_o + A_1 k_\perp^2 + A_2 k_\perp^4 + A_3 k_\perp^6 + \ldots\ldots\ldots \qquad (3\text{-}5)$$

Equation (3-2) has a unique solution when

$$\det|\bar{\bar{D}}| = 0. \qquad (3\text{-}6)$$

A dispersion polynomial in powers of $k_\perp^2$ is obtained. If the dispersion polynomial is inverse Fourier transformed, we obtain a differential equation of the following form

$$D_o + D_1 k_\perp^2 + D_2 k_\perp^4 + D_3 k_\perp^6 + \ldots. = 0 \qquad (3\text{-}7)$$

$$D_o' + D_1' \frac{\partial^2}{\partial x^2} + D_2' \frac{\partial^4}{\partial x^4} + D_3' \frac{\partial^6}{\partial x^6} + \ldots = 0. \qquad (3\text{-}8)$$

Equation (3-8) describes the coupling between different propagating modes within the plasma. This differential equation may be solved to obtain coupling coefficients between the fast and Ion Bernstein branches at the ion cyclotron and ion-ion hybrid resonance layers (See Chapter 5 and Refs. (1,6-19)).

Equation (3-7) and hence Eq. (3-8) breaks down as λ approaches unity. For 3.52 MeV alphas in NUWMAK

$$\lambda_\alpha \approx \frac{5.2 \times 10^3\ T_i}{B^2} \qquad \begin{array}{l}(T_i \text{ in eV}) \\ (B \text{ in Gauss}) \\ k_\perp \sim 1\ \text{cm}^{-1}\end{array} \qquad (3\text{-}9)$$

$$\lambda_\alpha \approx 5 > 1 \quad . \qquad (3\text{-}10)$$

For 30 keV deuterons in NUWMAK

$$\lambda_D \approx \frac{1.04 \times 10^4\ T_i}{B^2} \qquad \begin{array}{l}(T_i \text{ in eV}) \\ (B \text{ in Gauss}) \\ k_\perp \sim 1\ \text{cm}^{-1}\end{array} \qquad (3\text{-}11)$$

$$\lambda_D \approx .1. \qquad (3\text{-}12)$$

If we want to investigate the effects of alphas and hot ions on the RF power absorption and deposition, the small λ expansion should not be used.

Therefore, Eq. (3-6) is solved numerically using the full 3 x 3 hot plasma dispersion tensor (Eq. (3-4)). The dispersion relation includes electrons, deuterons, tritons, alphas and carbon in NUWMAK, and electrons, deuterons, protons and oxygen in PLT calculations. In the Fokker-Planck code FORCE (see Chapter 4), the dispersion relation finds $k_\perp$ at a single point (r = 0). In the space-time codes STICR-I and STICR-II (see Chapter 5), a local $k_\perp(r)$ is calculated at 117 points across the entire plasma cross section.

In the dispersion relation, five harmonics are summed over ($n = 0, \pm 1, \pm 2, \pm 3, \pm 4, \pm 5$). Therefore, the RF frequency can be between 0 and $4f_{ci}$ and $k_\perp(r)$ is accurate at any temperature. Though each species may have a different temperature, we have assumed that each distribution is an isotropic Maxwellian.

To test the accuracy of the dispersion relation code given in Appendix A, we have examined the same reactor plasma parameters as Stix(20). In Table 3-1, we find very close agreement with Stix's results. In the calculations, we have assumed a real RF frequency, ω, and parallel wavenumber, $k_\parallel$ determined by the launching structure. The perpendicular wavenumber, $k_\perp$, obtained is complex. Stix neglects the complex part, which is good approximation in the case he examines since

$$\frac{|\mathrm{Im}k_\perp|}{|\mathrm{Re}k_\perp|} << .1. \tag{3-13}$$

Besides comparison with Stix's case, we compare the hot plasma $k_\perp^2(r)$ with the cold plasma result(1,21)

$$\frac{S}{P} n_x^4 - (S - n_z^2)\, n_x^2 + (R - n_z^2)\,(L - n_z^2) = 0 \tag{3-14}$$

where

$$R = \sum_i \frac{\omega_{pi}^2}{\omega_{ci}(\omega + \omega_{ci})} \qquad L = -\sum_i \frac{\omega_{pi}^2}{\omega_{ci}(\omega - \omega_{ci})} \tag{3-15}$$

(3-15 continued)

$$S = \frac{R + L}{2} = -\sum_i \frac{\omega_{pi}^2}{(\omega^2 - \omega_{ci}^2)}$$

$$n_x^2 = \frac{k_\perp^2 c^2}{\omega^2} \qquad n_z^2 = \frac{k_\parallel^2 c^2}{\omega^2} . \qquad (3\text{-}15)$$

Away from the resonance zone, we find(16)

$$n_\perp^2 \approx \frac{(R - n_z^2)\,(L - n_z^2)}{S - n_z^2} \qquad (3\text{-}16)$$

where $n_z^2 = \frac{k_\parallel^2 c^2}{\omega^2}$. The $S = n_z^2$ appears to be a singular or resonant zone. However, near this point, the approximations used in deriving Eq. (3-16) break down and one should use Eq. (3-14). $R = n_z^2$ and $L = n_z^2$ describe cold plasma cutoff surfaces. Hot plasma effects allow propagation across these surfaces. Chapter 5 shows that the hot plasma $k_\perp$ is close to the cold plasma value except near the cyclotron resonance where cold plasma predicts a singularity.

In conclusion, we have seen that the hot plasma dispersion relation, which is numerically solved, produces values of $k_\perp$ which compare well with published and cold plasma results. Having confidence in the accuracy, we next proceed to calculate the effect that ICRF has on the ion and electron velocity space distributions in both a present day experiment (PLT) and a conceptual reactor(NUWMAK).

Table 3-1

Reactor Parameters

n_T	(cm^{-3})	5×10^{13}
T_i	(keV)	4
T_e	(keV)	4
B_o	(kG)	40
R	(cm)	274
a	(cm)	60
f	(MHz)	$30.5 = f_{cD}$

	STIX	BLACKFIELD
$k_{\parallel}(cm^{-1})$	.511	.500
$k_{\perp}^2(cm^{-2})$	.0642	$(.0641, 1.06 \times 10^{-4})$
$k_{\perp cp}^2$ cold plasma(cm^{-2})		.0644
K_{xx}	-1.41×10^3	$(-1.403 \times 10^3, .513)$
K_{yy}	-1.41×10^3	$(-1.406 \times 10^3, 5.515)$
K_{xy}	$-i2.12 \times 10^3$	$(-.715, -2.109 \times 10^3)$
K_{yz}	(3810, 445)	(3814, 577)
K_{zz}	$(-6.65 \times 10^5, 5.6 \times 10^6)$	$(-8.66 \times 10^5, 5.77 \times 10^6)$
ΔK_{yy}	5.14	5.03
ΔK_{yz}	3810	3814
ΔK_{zz}	5.65×10^6	5.77×10^6
$\lvert E_y/E_z \rvert$	1453	1478
$\lvert E_+/E_- \rvert$	.179	.180
E_+/iE_y	-.218	-.220
P_{TT}/P_{CT}	-.998	-.981
P_L/P_{CT}	-.514	-.515
P_{TT}/P_L	1.92	1.90

CHAPTER 3 REFERENCES

1. B. McVey, Univ. of Wisconsin-Madison Report PLP 716 (Feb., 1977).

2. T.K. Mau, Ph.D. Thesis, Univ. of Wisconsin-Madison (1977).

3. D.G. Swanson, Phys. of Fluids 10 (1967) 428.

4. D.T. Blackfield, UWFDM-278 (Jan., 1978).

5. S. Ichimaru, Basic Principles of Plasma Physics A Statistical Approach, W.A. Benjamin Inc. Reading, Mass. (1973).

6. R.R. Weynants, Phys. Rev. Lett. 33 (1974) 78.

7. D.G. Swanson, Y.C. Ngan, Phys. Rev. Lett. 35 (1975) 517.

8. D.G. Swanson, Phys. Rev. Lett. 36 (1976) 316.

9. Y.C. Ngan, D.G. Swandson, Phys. of Fluids 20 (1977) 1920.

10. J.E. Scharer, D.T. Blackfield, J.B. Beyer, T.K. Mau, Nuc. Fusion 17 (1977) 1920.

11. J. Jacquinot, B.D. McVey, J.E. Scharer, Phys. Rev. Lett. 39 (1977) 88.

12. F.W. Perkins, Nuc. Fusion 17 (1977) 1197.

13. F. Fidone, L. Gomberoff, Plasma Phys. 20 (1978) 689.

14. R. Klima, et al, Nuc. Fusion 15 (1975) 1157.

15. H. Takahashi, Journal de Physique 38 Supp. C-6 (Dec., 1977) 171.

16. B. McVey, PLP 755 (May, 1978); Nuc. Fusion 19 (1979) 461.

17. D.G. Swanson, in Radio Frequency Plasma Heating (Proc. 3rd Topical Conf., Pasadena, 1978) Paper D5.

18. J. Jacquinot, in Heating in Toroidal Plasmas (Proc. Joint Varenna-Grenoble Int'l. Symp. Grenoble, 1978) Vol. I, 127.

19. D.G. Swanson, "The Effects of Localized Absorption on the Mode Conversion Processes in the RF Heating of Plasmas," unpublished (1979).

20. T.H. Stix, Nuc. Fusion 15 (1975) 737.

21. T.H. Stix, The Theory of Plasma Waves, McGraw-Hill, N.Y. (1962).

CHAPTER 4

ANISOTROPY AND TAIL FORMATION IN ICRF HEATED TOKAMAK PLASMAS

4.A. The Fokker-Planck Equation

ICRF heating has produced velocity space anisotropy in ion distributions in several experiments to date (see Chapter 1). In this chapter we examine the ICRF produced anisotropy predicted by our model to occur in PLT and compare our results with the experiment. Finding good agreement, we proceed to examine the reactor regime to see if high energy ion tails are formed which enhance the fusion output, thereby reducing the auxiliary heating requirement.

To examine the time evolution of particle distributions, we start with the Boltzmann transport equation$^{(1-3)}$. This equation describes the statistical transport of particles in a plasma. A Fokker-Planck collision operator is used which takes into account small angle Coulomb scatterings between particles (two-body scattering). Upon adding a source term, due to neutral beam or alpha particle production, the following Fokker-Planck Equation is obtained

$$\frac{\partial f_\beta}{\partial t} + \overline{v} \cdot \frac{\partial f_\beta}{\partial \overline{r}} + \frac{\overline{F}}{m_\beta} \cdot \frac{\partial f_\beta}{\partial \overline{v}} = \left.\frac{\partial f_\beta}{\partial t}\right)_c + S_\beta \qquad (4\text{-}1)$$

for species "β", where $f_\beta(\bar{r},\bar{v},t)$ is the distribution function in the six dimensional phase space $(\bar{r},\bar{v})$ and $\left.\frac{\partial f_\beta}{\partial t}\right)_c$ is the Fokker-Planck collision operator in spherical coordinates. $S_\beta(\bar{r},\bar{v},t)$ is the source function and $\bar{F}$ is the force acting on species "β".

The multispecies, two dimensional in velocity space, 0-D in real space Fokker-Planck Radiofrequency heating Code, FORCE, is an improved version of HYBRID-III.(4-5) HYBRID-III, which included quasilinear ICRF heating terms, was an outgrowth of HYBRID-II(6) developed at Lawrence Livermore Laboratories. Since FORCE is spatially independent

$$\frac{\partial f_\beta}{\partial \bar{r}} = 0. \tag{4-2}$$

Any force which acts on species "β" is assumed to arise from an external magnetic field about which f_β possesses azimuthal symmetry. Therefore,

$$\frac{\bar{F}}{m_\beta} \cdot \frac{\partial f_\beta}{\partial \bar{v}} = 0. \tag{4-3}$$

Equation (4-1) becomes

$$\frac{\partial f_\beta}{\partial t} = \left.\frac{\delta f_\beta}{\delta t}\right)_c + S_\beta \tag{4-4}$$

and Eq. (4-4) takes the following form(7-12)

$$\frac{\partial f}{\partial t} = n_o \Gamma \left[\frac{1}{v^2} \frac{\partial}{\partial v} \left(\bar{A} f + \bar{B} \tilde{v} \frac{\partial f}{\partial v} + \bar{C} \frac{\partial f}{\partial \theta} \right) + \right. \tag{4-5}$$

$$\left. \frac{1}{\tilde{v} v^2 \sin^2 \theta} \frac{\partial}{\partial \theta} \left(\bar{D} f + \bar{E} \tilde{v} \frac{\partial f}{\partial v} + \bar{F} \frac{\partial f}{\partial \theta} \right) \right] + S$$

upon dropping the "β" subscript, where $\Gamma = \Gamma_\beta = 4\pi Z_\beta^4 A^4/m^2$ and $n_o = n_{o\beta}$ is a normalizing density; $\tilde{v}$ is a normalizing velocity; and the expressions $\bar{A},\bar{B},\bar{C},\bar{D},\bar{E},\bar{F}$ are functions of the distribution and independent variables (v,θ). To this Fokker-Planck equation, quasi-linear ICRF heating terms are added.

4.B. Quasi-Linear ICRF Theory

Quasi-linear theory describes the evolution of particle distributions under the action of a spectrum of uncorrelated waves, an inherently stochastic heating process. Stix(13) has argued that this formalism is applicable to the study of ICRF heating when the plasma is "sufficiently collisional". This means collisions are so frequent that wave-particle coherence is destroyed between successive transits of the particle through the resonant heating zone. Appendix B shows that both PLT and NUWMAK satisfy the "sufficiently collisional" condition.

Several assumptions are used in ICRF quasi-linear theory.(14) These are listed in Table 4-1. The last assumption implies that there is no strong dependence of the spatially averaged distribution function on the azimuthal velocity about the constant magnetic field, hence

$$\frac{\partial f}{\partial \phi} = 0. \qquad (4\text{-}6)$$

This assumption does allow the distribution to be strongly anisotropic, providing the time variation of the average particle distribution is small during one particle duration.

Beginning with the Vlasov equation,$^{(2-3,14)}$ with $f^+(\bar{r},\bar{v},t)$ describing the ions and $f^-(\bar{r},\bar{v},t)$ the electrons, we have

$$\frac{\partial f^{\pm}}{\partial t} + \bar{v} \cdot \bar{\nabla} f^{\pm} \pm \frac{e}{m \pm c}(c\bar{E} + \bar{v} \text{ x } \bar{B}) \cdot \frac{\partial f^{\pm}}{\partial \bar{v}} = 0. \qquad (4\text{-}7)$$

We now assume that $f^{\pm}$,$\bar{E}$ and $\bar{B}$ can be expressed as the sum of a spatially independent part and a small rapidly fluctuating part due to the RF wave. Let $\delta f^{\pm}$ be the rapidly fluctuating part of the distribution

$$\int d^3r \; \delta f^{\pm} = 0. \qquad (4\text{-}8)$$

Then

$$f^{\pm}(\bar{r},\bar{v},t) = g^{\pm}(\bar{v},t) + \int \frac{d^3k}{(2\pi)^3} \, \delta f^{\pm}(\bar{v},t) e^{i\bar{k} \cdot \bar{x}} \qquad (4\text{-}9)$$

with

$$g \equiv \lim_{V \to \infty} \frac{1}{V} \int d^3r f^{\pm}(\bar{r},\bar{v},t) \qquad (4\text{-}10)$$

where V is the volume of integration after Fourier analyzing f in space.

Fourier analyzing the magnetic and electric fields in space

$$\bar{B}(\bar{r},t) = B_o\hat{z} + \int \frac{d^3k}{(2\pi)^3} \bar{B}_k(t) \; e^{i\bar{k} \cdot \bar{x}}$$

$$\bar{E}(\bar{r},t) = \int \frac{d^3k}{(2\pi)^3} \bar{E}_k(t) \; e^{i\bar{k} \cdot \bar{x}}. \qquad (4\text{-}11)$$

Upon transforming from Cartesian to cylindrical coordinates, assuming real wave frequencies, and expanding g in the power of $1/\Omega^{\pm}$ to first order, we obtain the Kennel and Engelmann quasilinear diffusion equation(14) with $q^{\pm} \rightarrow f$

$$\frac{\partial f_{\beta}}{\partial t} = \lim_{V \to \infty} \sum_{n} \frac{\pi e^{2}}{m_{\beta}^{2}} \int \frac{d^{3}k}{V(2\pi)^{3}} L_{\perp} V \, \delta(\omega - k_{\parallel} v_{\parallel} - n\Omega_{\beta}) |\theta_{n,k}|^{2} L f_{\beta} \qquad (4\text{-}12)$$

where

$$L \equiv \left(1 - \frac{k_{\parallel} v_{\parallel}}{\omega}\right) \frac{1}{v_{\perp}} \frac{\partial}{\partial v_{\perp}} + \frac{k_{\parallel}}{\omega} \frac{\partial}{\partial v_{\parallel}}$$

and

$$\theta_{n,k} \equiv \frac{e^{i\psi}}{2} (E_{x} - iE_{y})_{k} J_{n+1} + \frac{e^{-i\psi}}{2} (E_{x} + iE_{y})_{k} J_{n-1} + \frac{v_{\parallel}}{v_{\perp}} (E_{z})_{k} J_{n} \qquad (4\text{-}13)$$

with

$$J_{n} \equiv J_{n}(k_{\perp} v_{\perp} / \Omega_{\beta}).$$

Equation (4-12) is for a spectrum of waves and contains a phase function Setting $\psi = 0$, assuming a monochromatic wave spectrum and transforming to spherical coordinates, Stix's quasi-linear diffusion equation is obtained(13)

$$
\begin{aligned}
\frac{\partial f_\beta}{\partial t} = {}& \frac{\pi e^2}{8m_\beta^2} \left|E_x + iE_y\right|^2 \Big\{\frac{1}{v^2}\frac{\partial}{\partial v} J_{n-1}^2 \delta(n\omega_{c\beta} - \omega + k_{\parallel}v_{\parallel})(v^2 \sin^2\theta \frac{\partial f_\beta}{\partial v} - \\
& v\sin\theta(\frac{k_{\parallel}v}{\omega} - \cos\theta)\frac{\partial f_\beta}{\partial \theta}) + \frac{1}{v^2 \sin\theta}\frac{\partial}{\partial \theta}(J_{n-1}\delta(n\omega_{c\beta} - \omega + k_{\parallel}v_{\parallel}) \\
& (-v\sin^2\theta(\frac{k_{\parallel}v}{\omega} - \cos\theta)\frac{\partial f_\beta}{\partial v} + \sin\theta(\frac{k_{\parallel}v}{\omega} - \cos\theta)^2 \frac{\partial f_\beta}{\partial v})\Big\} \\
& + \frac{\pi e^2}{8m_\beta^2} \left|E_x - iE_y\right|^2 \Big\{\frac{1}{v^2}\frac{\partial}{\partial v} J_{n+1}^2 (n\omega_{c\beta} - \omega + k_{\parallel}v_{\parallel})(v^2 \sin^2\theta \frac{\partial f_\beta}{\partial v} - \qquad (4\text{-}14) \\
& v\sin\theta(\frac{k_{\parallel}v}{\omega} - \cos\theta)\frac{\partial f_\beta}{\partial \theta}) + \frac{1}{v^2 \sin\theta}\frac{\partial}{\partial \theta}(J_{n+1}\delta(n\omega_{c\beta} - \omega + k_{\parallel}v_{\parallel}) \\
& (-v\sin^2\theta\,(\frac{k_{\parallel}v}{\omega} - \cos\theta)\frac{\partial f_\beta}{\partial v} + \sin\theta(\frac{k_{\parallel}v}{\omega} - \cos\theta)^2 \frac{\partial f_\beta}{\partial \theta}\,)\Big\} \\
& + \frac{\pi e^2}{8m_\beta^2} \left|E_{\parallel}\right|^2 \Big\{\frac{1}{v^2} J_n^2 \,\mathrm{ctn}^2\theta\,\delta(n\omega_{c\beta} - \omega + k_{\parallel}v_{\parallel})(v^2 \sin^2\theta \frac{\partial f_\beta}{\partial v} - \\
& v\sin\theta(\frac{k_{\parallel}v}{\omega} - \cos\theta)\frac{\partial f_\beta}{\partial \theta} + \frac{1}{v^2 \sin\theta}\frac{\partial}{\partial \theta}(J_n^2 \,\mathrm{ctn}^2\theta\,\delta(n\omega_{c\beta} - \omega + k_{\parallel}v_{\parallel}) \\
& (-v\sin^2\theta(\frac{k_{\parallel}v}{\omega} - \cos\theta)\frac{\partial f_\beta}{\partial v} + \sin\theta(\frac{k_{\parallel}v}{\omega} - \cos\theta)^2 \frac{\partial f_\beta}{\partial \theta})\Big\} \;.
\end{aligned}
$$

Rewriting Eq. (4-14) in the same form as Eq. (4-5), the following RF diffusion terms may be added to the terms in Eq. (4-5)$^{(13,15\text{-}16)}$

$$
\begin{aligned}
\bar{A}_{RF} &= 0 \\
\bar{B}_{RF} &= C\,\frac{v^2\sin^2\theta}{\tilde{v}} \\
\bar{C}_{RF} &= -C(v\sin\theta(\frac{k_{\parallel}v}{\omega} - \cos\theta)) \\
\bar{D}_{RF} &= 0 \\
\bar{E}_{RF} &= -\,C(v\sin^2\theta(\frac{k_{\parallel}v}{\omega} - \cos\theta)) \\
\bar{F}_{RF} &= C((\tilde{v}\sin\theta(\frac{k_{\parallel}v}{\omega} - \cos\theta)^2)
\end{aligned}
\qquad (4\text{-}15)
$$

where

$$C = \{|(E_x + iE_y)J_{n-1}|^2 + |(E_x - iE_y)J_{n+i}|^2 + |E_{\parallel}J_n|^2\text{ctn}^2\theta\}\cdot \frac{\delta(n\Omega_\beta - \omega + k_{\parallel}v_{\parallel})}{32\,Z_\beta^2 e^2 n_{o\beta}}\,. \qquad (4\text{-}16)$$

To eliminate the delta function we integrate over a magnetic flux surface of radius "a" to obtain the following expression for C (see Appendix C and refs. (13,15-16)).

$$C \rightarrow \frac{\{|E_+J_{n-1}|^2 + |E_-J_{n+1}|^2 + |E_{\parallel}J_n|^2\text{ctn}^2\theta\}}{32\pi a\, Z_\beta^2 e^2 n_{o\beta} n\Omega_\beta(r=0)\xi} \qquad (4\text{-}17)$$

where

$$
\begin{aligned}
E_+ &\equiv E_x + iE_y \\
E_- &\equiv E_x - iE_y \\
\xi &= (1 - (\frac{R}{a})^2\,(\frac{n\Omega_\beta(r=0)}{\omega + k_{\parallel}v_{\parallel}} - 1)^2)^{1/2}\,.
\end{aligned}
$$

In Eq. (4-14), the fast wave $k_\perp$ and the RF electric fields are used. FORCE uses Eqs. (3-4 and 6) to find these. Since FORCE is 0-D in real space, mode conversion is neglected and only the smallest or fast wave root is used.

Equation (3-2) is solved to obtain the ratios E_y^f/E_x^f and E_z^f/E_x^f. E_x^f is assumed real to fix the phase of the electric field. Taking the second moment of the quasi-linear operator, the following power balance equation is obtained

$$\int \frac{1}{2} mv^2 \frac{\partial f}{\partial t} d^3v = \frac{\partial E}{\partial t} = P_{RF}. \qquad (4\text{-}18)$$

The RF electric field is normalized so that all the RF power is absorbed to the plasma

$$P_{RF} \equiv \text{Input RF Power} = \sum_\beta \int \frac{1}{2} mv^2 D_{RF}^\beta d^3v \qquad (4\text{-}19)$$

where D_{RF}^β is the RF quasi-linear Diffusion Operator, Eq. (4-14).

The RF dispersion relation assumes that each species is an isotropic Maxwellian. To take into account nonMaxwellian effects, an equivalent Maxwellian temperature is used

$$T_\beta \equiv \frac{\frac{2}{3}\int \frac{1}{2} m_\beta v^2 f_\beta(\bar{v}) d^3v}{\int f_\beta(\bar{v}) d^3v} . \qquad (4\text{-}20)$$

4.C-1. PLT

The effects of Coulomb collisions and the RF quasi-linear operator on the time evolution of the electron, deuteron, proton, and oxygen particle distributions will now be examined. A global picture is used except in the RF calculations where $\omega = n\omega_{cio}$. PLT parameters are given in Table 4-2.

The fast wave $k_\perp^2$ increases slightly in time. The real part is close to the cold plasma value as shown in Fig. (4-1). For PLT $\frac{\mathrm{Im}k_\perp^2}{\mathrm{Re}k_\perp^2} < 0.1$ so the imaginary part may be neglected.

The spatially averaged RF electric field components are shown in Figs. (4-2-4). Due to the presence of hydrogen in PLT, there is an increase in the E_+ contribution to the wave field

$$\frac{|E_+|}{|E_-|} \sim .1 \qquad (4\text{-}21)$$

while the $E_\parallel$ component is much smaller

$$\frac{|E_\parallel|}{|E_-|} \sim 3 \times 10^{-4}. \qquad (4\text{-}22)$$

The plasma conductivity increases with increasing temperature. To keep the RF power level constant, the magnitude of the wave field decreases. The RF power flow to the ions increases in time since $\mathrm{Im}k_\perp^2$ increases. In Fig. (4-5) the RF power to deuterium, hydrogen and electrons is plotted. Over 90% of the power is absorbed by the protons through fundamental minority damping. There is very little second harmonic damping by the deuterons. Though the electrons initially absorb 40 kW of power, as the ion temperature increases this amount drops to 10 kW.

In the PLT experiments,$^{(17)}$ the plasma reached a steady state 40 ms after the RF was turned on. All the species appeared to be isotropic. Hydrogen was the only species containing a high energy tail, with an effective temperature of 15 keV.(17-18)

In PLT, the bulk plasma ions increase 200 eV in temperature while the electrons do not appear to be heated.(17,19)

Since the Fokker-Planck collision operator conserves energy, the entire plasma cannot reach an equilibrium when only a source term is present. Some of the distributions may reach a steady state if collisional losses with cooler species balance with the direct RF heating term and collisions with hotter species.

Computationally, PLT does not reach equilibrium during the RF pulse. The total system energy increases in time. Since there are no overall plasma energy loss mechanisms

$$\Delta E_{\text{plasma}} \equiv E_{RF} = 350 \text{ kW x } 100 \text{ ms.} \tag{4-23}$$

Figure (4-6) shows that none of the distributions reach steady state. The electrons are seen to increase in temperature from 650 eV at t=0 to 1120 eV when the RF is shut off at t = 100 ms. Since $T_e < T_H$ at t = 100 ms, the electrons continue to heat to a temperature of 1200 eV at t = 130 ms. The distributions reach a steady state 30 ms after the RF is turned off. The deuterium temperature increases 930 eV during the RF pulse, over 4 times the experimental value. After the RF is shut off, the deuterons continue to heat due to hotter protons slowing down on the deuterons, reaching a steady state value of 1890 eV. The oxygen closely follows the deuterium temperature.

Since the protons receive over 300 kW of RF power, T_H is the highest temperature during the RF pulse with $\frac{T_H}{T_D} \sim 2.1$ at t = 100 ms.

Initially $T_e > T_H, T_D, T_O$ so energy flows from the electrons to the ions and T_e drops (Fig. (4-7)). After 10 ms, $T_e < T_H$, power flows from the hotter protons to the electrons and T_e increases until well after the RF is turned off. Only the protons cool after the RF is shut off, $T_H > T_e, T_D, T_O$. All species reach the same temperature ∿ 1.2 keV, 30 ms after the RF is off.

FORCE assumes that electrons are isotropic since the electron isotropization time is short(20)

$$\tau^e_{iso} \sim \frac{T_e^{3/2}}{8.2 n_e \ln\Lambda} \simeq 10^{-9} \text{ sec.} \qquad (4\text{-}24)$$

The electrons absorb a small amount of RF power, so they remain Maxwellian. The deuterons and fully stripped oxygen impurities, like the electrons, remain isotropic Maxwellians.

Since the protons absorb over 90% of the RF power, we find a significant deviation in the distribution from the initial Maxwellian. According to theory,(13,21-24) in the absence of other processes a high energy tail, stronger in the $v_\perp$ direction, should appear. A large high energy proton tail and anisotropy can be found on examining Figs. (4-8-10). In addition to the overall heating, the hydrogen distribution becomes elongated in the $v_\perp$ direction. The amount of anisotropy increases in time, reaching a peak value at t=100 ms of

$$\frac{T_{\perp H}}{T_{\parallel H}} = \frac{E_{\perp H}}{2E_{\parallel H}} = 1.3 \qquad (4\text{-}25)$$

as shown in Fig. (4-8).

From Figs. (4-9-10) we see a high energy tail forms which is somewhat stronger in the $v_\perp$ direction. From Figs. (4-11-12), we see that the hydrogen distribution relaxes back to an isotropic Maxwellian within 30 ms after the RF is off.

An estimate of the effective tail temperature can be obtained from examining the log f versus energy plots. The initial Maxwellian distribution is a straight line. Since

$$f_\beta \propto e^{-E/kT_\beta} \tag{4-26}$$

we can define an effective tail temperature

$$T_{eff} \equiv \frac{E_2 - E_1}{\log f(v_1) - \log f(v_2)} \quad . \tag{4-27}$$

Figure (4-10) shows in the tail

$$T_{eff} \sim 40 \text{ keV}. \tag{4-28}$$

This effective tail temperature is too high when compared to the experimental value.

The isotropization time for hydrogen in PLT is(20)

$$\tau_{iso}^{H,D} \sim \frac{m_H^{1/2} \; T_{\parallel H}^{3/2} \; A_H^2}{2\sqrt{\pi} \; e_H^4 n_H \ln\Lambda_{HD}} \left[-3 + (A_H+3) \frac{\tan^{-1} A_H^{1/2}}{A_H^{1/2}} \right]^{-1} \tag{4-29}$$

$$\sim 3 \text{ ms} (T_{\perp H}/T_{\parallel H} \sim 3). \tag{4-30}$$

The thermal equilibration time for hydrogen on deuterium for PLT is(20)

$$\tau_{eq.}^{H,D} = \frac{(m_D T_H + m_H T_D)^{3/2}}{1.8 (m_D m_H)^{1/2} n_D \ln\Lambda_{HD}} \times 10^{19} \text{ sec} \tag{4-31}$$

$$\sim 5 \text{ ms } (T_H = 2 \text{ keV}, \; T_D = 1 \text{ keV}) \tag{4-32}$$

while the slowing down time is(25-26)

$$\tau^{H}_{slow} = \tau \ln \frac{(E^{3/2}_{Ho} + E^{3/2}_{crit})}{(T^{3/2}_{e} + E^{3/2}_{crit})} \qquad (4\text{-}33)$$

where

$$\tau^{-1} \equiv \frac{1.5 \times 10^{-19} Z^2 n_e \ln\Lambda_e}{A_{plasma} T^{3/2}_{e}} \qquad (4\text{-}34)$$

$$\sim 12 \text{ ms } (E_{Ho} = 10 \text{ keV}, \ T_e = 1 \text{ keV}). \qquad (4\text{-}35)$$

On the time scale of the experiment (∿100 ms), one expects to observe a hot anisotropic hydrogen distribution with a high energy tail. In comparison to the experiment, the overall ion and electron temperature increases calculated by FORCE are too large. In addition, the hydrogen distribution is too anisotropic with too large a tail. There are several factors which might cause this discrepancy.

The RF power level has been taken to be

$$\langle P_{RF} \rangle = \frac{350 \text{ kW}}{\text{Volume}} = 0.067 \text{ W/cm}^3. \qquad (4\text{-}36)$$

The RF effects would be lessened if $\langle P_{RF} \rangle$ was smaller. However, from space-time calculations, we find $\langle P_{RF} \rangle$ at the center to be larger than Eq. (4-36). Therefore, the RF induced high energy tail should be larger in the center, not smaller.

In the previous figures, the RF heating was averaged over a magnetic flux surface with a minor radius of 10 cm. As this radius increases, fewer ions can satisfy the Doppler shifted resonance condition.

$$\omega + k_{\parallel}v_{\parallel}(r) - n\omega_{ci}(r) = 0. \tag{4-37}$$

If the total RF absorption is kept constant, as "a" increases, the amount of electron absorption must increase. This increased electron absorption would decrease the amount of hydrogen anisotropy and tail formation. The electron absorption is shown in Fig. (4-13) for three different radii, a = 1 cm, 10 cm, 20 cm. The decrease in hydrogen absorption is shown in Fig. (4-14). Figure (4-15) shows there is little change in the amount of hydrogen anisotropy as "a" increases from 10 cm to 20 cm. There is also little change in the tail formation. Chapter 5 shows for the RF heating zone, $a \leq 10$ cm, the actual amount of anisotropy and tail formation should be even larger.

Evidently, there must be other processes which greatly modify the ICRF power balance in PLT. These processes should also lead to steady state distributions during the RF pulse. Some possible processes are examined later in this chapter. For now, realizing that FORCE tends to overestimate the RF heating effects, we proceed to examine ICRF heating in the reactor regime. By including only RF and Coulomb collisions, an upper limit on the RF induced effects can be obtained.

4.C-2. Fundamental Minority Heating of Deuterium in NUWMAK

In this section and the next, we examine the effects of ICRF heating on particle distributions in the NUWMAK conceptual tokamak reactor(27-28). The space-time transport codes STICR-I and STICR-II assume that ions and electrons are nearly Maxwellian and all ions have the same temperature. In this section we examine these assumptions for minority heating of deuterium in NUWMAK.

The NUWMAK reactor parameters for a 10%D-90%T plasma are given in Table 4-3. We again assume a global picture using the average densities and temperatures and a RF power density

$$\langle P_{RF} \rangle = \frac{150\ \text{MW}}{\text{Volume}} = 0.71\ \text{W/cm}^3. \qquad (4\text{-}38)$$

From Chapter 5, we will find that the plasma ignites with 150 MW of RF power provided for 2.0 sec. By neglecting all loss mechanisms in this and the next section (charge exchange, radiation, finite radial confinement), an upper limit of the RF effects on the plasma will be obtained.

Figure (4-16) plots the hot and cold plasma $k_\perp^2$ as a function of time. $\text{Im}\,k_\perp^2$ is again small and could be neglected. Figures (4-17-19) show the value of the spatially-averaged RF electric field is the same order of magnitude as computed for PLT.

The presence of a minority concentration of deuterons again produces a large E_+ component

$$\frac{|E_+|}{|E_-|} \sim 0.1. \qquad (4\text{-}39)$$

$E_{\parallel}$ as in PLT, is again small

$$\frac{|E_{\parallel}|}{|E_{-}|} \sim 1.5 \times 10^{-3}. \tag{4-40}$$

In Fig. (4-20) the solid lines indicate RF power absorption when only collisions are present. Initially, the deuterons absorb over 90% of the RF power.

We have assumed a $10^{8} - 10^{9}$ cm^{-3} density of fully stripped carbon impurity at the center. This impurity, having the same cyclotron frequency as deuterium, absorbs the remaining RF energy (initially 3 MW). Since the concentration is quite low, and no losses are present, the carbon ions become quite hot and nonMaxwellian. As the carbon ions heat, they absorb more power until at t = 2.0 sec, they absorb ∿35 MW. In Fig. (4-21), we see $E_C \sim 800$ keV with $\frac{E_C}{E_T} \sim 80$. The impurities become highly anisotropic with

$$\frac{T_{\perp C}}{T_{\parallel C}} \sim 28. \tag{4-41}$$

Fig. (4-22) shows that a large high energy tail component appears and then disappears within 500 ms after the RF is off.

This computational result should not occur in NUWMAK. If we include a loss term due to finite radial confinement ($\tau_E^C \sim 5$ sec), we find that carbon remains cooler and absorbs less power (shown by the dash line in Fig. (4-20). The carbon absorbs less than 6 MW at t = 2.0 sec, becomes cooler, and

$$\frac{T_{\perp C}}{T_{\parallel C}} \sim 1.8 \; . \qquad (4\text{-}42)$$

From Chapter 5, we find over 60% of the RF power damped by the electrons before the fast wave reaches the cyclotron resonance layer at the plasma center. The carbon impurities at the center should absorb a significantly lower amount of power and, therefore, remain Maxwellian. If the resonant zone is moved to the plasma edge, the impurities may absorb a large amount of power and become highly anisotropic. If their transport out of the plasma is enhanced, ICRF with $\omega = \omega_{CZ}$ (r = outside edge) may provide a good barrier against impurity penetration to the plasma center.

When the RF is shut off, the system energy continues to increase due to fusion produced alphas which slow down in the plasma. The steep rise in the fusion energy curve near the RF shutoff (see Fig. (4-23)) indicates ignition. At the time the RF is turned off

$$Q \equiv \frac{\text{FUSION POWER}}{\text{RF POWER}} \simeq 1.27 \; . \qquad (4\text{-}43)$$

The electron temperature increases from an Ohmically heated value of 2.0 keV to 6.3 keV at t = 2.0 sec, reaching a value of 7.2 keV at 2.5 sec (Fig. (4-24)). The electrons remain Maxwellian during the entire startup phase, being heated only through collisional processes (Ohmic heating being small at high temperatures).

Figure (4-24) shows the initial tritium temperature of 2.0 keV increases to 6.2 keV at the time the RF is turned off. At

$t = 2.5$ sec, $T_T \sim 7.0$ keV. During the RF phase $T_T \approx T_e$. The alphas slow down preferentially on the electrons. After the RF is off and there is a great number of fusion events occuring, the electrons absorb more fusion energy than the tritons so the electrons become slightly hotter.

The tritons remain an isotropic Maxwellian. This is again expected since the tritons are only heated by collisions with hotter species. On the other hand, the deuterons absorb over 90% of the RF power. One may expect, in analogy to the protons in PLT, that deuterium becomes nonMaxwellian and hotter than the other species (excepting the alphas).

From Fig. (4-24) we find that during the RF phase $T_D \approx T_T$. At $t = 2.0$ sec, $\frac{T_D}{T_T} = 1.03$. Both the plots of $f(v_\perp)$, $f(v_\parallel)$ (Figs. (4-25-26)) show that deuterium ions remain isotropic and no high energy tail develops. Although the deuterons absorb almost 150 MW of power, they remain Maxwellian. These results, which differ with PLT, can be explained.

First, the amount of RF energy per minority heated particle is smaller. In PLT, we have

$$\frac{\langle P_{RF} \rangle}{n_H} \sim 3.5 \times 10^{-14} \text{ W/particle} \qquad (4\text{-}44)$$

while in NUWMAK

$$\frac{\langle P_{RF} \rangle}{n_D} \sim 2.3 \times 10^{-14} \text{ W/particle.} \qquad (4\text{-}45)$$

The amount of energy available to drive an individual ion into the tail is less in NUWMAK. In addition, the various Maxwellian producing characteristic times (Eqs. (4-29,31,33)) are shorter in NUWMAK

$$\tau_{iso} \sim 0.4 \text{ ms } (T_\perp / T_\parallel = 3) \qquad (4\text{-}46)$$

$$\tau^{D,T}_{eq.} \sim 2.7 \text{ ms } (T_D = 6 \text{ keV}, T_T = 4 \text{ keV}) \qquad (4\text{-}47)$$

$$\tau_{slow} \sim 0.7 \text{ ms } (E_{Do} = 10 \text{ keV}, T_e = 4 \text{ keV}). \qquad (4\text{-}48)$$

These faster times, together with the lower P_{RF} per particle value leads to isotropic Maxwellian deuterons. The short equilibration time causes the tritium and electron temperatures to closely follow the deuterium temperature.

One reason ICRF appeared to be an attractive heating source was its potential for producing high energy ions which would enhance the fusion output. Earlier calculations(4) showed Q enhancement for ICRF heating would be less than 11%. If charge exchange, radiation, Ohmic heating and radial losses are included, any Q enhancement would be decreased. When space-time results are examined, we can see there should be very little, if any, Q enhancement for minority heating of deuterium in NUWMAK.

Unlike PLT, it appears a one ion temperature fluid model, as in STICR-II, is a good approximation for NUWMAK if the alphas are not included. Initially, we have assumed a Maxwellian alpha population with $n_\alpha = 8\text{x}\ 10^8\ \text{cm}^{-3}$ is present in NUWMAK with a temperature of 2.0 keV. Since the alphas are born at 3.52 MeV, a high energy tail is formed, shown in Fig. (4-27). The distribution averaged alpha energy is quite high, shown in Fig. (4-28). As the plasma heats, the alphas slow down on an increasingly hotter background, producing an increasing average alpha energy. The alpha density is only $2.75 \times 10^{11}\ \text{cm}^{-3}$ by the time the RF is turned off, so the alphas do not absorb any RF power.

STICR-II assumes the alphas instantaneously deposit their energy in the background plasma. The alpha temperature is then the same as the other ions. This is the case for the majority of alphas. However, since there are a significant number of alphas always in the process of slowing down, indicated by the tail, STICR-II overestimates the amount of fusion energy during the startup phase, although the difference is small.

In the NUWMAK reactor, we find

$$k_\perp \rho_i \sim \frac{k_\perp (2E_i m_i c^2)^{\frac{1}{2}}}{q_i\ B_o} \qquad (4\text{-}49)$$

$$k_\perp \rho_\alpha \sim .4 \; (k_\perp \sim 1 \text{ cm}^{-1}) \tag{4-50}$$

for alphas and

$$k_\perp \rho_C \sim .5 \; (k_\perp \sim 1 \text{ cm}^{-1}) \tag{4-51}$$

for carbon. In this case, the small gyroradius expansion is not appropriate and one needs to use the complete 3 x 3 determinant as done in FORCE.

Except for alphas and possibly impurities, the ions and electrons remain Maxwellian for minority heating in NUWMAK. A fluid model should be accurate in NUWMAK and is used in Chapter 5. We now examine in our idealized picture a similar plasma to that used in Chapter 2.

4.C-3. Second Harmonic Deuterium Heating in NUWMAK

Since fundamental minority heating in the reactor regime does not produce high energy tails, we now proceed to the next higher harmonic. Since

$$P_{RF} \propto (k_\perp^2 v_\perp^2)^{n-1} \propto (k_\perp \rho_i)^{n-1} \tag{4-52}$$

second harmonic heating might produce a larger tail.

For this case, we have a 50%D-50%T plasma with parameters given in Table 4-3. In second harmonic heating $k_\perp^2$ is larger as shown in Fig. (4-29). This larger value of $k_\perp^2$ should also help produce a larger ion tail.

By increasing the concentration of deuterium to 50%, the E_+ component of the wave field is increased. Figs. (4-30-32) show

$$\frac{|E_+|}{|E_-|} \sim \frac{1}{3} \qquad (4\text{-}53)$$

while the $E_{\parallel}$ component is still very small

$$\frac{|E_{\parallel}|}{|E_-|} \sim 9 \times 10^{-4}. \qquad (4\text{-}54)$$

Second harmonic absorption is weaker than fundamental damping. To produce the same amount of RF heating we find the RF electric field must be larger

$$\frac{|E_+|_{\text{second harmonic}}}{|E_+|_{\text{fundamental}}} \sim 4.4 \text{ and } \frac{|E_-|_{\text{second harmonic}}}{|E_-|_{\text{fundamental}}} \sim 1.5. \qquad (4\text{-}55)$$

The increased concentration of deuterium produces more fusion alphas for the same plasma temperature. In Chapter 5 we find only 100 MW for 1.5 sec is needed to ignite the reactor. For the same temperature and total ion density, the amount of increased fusion power is

$$\frac{P_\alpha^{50-50}}{P_\alpha^{10-90}} = \frac{(\frac{1}{2})\,(\frac{1}{2})}{(\frac{1}{10})\,(\frac{9}{10})} = 2.8 \quad . \qquad (4\text{-}56)$$

Figure (4-33) shows that 97 MW of RF power is deposited in the deuterons. Tritium, through third harmonic damping, absorbs only 0.7-1.0 MW, while 2 MW is deposited in the electrons. In contrast with the previous case, the carbon impurities absorb a negligible amount of RF power (~100 kW) as do the alphas.

Figure (4-34) shows ignition is again reached. The total system energy increases after the RF is turned off and there is again a steep rise in the fusion energy curve. At t = 1.5 sec

$$Q \sim 1.33 \ . \qquad (4\text{-}57)$$

In Fig. (4-35), the initial electron temperature of 2.0 keV increases to 4.6 keV at t = 1.5 sec and reaches a value of 5.3 keV at t = 2.0 sec. The electrons again remain Maxwellian during the startup phase.

Figure (4-35) shows that the tritium and carbon temperatures are now equal. At the RF shutoff point, $T_T = T_C = 4.6$ keV. After ignition, the electrons are again slightly hotter. At t = 2.0 sec, $T_T = T_C = 5.2$ keV. Tritium remains an isotropic Maxwellian, while in contrast with the minority heating case, the carbon impurity is also an isotropic Maxwellian. Second harmonic damping on impurities is small since RF power absorption is proportional to the density. With the carbon density low, the impurities are not heated.

The alphas again have a much higher average energy, shown in Fig. (4-36) and there is again a high energy component due to thermalizing alphas (Fig. (4-37)).

From Figs. (4-38-39) we see the deuterons, as before, remain an isotropic Maxwellian. Although 97% of the RF power is deposited in the deuterons we again find $T_D \approx T_T$ ($\frac{T_D}{T_T} \sim 1.01$ at $t = 1.5$ sec, in Fig. (4-35)). The characteristic slowing down, isotropization, and equilibration times calculated in Eqs. (4-46-48) together with the decreased amount of RF power per particle heated

$$\frac{\langle P_{RF} \rangle}{n_D} \sim 3.1 \times 10^{-15} \text{ W/particle} \tag{4-58}$$

again counteract any anisotropization or tail formation in the deuterons. If the energy losses are included along with spatial effects, we can again expect that any Q enhancement will be negligible. If the shorter characteristic times for NUWMAK are ignored, to get the same RF power per particle heated as in PLT, one would need to supply 1000 MW. If the shorter characteristic times are included, almost 10 GW of RF power would be needed to get the same amount of anisotropy and tail formation as in PLT.

4.C-4. Conclusions for ICRF Heating of NUWMAK

From examination of fundamental and second harmonic heating of NUWMAK in our model, we find that deuterons, tritons, and electrons all remain isotropic Maxwellians. Although the deuterons absorb over 90% of the RF power, the reactor equilibration time is so short that $T_D \approx T_T$.

The alphas are not Maxwellian in either case. However, since they do not absorb a significant amount of RF power, the Maxwellian assumption used in STICR-II should not affect the RF calculations. The assumption of alphas slowing down instantaneously does not change the auxiliary heating requirement since the amount of alpha energy in the tail during the RF startup is small.

The carbon impurities remain Maxwellian in the second harmonic heating case. In fundamental heating, we found that impurities could become quite hot and nonMaxwellian in the absence of any energy loss mechanisms. When finite radial confinement losses are included, these effects are greatly reduced. When these results are coupled with spatial effects, found in Chapter 5, we conclude that impurities should remain Maxwellian with $T_D \approx T_T \approx T_C$.

We can conclude from our FORCE reactor calculations that a fluid model with a single ion energy equation should be accurate for ion harmonic heating with the resonance zone near the plasma center. There is little tail produced Q enhancement. However, to be sure of our conclusions, we need to return to the PLT results, include possible plasma processes which tend to inhibit RF heating and see if FORCE agrees with the experiment.

4.D. PLT-Additional Heating and Cooling Processes

In the previous examination of PLT, when only collisions and RF heating were considered, the results obtained from FORCE differed substantially from the experiment. Either the RF model is in error, or other processes must be included. In this section, we examine several heating and cooling mechanisms which when included, provide good agreement. We then conclude that if "PLT" scaling holds in the reactor regime, our results, which found no anisotropy or tail formation, should be valid for an ICRF reactor startup.

First, there is radial particle and energy transport due to finite particle (τ_P) and energy (τ_E) confinement. To model radial losses$^{(29)}$

$$\int \frac{\partial f_\beta}{\partial t} \, d^3v = \frac{\partial n_\beta}{\partial t} \rightarrow - \frac{n_\beta}{\tau_P^\beta} \tag{4-59}$$

and

$$\int \frac{1}{2} m_\beta v^2 \frac{\partial f_\beta}{\partial t} \, d^3v = \frac{\partial E_\beta}{\partial t} \rightarrow - \frac{E_\beta}{\tau_E^\beta} \, . \tag{4-60}$$

Dimensionally, this transport is modelled by inputing a τ_P and τ_E for each species consistent with the PLT experiment. Equation (4-5) together with eqs. (4-16,18) now become

$$\frac{\partial f_\beta}{\partial t} = \left.\frac{\delta f_\beta}{\delta f}\right)_c + S_\beta + D_{RF}^{\beta} - \frac{f_\beta}{\tau_P^\beta} + \frac{1}{2v^2} \frac{\partial}{\partial v} \frac{f_\beta v^3}{\tau_E^\beta} \tag{4-61}$$

or

$$= n_o\Gamma \left\{ \frac{1}{v^2}\frac{\partial}{\partial v} \left[A'f + B'\tilde{v}\frac{\partial f}{\partial v} + C'\frac{\partial f}{\partial \theta}\right] + \frac{1}{\tilde{v}v^2\sin^2\theta}\frac{\partial}{\partial \theta}\left[D'f + E'\tilde{v}\frac{\partial f}{\partial v} + F'\frac{\partial f}{\partial \theta}\right]\right\} + S - \frac{f}{\tau_P} + \frac{1}{2v^2}\frac{\partial}{\partial v}\frac{v^3 f}{\tau_E}. \quad (4\text{-}62)$$

Recycling in PLT keeps the ion densities constant during the RF pulse. To model this, we set all the particle confinement times to infinity. Later, when a neutral gas density is added, impact ionization creates a source of ions. The various ion particle confinement times are then readjusted to keep the ion density constant.

To find the electron energy confinement time we use the fact that in PLT, the electrons reach a quasi-equilibrium during the Ohmic heating phase before the RF is on

$$\frac{\partial E_e}{\partial t} + \nabla\cdot[Q_e' + E_e\Gamma_e] = P_{ei} + P_{OH} \qquad (4\text{-}63)$$

where P_{OH} is Ohmic heating; P_{ei} is electron-ion rethermalization; $\nabla\cdot[Q_e' + E_e\,\Gamma_e]$ represent conduction and convection losses. Setting

$$\nabla\cdot[Q_e' + \Gamma_e\,E_e] = \frac{E_e}{\tau_E^e} \qquad (4\text{-}64)$$

at equilibrium, Eqs. (4-63 and 64) become

$$\frac{-E_e}{\tau_E} = P_{OH} + P_{ei}. \qquad (4\text{-}65)$$

Since $P_{ei} << P_{OH}$, using Eq. (4-65) we find

$$\tau_E^e = \frac{-E_e}{P_{OH}} \sim 45 \text{ ms} \qquad (4\text{-}66)$$

for PLT with I = 350 kA, in agreement with the measured value.

In determining the hydrogen energy confinement time, we use the result from Chapter 5 which finds over 90% of the RF power goes to heating the protons in the plasma center. To model this spatial heating we set

$$\tau_E^H = C_{RF} \times \tau_E^D, \; C_{RF} = 2 \qquad (4\text{-}67)$$

where τ_E^D represents the bulk ion energy confinement time. The correction factor will be shown to be noncritical. Unless $\tau_E^H << \tau_E^D$, not seen experimentally, the hydrogen radial energy loss is small.

To find τ_E^D and τ_E^0, we use a parameter study of tokamak experiments by Hugill and Sheffield$^{(30)}$. The four parameter fit, reproduced in Fig. (4-40) is

$$\tau_E \sim 2.7 \; \bar{n}_e^{\,0.61} \; a^{1.57} \; B^{0.88} \; A_i^{\,0.65} \; (\text{ms}) \qquad (4\text{-}68)$$

where n is in 10^{13} cm^{-3}; a is in m; B is in kG; A_i is the atomic mass number. Although PLT was not used in deriving the empirical fit, they found the experimental value to be close to the fit. For PLT

$$\begin{aligned} \tau_E^D &\sim 30 \text{ ms} \\ \tau_E^0 &\sim 110 \text{ ms} \end{aligned} \qquad (4\text{-}69)$$

using the parameters in Table 4-4. Equation (4-67) becomes

$$\tau_E^H = 60 \text{ ms} \ . \qquad (4\text{-}70)$$

With only radial losses included in Eq. (4-62), FORCE was unable to simulate the experiment$^{(4)}$. Other processes besides radial transport need to be included. We now examine additional processes which affect the electrons.

4.D-1. Electrons in PLT

Besides Landau and transit time damping, Coulomb collisions and radial transport, the electrons are Ohmically heated and radiate energy away. On colliding with a hydrogen or deuterium neutral atom, an electron may lose 13.6 eV. Electron impact ionization increases the ion density and cools the electrons. By adding these three effects, we may define an effective electron energy confinement time

$$P_{OH} - P_Z - P_{EP} = \frac{E_e}{\tau_E^{*e}} \qquad (4\text{-}71)$$

where P_{OH} is the Ohmic heating term

$$P_{OH} = \eta_{SP} \, J^2 \qquad (4\text{-}72)$$

and where η_{SP} is the Spitzer resistivity.

P_Z is the radiation loss term (see Chapter 5)

$$P_Z = n_e n_Z L_Z \tag{4-73}$$

where L_Z is a polynomial fit to the reaction rate(31)

$$\mathrm{Log}_{10} L_Z = \sum_{i=0}^{5} A_i (\mathrm{Log}_{10} T_e)^i . \tag{4-74}$$

The A_i are numerical coefficients. P_{EP} is the electron impact ionization loss term(32)

$$P_{EP} \equiv n_e (n_{D^o} + n_{H^o}) \langle\sigma v\rangle_{EP} (-13.6 \text{ ev}) \tag{4-75}$$

with

$$\ln\langle\sigma v\rangle_{EP} = \sum_{i=0}^{5} B_i (\ln E)^i \tag{4-76}$$

also a polynomial fit with the assumption that ionization cross sections for H^o and D^o are equal.

Since FORCE preserves charge neutrality, an effective τ_P^{*e} is not needed. However, both a τ_P^* and a τ_E^* must be calculated for the hydrogenic species in PLT.

4.D-2. Hydrogenic Species in PLT

Impact ionization and charge exchange may cause the proton and deuteron densities to vary. We need to model an effective particle τ_P^* as well as energy τ_E^* confinement times for each species.

Let R designate the event rate for either ionization or charge exchange. A deuterium density balance equation can then be written

$$\frac{\partial n_D}{\partial t} = R_{cx}^{H,D^o} - R_{cx}^{D,H^o} + R_{ED^o} + R_{PD^o} \approx \frac{n_D}{\tau_P^{*D}} \qquad (4\text{-}77)$$

where R_{Cx}^{H,D^o} is the rate at which a proton collides with a deuterium neutral, D^o, to produce a hydrogen neutral, H^o, and a deuteron, D^+,

$$R_{cx}^{H,D^o} \equiv n_H n_{D^o} \langle\sigma v\rangle_{cx}. \qquad (4\text{-}78)$$

R_{cx}^{H,D^o} determines the rate at which a deuteron charge exchanges with a hydrogen neutral, becoming a deuterium neutral with a resulting decrease in the deuteron density

$$R_{cx}^{D,H^o} \equiv n_D n_{H^o} \langle\sigma v\rangle_{cx}. \qquad (4\text{-}79)$$

R_{ED^o} is the rate at which electrons ionize neutral deuterium(32)

$$R_{ED^o} \equiv n_e n_{D^o} \langle\sigma v\rangle_{EH} \qquad (4\text{-}80)$$

while R_{PD^o} is the rate at which hydrogenic ions ionize deuterium[32]

$$R_{PD^o} \equiv (n_H + n_D)\, n_{D^o} \langle\sigma v\rangle_{PH} \,. \tag{4-81}$$

In an analogous fashion, an effective τ_P^{*H} for hydrogen can be written

$$\frac{\partial n_H}{\partial t} = R_{cx}^{D,H^o} - R_{cx}^{H,D^o} + R_{EH^o} + R_{PH^o} \approx \frac{n_H}{\tau_P^{*H}} \tag{4-82}$$

where

$$R_{cx}^{D,H^o} \equiv n_D n_{H^o} \langle\sigma v\rangle_{cx}$$

$$R_{cx}^{H,D^o} \equiv n_H n_{D^o} \langle\sigma v\rangle_{cx}$$

$$R_{EH^o} \equiv n_e n_{H^o} \langle\sigma v\rangle_{EH}$$

$$R_{PH^o} \equiv (n_H + n_D)\, n_{H^o} \langle\sigma v\rangle_{PH} \,. \tag{4-83}$$

In the energy equation we again assume that 13.6 eV is lost per ionization event. In a charge exchange event, the ion and neutral effectively exchange energies. Therefore, for deuterium

$$\frac{\partial E_D}{\partial t} = P_{cx}^{H,D^o} - P_{cx}^{D,D^o} - P_{cx}^{D,H^o} - P_{DD^o} - P_{DH^o} \approx \frac{E_D}{\tau_E^{*D}} \tag{4-84}$$

and for hydrogen

$$\frac{\partial E_H}{\partial t} = P_{cx}^{D,H^o} - P_{cx}^{H,H^o} - P_{cx}^{H,D^o} - P_{HH^o} - P_{DH^o} \approx \frac{E}{\tau_E^{*H}} \tag{4-85}$$

where

$$P_{cx}^{\alpha,\beta^o} \equiv n_\alpha n_{\beta^o} <\sigma v>_{cx} (E_\alpha - E_{\beta^o})$$

$$P_{\alpha\beta^o} \equiv n_\alpha n_{\beta^o} <\sigma v>_{PH} (-13.6 \text{ eV}) \qquad (4\text{-}86)$$

for $\alpha = D,H$

$\beta^o = D^o,H^o$.

In the evaluation of the charge exchange and ionization cross sections, we have again assumed there is no difference between protons and deuterons. The general hydrogenic species charge exchange is(32)

$$\ln<\sigma v>_{cx} = \sum_i C_i(\ln E)^i \qquad (4\text{-}87)$$

while the ion impact cross section is

$$\ln<\sigma v>_{PH} = \sum_i D_i(\ln E)^i. \qquad (4\text{-}88)$$

The Fokker-Planck equation can now be written

$$\frac{\partial f}{\partial} = n_o\Gamma\left\{\frac{1}{v^2}\frac{\partial}{\partial v}[A'f + B'\tilde{v}\frac{\partial f}{\partial v} + C'\frac{\partial f}{\partial \theta}] + \right.$$

$$\frac{1}{\tilde{v}v^2\sin^2\theta}\frac{\partial}{\partial\theta}[D'f + E'\tilde{v}\frac{\partial f}{\partial\theta} + F'\frac{\partial f}{\partial\theta}]$$

$$\left. - \frac{f}{\tau_P} + \frac{1}{2v^2}\frac{\partial}{\partial v}v^3\frac{f}{\tau_E} - \frac{f}{\tau_P^*} + \frac{1}{2v^2}\frac{\partial}{\partial v}v^3\frac{f}{\tau_E^*}\right\} . \qquad (4\text{-}89)$$

$S_\beta \to 0$ and τ_P^{*e} , τ_P^{*o} , $\tau_E^{*o} \to \infty$ since there are no external sources, charge neutrality holds, and the impurities have no sources or sinks.

In the evaluation of the cross sections used in Eq. (4-89), all species were assumed to be isotropic Maxwellians with temperatures determined from the previous time step. Since the time step is .01 ms, the distributions do not change greatly over one step and this approximation should be valid. From Fig. (4-41) for PLT with T_e, $T_i \sim 1.0$ keV, charge exchange is the dominant cross section and proton impact is negligible. We now use FORCE to examine ICRF heating in PLT.

4.D-3. PLT Results

For the average neutral gas density in PLT, we have assumed $n_o = 2.2 \times 10^8$ cm^{-3} composed of 10% H^o and 90% D^o both at a temperature of 5 eV. This density results in a hydrogen charge exchange loss comparable to the experiment. A list of parameters for PLT, with these additional processes included, can be found in Table 4-4. When Figs.(4-1 and 42) are compared, we see these additional processes have a minimal effect on the dispersion relation, since the fast wave $k_\perp^2$ is weakly dependent on temperature. Figures (4-43-45) show the electric field components are not significantly changed either.

Again we see in Fig. (4-46) that fundamental damping is the strongest RF heating mechanism; 310-330 kW of RF power is absorbed by the protons. From these plots we see the RF heating process is unaffected by the various additions to the Fokker-Planck equation. However, the particle distributions are greatly altered.

In contrast with our earlier result, Fig. (4-47) shows the plasma now reaches a steady state, with $\tau_{RF} \sim 40-60$ ms, comparable to the experiment. The total system energy at t = 100 ms is now lower due to the losses, 3.4×10^{13} keV/cm^3 compared to 8.4×10^{13} keV/cm^3. Figure (4-48) shows all the distributions reach equilibria 40-60 ms after the RF pulse is turned on. In good agreement with PLT, the spatially averaged electron temperature does not increase significantly during the RF pulse. The FORCE code obtains $\overline{\Delta T_e} \sim 40$ eV.

FORCE has the average deuterium or bulk plasma ion temperature increasing 150 eV, in agreement with PLT. The average proton energy increase is now 450 eV as compared to 2240 eV calculated previously. At t = 100 ms, $\frac{T_H}{T_D} \sim 1.8$.

Figure (4-49) shows the importance of Ohmic heating, radial and radiation losses on the electron temperature. The amount of power in Ohmic heating ($\sim$550 kW) and radial transport ($\sim$460 kW) is larger than the total RF power (350 kW). Radiation losses cancel the direct RF electron absorption term. Since the Ohmic heating term is larger than the radial transport term, a rise in the electron temperature might be expected. However, $T_e > T_D$, T_o and the electrons lose energy via collisions. The high energy protons which slow down on the electrons do not provide enough power to counteract the electron collisional losses. After the RF is turned off, T_e drops. The drop in T_e causes an increase in the Ohmic power since $P_{OH} \propto T_e^{-3/2}$ while the radial losses decrease since $P_{Rad} \propto T_e$. The net result is little electron heating.

Deuterium radial ($\sim$360 kW) and charge exchange ($\sim$190 kW) losses are large as shown in Fig. (4-50). Second harmonic absorption is minimal (< 2.5 kW). For the average deuterium temperature to rise 150 eV, over 550 kW of power must be received from collisions with electrons and high energy protons.

From Fig. (4-52) we see the low concentration of hydrogen results in small charge exchange ($\sim$30 kW) and radial losses ($\sim$20 kW). The dominant terms in the hydrogen energy balance are RF heating and Coulomb collisions with the cooler species. Setting $\tau_E^H = \tau_E^D$ would raise the radial losses to $\sim$45 kW, still a small amount. Unless $\tau_E^H << 60$ ms, which has not been observed, the RF correction factor in Eq. (4-67) has a small effect. The small radial and charge exchange losses and the large amount of direct RF heating cause the protons to become much hotter than the background deuterons and electrons.

The initial Maxwellian electrons and deuterons again remain Maxwellian during the RF heating phase. The deuterons, although being heated during the RF pulse, remain isotropic.

The protons, which absorb most of the RF, become nonMaxwellian. Figure (4-51) shows the protons becoming slightly anisotropic during the the RF pulse. The amount of anisotropy at t = 100 ms has now decreased, $\frac{T_\perp}{T_\parallel} \sim 1.17$ as compared to $\frac{T_\perp}{T_\parallel} \sim 1.29$ predicted before. This anisotropy again disappears within 30 ms after the RF pulse is off.

The hydrogen temperature is now lower than in our idealized picture, dropping from 2.55 keV to 0.76 at t = 100 ms.

In comparison with the earlier model, Figs. (4-53-54) show that a smaller high energy tail forms which quickly disappears once the RF is off. Figure (4-55) shows the effective hydrogen tail temperature, 18 keV, agrees with the experiment.

4.E. Conclusions

We have seen that besides RF heating and collisions, Ohmic heating, radial, charge exchange and radiation losses are important in interpreting the RF heating experiments in PLT. When all these processes are included, FORCE obtains good agreement with the experiment.

Only the protons become nonMaxwellian with an effective tail temperature of 15-20 keV. The protons absorb over 90% of the available RF power through fundamental minority damping. The protons are slightly anisotropic and quickly isotropize once the RF is off.

The deuterons, which make up the bulk of the plasma, double in temperature. They remain Maxwellian, being heated by collisions, not by the RF. The electrons are not heated substantially. The oxygen impurities have little affect on RF absorption. All these results agree well with the PLT experiment.

In the reactor regime, our idealized model has shown that there is little Q enhancement. Both the deuterons and the tritons are Maxwellian with $T_D \approx T_T$. Stix(13) finds tail formation because he neglects other processes such as radial transport and charge exchange. In addition, his reactor model has a lower plasma density which leads to longer slowing down and isotropization times. Finally, Stix assumes much higher power densities than are needed in NUWMAK. For $\zeta = 10$

$$\frac{<P_{RF}>}{n_D} = 6.5 \times 10^{-14} \text{ W/particle} \tag{4-90}$$

while for $\zeta = 100$

$$\frac{<P_{RF}>}{n_D} = 6.5 \times 10^{-13} \text{ W/particle.} \tag{4-91}$$

For NUWMAK, ζ should be less than 3.

We have seen that alphas do not absorb much power. The impurities should not absorb much RF power when the resonance zone is near the plasma center. Any additional processes which could be added to our idealized model would decrease further any RF induced nonMaxwellian effects.

The space-time codes STICR-I and STICR-II discussed in the next chapter assume isotropic, nearly Maxwellian distributions with only a single ion temperature. FORCE has shown this to be an accurate picture. A Fokker-Planck formulation is not needed. However, FORCE has shown, as has the experiment, that for PLT this assumption is not valid. All the species, except the protons, are isotropic Maxwellian with $T_D = T_O$. However, the protons are nonMaxwellian with $\frac{T_H}{T_D} \sim 1.7$ at $t = 100$ ms. Since the protons are only slightly anisotropic, the fluid equations should still be valid.

However, FORCE neglects several effects which the space-time codes include. The Fokker-Planck description neglects all spatial effects, using only a spatially-averaged density and energy for each species. FORCE also assumes $\omega = n\omega_{ci}$ (r=0) everywhere (RF heating is concentrated near the center). FORCE neglects both mode conversion processes if present, and absorption outside of the cyclotron resonance layer. These spatial effects may lead to a further reduction in any ICRF induced effects in both NUWMAK and PLT.

Although the PLT space-time code STICR-I has only one ion temperature, we are able to incorporate into the RF calculations a separate hydrogen temperature

$$T_H = C_H \times T_i \qquad (4\text{-}92)$$

where C_H is an input variable greater than 1. We shall see that C_H plays an important role in determining the mode conversion threshold in PLT.

Table 4-1
Quasi-Linear RF Assumptions

1) Nonrelativistic, collisionless, infinite, spatially uniform plasma exists in the absence of wave excitation.

2) There is a constant, static magnetic field, B_o, with no curvature oriented along the Z axis.

3) No static electric field exists.

4) Direct nonlinear coupling between waves can be neglected.

5) Spatially averaged distribution functions change slowly compared to the gyroperiod and characteristic times of the wave motion.

6) The constant magnetic field is strong enough that particles gyration frequencies are larger than the damping rate of the waves.

Table 4-2

PLT

Toroidal field (kG)	16.4	τ_p	∞
Major radius (cm)	130	τ_E	∞
Minor radius (cm)	45	Z_{eff}	~ 2.0
Plasma volume (cm^3)	$5.2x10^6$	$k_{\parallel}$ (cm^{-1})	0.1
n_e (cm^{-3})	~ $2.50x10^{13}$	Minor radius of heating (cm)	10
n_D (cm^{-3})	~ $1.95x10^{13}$	RF frequency (MHz)	25
n_H (cm^{-3})	~ $1.95x10^{12}$	RF power (kW)	350
n_z (cm^{-3}) (oxygen)	~ $4.46x10^{11}$	RF pulse (ms)	100
Initial $\bar{T}_D = \bar{T}_H = \bar{T}_z$ (eV)	300	Δt_{step} (ms)	0.02
Initial $\bar{T}_e$ (eV)	650	P_H/N_H ($x10^{-14}W$)	~ 3.5
		at t = 100 ms	
P^e_{RF} (kW)	~ 6	$\Delta\bar{E}_D$(eV)	~ 1400
P^D_{RF} (kW)	~ 7	$\Delta\bar{E}_H$(eV)	~ 3370
P^H_{RF} (kW)	~ 337	$\Delta\bar{E}_o$(eV)	~ 1430
P^o_{RF} (kW)	~ 0.2	$\|E_+\|$(V/cm)	~ 3.3
$\Delta\bar{E}_e$ (eV)	~ 715	$\|E_-\|$(V/cm)	~ 25.4
		$\|E_{\parallel}\|$(V/cm)	~ 0.01

Table 4-3

NUWMAK

	Fundamental	Second Harmonic
Toroidal field (kG)	60.4	60.4
Major radius (cm)	512.5	512.5
Minor radius (cm)	144.0	144.0
Plasma volume (cm^3)	2.1×10^8	2.1×10^8
$\bar{n}_e$ (cm^{-3})	3.0×10^{14}	3.0×10^{14}
$\bar{n}_D$ (cm^{-3})	3.0×10^{13}	1.5×10^{14}
$\bar{n}_T$ (cm^{-3})	2.7×10^{14}	1.5×10^{14}
Initial $\bar{n}_c$ (cm^{-3})	1.0×10^{11}	1.0×10^{11}
Initial $\bar{n}_\alpha$ (cm^{-3})	8.0×10^8	8.0×10^8
Initial $\bar{T}_D=\bar{T}_p=\bar{T}_c=\bar{T}_\alpha$ (keV)	2.0	2.0
Initial T_e (keV)	2.0	2.0
τ_p	∞	∞
τ_E	∞	∞
Z_{eff}	~ 1	~ 1
$k_\parallel$ (cm^{-1})	0.2	0.2
Minor radius of heating (cm)	10	10
RF frequency (MHz)	46	92
RF power (MW)	150	100
RF pulse (sec)	2.0	1.5
Δt_{step} (ms)	0.5	0.5
P_D/N_D ($\times 10^{-14}$W)	~ 1.8	~ 0.33

Table 4-3 (cont.)
at RF Shutoff

	Fundamental	Second Harmonic
RF shutoff (sec)	2.0	1.5
P^e_{RF} (MW)	~ 0.26	~ 1.6
P^D_{RF} (MW)	~ 114	~ 97
P^T_{RF} (MW)	~ 0	~ 1.6
P^c_{RF} (MW)	$\lesssim 35$	~ 0.07
P^α_{RF} (MW)	~ 0.008	~ 0
P_α (MW)	~ 190	~ 130
Q	~ 1.27	~ 1.33
$\Delta\bar{E}_e$ (keV)	6.4	3.9
$\Delta\bar{E}_D$ (keV)	6.8	4.0
$\Delta\bar{E}_T$ (keV)	6.6	4.0
$\Delta\bar{E}_c$ (keV)	$\lesssim 800$	4.0
$\lvert E_+\rvert$(V/cm)	~ 3.1	~ 7.9
$\lvert E_-\rvert$(V/cm)	~ 33.2	~ 24.0
$\lvert E_\parallel\rvert$(V/cm)	~ 0.05	~ 0.02
$n_c(\mathrm{cm}^{-3})$	$\gtrsim 4.5\times10^9$	$\sim 9.1\times10^{10}$
$n_\alpha(\mathrm{cm}^{-3})$	2.76×10^{11}	1.80×10^{11}

Table 4-4

PLT

Toroidal field (kG)	16.4	τ_p^D (ms)	150
Major radius (cm)	130	τ_p^H (ms)	200
Minor radius (cm)	45	τ_p^z (ms)	∞
Plasma current (kA)	400	τ_E^e (ms)	45
Plasma volume (cm^3)	5.2×10^6	τ_E^D (ms)	30
$\bar{n}_e$ (cm^{-3})	$\sim2.50\times10^{13}$	τ_E^H (ms)	60
$\bar{n}_D$ (cm^{-3})	1.95×10^{13}	τ_E^z (ms)	110
$\bar{n}_H$ (cm^{-3})	1.95×10^{12}	Z_{eff}	$\sim$ 2.0
$\bar{n}_z$ (cm^{-3}) (oxygen)	4.46×10^{11}	$k_\parallel$ (cm^{-1})	0.1
n_o (cm^{-3}) (10%H^o-90%D^o)	2.2×10^8	RF frequency (MHz)	25
Initial $T_D=T_H=T_z$ (eV)	300	RF pulse (ms)	100
Initial Te (eV)	650	Δt_{step} (ms)	0.02
T_o (eV)	5	Minor radius at heating (cm)	10
RF power (kW)	350	P_H/N_H($\times10^{-14}$W)	$\sim$ 3.5

Table 4-4 (cont.)

At RF Shutoff

P^e_{RF} (kW)	~ 16	P^H_{cx} (kW)	~ 26
P^D_{RF} (kW)	~ 2.4	P^H_{radial} (kW)	~ 22
P^H_{RF} (kW)	~ 332	P^z_{radial} (kW)	~ 2.4
P^z_{RF} (kW)	~ 0.06	$\Delta\bar{E}_e$ (eV)	55
P_{OH} (kW)	~ 534	$\Delta\bar{E}_D$ (eV)	227
P_z (kW)	~ 17	$\Delta\bar{E}_H$ (eV)	685
P_{EP}(kW)	~ 1.5	$\Delta\bar{E}_z$ (eV)	255
P^e_{radial} (kW)	~ 460	$\lvert E_+\rvert$(V/cm)	~ 3.3
P^D_{cx} (kW)	~ 186	$\lvert E_-\rvert$(V/cm)	~ 39.5
P^D_{radial} (kW)	~ 370	$\lvert E_\parallel\rvert$(V/cm)	~ 0.01

LIST OF FIGURES

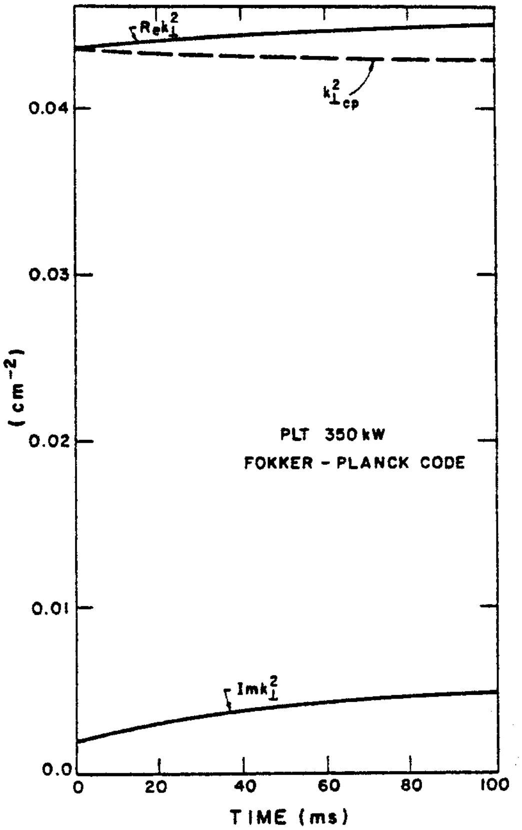

Fig.(4-1)

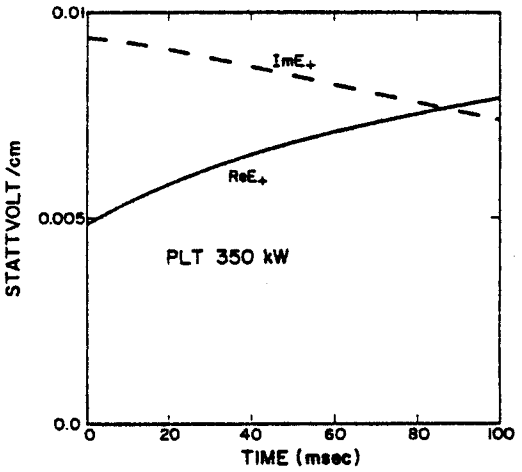

Fig.(4-2)

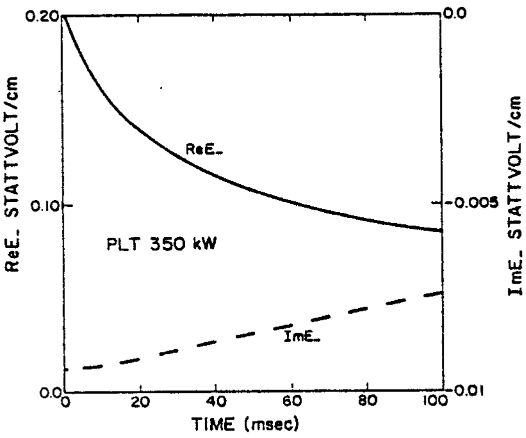

Fig.(4-3)

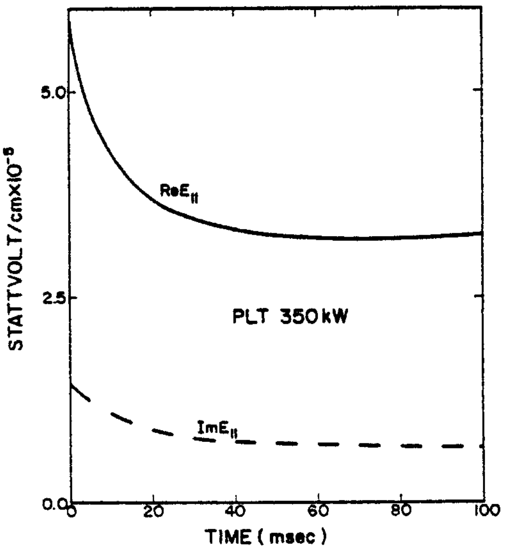

Fig.(4-4)

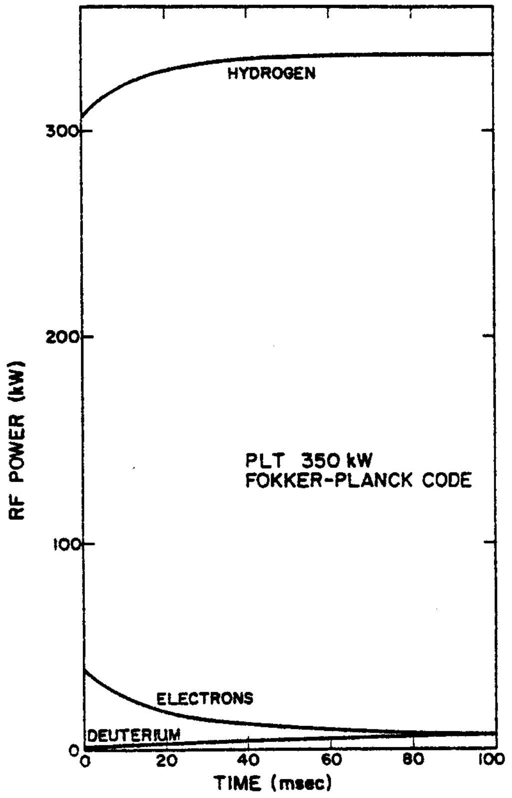

Fig.(4-5)

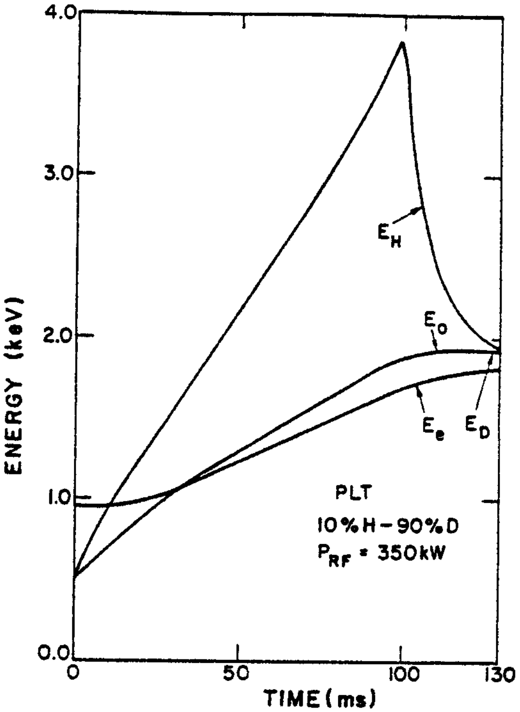

Fig.(4-6)

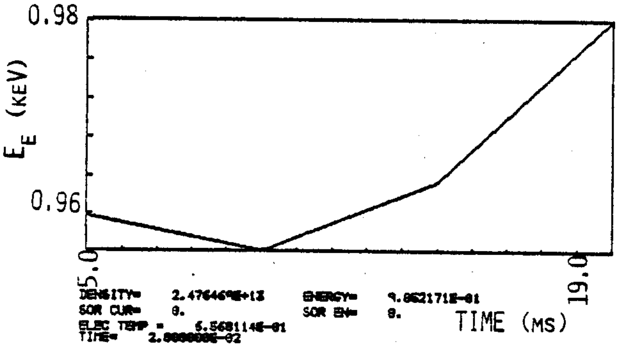

```
DENSITY=     2.476469E+13        ENERGY=     9.862171E-01
SOR CUR=     0.                  SOR EN=     0.
ELEC TEMP =      6.568114E-01
TIME=     2.000000E-02
```

Fig.(4-7)

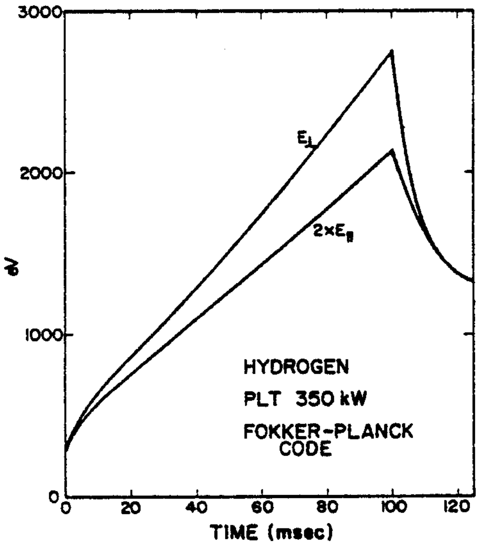

Fig.(4-8)

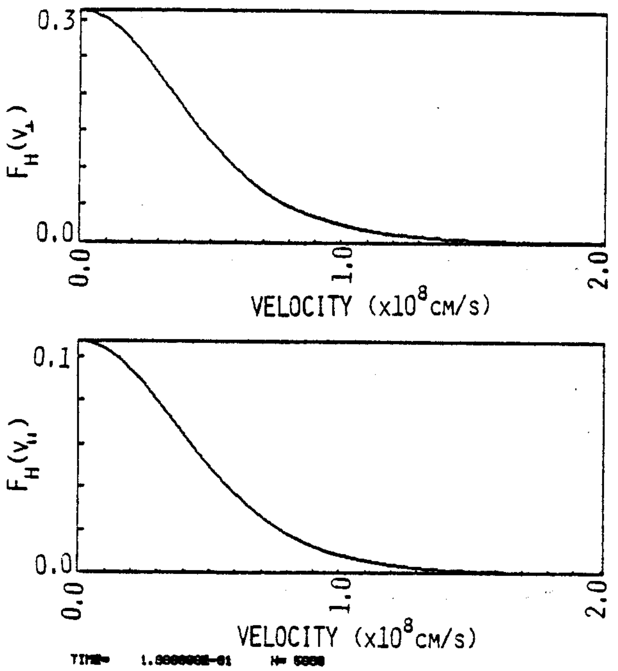

Fig.(4-9)

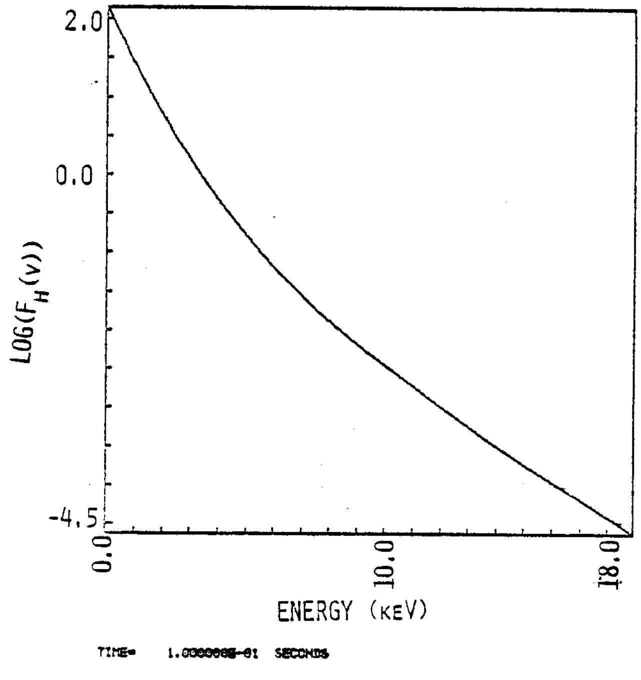

Fig.(4-10)

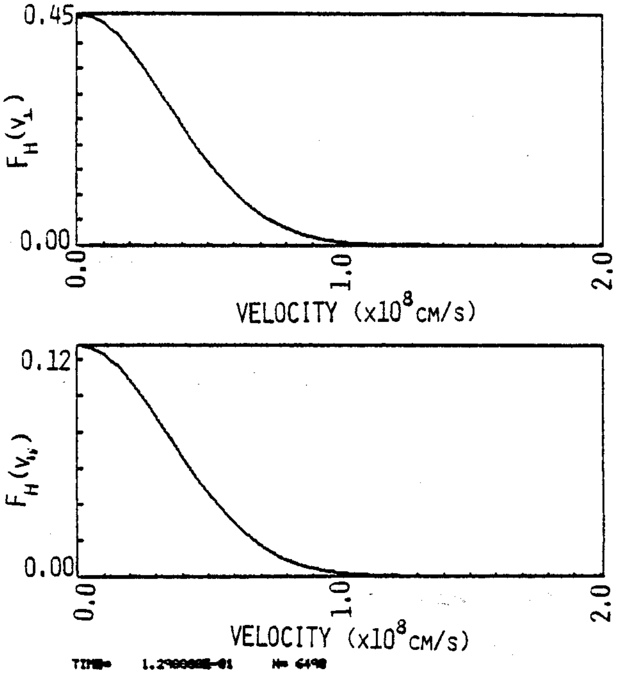

Fig.(4-11)

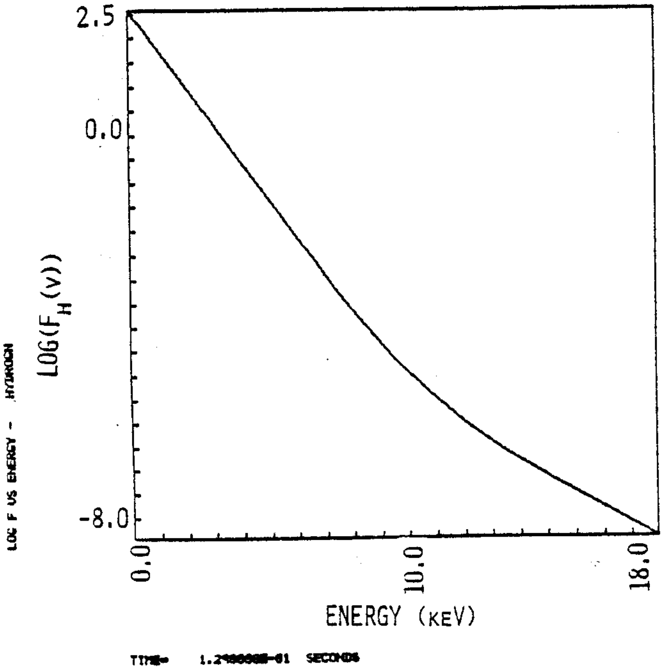

Fig.(4-12)

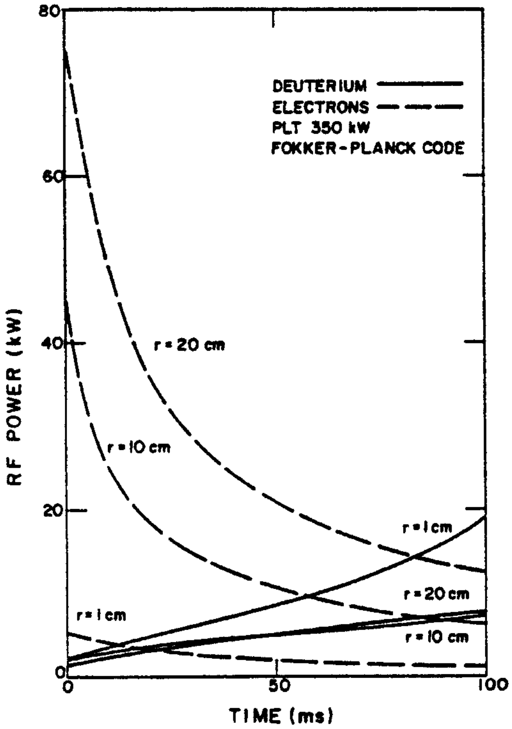

Fig.(4-13)

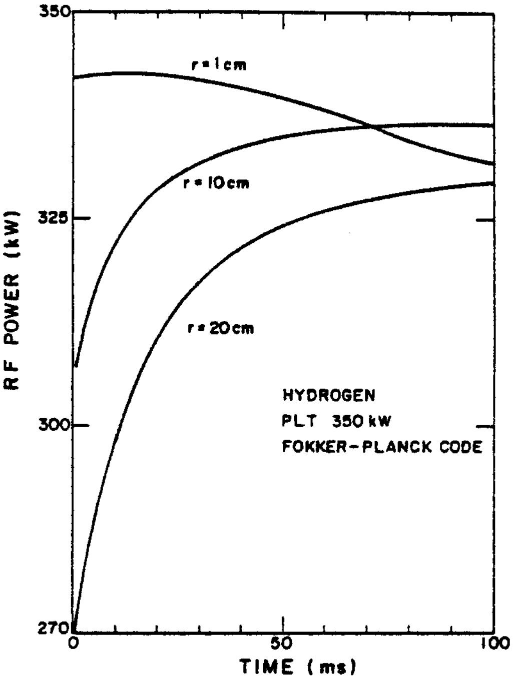

Fig.(4-14)

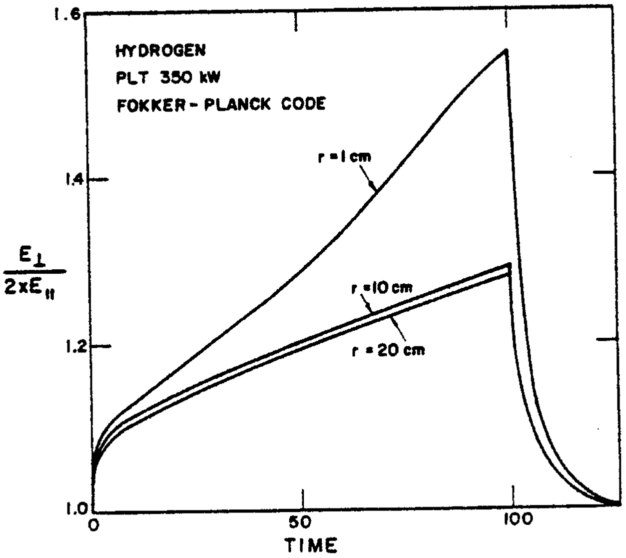

Fig.(4-15)

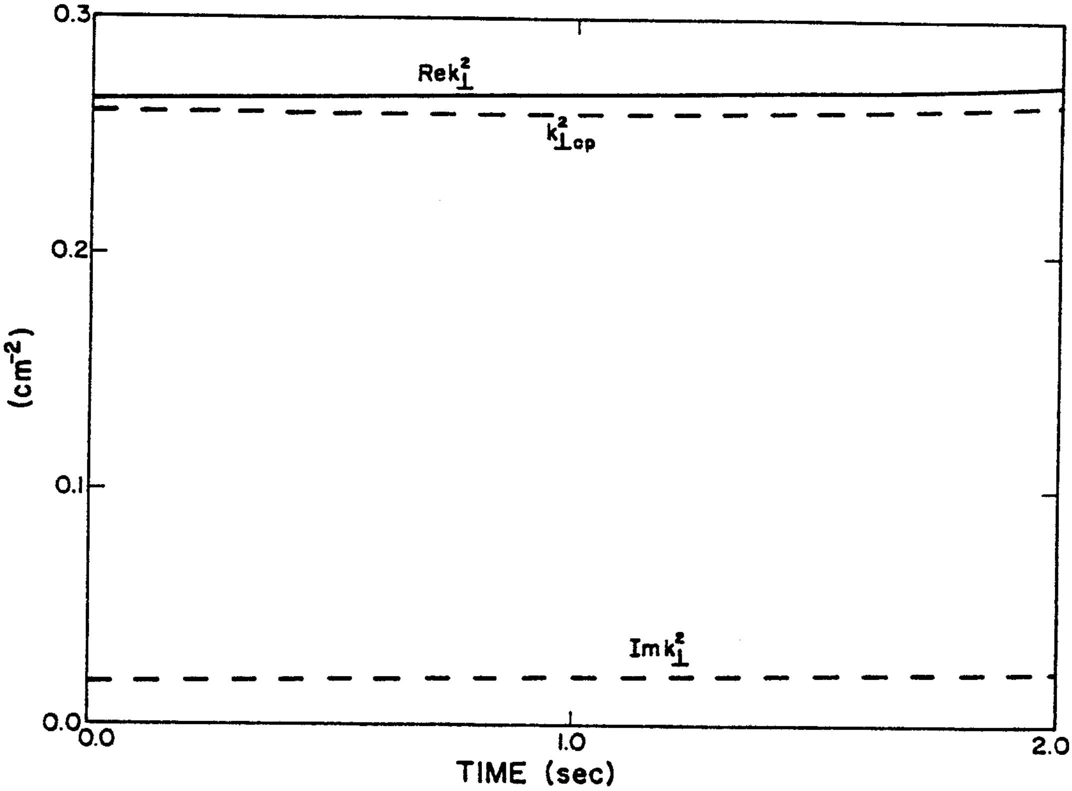

Fig.(4-16)

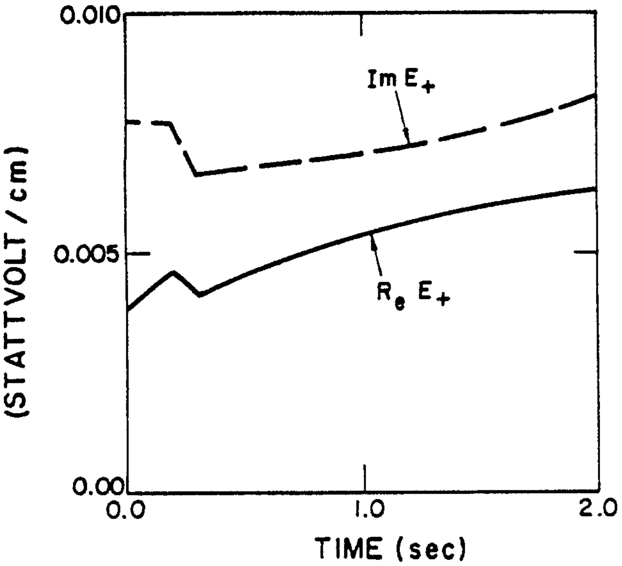

Fig.(4-17)

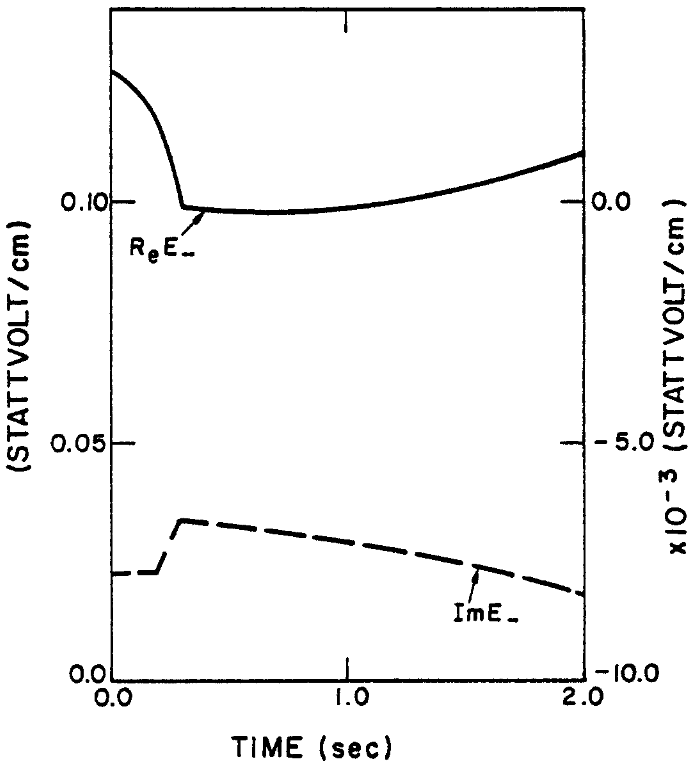

Fig.(4-18)

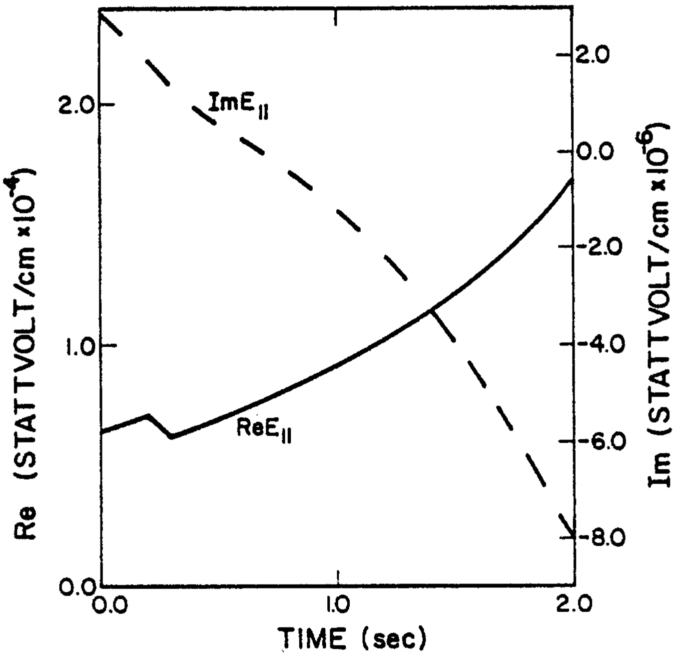

Fig.(4-19)

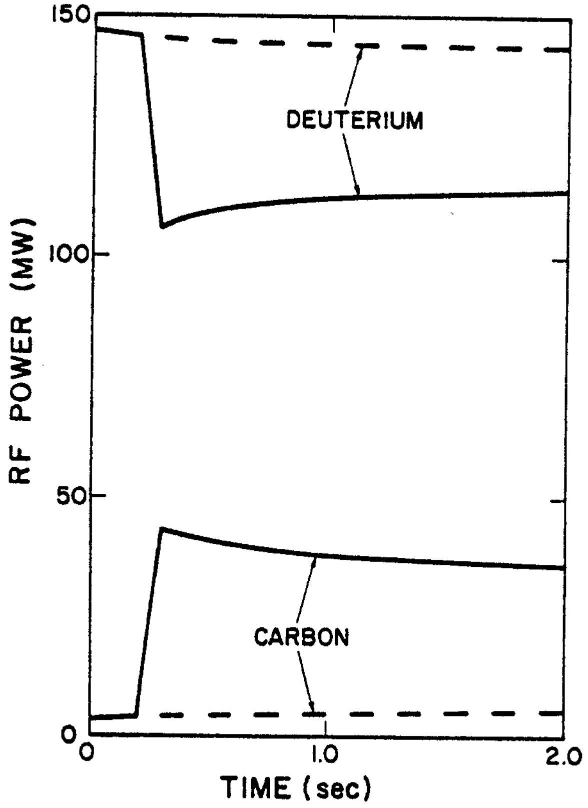

Fig.(4-20)

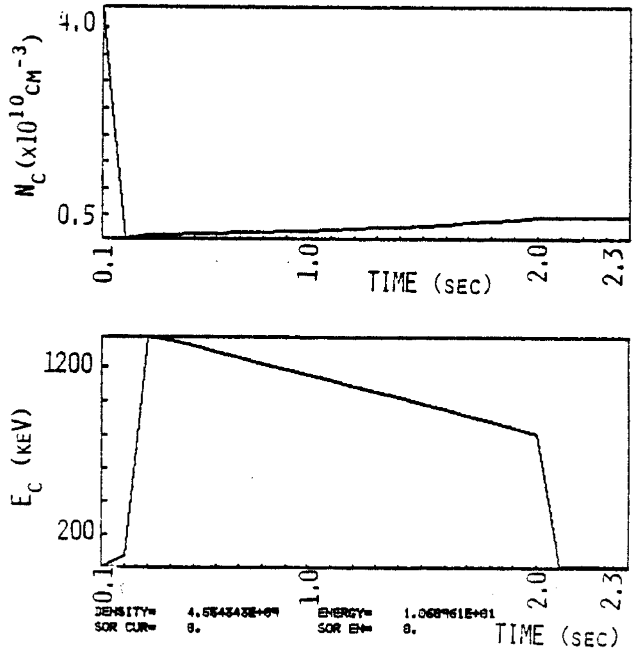

```
DENSITY=    4.554343E+09         ENERGY=    1.068961E+01
SOR CUR=    0.                   SOR EN=    0.

TIME=    2.499500E+00
```

Fig.(4-21)

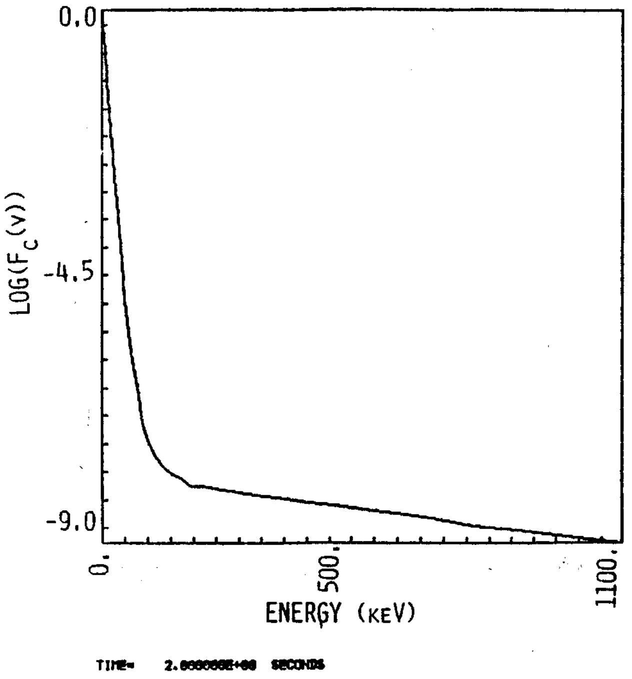

Fig.(4-22)

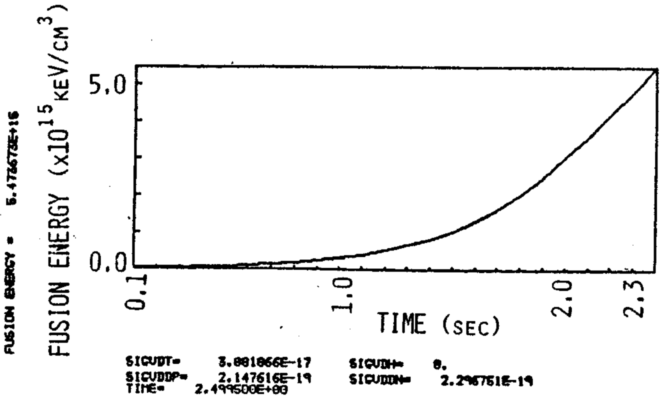

Fig.(4-23)

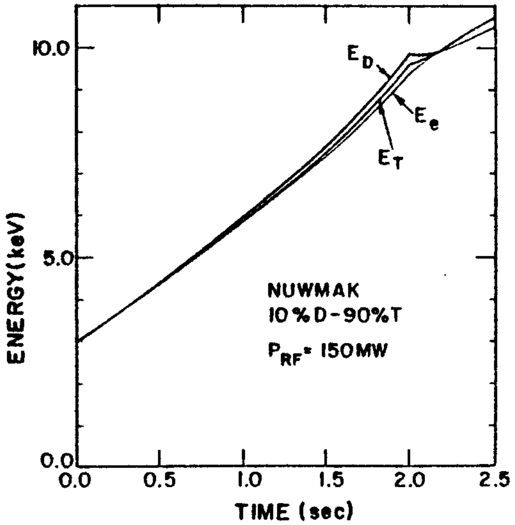

Fig.(4-24)

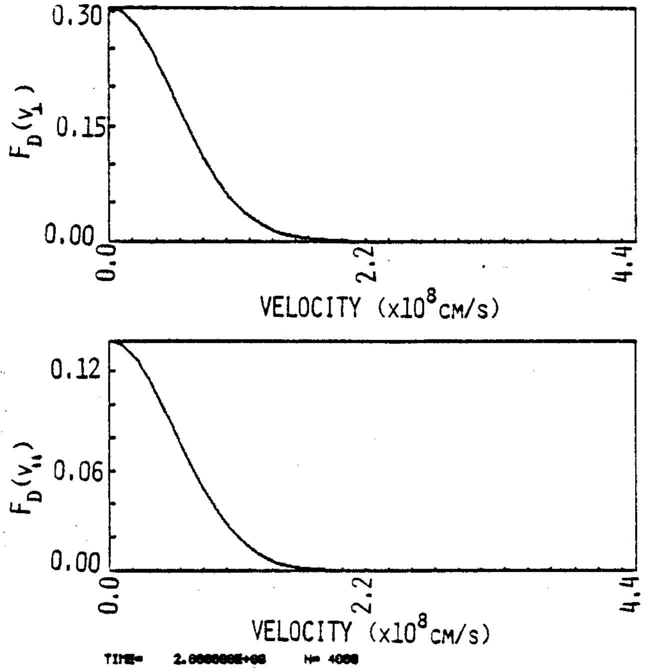

Fig.(4-25)

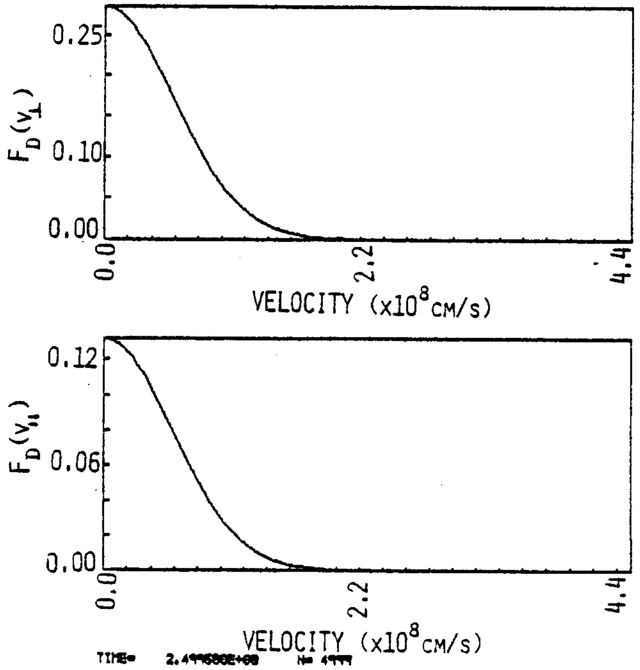

Fig.(4-26)

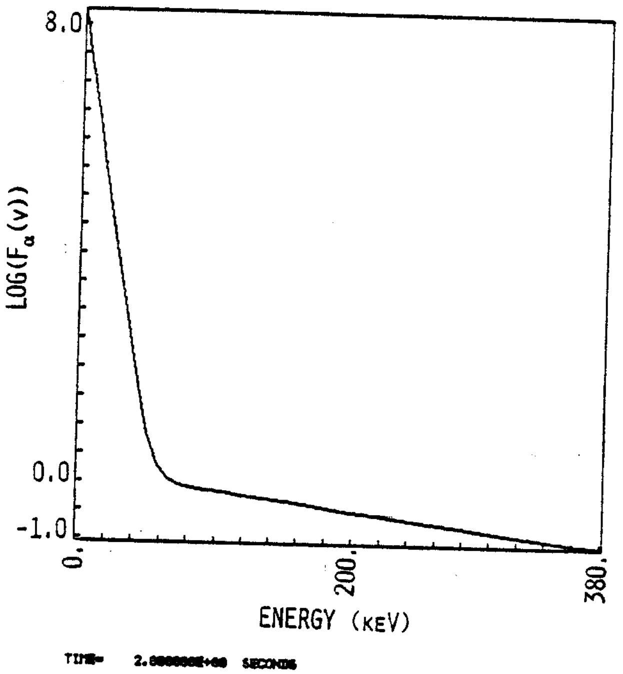

Fig.(4-27)

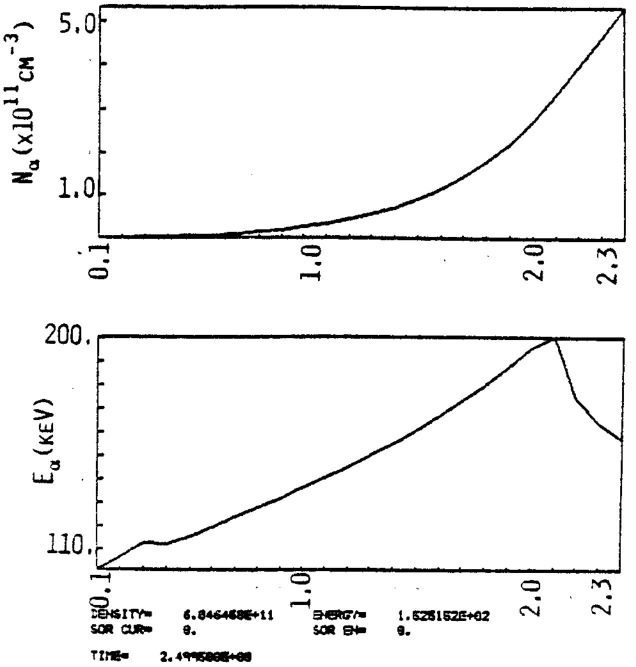

Fig.(4-28)

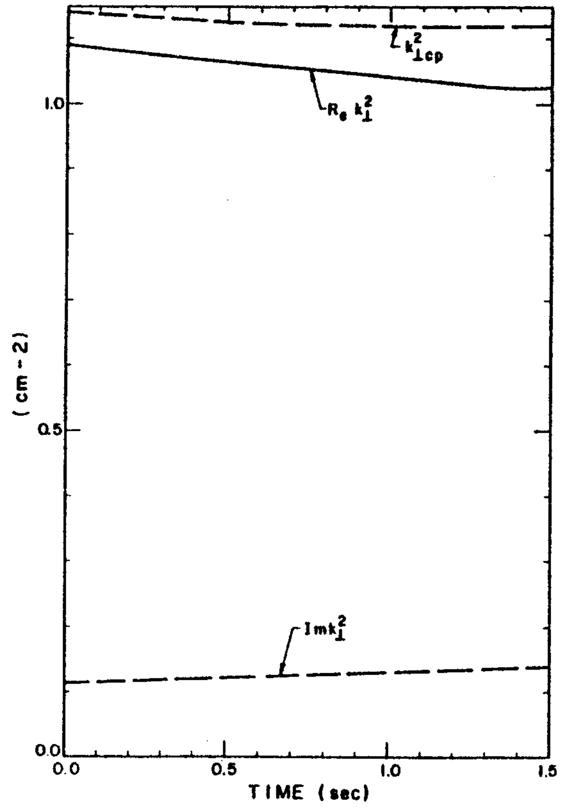

Fig.(4-29)

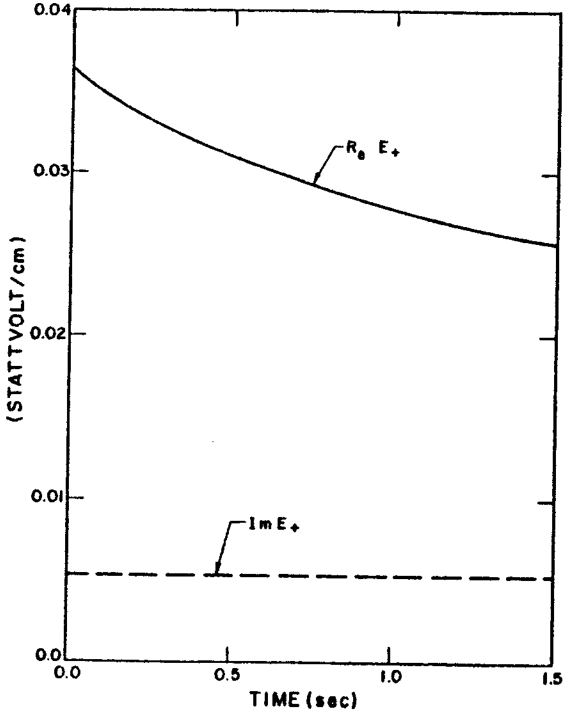

Fig.(4-30)

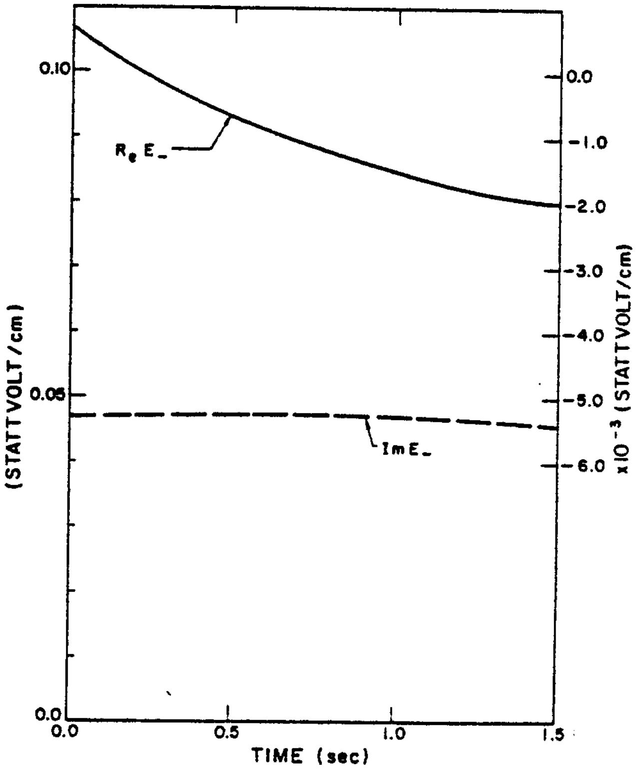

Fig.(4-31)

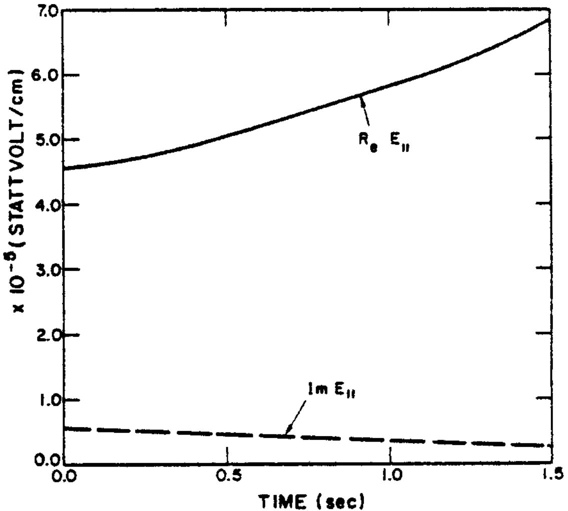

Fig.(4-32)

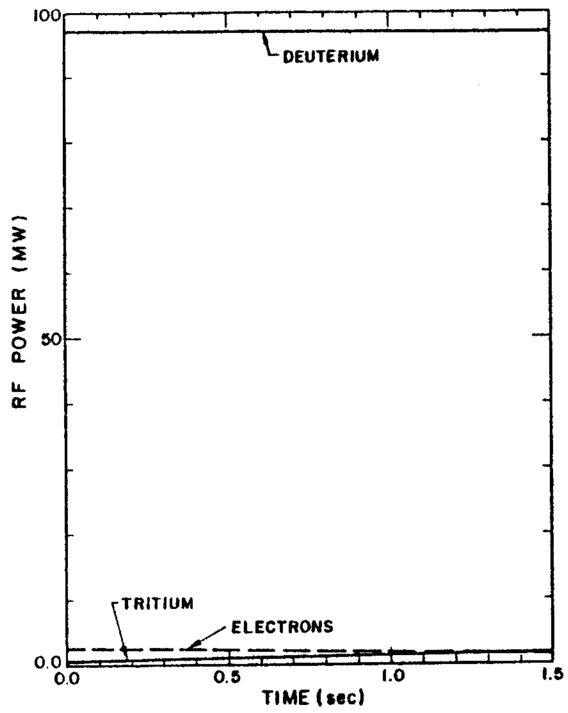

Fig.(4-33)

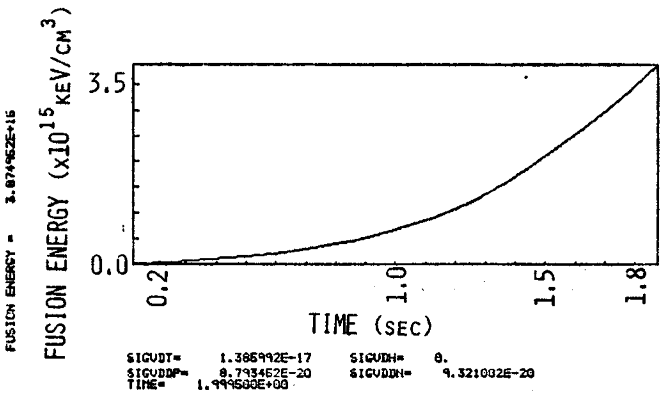

Fig.(4-34)

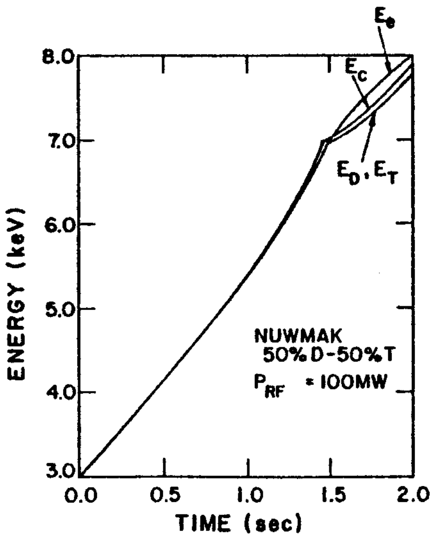

Fig.(4-35)

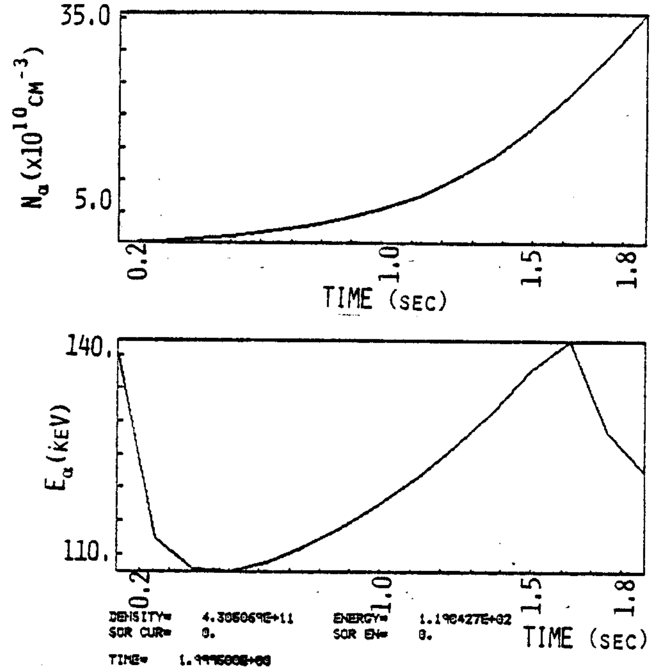

Fig.(4-36)

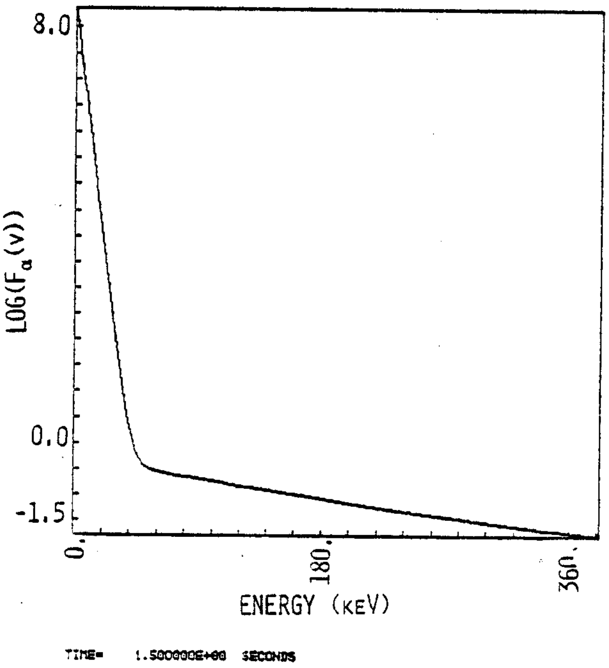

Fig.(4-37)

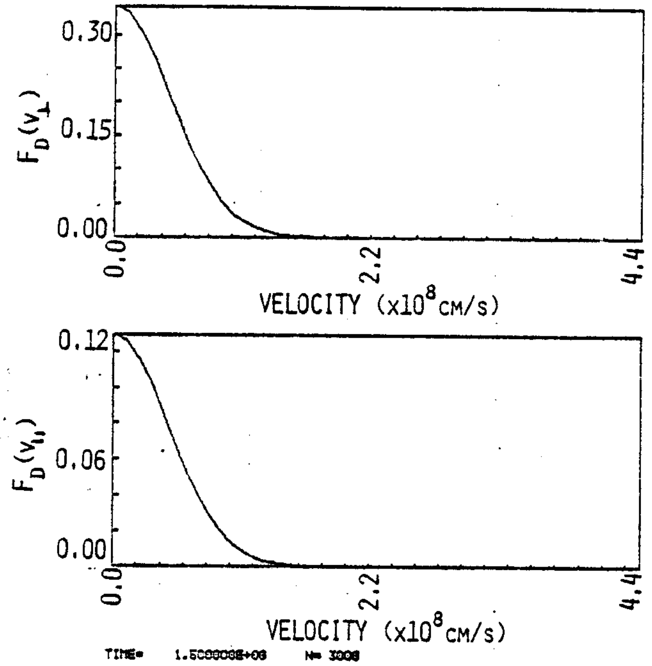

Fig.(4-38)

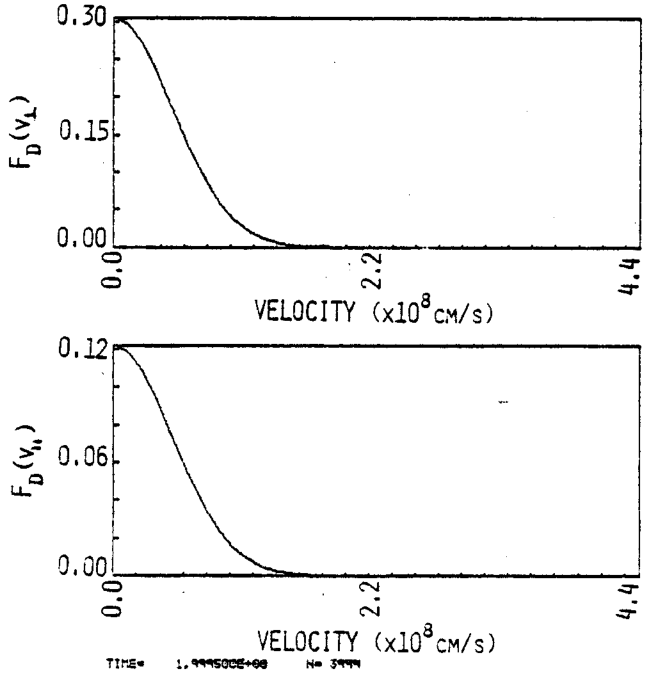

Fig.(4-39)

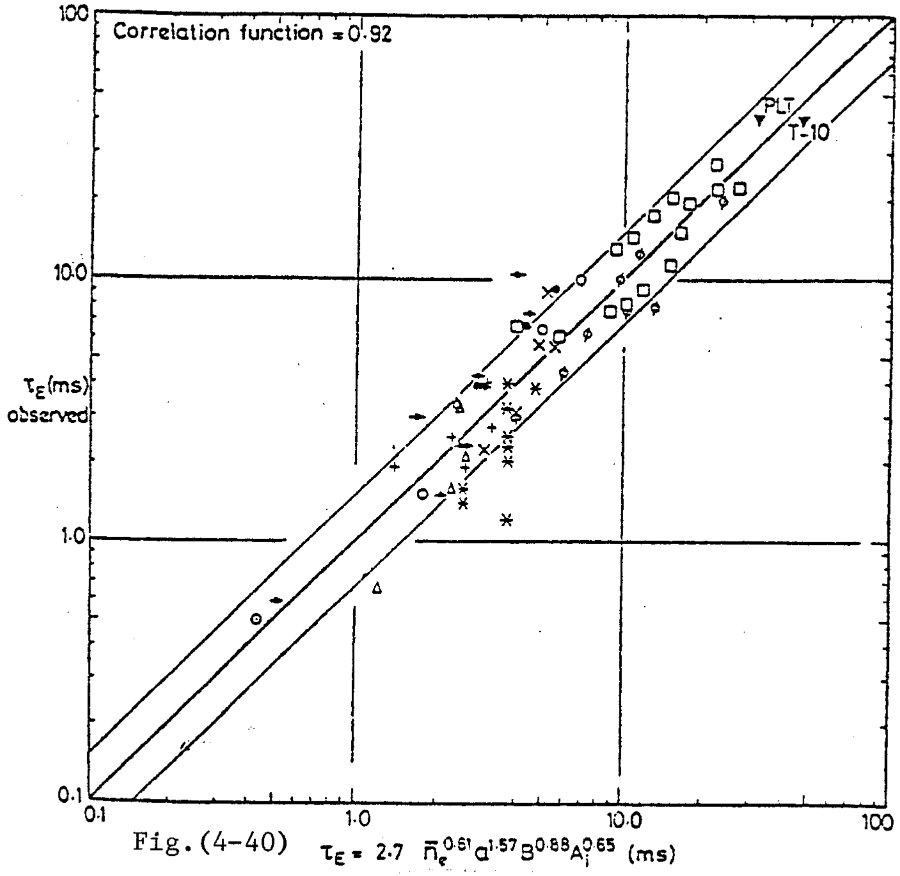

Fig.(4-40)

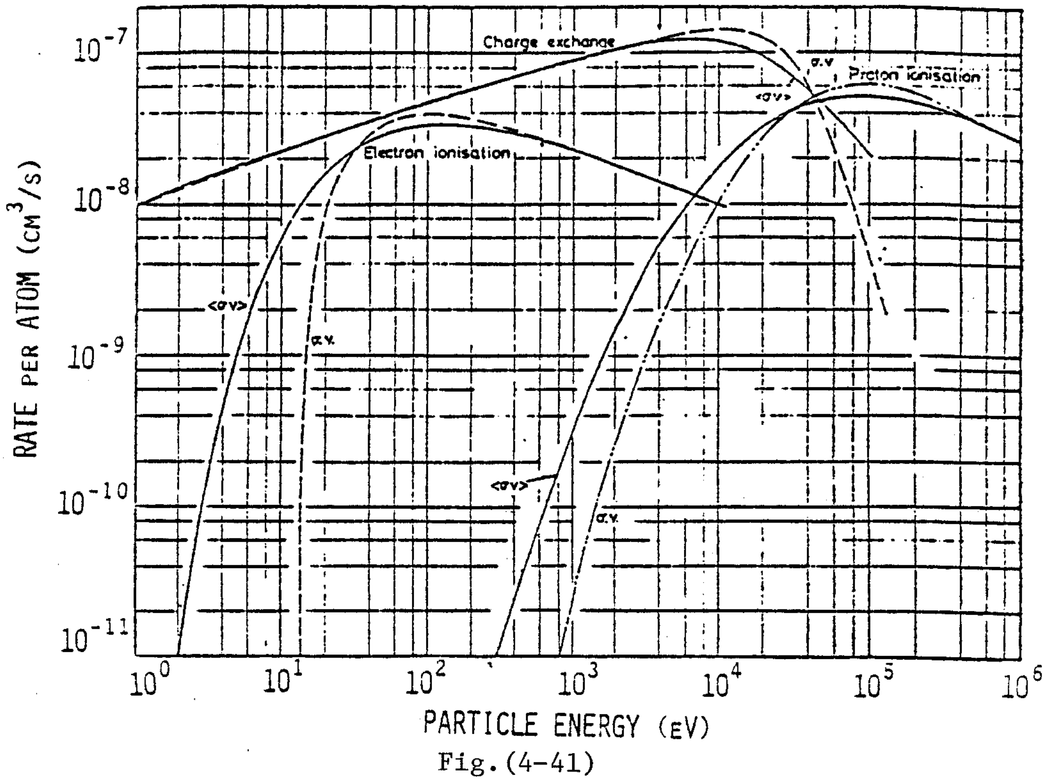

Fig.(4-41)

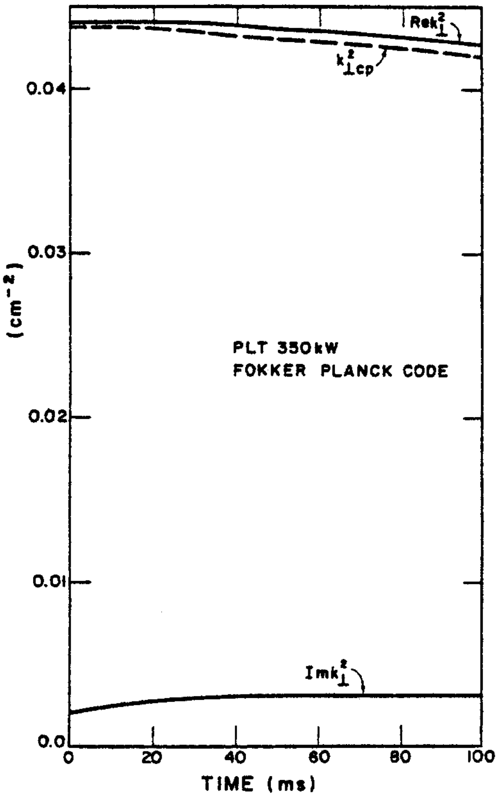

Fig.(4-42)

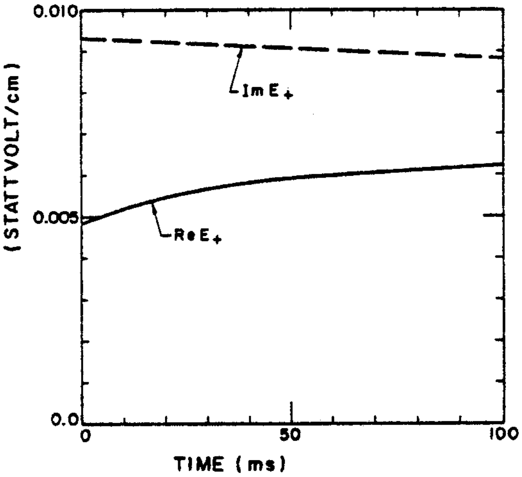

Fig.(4-43)

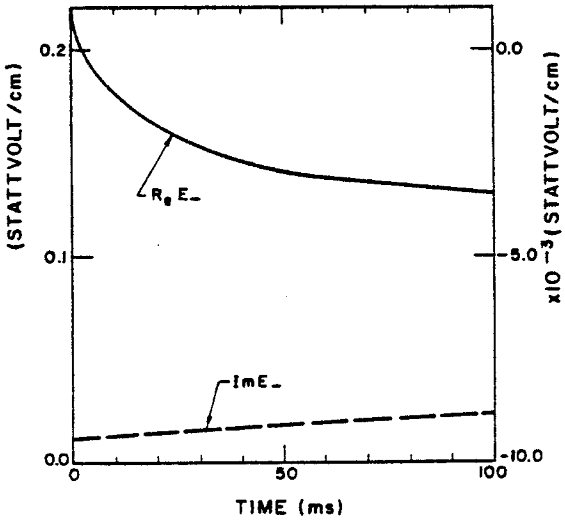

Fig.(4-44)

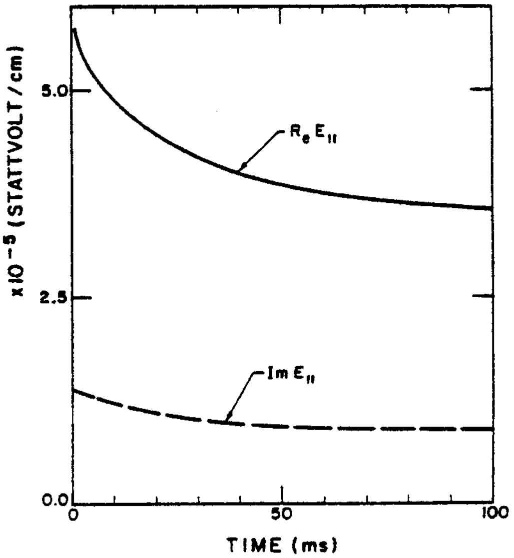

Fig.(4-45)

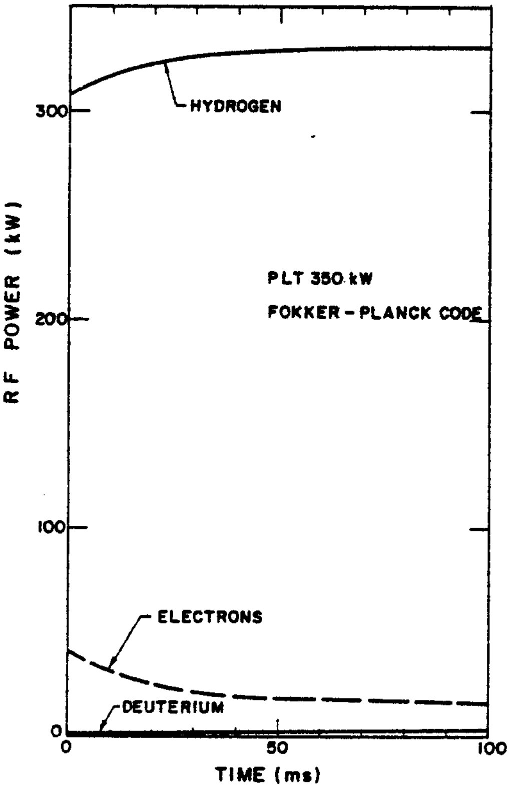

Fig.(4-46)

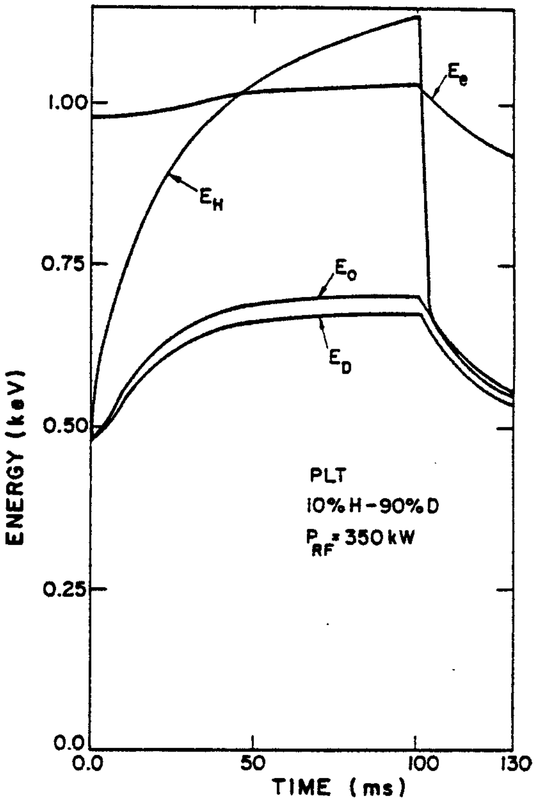

Fig.(4-47)

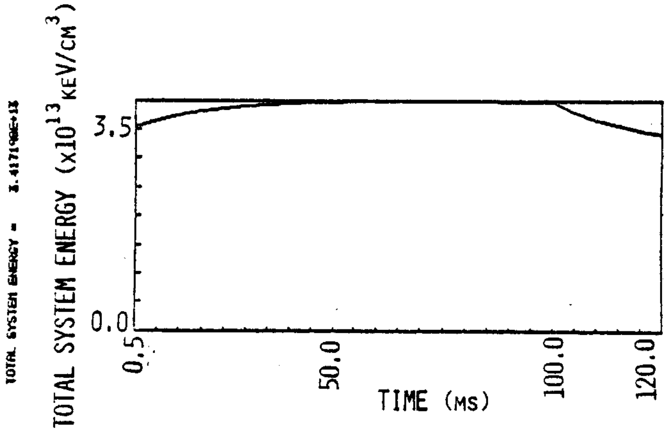

Fig.(4-48)

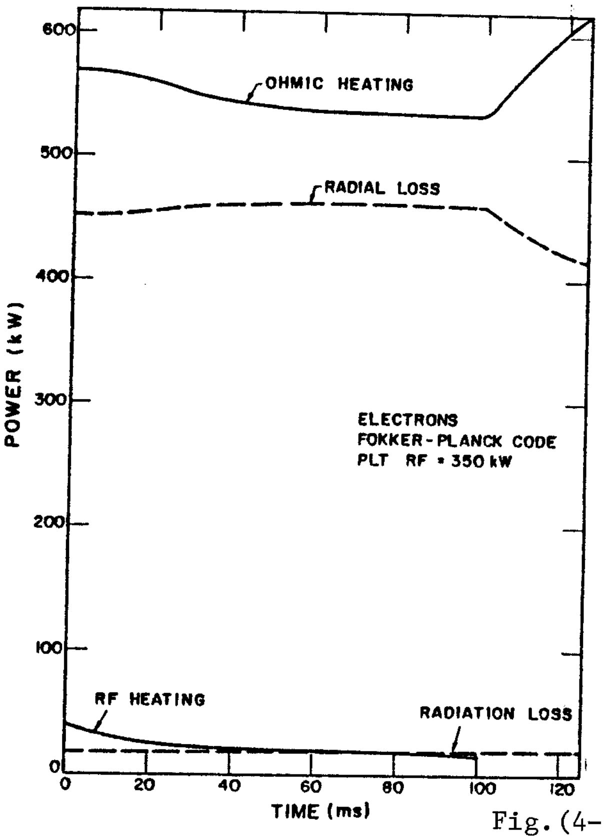

Fig.(4-49)

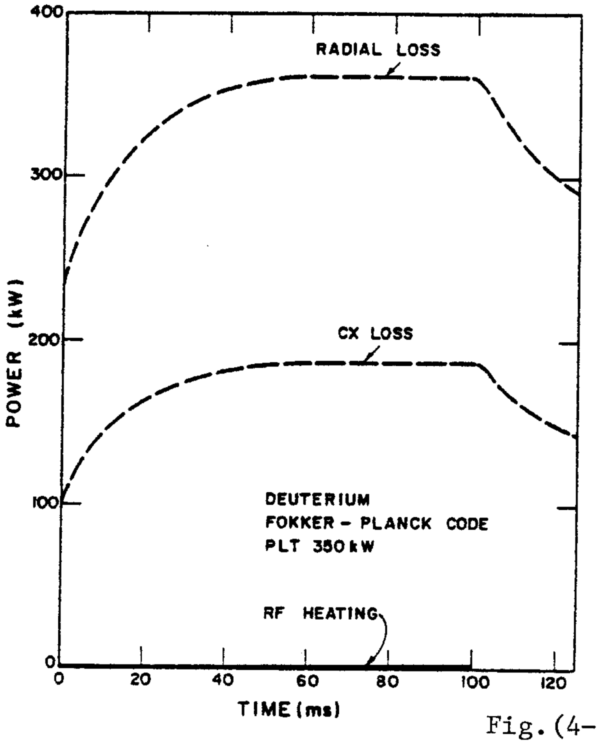

Fig.(4-50)

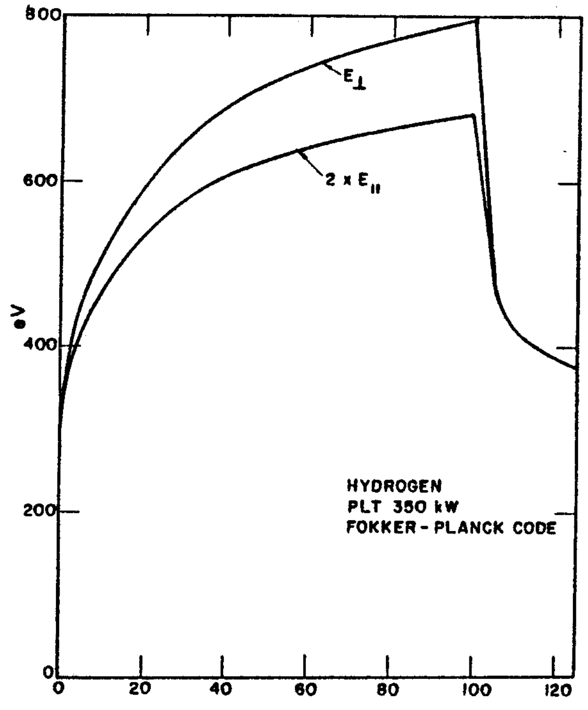

Fig.(4-51)

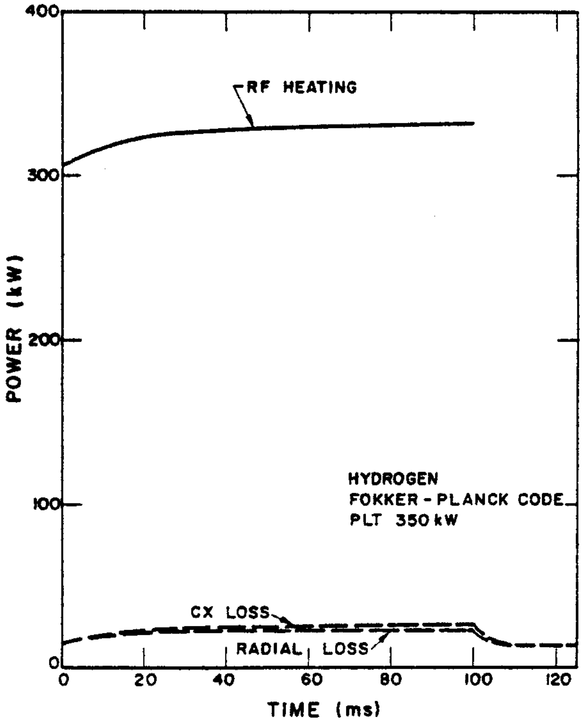

Fig.(4-52)

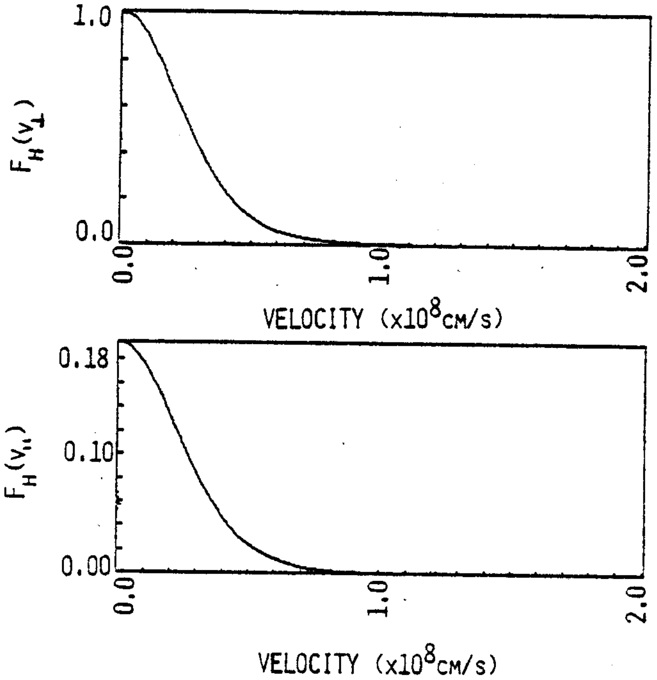

Fig.(4-53)

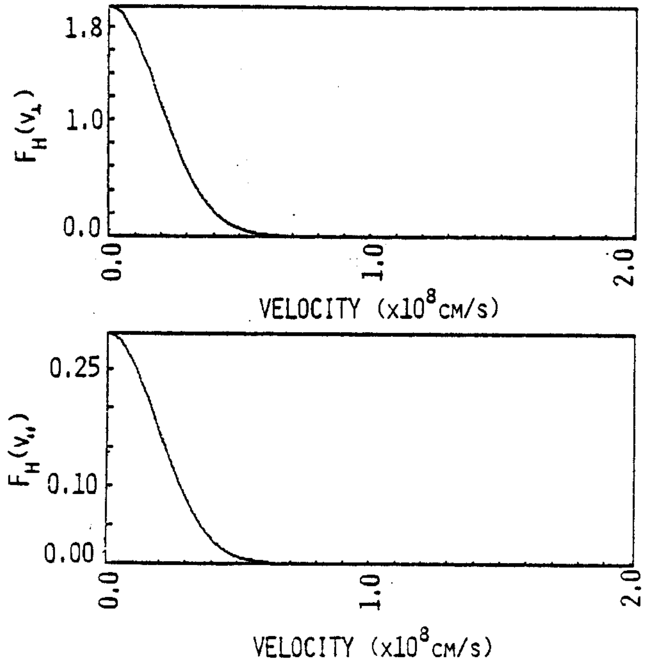

Fig.(4-54)

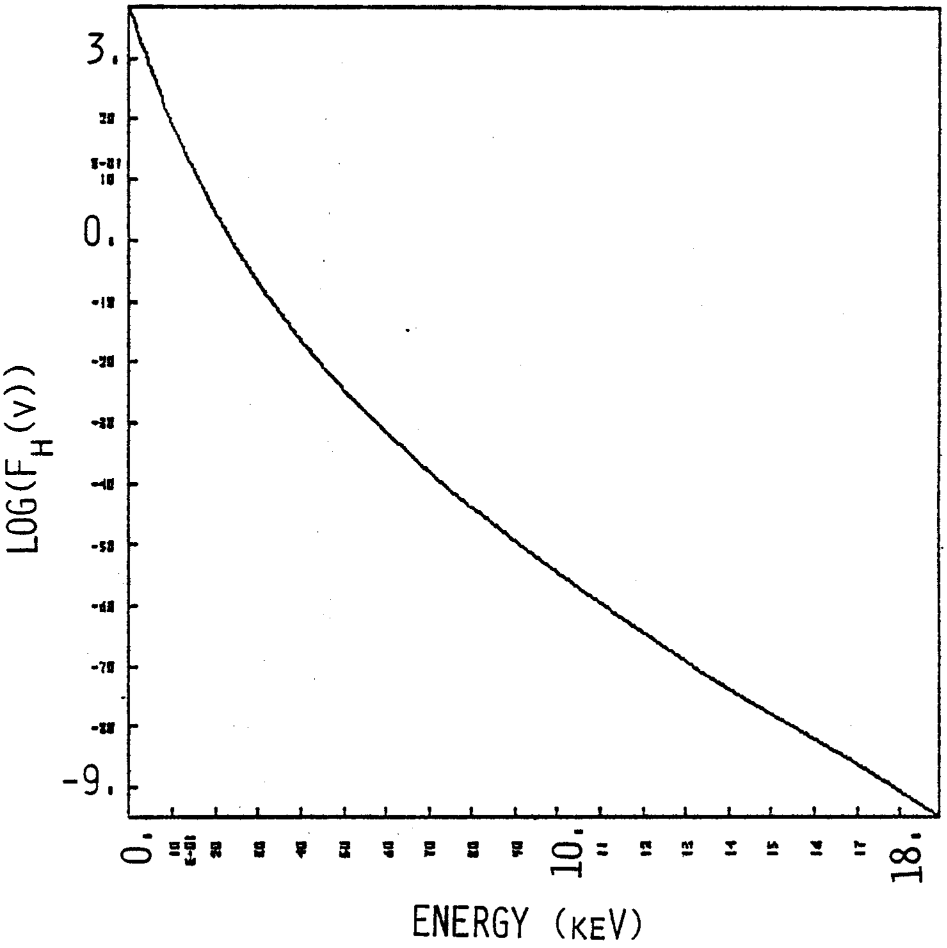

Fig.(4-55)

REFERENCES

CHAPTER 4

1. J. Killen, K.D. Marx, Methods in Computational Physics, Academic Press, Inc., N.Y. (1970) 9, 387.

2. N.A. Krall, A.W. Trivelpiece, Principles of Plasma Physics, McGraw-Hill, Inc., N.Y. (1973) 312.

3. D.C. Montgomery, D.A. Tidman, Plasma Kinetic Theory, McGraw-Hill, Inc., N.Y. (1964).

4. D.T. Blackfield, T.K. Mau, J. Kesner, J.E. Scharer, Bull. Am. Phys. Soc. 23 (1978) 821.

5. J.E. Scharer, D.T. Blackfield, Bull. Am. Phys. Soc. 24 (1979) 1063.

6. A.A. Mirin, Lawrence Livermore Laboratories Report UCRL-51615 Rev. 1 (Feb., 1975).

7. J. Killen, T.H. Johnson, et al, Methods in Computational Physics, 16 (1975) 387.

8. J.P. Shkarofsky, T.W. Johnson, M.P. Bachynski, The Particle Kinetics of Plasmas, Addison Wesley Publ. Co., Mass. (1966).

9. S.S. Chern, Math 140 Notes, Dept. of Math., Univ. of California-Berkeley (Aug., 1971).

10. E. Butkov, Mathematical Physics, Addison-Wesley Pub. Co., Mass. (1968).

11. A.H. Futch, Jr., et al, Plasma Phys. 14 (1972) 211.

12. M.N. Rosenbluth, W.M. MacDonald, D.L. Judd, Phys. Rev. 107 (1957) 1.

13. T.H. Stix, Nuc. Fusion 15 (1975) 737.

14. C.I. Kennel, F. Engelmann, Phys. of Fluids 9 (1966) 2377.

15. D.T. Blackfield, UWFDM-278 (Jan., 1979).

16. J. Kesner, Nuc. Fusion 18 (1978) 781; UWFDM-213 Revised (Jan., 1970).

17. J. Hosea, et al, PPL-1588 (Aug., 1979).

18. J. Hosea, Private Communication.

19. J. Hosea, et al, PPPL-1554 (May, 1979).

20. D.L. Book, NRL Memorandum Report No. 3332 Rev. (1978).

21. T.H. Stix, Phys. of Fluids 1 (1958) 308.

22. S. Yoshikawa, M.A. Rothman, R.M. Sinclair, Phys. Rev. Lett 14 (1965) 214.

23. J. Adam, A. Samain, Fontenay-aux-Roses Report EUR-CEA-FC-579 (1971).

24. F.W. Perkins in Plasma Heating and Injection (Proc. Symp. Varenna, 1972) 20.

25. W. Houlberg, UWFDM-103 (May, 1974).

26. W. Houlberg, Ph.D. Thesis, Univ. of Wisconsin-Madison (1977).

27. B. Badger et al, UWFDM-330 (March, 1979).

28. J.E. Scharer, D.R. Blackfield, J.B. Beyer, T.K. Mau, Nuc. Fusion 19 (1979) 1171.

29. B. Badger, et al, EPRI ER-368 (July, 1976).

30. J. Hugill, J. Sheffield, Nuc. Fusion 18 (1978) 15; JET Project Report EUR 5791e (1977) 175.

31. D.E. Post, et al, Atomic Data and Nuc. Data Tables 20 (1977) 397.

32. R.L. Freeman, E.M. Jones, Culham Laboratory Report CLM-R-137 (1974).

CHAPTER 5

SPATIAL ASPECTS OF ICRF HEATING IN TOKAMAK PLASMAS

5.A. 1-D Fluid Model

In this chapter we investigate the spatial aspects of ICRF heating in PLT and NUWMAK using a multi-species, 1-D transport code with a WKB slab model of RF heating. Spatial RF power depositions and temperature and density profiles are obtained. We also find an estimate for minority concentrations, which determine the mode conversion threshold. The amount of auxiliary power needed to ignite NUWMAK is calculated. Finally, we examine various RF heating scenarios which minimize the effects of complex and unresolved physical processes (mode conversion and ion-ion hybrid resonance effects).

Starting with the Boltzmann equation(1-4)

$$\frac{\partial f_\beta}{\partial t} + \overline{v} \cdot \overline{\nabla} f_\beta + \frac{e_\beta}{m_\beta} (\overline{E} + \overline{v} \times \overline{B}) \cdot \overline{\nabla}_v f_\beta = C_\beta \tag{5-1}$$

where C_β is the Fokker-Planck Collision operator. On taking the zeroth moment of Eq. (4-1) we obtain the density balance equation

$$\frac{\partial n_\beta}{\partial t} + \overline{\nabla} \cdot \overline{\Gamma}_\beta = 0 \tag{5-2}$$

where $n_\beta \equiv \int f_\beta \, d^3v$, and $\overline{\Gamma}$ represents a particle flux

$$\overline{\Gamma}_\beta \equiv n_\beta \, \overline{V}_\beta = \int \overline{v} \, f_\beta \, d^3v. \tag{5-3}$$

In obtaining Eq. (5-2) we find

$$\int (\overline{E} + \overline{v} \times \overline{B}) \cdot \overline{\nabla}_v \, f_\beta \, d^3v = 0 \tag{5-4}$$

and

$$\int C_\beta d^3v = 0$$

since Coulomb scattering conserves particles. Taking the first moment of Eq. (5-1)

$$n_\beta m_\beta \frac{\partial}{\partial t} \overline{V}_\beta + n_\beta m_\beta \overline{V}_\beta \cdot \overline{\nabla} \, V_\beta = n_\beta e_\beta (\overline{E} + \overline{V} \times \overline{B}) - \overline{\nabla} \cdot \overline{\overline{P}}_\beta$$

$$+ m_\beta \int \overline{v} \, C_\beta \, d^3v \tag{5-5}$$

where $\overline{\overline{P}}$ is the pressure tensor

$$\overline{\overline{P}}_\beta \equiv m_\beta \int (\overline{v} - \overline{V}_\beta) \, (\overline{v} - \overline{V}_\beta) \, f_\beta \, d^3v \, . \tag{5-6}$$

Assuming a spherically symmetric velocity distribution for species "β" (see Chapter 4), the pressure tensor can be represented by a diagonal tensor with a single scalar pressure p

$$p_\beta = \frac{m_\beta}{3} \int (\bar{v} - V_\beta)^2 \, f_\beta \, d^3v \equiv n_\beta \, T_\beta . \tag{5-7}$$

The Fokker-Planck Collision operator conserves momentum in collisions between similar particles, hence

$$\int C_\beta \bar{v} \, d^3v = 0. \tag{5-8}$$

The second moment of Eq. (5-1) yields the following energy balance equation

$$\frac{\partial}{\partial t} \left(n_\beta \, \frac{m_\beta}{2} V_\beta^2 + \frac{3}{2} n_\beta \, T_\beta\right) = n_\beta e_\beta \, \bar{E} \cdot \bar{V}_\beta - \bar{\nabla} \cdot \bar{H}_\beta + \frac{m_\beta}{2} \int v^2 C_\beta d^3v \tag{5-9}$$

where

$$\bar{H} \equiv \frac{3}{2} m_\beta \int \bar{v} \, v^2 \, f_\beta \, d^3v \tag{5-10}$$

and

$$\frac{\partial}{\partial t} \left(\frac{3}{2} n_\beta T_\beta\right) = - \bar{V}_\beta \cdot \left(\frac{3}{2} T_\beta \bar{\Gamma}_\beta + \bar{Q}_\beta\right) - n_\beta T_\beta \bar{\nabla} \cdot \bar{V}_\beta$$

$$+ n_\beta e_\beta \bar{E} \cdot \bar{V}_\beta + \frac{m_\beta}{2} \int v^2 \, C_\beta d^3v \tag{5-11}$$

where $\overline{Q}_\beta$ is the heat flow vector

$$\overline{Q}_\beta \equiv \frac{m_\beta}{2} \int \overline{v}\,(\overline{v} - \overline{V}_\beta)^2\, f_\beta d^3v. \tag{5-12}$$

In $\overline{Q}_\beta$, we neglect energy flow due to nonisotropic particle distributions. Chapter 4 shows this to be valid for NUWMAK. In PLT, this approximation should be good for all species except possibly the protons. Experimentally $T_{\perp_H} \approx T_{\parallel_H}$ (5-6).

In Eq. (5-11) $\overline{\nabla} \cdot (\frac{3}{2} T_\beta \overline{\Gamma}_\beta)$ represents energy flow due to diffusing particles while $\overline{\nabla} \cdot \overline{Q}_\beta$ represents energy flow due to thermal conduction. The term, $-n_\beta T_\beta \overline{\nabla} \cdot \overline{V}_\beta$ represents a compressive energy flow which is usually small and therefore neglected. The Ohmic heating term is $n_\beta e_\beta \overline{E}_\beta \cdot \overline{V}$ while $\frac{m_\beta}{2} \int V^2 C_\beta d^3v$ describes the rate of energy transfer between collison of unlike particles.

When the Fokker-Planck Collision operator is used, Eqs. (5-2,5 and 9) form a closed system and neoclassical transport is obtained(1,7-10).

By averaging over a magnetic flux surface, one-dimensional particle and energy fluid transport equations are obtained. Whereas previous work assumed that deuterium and tritium did not transport separately(11-12), and impurities were neglected(13,14), the Space-Time Ion Cyclotron Resonance heating code STICR-II can calculate separate deuterium, tritium, impurity, and alpha particle transport in NUWMAK.

$$\frac{\partial}{\partial t} n_D = - \frac{1}{r} \frac{\partial}{\partial r} (r \Gamma_D) - n_D n_T <\sigma v> + S_D$$

$$\frac{\partial}{\partial t} n_T = - \frac{1}{r} \frac{\partial}{\partial r} (r\Gamma_T) - n_D n_T <\sigma v> + S_T$$

$$\frac{\partial}{\partial t} n_\alpha = - \frac{1}{r} \frac{\partial}{\partial r} (r \Gamma_\alpha) + n_D n_T <\sigma v>$$

$$\frac{\partial}{\partial t} n_z = - \frac{1}{r} \frac{\partial}{\partial r} (r\Gamma_z) \tag{5-13}$$

where particle sources and sinks due to alpha fusions(15-16), charge exchange, and impact ionization have been added. In PLT, hydrogen is present instead of tritium and oxygen is the dominant impurity. STICR-I solves the following density equations

$$\frac{\partial}{\partial t} n_D = - \frac{1}{r} \frac{\partial}{\partial r} (r\Gamma_D) + S_D$$

$$\frac{\partial}{\partial t} n_H = - \frac{1}{r} \frac{\partial}{\partial r} (r\Gamma_H) + S_H$$

$$\frac{\partial}{\partial t} n_o = - \frac{1}{r} \frac{\partial}{\partial r} (r\Gamma_o) \tag{5-14}$$

where the only sources and sinks are from charge exchange and impact ionization.

Adding sources and sinks to the electron energy balance equation we find

$$\frac{\partial}{\partial t}\left(\frac{3}{2} n_e T_e\right) = n_D n_T <\sigma v> E_\alpha U_{\alpha e} - \frac{1}{r}\frac{\partial}{\partial r}\left[r\left(Q_e + \frac{3}{2} T_e \Gamma_e\right)\right]$$

$$- P_{EP} - P_{ei} - P_z + P_{OH} + P_{RF}^e \qquad (5\text{-}15)$$

where $n_D n_T <\sigma v> E_\alpha$ is the alpha energy production term; $E_\alpha = 3.52$ MeV for NUWMAK and 0 for PLT; $U_{\alpha e}$ is the fraction of alpha energy deposited in the electrons(1,17); P_{ei} is the electron-ion rethermalization term; P_z is the radiation loss term; P_{EP} is the electron impact ionization loss term; P_{OH} is the Ohmic heating term; and P_{RF}^e is the RF heating term from Landau and transit time damping.

Both STICR-I and STICR-II assume that all ions have the same temperature. The ion energy balance equation with sources and sinks is

$$\frac{\partial}{\partial t}\left(\frac{3}{2} n_i T_i\right) = n_D n_T <\sigma v> E_\alpha U_{\alpha i} - \frac{1}{r}\frac{\partial}{\partial r}\left[r\left(Q_i + \frac{3}{2} T_i \Gamma_i\right)\right]$$

$$+ P_{ei} - P_{IP} - P_{cx} + P_{RF}^i \qquad (5\text{-}16)$$

where E_α = 3.52 MeV for NUWMAK and 0 for PLT; $U_{\alpha i} = 1 - U_{\alpha e}$ is the fraction of alpha energy deposited in the ions; P_{cx} is the charge exchange term; P_{IP} is ion impact ionization loss term; and P^{i}_{RF} is the ion RF heating term.

Since charge neutrality is assumed in NUWMAK

$$n_e = n_D + n_T + 2n_\alpha + \langle z\rangle n_z \tag{5-17}$$

whereas in PLT

$$n_e = n_D + n_H + 8\, n_o . \tag{5-18}$$

The particle transport coefficient Γ_β can be written as$^{(9)}$

$$\Gamma_\beta = - \sum_b D_{\beta b} \nabla F_b \tag{5-19}$$

while the energy transport coefficient Q_β can be expressed as$^{(9)}$

$$Q_e = - \sum_b \chi_{eb}\, \nabla F_e$$

$$Q_i = - \sum_b \chi_{ib}\, \nabla F_i \tag{5-20}$$

where F_b is either density, ion or electron temperature and b = e, D, T, α, C for NUWMAK or b = e, D, H, O for PLT.

The conductivity and diffusion terms in Eqs. (5-15,16) now include the collisional effects in Eq. (5-9). Previously, trapped particle scaling(1,7,13-14,18) was assumed to describe the plasma transport. However, trapped particle scaling has yet to be seen in any tokamak to date. With collisonal effects incorporated into $D_{\beta b}$ and $\chi_{\beta b}$, "empirical" scaling can be used. Although "PLT empirical" scaling is not fully understood from a theoretical standpoint, computationally this scaling has produced good agreement with both PLT Ohmic heating and neutral beam heating experiments. Having shown that ICRF heating does not affect the bulk plasma distribution, we have assumed this scaling holds for the RF experiments.

After obtaining agreement with the present day PLT RF heating experiments(6), we next assume that "PLT empirical" scaling predicts particle and energy transport in NUWMAK. The transport scaling, although not affecting the RF power deposition, greatly influences the auxiliary heating requirement.

For high density and temperature plasmas, "PLT empirical" scaling is(19)

$$
\begin{aligned}
D_\beta &= \frac{1.25 \times 10^{17}}{n_e} \ \mathrm{cm}^2/\mathrm{sec} + \text{neoclassical}^{(9)} \\
\chi_i &= \text{neoclassical}^{(9)} \\
\chi_e &= \frac{1.0 \times 10^{17}}{n_e} \ \mathrm{cm}^2/\mathrm{sec} + \text{neoclassical}^{(9)} \qquad \text{for } \frac{1.0 \times 10^{17}}{n_e} < 2 \times 10^5 \ \mathrm{cm}^2/\mathrm{sec} \\
&= 2 \times 10^5 \ \mathrm{cm}^2/\mathrm{sec} + \text{neoclassical}^{(9)} \qquad \text{for } \frac{1.0 \times 10^{17}}{n_e} \geq 2 \times 10^5 \ \mathrm{cm}^2/\mathrm{sec}.
\end{aligned}
\tag{5-21}
$$

In STICR-I and STICR-II, the classical electron-ion equilibration term is used(1)

$$P_{ei} = \frac{3n_e}{\tau_{ei}} \frac{m_e}{m_i} (T_e - T_i) \qquad (5\text{-}22)$$

where τ_{ei} is the electron-ion equilbration time(20)

$$\tau_{ei} = \frac{3m_e^{1/2} \, T_e^{3/2}}{4(2\pi)^{\frac{1}{2}} e^4 \, n_i \, \ln\Lambda} \qquad (5\text{-}23)$$

with $m_i \equiv \sum_j \frac{m_j n_j}{n_e}$. This expression for P_{ei} is used since this provides good agreement with experiments(1).

The Ohmic heating term is calculated using neoclassical theory

$$P_{OH} = E_\phi J_\phi \qquad (5\text{-}24)$$

$$E_\phi = \eta_{nc} J_\phi \qquad (5\text{-}25)$$

where η_{nc} is the neoclassical resistivity(11,13)

$$\eta_{nc} = \eta_{sp} \, (1 - 1.95(r/R)^{\frac{1}{2}} + .95(r/R))^{-1} \qquad (5\text{-}26)$$

η_{sp} is the Spitzer resistivity(21).

Because PLT and NUWMAK are assumed to be transparent to their own radiation, a coronal equilibrium model$^{(22)}$ is used. Radiation in this model results from Bremsstrahlung, radiative recombination and line transitions. Using coronal equilibrium, the radiation loss term is$^{(22)}$

$$P_z = n_e n_z L_z \tag{5-27}$$

$$L_z = \sum_{i=o}^{5} A_i \left\{ \mathrm{Log}_{10}\, T_e \right\}^i \quad (T_e \text{ in keV}) \tag{5-28}$$

and A_i are coefficients of a polynomial least square fit to the radiation cooling rate.

For charge exchange and impact ionization, analytical or polynomial expressions were fitted to the experimental data$^{(23)}$. These expressions, when integrated over Maxwellian distributions, were fitted to polynomials to obtain the cooling rates. For charge exchange

$$P_{cx} = n_i n_o \langle\sigma v\rangle_{cx} \, (E_i - E_o) \quad (o \equiv \text{neutral atom}) \tag{5-29}$$

where

$$\langle\sigma v\rangle_{cx} = \sum_{i=o}^{5} B_i (\ln E\,)^i \quad (E \text{ in eV}) \tag{5-30}$$

with E in eV; n_o is the neutral gas density; E_i is the incoming ion energy; and E_o is the neutral gas energy. For ion impact ionization

$$P_{IP} = n_i n_o \langle \sigma v \rangle_{IP} \ (-13.6 \text{ eV}) \tag{5-31}$$

while electron impact ionization has

$$P_{EP} = n_e n_o \langle \sigma v \rangle_{EP} \ (-13.6 \text{ eV}) \tag{5-32}$$

where

$$\langle \sigma v \rangle_{IP} = \sum_{i=o}^{5} C_i (\ln \ E\ )^i \qquad\qquad E \text{ in eV}$$

$$\langle \sigma v \rangle_{EP} = \sum_{i=o}^{5} D_i (\ln E\ )^i . \tag{5-33}$$

The incoming ion or electron is assumed to lose 13.6 eV in ionizing a neutral atom. In the charge exchange calculation, the initial or first generation charge exchange event has a neutral atom energy of 5 eV.

The radiation, charge exchange and impact ionization terms are calculated at every grid point along the minor cross section.

Electron and ion impact are a source of ions in Eqs. (5-13,14)

$$S_D = n_i n_{D^o} \langle \sigma v \rangle_{IP} + n_e n_{D^o} \langle \sigma v \rangle_{EP}$$

$$S_T = n_i n_{T^o} \langle \sigma v \rangle_{IP} + n_e n_{T^o} \langle \sigma v \rangle_{EP} \qquad \text{(for NUWMAK)}$$

$$S_H = n_i n_{H^o} \langle \sigma v \rangle_{IP} + n_e n_{H^o} \langle \sigma v \rangle_{EP} \qquad \text{(for PLT).} \tag{5-34}$$

When the neutral gas has a different concentration of hydrogenic species than the plasma, charge exchange can alter the ion concentration. For PLT

$$S_D = n_H n_{D^o} \langle \sigma v \rangle_{cx} - n_D n_{H^o} \langle \sigma v \rangle_{cx}$$

$$S_H = n_D n_{H^o} \langle \sigma v \rangle_{cx} - n_H n_{D^o} \langle \sigma v \rangle_{cx} \tag{5-35}$$

while for NUWMAK

$$S_D = n_T n_{D^o} \langle \sigma v \rangle_{cx} - n_D n_{T^o} \langle \sigma v \rangle_{cx}$$

$$S_T = n_D n_{T^o} \langle \sigma v \rangle_{cx} - n_T n_{D^o} \langle \sigma v \rangle_{cx}. \tag{5-36}$$

STICR-I and STICR-II assume that a feedback control exists which keeps both hydrogenic ion densities constant. Particles are added or removed using a flat profile, which leaves the temperature profiles unchanged. In PLT(5-6), recycling and wall sputtering keep the plasma density fairly constant over the RF pulse. By adding particles without affecting the temperature profiles, we can simulate PLT and obtain good agreement.

Unlike PLT, we have no source of impurities; consequently, Z decreases. In PLT experiments, the impurity density actually increases during the RF pulse. Since radiation losses appear to be small, this discrepancy between impurity densities has a small effect. Since the PLT electron temperature rise is uncertain at this time(6), it is difficult to compare our electron temperature profiles to the experiment. The radiation and impurity transport models should not affect either the ion temperature profiles or the RF power deposition.

We now examine the ICRF heating model which calculates the RF heating terms in Eqs. (5-15,16).

5.B. 1-D WKB Slab Model of ICRF Heating

The full 3 x 3 hot plasma dispersion tensor (Eq. (3-4)) is used to obtain a local complex $k_\perp$ for a given real ω and $k_\parallel$. The plasma minor cross section is divided into 117 points, neglecting curvature and edge effects (see Fig. (5-1)). At each point r_i, $n(r_i)$, $T(r_i)$, and $B(r_i)$ are used to calculate $k_\perp(r_i)$. All densities and temperatures are assumed to be symmetric in minor radius. Mau(24) has shown density and temperature gradient effects on the dispersion relation to be small.

To find the power deposition for each species "β" at each point r_i, the weak damping formula is used(25-26)

$$P^{\beta}_{RF}(r) = \omega \bar{E}(\overset{*}{r}) \cdot \bar{\bar{K}}^{a}_{\beta}(r) \cdot \bar{E}(r)/2 \ (W/cm^3) \tag{5-37}$$

which is valid when $\left|\frac{\mathrm{Im}k_{\perp}}{\mathrm{Re}k_{\perp}}\right| << 1$. The validity of Eq.(5-37) is examined in Appendix D. The weak damping formula holds over the entire cross section in NUWMAK. For PLT, it breaks down over the cyclotron resonance layer. Near this layer, mode conversion may also occur. We address this problem later.

A local description is again used to calculate the RF electric field component ratios E_y/E_x, E_z/E_x at each point along the minor cross section

$$\bar{\bar{D}}(r) \cdot \bar{E}(r) = 0. \tag{5-38}$$

An incoming fast wave may mode convert into an electrostatic Ion Bernstein wave(27-28). The RF dispersion relation

$$\det|\bar{\bar{D}}(r)| = 0 \tag{5-39}$$

has an infinite number of solutions. The smallest root corresponds to the fast wave root ($k_{\perp f}$). The next smallest root is associated with an electrostatic ion cyclotron mode called an Ion Bernstein wave ($k_{\perp I.B.}$). Equations (5-38-39) are solved at each point using both roots

$$\det|\bar{\bar{D}}_f(r)| = 0 \qquad \bar{\bar{D}}_{f(r)} \cdot \bar{E}^f(r) = 0$$

and

$$\det|\bar{\bar{D}}_{I.B.}(r)| = 0 \qquad \bar{\bar{D}}_{I.B.}(r) \cdot \bar{E}^{I.B.}(r) = 0 \tag{5-40}$$

Equation (5-40) yields $k_{\perp f}$, $k_{\perp I.B.}$ and the ratios E_y^f/E_x^f, E_z^f/E_x^f, $E_y^{I.B.}/E_x^{I.B.}$, $E_z^{I.B.}/E_x^{I.B.}$ where f designates the fast wave and I.B. the Ion Bernstein mode. So far, each point has been calculated independently. We now must "connect" these points to form a 1-D picture. To accomplish this a WKB type plane wave equation for $E_x^\gamma(r)$ is used

$$\frac{d^2E_x^\gamma}{d^2r} + k_{\perp\gamma}^2(r)E_x^\gamma(r) = 0 \tag{5-41}$$

where γ=f, I.B. The solution to Eq. (5-41) has the following form[30]

$$E_x^\gamma \propto \frac{1}{(k_{\perp\gamma})^{1/2}} e^{i\int \bar{k}_{\perp\gamma} \cdot d\bar{r}} \tag{5-42}$$

The validity of this solution is investigated in Appendix D and found to hold over the entire cross section NUWMAK. In PLT, the WKB solution also breaks down in the vicinity of the cyclotron resonance.

It is not obvious that a slab model holds for PLT, a much smaller device than NUWMAK. However, the temperature profiles obtained by STICR-I agree with the experiment. Although a 2-D or 3-D cylindrical model$^{(27)}$ would be more accurate, the differences may not affect the temperature profiles.

We now need to find the magnitude of the electric field. We first fix the phase by assuming that the fast wave has a real E_x^f at the low field edge

$$E_x^f(r = \text{edge}) = C(1.,0.) \,. \tag{5-43}$$

To find C, we normalize the electric field assuming all the wave energy launched is absorbed by the plasma

$$P_{RF} = \frac{\omega}{2} \sum_{\beta} \sum_{i} \bar{E}^{*f}(r_i) \cdot \bar{\bar{K}}^{a}_{\beta f}(r_i) \cdot \bar{E}^{f}(r_i) + \bar{E}^{*I.B.}(r_i) \cdot \bar{\bar{K}}^{a}_{\beta_{I.B.}}(r_i) \cdot \bar{E}^{I.B.}(r_i) \tag{5-44}$$

where we sum over the RF energy deposited at each point r_i, for each species, for both the fast and Ion Bernstein modes. Writing the normalized electric field as

$$\bar{E}^{\gamma} = C\tilde{E}^{\gamma} \tag{5-45}$$

where $\tilde{E}$ is the unnormalized field, C is

$$C \equiv \frac{P_{RF}}{\frac{\omega}{2} \sum_{\gamma} \sum_{\beta} \sum_{i} \tilde{E}^{*}(r_i) \cdot \bar{\bar{K}}^{a}_{\gamma}(r_i) \cdot \tilde{E}^{*\gamma}(r_i)} \,. \tag{5-46}$$

In PLT and NUWMAK, a plane fast wave is launched from the low field edge. At each point r, as the wave propagates inwards, $k_{\perp f}^2(r_i)$ and $k_{\perp I.B.}^2(r_i)$ are calculated. If $\mathrm{Re}k_{\perp f}^2 \approx \mathrm{Re}k_{\perp I.B.}^2$ to within 10%, over a finite mesh width, mode conversion is assumed to occur. Jacquinot$^{(29,31)}$ has obtained the following approximate expression for the mode conversion threshold in PLT

$$n_H \geq \frac{n_D\ k_\parallel V_{th}(H)}{\omega} \left(\frac{4}{3} + \frac{k_\parallel^2 c^2}{\omega_{PD}^2}\right). \qquad (5\text{-}47)$$

This equation agrees with the computational threshold.

When mode conversion does not occur, $E^{I.B.} = 0$ and Eq. (5-44) is evaluated using the fast wave mode. If mode conversion does occur, reflection, transmission and mode conversion coefficients are calculated at the mode conversion surface (see Fig. (5-2)). Upon reaching the mode conversion surface, part of the incoming fast wave is reflected back towards the low field side with an initial electric field $R\bar{E}$, where R is the reflection coefficient and $\bar{E}$ the incident electric field. Some of the incoming wave is transmitted through the mode conversion layer with an electric field $T\bar{E}$, where T is the transmission coefficient. In NUWMAK, the remaining wave energy is assumed to mode convert into an Ion Bernstein wave which propagates towards the high field side with an initial electric field $C\bar{E}$, with C being the mode conversion coefficient.

For PLT, Swanson has shown(28) that some of the wave energy may be deposited in the mode conversion layer. To model this, STICR-I assumes that in the mode conversion layer the electric fields are constant and the absorbed energy is equally divided between the two branches. We shall see that mode conversion appears to play a minor role in both PLT and NUWMAK.

5.C. Mode Conversion Coefficients - NUWMAK

By inverse Fourier transforming a small ion gyroradius expansion of Eq. (5-38), a fourth order differential equation can be obtained to describe coupling between the fast and Ion Bernstein branches(27)

$$\frac{d^4E}{dr^4} + \lambda r \frac{d^2E}{dr^2} + (\lambda r + \gamma)E = 0 \tag{5-48}$$

where λ, γ are constants. Using Laplace's method and analytical continuation of the contours of integration, the WKB solution for the wave electric field on each side of the mode conversion layer can be connected using various connection formulae. The following transmission, reflection and mode conversion coefficients are obtained for small $k_{\parallel}$

$$|T| = e^{-\pi\eta/2}$$

$$|R| = |1 - e^{-\pi\eta}|$$

$$|C|^2 = 1 - |T|^2 - |R|^2 = e^{-\pi\eta} - e^{-2\pi\eta} \tag{5-49}$$

where

$$\eta = \frac{R_o}{2} \frac{\omega_{PD}}{c} \beta \left(1 + \frac{n_H}{n_e} \beta^{-1}\right) \tag{5-50}$$

Equations (5-49-50) are valid for a fast wave launched from the low field side.

5.D. Mode Conversion Coefficients-PLT

Swanson(28) has derived mode conversion coefficients for fundamental minority heating in PLT. Instead of Eq. (5-48), Swanson obtains fourth order coupled differential equations which describe mode coupling. Swanson finds the following mode conversion coefficients

$$T = e^{-\eta}$$

$$R = -(1 - e^{-2\eta} + I_{22})$$

$$C = -e^{-\eta}(1 - e^{-2\eta})(1 + I_{02}) \tag{5-51}$$

where

$$\eta = \frac{\pi \omega_{PD} R_o}{4c(1+p^2)^2} \alpha^3 \left(\alpha^2 \beta_D + \frac{n_H}{n_e}\right) \tag{5-52}$$

and

$$\alpha^2 = (1 + p^2)(1 - 3p^2)/(1 + 3p^2)$$

$$p = \frac{k_\parallel V_A}{\omega} \tag{5-53}$$

for $\frac{n_H}{n_e}$ small. Since rotational transform effects are small$^{(28)}$, they are neglected.

In Eq. (5-51) I_{02} and I_{22} must be solved numerically. Swanson has found $C = (C_{r2}, C_{i2})$ and $R = (R_{r2}, R_{i2})$ for $\bar{n}_e = 6.2 \times 10^{13}$ cm^{-3}, $B_o = 36$ kG, $\beta_D = 0.01$, $\frac{n_H}{n_e} = 0$ (see Fig. 5-3)). For those parameters and $k_{\parallel} = 0.1$ cm^{-1},

$$|C| \approx 0.01$$

$$|R| \approx .05 \tag{5-54}$$

so

$$I_{22} \sim -0.34$$

$$I_{02} \sim -0.97 \tag{5-55}$$

with $\eta \sim 0.25$.

We assume that I_{22} and I_{02} do not change significantly when PLT parameters in TABLE 5-1 are used. In deriving Eqs. (5-51-53) Swanson neglects electrons and nonMaxwellian effects. Using Eqs. (5-51-53,55) we find that $|C|$ and $|R|$ are small. Most of the energy is either transmitted or absorbed in the resonance zone

$$E_{absorb} = 1 - |R|^2 - |T|^2 - \rho|C|^2 \tag{5-56}$$

with

$$\rho = (1 - e^{-2\eta})^{-1} \tag{5-57}$$

We now examine ICRF heating in PLT.

5.E. Numerical Results - PLT

The PLT parameters are listed in Table 5-1. Parabolic densities (Figs. (5-4-6)) and parabolic squared temperatures (Figs. (5-7-8)) are the initial profiles. Oxygen is assumed to be the dominant impurity with $Z_{eff} \sim 2$. At the edge $T_i = T_e = 5$ eV.

In Fig. (5-9), the cold plasma $k_{\perp cp}^2(r)$ (dotted line) is close to $\mathrm{Re}k_{\perp f}^2$ (solid line) except at the resonance layer, where the cold plasma root $\to \infty$. T2 equals 1.0 indicates the fast wave is transmitted through the resonance zone, there being no mode conversion. In Fig. (5-8), HTEMPC equals 1.5 indicates that $T_H = 1.5 \times T_i$ in the RF calculations. If $T_H = T_i$, mode conversion would occur.

In Fig. (5-9) $\mathrm{Re}k_{\perp f}^2(r) < 0$ over a small region near r = 123 cm, indicating a possible evanescent zone. Since this region is small, no reflection or absorption is assumed to occur over this region. This evanescent zone lies in the region where both weak damping and WKB theory break down (see Appendix D). The steep rise in $\mathrm{Im}k_{\perp f}^2(r)$ near this region is a result of the presence of the ion-ion hybrid resonance(32).

$$\omega^2 = \frac{\chi_D f_H + \chi_H f_D}{\chi_D f_D + \chi_H f_H}\,\omega_{CH}\omega_{CD}$$

$$\chi_D = n_D/n_e \qquad f_D = m_e/m_D$$

$$\chi_H = n_H/n_e \qquad f_H = m_e/m_H \tag{5-58}$$

which lies near the $\omega = \omega_{CH} = 2\omega_{CD}$ resonance layer when $n_H \rightarrow 0$. As $n_H \rightarrow 0$, the evanescent zone and peaking of $\mathrm{Im}k_{\perp f}^2$ disappear, resulting in a smoothing of the RF spatial depositions.

The fast wave electric field components are shown in Figs. (5-10-12). Solid lines indicate real parts while dashed lines correspond to the imaginary parts. The peaking of $\mathrm{Im}k_{\perp f}^2$ and the evanescent zone produces a corresponding peaking of the electric field. The number of oscillations in the electric field indicates approximately four wavelengths fit within the device. Since the WKB approximation assumes the plasma density and temperature do not vary over a wavelength, this assumption is not as appropriate in PLT as in a reactor. However, WKB theory seems to provide reasonably accurate results when compared to the experiment.

Figures (5-10-12) show a drop in $|E^f|$ from $\sim$100 V/cm at the low field edge to $\sim$20 V/cm at the high field side. This drop implies the fast wave is absorbed within one pass across the cross section. No eigenmodes are observed in PLT, indicating this is correct. Both STICR-I and STICR-II neglect possible eigenmode effects. The electric field profile is obtained neglecting edge effects, a good approximation when no eigenmodes are established.

Over 93% of the RF power is deposited near the center (Figs. (5-13-14)), again indicating the RF is absorbed within one pass across the minor radius. The peaking in $\mathrm{Im}k_{\perp f}^2$ and $\overline{E}^f$ result in a sharp peaking of the hydrogen and deuterium RF power profiles. The evanescent zone causes the sharp decrease in the deuterium and electron absorption profiles.

Figure (5-13) shows the fundamental minority heating of hydrogen deposition along the entire plasma cross section. Upon averaging over magnetic flux surfaces, Fig. (5-14) is obtained. This drop in power at $r = 0$ occurs because there is only one point in the flux surface. Every other region has contributions from both $+r$ and $-r$.

The deuterons, through second harmonic damping, absorb only 3% of the total RF power (Fig. (5-15)). The remaining 6.5% is deposited in the electrons over a relatively broad heating zone.

As time increases, the impurity density drops, shown in Fig. (5-16). Figures (5-17-18) show the central deuterium and hydrogen densities to increase while the edge decreases. The proton density increase at the center is faster than the deuterium increase. After 60 ms, $\frac{n_H}{n_e} < 11\%$. This increase in n_H at the center, together with the decrease in electron density, lowers the mode conversion threshold. Over the last 40 ms of the RF pulse, STICR-I finds mode conversion occuring. Since the impurity level actually increases in the experiment, the mode conversion threshold should not decrease with time.

In any case, Figs. (5-19-20) show that temperature profiles are unchanged when mode conversion appears. The ion and electron temperature profiles reach steady state 40-60 ms after the RF is on, in agreement with the experiment. Figures (5-21-22) show that the electron and ion RF heating profiles remain unaffected as well.

At the end of the RF pulse, the density profiles are still parabolic. The average electron density has dropped from 3.0 x 10^{13} cm^{-3} to 2.6 x 10^{13} cm^{-3}. The temperature profiles are shown in Figs. (5-23-24). The electrons are not heated while the average ion temperature increases 225 eV with $\Delta T(0) \sim 600$ eV in agreement with the experiment(6).

After 60 ms, mode conversion appears with the mode conversion layer between the 78th and 79th grid points (120.0 cm $\leq$ r $\leq$ 120.5 cm). There is still an evanescent zone which lies between the launching structure and the mode conversion layer. Between r = 121 cm and 135 cm, $\mathrm{Im}k^2_{\perp f} < 0$ indicating that most of the RF wave energy may be damped before the mode conversion layer is reached. Swanson's mode conversion coefficients indicate over 58% of the wave energy which reaches the mode conversion layer is absorbed. Over 37% of the energy is reflected. Only 4.7% of the wave energy is transmitted through the layer and none of the energy is converted into the Ion Bernstein branch.

Figures (5-25-26) show the wave energy is largely damped before the wave reaches the mode conversion layer at r = 120.5 cm. Over 90% of the RF power is still deposited in the protons over the same width as occurs when mode conversion is absent. Second harmonic damping increases slightly from 3% to 6% while the electron absorption decreases slightly to 4% of the total RF power.

The cyclotron resonance is between the mode conversion layer and the low field edge. Therefore, the fast wave undergoes appreciable damping before the mode conversion layer is reached. Over 37% of the RF energy is reflected back towards the low field side. This wave must again pass through the resonance layer. This further reduces the amount of reflected power. There is some interference between the incident and reflected fast waves. A standing wave develops over half the plasma cross section. This produces oscillations in the broad electron RF heating term (Fig. (5-22)). However, electron absorption is small and the ion heating terms do not change significantly. We therefore conclude that there is very little power in the reflected wave. Mode conversion plays a small role since most of the energy is deposited in the plasma before the mode conversion layer is reached. Approximately 58% of the available mode conversion energy is deposited in the mode conversion layer, lying close to the resonance zone. Without mode conversion, the RF heating profiles would not change.

Figure (5-19) shows the electron temperature profile remaining fairly constant during the RF pulse, except for an initial drop at t = 0 ms. The peak temperature drops from 1300 eV to 950 eV at t = 100 ms while the average value drops from 440 eV to 395 eV with STICR-I. In agreement with the experiment, it showed no significant heating of the electrons. The initial drop in T_e indicates that the equilibrium Ohmic heating electron temperature profile predicted by STICR-I differs from the experimental value. With all the uncertainties in edge effects, radiation modeling, and transport, this is to be expected. The electron temperature drops initially because the loss mechanisms (predominantly transport and radiation) are too large. The drop in T_e is relatively small, indicating at least reasonable agreement in the electron temperature calculation with PLT.

The ion temperature is better known experimentally and is much less sensitive to impurity levels and radiation models. Although the ion RF heating profile $P^{i}_{RF}(r) = P^{D}_{RF}(r) + P^{O}_{RF}(r) + P^{H}_{RF}(r)$ is sharply peaked, the ion temperature is broader. Radial transport and charge exchange keep the ion temperature from becoming as peaked. The RF power is peaked enough that $T_i(0)$ rises from 600 eV to 1200 eV in good agreement with the experiment. However, the ion temperature is broad enough that the average ion temperature increases from 206 eV to 426 eV, also in agreement with the experiment. Having obtained agreement with PLT experiments we now use STICR-I to examine the mode conversion threshold.

5.F. Mode Conversion in PLT

With $\frac{T_H}{T_i} = 1.5$, mode conversion does not occur during the first 60 ms of the RF pulse. As time increases, $\frac{n_H}{n_e}$ increases to 11% while n_e and n_o decrease. These effects appear to lower the mode conversion threshold. With mode conversion occurring over the final 40 ms, neither density, temperature, nor RF heating profiles are greatly altered.

Initially $\frac{T_H}{T_i} = 1$ in PLT. Setting $C_H = 1.0$, STICR-I finds mode conversion occuring during the entire RF pulse. Figure (5-27) shows the dispersion relation at t = 0 ms. There is little change in the RF dispersion relation during the RF pulse. At t = 0 ms, 58% of the RF energy reaching the mode conversion layer is absorbed, 37% reflected, and 4.7% transmitted. At t = 100 ms, these numbers change to 59%, 27% and 14%. No wave energy is mode converted. The mode conversion layer shifts slightly from 122.5 cm $\leq r \leq$ 123.0 cm to 120.0 cm $\leq r \leq$ 121.0 cm .

This shift in the mode conversion layer has little affect on the RF power deposition. Most of the wave energy is absorbed before the mode conversion layer is reached. Over 90% of the RF power is still deposited in the protons in the same heating zone as before. Neither the equilibrium densities nor temperatures change. Equilibrium is still obtained during the RF pulse.

When $C_H = 2.0$, mode conversion never occurs. Figures (5-28-29) show the evanescent zone disappearing as the ion temperature increases. As the evanescence shrinks, the dip in both the deuterium and electron heating profiles lessens. The dominant heating mechanism remains minority heating. Figures (5-30-31) show little change in the hydrogen heating profile. When $C_H = 2.0$, there is a slight decrease in the amount of hydrogen heating, from 89.6% to 88%. The heating zone increases slightly with temperature from 12-14 cm to 20 cm. As the ion resonant heating zone widens, second harmonic damping increases from 3% to 7% at the expense of electron heating, dropping from 7% to 4.6% of the RF power.

Again we find little change in the equilibrium densities and temperatures with equilibrium being reached between 40-60 ms.

From these three cases, C_H = 1.0, 1.5, 2.0, the following conclusions can be made. After the Ohmic heating phase, $T_H = T_i$ so the PLT RF heating phase begins in the mode conversion regime. Although mode conversion occurs, fundamental minority heating of protons is the dominant ion heating mechanism. Chapter 4 showed C_H becoming larger than one as time increases. As C_H increases, the mode conversion threshold rises until mode conversion disappears. As T_i increases, the ion resonant heating width increases from 12-14 cm to 20 cm.

However, the presence of mode conversion or the increase of the cyclotron resonance layer does not alter the density and temperature profiles. Mode conversion may be difficult to find in PLT since these profiles are not changed in its presence. Whether mode conversion occurs or not, STICR-I finds good agreement with the experiment.

To investigate the influence of $k_{\parallel}$ on mode conversion, we change $k_{\parallel}$ from 0.1 cm^{-1} to 0.2 cm^{-1} with $C_H = 1.5$. The equilibrium plot of $k_{\perp f}^2(r)$ (Fig. (5-32)) shows that mode conversion is eliminated. The resonance zone is now very broad and $\mathrm{Im}k_{\perp f}^2$ no longer has a sharp peak. There are now wide evanescent regions on the plasma edges. Although these regions may result in surface heating(24,27), we assume that the fast wave can penetrate through the low field evanescent zone without losing energy.

The proton heating width is quite broad, increasing from 25 cm at t = 0 ms to 35 cm at t = 100 ms. This widening produces an increase in fundamental heating from 233 kW at t = 0 to 302 kW at 100 ms (Fig. (5-33)). Initially, when $k_\parallel$ is increased electron Landau and transit time damping is much larger than in the smaller $k_\parallel$ case, 91 kW compared to 23 kW. As the ion temperature increases, the amount of electron heating drops, reaching 40 kW at 100 ms (Fig. (5-35)). Figure (5-34) shows the deuterium RF profile.

The broadening of the ion heating profiles and the increase in electron heating do not affect the density or electron temperature profiles. However, the ion temperature profile (Fig. (5-36)) is changed. While $\Delta\overline{T}_i \sim 220$ eV is close to our previous results, $\Delta T_i(0) \sim 500$ eV is too low. If the ion heating zone is substantially larger than 20 cm, the RF power density at the center must drop. This drop in power density results in a smaller ion temperature increase in the center. Whereas the occurrence of mode conversion does not affect our results, a broadening of the heating zone does.

Although the WKB slab model breaks down in the plasma center, the RF heating width appears to agree with the experiment. The RF power deposition within this zone may vary (perhaps a smoothing of the power deposition) when a more complete treatment is used. However, changes in temperatures and densities should be minimal.

We conclude that our RF heating model simulates accurately the density and temperature profiles in PLT.

In a reactor, Appendix D shows the WKB slab model to be valid over a wider region than in PLT. The WKB model assumes that the densities and temperatures do not change over distances of a wavelength. In a reactor, the characteristic scale lengths over which the plasma density and temperature vary are larger than in PLT. In addition, the wavelengths, shown in Figs. (5-50-52), become shorter. These two effects tend to improve the WKB approximations.

In simulating a reactor startup it is necessary to compute, as accurately as possible, the probable density and temperature profiles. If NUWMAK follows "PLT empirical" scaling we conclude that STICR-II, using the 1-D WKB slab model of ICRF heating, should be more accurate in a reactor(27) and should predict the density, temperature and RF heating profiles.

5.G. Fundamental Minority Heating of Deuterium in NUWMAK

In this section we examine fundamental heating of deuterium in the NUWMAK conceptual tokamak reactor(14,18). Table 5-2 lists the plasma parameters. In this scenario, $\omega = \omega_{CD}(r=0)$ or $f = 46$ MHz. To avoid the possible mode conversion complications and to reduce the influence of the ion-ion hybrid resonance, the maximum concentration of deuterium in a tritium plasma is found to be 10%. When the concentration of deuterium is increased, mode conversion at the ion-ion hybrid resonance begins to dominate over fundamental heating. Although heating at this resonance has been observed in TFR(31) and has been examined theoretically(27-28,33), the physics is not clearly understood. Therefore, we examine RF heating scenarios which minimize the influence of this resonance.

The initial parabolic densities and temperatures, obtained after the Ohmic heating phase, are shown in Figs. (5-37-41). Fully stripped carbon with an initial parabolic profile of average density, $\overline{n}_c = 5.5 \times 10^{10}$ cm^{-3}, is assumed to be the dominant impurity. To avoid initial numerical oscillations at the edge, n_e (edge) = 3×10^{13} cm^{-3}. As time increases, n_e(edge) drops to 1.0×10^{12} cm^{-3}. STICR-II finds that approximately 125 MW of RF power for 2.0 sec provides enough heating to ignite the plasma. The temperature profiles at the time of RF shutoff are shown in Figs. (5-42-43). The average plasma temperature has increased from 1.5 keV to 6.3 keV. Since there is no source of impurities, the carbon density remains parabolic but decreases to a spatially averaged value of 3.35×10^{10} cm^{-3}.

The fast wave and cold plasma $k^2_{\perp cp}(r)$ are shown in Fig. (5-44). T2 = 1.0 indicates that no mode conversion occurs. The fast wave is transmitted through the mode conversion layer. Figure (5-44) shows a broad region, 50-100 cm wide, where $\mathrm{Im} k^2_{\perp f} > 0$. This broad resonance surface lies between the antenna and the mode conversion surface. As the plasma heats, this layer becomes wider (see Fig. (5-45)). The resonance layer produces substantial damping of the incoming wave through electron Landau and transit time damping, before the wave energy can reach the mode conversion layer. This damping greatly diminishes any mode conversion effect on the heating profiles.

The initial electron RF power deposition is shown in Figs. (5-46-47). Figure (5-46) shows that electron heating occurs before mode conversion layer is reached, which Fig. (5-47) shows to be over 62% of the total RF power.

The remaining RF power is deposited in the deuterons as shown in Figs. (5-48-49). Since the mode conversion layer lies near r = 490 cm, we see that most of the deuterium heating also occurs before this layer is reached.

The components of the RF electric field are shown in Figs. (5-50-52). The wave damping is very strong in the cyclotron resonance zone. The electric field strength is greatly reduced by the time the wave reaches the mode conversion layer. From these figures and the RF power deposition, we can conclude that even if mode conversion did occur, as in PLT, the RF power deposition would not change. The wave is too strongly damped before the mode conversion layer is reached.

As the plasma heats and the resonance zone widens, the RF power deposition shifts towards the low field side, away from the mode conversion layer. At t = 1.5 sec, the peak electron heating has shifted ∿28 cm and been reduced from 79 MW to 75 MW (Figs.

(5-53-54)). Figures (5-55-56) show the deuterium heating also shifting towards the low field side. The broadening of the cyclotron resonance layer produces a stronger damping of the incoming fast wave and an increase in fundamental minority heating.

Figure (5-57) shows the alpha heating remains center-peaked. At t = 2.0 sec, 233 MW of power goes to the electrons while 68 MW goes to the ions. Since the alphas are preferentially slowing down on the electrons $T_e > T_i$. Keeping the alpha power peaked near the center can reduce the amount of auxiliary heating needed to reach ignition(34). Ignition can be achieved in the center before global ignition is reached. An outwardly propagating burn wave can then ignite the remaining plasma.

The feedback control keeps the deuterium and tritium densities constant with time, while the alpha density increases with time. However, at the RF shut off point, the alpha density is only 1.3×10^{12} cm^{-3} (Fig. (5-58)), still too low to absorb any RF power. The plasma temperature runs away under "PLT empirical" scaling. Both $T_e(0)$ and $T_i(0) > 36$ keV at t = 3.0 sec. There is enough alpha power being produced by the time the RF is turned off to keep the plasma ignited.

A 50%D-50%T plasma would be optimal from the standpoint of alpha production. Therefore, we now return to the heating scenario examined in Chapter 2.

5.H. Second Harmonic Heating of Deuterium in NUWMAK

Table 5-3 lists the plasma parameters for this second harmonic heating scenario. The increased concentration of deuterium (50%D-50%T) produces the greatest number of alpha fusions for the same plasma temperature. Approximately 100 MW of RF power (f = 92 MHz) for 1.5 sec must be provided for the plasma to reach ignition. The initial electron, deuterium and tritium density profiles are again parabolic with $\bar{n}_D = \bar{n}_T = 1.5 \times 10^{14}$ cm^{-3}. The initial alpha, carbon and temperature profiles are the same as before (Figs. (5-40-41)).

With the increased concentration of deuterium, Fig. (5-59) shows that mode conversion now occurs. The mode conversion layer is between the 65th and 66th grid points (503.5 cm $\leq$ r $\leq$ 504.5 cm). As the temperature increases, the cyclotron resonance layer again widens. At t = 1.5 sec, the resonance layer increases up to 50 cm in width towards the low field side. Meanwhile, the mode conversion layer shifts towards the high field side while also increasing in width. At t = 1.5 sec, the mode conversion layer lies between the 71st and 75th mesh points (404.5 cm $\leq$ r $\leq$ 492.5 cm).

Using the mode conversion coefficients in Eqs. (5-49-50), we find that the fast wave is completely reflected at the mode conversion layer. However, as in the previous scenario, the incoming fast wave is so strongly damped before the mode conversion layer is reached that mode conversion effects are minimal.

Second harmonic heating of deuterium with third harmonic heating of tritium ($\omega = 2\omega_{CD} = 3\omega_{CT}$) was first proposed as a heating scheme because direct ion heating was thought to occur(13-14, 35-36). However, the higher densities and temperatures which will occur in the reactor regime lead to substantial electron Landau and transit time damping of the fast wave before the center is reached. Figures (5-60,62) show that initially, over 84% of the RF power is damped on the electrons before the mode conversion layer is reached. The remaining power is also deposited in the deuterons before the mode conversion layer is reached (Figs. (61, 63)). No power is deposited directly in the tritons.

As the plasma temperature increases, the RF heating again shifts away from the mode conversion layer and towards the low field side. As the averaged electron temperature increases, more power is deposited in the electrons. At t = 1.5 sec, over 96% of the RF power is absorbed by the electrons. The shift in the peak RF heating is small enough to keep both the densities and temperatures peaked at the center. The alpha heating profiles are still centrally peaked at t = 1.5 sec (Fig. (5-64)). When the RF is turned off, there is almost 200 MW of alpha power being deposited in the plasma.

The electron and ion RF time-dependent heating profiles are shown in Figs. (5-62-63). The deuterium and tritium densities again remain constant. The carbon density, although decreasing, also remains parabolic. Figures (5-65-66) show that the carbon and alpha densities are too low during the RF pulse to absorb any power. Figures (5-67-68) again show the central ion and electron temperatures running away under PLT scaling.

When $k_{\parallel} = 0.2\ \mathrm{cm}^{-1}$, we again conclude that electron Landau and transit time damping, away from the mode conversion zone, are the dominant RF heating processes. Mode conversion appears to play a minor role in this case.

When $k_{\parallel}$ is decreased from $0.2\ \mathrm{cm}^{-1}$ to $0.1\ \mathrm{cm}^{-1}$, the mode conversion layer increases. For the same initial conditions as before, the cyclotron resonance layer decreases while the mode conversion layer increases in width ($502.5\ \mathrm{cm.} \leq r \leq 504.5\ \mathrm{cm}$), as shown in Fig. (5-69). In this case, both deuterium (∿59 MW) and direct tritium absorption (∿0.6 MW) increase while electron heating decreases (∿41 MW). Although the ion heating is more peaked in this case, neither the density nor temperature profiles are affected. The same amount of RF power is needed to reach ignition.

When $k_{\parallel}$ is changed to $0.3\ \mathrm{cm}^{-1}$, mode conversion is completely eliminated (Fig. (5-70)). Electron Landau and transit time damping is again the dominant heating process absorbing over 84% of the RF power at $t = 0$ sec. The remaining power is deposited in the deuterons. Figure (5-71) shows that the electron heating profile does not differ from Fig. (5-62) where mode conversion occurred. Increasing $k_{\parallel}$ increases the deuterium heating width (Fig. (5-72)). However, the density and temperature profiles are unaffected. The same amount of power is needed as in the previous example.

From these three cases, $k_{\parallel} = 0.2\ \mathrm{cm}^{-1}$, $0.1\ \mathrm{cm}^{-1}$, $0.3\ \mathrm{cm}^{-1}$, we find that as $k_{\parallel}$ increases, the mode conversion threshold rises. Mode conversion appears to be eliminated for $k_{\parallel} \geq 0.3\ \mathrm{cm}^{-1}$. As $k_{\parallel}$ increases, the cyclotron resonance zone increases in width. Using McVey's mode conversion coefficients, we find that mode conversion does not affect the temperature and density profiles or the amount of RF power needed to reach ignition. The energy which reaches the mode conversion layer is reflected and passes through the resonance layer again on the way back to the low field side. If a standing wave developed, it would occur over half of the minor cross section and not contain much energy. In our model, it appears that the fast wave is damped within one pass across the minor cross section and no eigenmode should develop.

In both fundamental and second harmonic heating, electron heating is the dominant RF process. Both the Fokker-Planck and space-time studies show that $T_i \approx T_e$ in a reactor as long as the auxiliary heating is near the center. The amount of auxiliary power needed is independent of which species, ions or electrons, is heated. The requirement is dependent on the relative concentration of deuterium to tritium. Since electron heating appears to dominate, we investigate higher ion harmonic heating.

5.I. Third Harmonic Heating of Deuterium in NUWMAK

We now examine a 50%D-50%T plasma with $\omega = 3\omega_{CD}$ (f = 138 MHz). As the RF frequency increases, waveguides decrease in size.

If waveguides are used for the launching structure, a three meter wide waveguide for $\omega = \omega_{CD}$ becomes one meter wide in this case. A waveguide one meter wide should be smaller than neutral beam ports in a reactor. At RF frequencies of 100-200 MHz, efficient high power RF sources are still available. Therefore, 3rd or 4th ion harmonic heating could be an attractive heating scheme from a technological viewpoint.

For $\omega = 3\omega_{CD}$, the same initial profiles as in the $2\omega_{CD}$ cases are used. As the plasma temperature increases, the cyclotron resonance surface again widens (Figs. (5-73-74)). Although mode conversion appears within 500 ms after the RF is turned on, there is again no affect on the temperature and density profiles. Figure (5-75) shows 97% of the RF power being deposited in the electrons before the mode conversion layer is reached. The remaining power is deposited in the deuterons. The ion heating profile is shown in Fig. (5-76). The electron heating again shifts towards the low field side as the electron temperature increases.

As the electron heating shifts, the temperature profiles begin to flatten in the center (Figs. (5-77-78)). The density profiles remain parabolic, causing the alpha power production to remain centrally peaked (Fig. (5-79)). The amount of RF heating needed to reach ignition equals that required in second harmonic heating.

We conclude that $\omega = 3\omega_{CD}$ appears to be an attractive heating regime. There is substantial electron heating, close to the center but away from the mode conversion layer. Mode conversion effects on densities and temperatures should be minimal. In the next chapter, we compare the results obtained by the three different RF models which have been used.

Table 5-1

PLT

		Initial $\bar{n}_0$ (cm^{-3})		~ 5.4×10^{11}
Toroidal field (kG)	16.4	Initial n_D (edge) (cm^{-3})		5.8×10^{12}
Major radius (cm)	45	Initial n_H (edge) (cm^{-3})		5.8×10^{11}
Mirror radius (cm)	130	T_i (edge) (eV)		5
Plasma current (kA)	400	T_e (edge) (eV)		5
$\bar{n}_D$ (cm^{-3})	2.34×10^{13}	T_o (eV)		5
$\bar{n}_T$ (cm^{-3})	2.34×10^{12}	Initial $T_i(o)$ (eV)		600
n_o (cm^{-3})	1.5×10^{8}	Initial $T_e(o)$ (eV)		1300
Z_{eff}	≤ 2.0	Initial $\bar{T}_i$ (eV)		~ 206
P_{RF} (kW)	350	Initial $\bar{T}_e$ (eV)		~ 440
RF pulse (ms)	100			
RF frequency (MHz)	25			
$k_\parallel$ (cm^{-1})	0.1	0.1	0.1	0.2
$C_H \equiv T_H/T_i$	1.0	1.5	2.0	1.5

Table 5-1 (cont.)

At RF Shutoff

P^e_{RF} (kW)	13	14	16	40
P^D_{RF} (kW)	22	20	26	8
P^H_{RF} (kW)	315	316	308	302
P^z_{RF} (kW)	~ 0	~ 0	~ 0	~ 0
ΔT_i (o) (eV)	620	600	600	315
ΔT_e (o) (eV)	-340	-340	-350	-200
$\Delta \bar{T}_i$ (eV)	220	216	219	213
$\Delta \bar{T}_e$ (eV)	-45	-49	-45	-57
τ^i_e (ms)	137	137	137	133
τ^D_p (ms)	155	155	155	155
τ^H_p (ms)	210	210	210	210
P_z (kW)	5.7	5.6	5.7	5.7
P_{cx} (kW)	220	216	216	235

Table 5-1 (cont.)

P_{OH} (kW)	390	390	391	390
P_{ei} (kW)	126	124	122	48
P^e_{radial} (kW)	505	505	505	507
P_{EP} (kW)	12.4	12.5	12.4	12.4
P^i_{radial} (kW)	423	422	422	416
$\bar{n}_c$ (cm^{-3})	4.4x10^{10}	4.2x10^{10}	4.3x10^{10}	4.3x10^{10}
Mode conversion	Yes	Yes (for $t \geq 60$ ms)	**No**	No

Table 5-2

NUWMAK

Toroidal field (kG)	60.4	Initial T_i (0)(keV)	3.0
Major radius (cm)	512.5	Initial T_e (0)(keV)	3.0
Minor radius (cm)	144.0	T_i (edge)(eV)	5
Plasma current (MA)	5.0	T_e (edge)(eV)	5
$\bar{n}_e$ (cm^{-3})	$3.0x10^{14}$	Initial $\bar{T}_i$ (keV)	1.5
$\bar{n}_p$ (cm^{-3})	$3.0x10^{13}$	Initial $\bar{T}_e$ (keV)	1.5
$\bar{n}_T$ (cm^{-3})	$2.7x10^{14}$	$\bar{T}_o$ (eV)	5
$\bar{n}_o$ (cm^{-3})(10%D-90%T^o)	$1.0x10^{10}$	P_{RF} (MW)	~ 125
Initial $\bar{n}_c$ (cm^{-3})	$5.5x10^{11}$	RF frequency (MHz)	92
Initial $\bar{n}_\alpha$ (cm^{-3})	$3.3x10^8$	$k_{\parallel}$ (cm^{-1})	0.2
		RF pulse (sec)	2.0

Table 5-2 (cont.)

At RF Shutoff

$\bar{n}_c$ (cm^{-3})	3.4×10^{10}	P^{α}_{RF} (MW)	2.4
$\bar{n}_{\alpha}$ (cm^{-3})	1.3×10^{10}	P^{i}_{α} (MW)	68
T_i (o)(keV)	13.8	P^{e}_{α} (MW)	233
$\bar{T}_e$ (o)(keV)	14.2	P_{OH} (MW)	0.57
$\bar{T}_i$ (keV)	6.5	P_{ei} (MW)	-36
$\bar{T}_e$ (keV)	6.4	P^{e}_{radial}	65
P^{e}_{RF} (MW)	65	P_{EP}	0.14
P^{D}_{RF} (MW)	59	P_z	70
P^{T}_{RF} (MW)	~ 0.2	P^{i}_{radial}	61
P^{C}_{RF} (MW)	~ 0.03	P_{cx}	33
MODE CONVERSION	No (for $\frac{N_D}{N_e} \lesssim 10\%$)		

Table 5-3

NUWMAK

Toroidal field (kG)	60.4	Initial T_i (0)(keV)		3.0
Major radius (cm)	512.5	Initial T_e (0)(keV)		3.0
Minor radius (cm)	144.0	T_i (edge)(eV)		5
Plasma current (MA)	5.0	T_e (edge)(eV)		5
$\bar{n}_e$ (cm^{-3})	3.0×10^{14}	Initial $\bar{T}_i$ (keV)		1.5
$\bar{n}_D$ (cm^{-3})	1.5×10^{14}	Initial $\bar{T}_e$ (keV)		1.5
$\bar{n}_T$ (cm^{-3})	1.5×10^{14}	$\bar{T}_o$ (eV)		5
$\bar{n}_o$ (cm^{-3})(50%D-50%T)	1.0×10^{10}	RF pulse (sec)		1.5
Initial $\bar{n}_c$ (cm^{-3})	5.1×10^{10}	Initial $\bar{n}_\alpha$ (cm^{-3})		3.0×10^{8}
RF frequency (MHz)	92	92	92	138
$k_\parallel$ (cm^{-1})	0.1	0.2	0.3	0.2
RF power (MW)	~ 120	~ 105	~ 100	~ 105
RF pulse (sec)	1.5	1.5	1.5	1.5
MODE CONVERSION	Yes	Yes	No	Possibly for $t \geq 500$ ms

Table 5-3 (cont.)

At RF Shutoff

n_c (cm^{-3})	$3.1\text{x}10^{10}$	$3.4\text{x}10^{10}$	$3.4\text{x}10^{10}$	$3.3\text{x}10^{10}$
$\bar{n}_\alpha$ (cm^{-3})	$1.1\text{x}10^{13}$	$6.2\text{x}10^{11}$	$3.7\text{x}10^{11}$	$6.9\text{x}10^{11}$
$T_i(o)$	~ 102	8.5	6.6	7.6
$T_e(o)$	~ 78	8.8	6.6	7.8
$\bar{T}_i$	~ 24	4.1	3.6	4.5
$\bar{T}_e$	~ 20	4.1	3.6	4.6
P_{RF}^e (MW)	121	103	92	103
P_{RF}^D (MW)	0.3	3.8	11	0.08
P_{RF}^T (MW)	~ 0	0.03	0.08	3.1
P_{RF}^c (MW)	~ 0	~ 0	~ 0	~ 0
P_{RF}^α (MW)	~ 0	~ 0	~ 0	~ 0
P_α^i (MW)	225	27.5	11	30
P_α^e (MW)	1107	170	90	183
P_{OH} (MW)	0.5	0.8	0.9	0.48

Table 5-3 (cont.)

P_{ei} (MW)	+143	-74	-45	-78
P^{e}_{radial} (MW)	98	46	43	53
P_{EP} (MW)	0.22	0.17	0.16	0.16
P_{z} (MW)	152	51	45	52
P^{i}_{radial} (MW)	98	41	38	46
P_{cx} (MW)	16	21	24	28

LIST OF FIGURES

(5-14) Hydrogen RF power deposition summed over flux surfaces in PLT at t = 0 ms.

(5-15) Deuterium RF power deposition summed over flux surfaces in PLT at t = 0 ms.

(5-16) Oxygen density profile in PLT.

(5-17) Deuterium density profile in PLT.

(5-18) Hydrogen density profile in PLT,

(5-19) Electron temperature profile in PLT.

(5-20) Ion temperature profile in PLT.

(5-21) Ion RF power deposition in PLT ($P^i_{RF} = P^D_{RF} + P^H_{RF} + P^O_{RF}$); P_{RF} = 350 kW.

(5-22) Electron RF power deposition in PLT; P_{RF} = 350 kW.

(5-23) Electron temperature in PLT at RF shutoff, t = 100 ms.

(5-24) Ion temperature in PLT at t = 100 ms.

(5-25) Hydrogen RF power deposition along the entire cross section in PLT at t = 100 ms.

(5-26) Hydrogen RF power deposition summed over flux surfaces in PLT at t = 100 ms.

(5-27) $\mathrm{Re}k^2_{\perp f}$ and $\mathrm{Re}k^2_{\perp I.B.}$ (solid lines) and $\mathrm{Im}k^2_{\perp f}$ and $\mathrm{Im}k^2_{\perp I.B.}$ (dashed lines) for PLT, $k_\parallel = 0.1\ \mathrm{cm}^{-1}$, $T_H / T_D = C_H = 1.0$ at t = 0 ms. Mode conversion occurs between grid points 73 and 74 (122.5 cm $\leq$ r $\leq$ 123.0 cm).

(5-28) $\mathrm{Re}k^2_{\perp f}$ and $\mathrm{Re}k^2_{\perp I.B.}$ (solid lines) and $\mathrm{Im}k^2_{\perp f}$ and $\mathrm{Im}k^2_{\perp I.B.}$ (dashed lines) for PLT, $k_\parallel = 0.1\ \mathrm{cm}^{-1}$, $C_H = 2.0$ at t = 0 ms. No mode conversion occurs.

(5-29) $\mathrm{Re}k^2_{\perp f}$ and $\mathrm{Re}k^2_{\perp I.B.}$ (solid lines) and $\mathrm{Im}k^2_{\perp f}$ and $\mathrm{Im}k^2_{\perp I.B.}$ (dashed lines) for PLT $k_\parallel = 0.1\ \mathrm{cm}^{-1}$, $C_H = 2.0$, t = 100 ms. Evanescent zone in center disappears.

(5-30) Hydrogen RF power deposition summed over flux surfaces in PLT, $C_H = 2.0$, t = 0 ms.

(5-48) Deuterium RF power deposition along the entire cross section in NUWMAK, $f = f_{cD}$, $t = 0$ sec.

(5-49) Deuterium RF power deposition summed over flux surfaces in NUWMAK, $f = f_{cD}$, $t = 0$ sec.

(5-50) $\mathrm{Re}E_+$ (solid line) and $\mathrm{Im}E_+$ (dashed line) in NUWMAK, $f = f_{cD}$, $t = 0$ sec.

(5-51) $\mathrm{Re}E_-$ (solid line) and $\mathrm{Im}E_-$ (dashed line) in NUWMAK, $f = f_{cD}$, $t = 0$ sec.

(5-52) $\mathrm{Re}E_\parallel$ (solid line) and $\mathrm{Im}E_\parallel$ (dashed line) in NUWMAK, $f = f_{cD}$, $t = 0$ sec.

(5-53) Electron RF power deposition along the entire cross section in NUWMAK, $f = f_{cD}$, $t = 1.5$ sec.

(5-54) Electron RF power deposition summed over flux surfaces in NUWMAK, $f = f_{cD}$, $t = 1.5$ sec.

(5-55) Deuterium RF power deposition along the entire cross section in NUWMAK, $f = f_{cD}$, $t = 1.5$ sec.

(5-56) Deuterium RF power deposition summed over flux surfaces in NUWMAK, $f = f_{cD}$, $t = 1.5$ sec.

(5-57) Alpha power deposited in the electrons and ions in NUWMAK, $f = f_{cD}$, at RF shutoff, $t = 2.0$ sec.

(5-58) Alpha density in NUWMAK, $f = f_{cD}$, $t = 2.0$ sec.

(5-59) $\mathrm{Re}k^2_{\perp f}$ and $\mathrm{Re}k^2_{\perp \mathrm{I.B.}}$ (solid lines) and $\mathrm{Im}k^2_{\perp f}$ and $\mathrm{Im}k^2_{\perp \mathrm{I.B.}}$ (dashed lines) in NUWMAK, $f = 2f_{cD}$, $t = 0$ sec. Mode conversion occurs with the mode conversion layer between the 65th and 66th grid points ($503.5 \text{ cm} \leq r \leq 504.5 \text{ cm}$).

(5-60) Electron RF power deposition along the entire cross section in NUWMAK, $f = 2f_{cD}$, $t = 0$ sec.

(5-61) Deuterium RF power deposition along the entire cross section in NUWMAK, $f = 2f_{cD}$, $t = 0$ sec.

(5-62) Electron RF power profile in NUWMAK, $f = 2f_{cD}$.

(5-63) Ion RF power profile in NUWMAK, $f = 2f_{cD}$, $P^{i}_{RF} = P^{D}_{RF} + P^{T}_{RF} + P^{C}_{RF} + P^{\alpha}_{RF}$.

(5-64) Alpha power deposited in the electrons and ions in NUWMAK, $f = 2f_{cD}$ at RF shutoff, $t = 1.5$ sec.

(5-65) Carbon density in NUWMAK, $f = 2f_{cD}$, $t = 1.5$ sec.

(5-66) Alpha density in NUWMAK, $f = 2f_{cD}$, $t = 1.5$ sec.

(5-67) Ion temperature in NUWMAK, $f = 2f_{cD}$, $t = 1.5$ sec.

(5-68) Electron temperature in NUWMAK, $f = 2f_{cD}$, $t = 1.5$ sec.

(5-69) $\mathrm{Re}k^{2}_{\perp f}$ and $\mathrm{Re}k^{2}_{\perp I.B.}$ (solid lines) and $\mathrm{Im}k^{2}_{\perp f}$ and $\mathrm{Im}k^{2}_{\perp I.B.}$ (dashed lines) in NUWMAK, $f = 2f_{cD}$, $k_{\parallel} = 0.1\ \mathrm{cm}^{-1}$, $t=0$ sec. Mode conversion occurs with the mode conversion layer between the 65th and 67th grid points ($502.5\ \mathrm{cm} \leq r \leq 504.5\ \mathrm{cm}$).

(5-70) $\mathrm{Re}k^{2}_{\perp f}$ and $\mathrm{Re}k^{2}_{\perp I.B.}$ (solid lines) and $\mathrm{Im}k^{2}_{\perp f}$ and $\mathrm{Im}k^{2}_{\perp I.B.}$ (dashed lines) in NUWMAK, $f = 2f_{cD}$, $k_{\parallel} = 0.3\ \mathrm{cm}^{-1}$, $t = 0$ sec. No mode conversion occurs.

(5-71) Electron RF power profile in NUWMAK, $f = 2f_{cD}$, $k_{\parallel} = 0.3\ \mathrm{cm}^{-1}$.

(5-72) Deuterium RF power profile in NUWMAK, $f = 2f_{cD}$, $k_{\parallel} = 0.3\ \mathrm{cm}^{-1}$.

(5-73) $\mathrm{Re}k^{2}_{\perp f}$ (solid line), $\mathrm{Im}k^{2}_{\perp f}$ (dashed line) and cold plasma $k^{2}_{\perp}$ (dotted line) in NUWMAK, $f = 3f_{cD}$, $t = 0$ sec.

(5-74) $\mathrm{Re}k^{2}_{\perp f}$ (solid line), $\mathrm{Im}k^{2}_{\perp f}$ (dashed line) and cold plasma $k^{2}_{\perp}$ (dotted line) in NUWMAK, $f = 3f_{cD}$, $t = 1.5$ sec.

(5-75) Electron RF power profile in NUWMAK, $f = 3f_{cD}$.

(5-76) Ion RF power profile in NUWMAK, $f = 3f_{cD}$, $P^{i}_{RF} = P^{D}_{RF} + P^{T}_{RF} + P^{C}_{RF} + P^{\alpha}_{RF}$.

(5-77) Electron temperature in NUWMAK, $f = 3f_{cD}$ at RF shutoff, $t = 1.5$ sec.

(5-78) Ion temperature in NUWMAK, $f = 3f_{cD}$, $t = 1.5$ sec.

(5-79) Alpha power deposited in the electrons and ions in NUWMAK, $f = 3f_{cD}$, $t = 1.5$ sec.

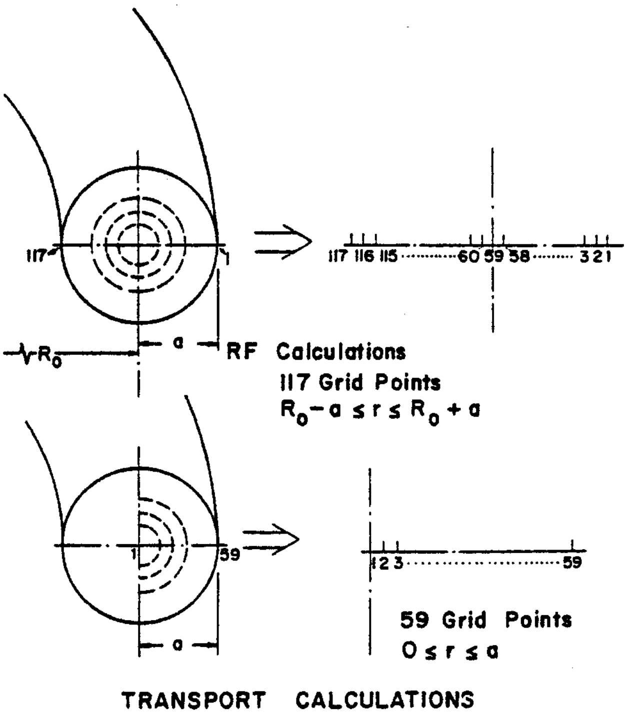
117
1
117 116 115 60 59 58 3 2 1
R_0
a
RF Calculations
117 Grid Points
$R_0 - a \le r \le R_0 + a$
1
59
1 2 3 59
a
59 Grid Points
$0 \le r \le a$
TRANSPORT CALCULATIONS

Fig.(5-1)

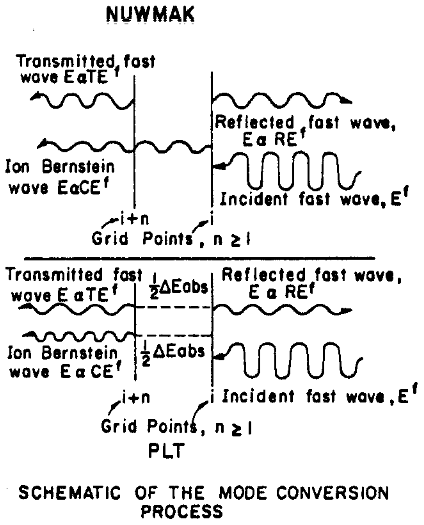
NUWMAK
Transmitted fast wave EaTE^f
Reflected fast wave, Ea RE^f
Ion Bernstein wave EaCE^f
Incident fast wave, E^f
i+n
i
Grid Points, n ≥ 1
Transmitted fast wave E a TE^f
$\frac{1}{2}\Delta$Eabs
Reflected fast wave, E a RE^f
Ion Bernstein wave E a CE^f
$\frac{1}{2}\Delta$Eabs
i+n
i Incident fast wave, E^f
Grid Points, n ≥ 1
PLT
SCHEMATIC OF THE MODE CONVERSION PROCESS

Fig.(5-2)

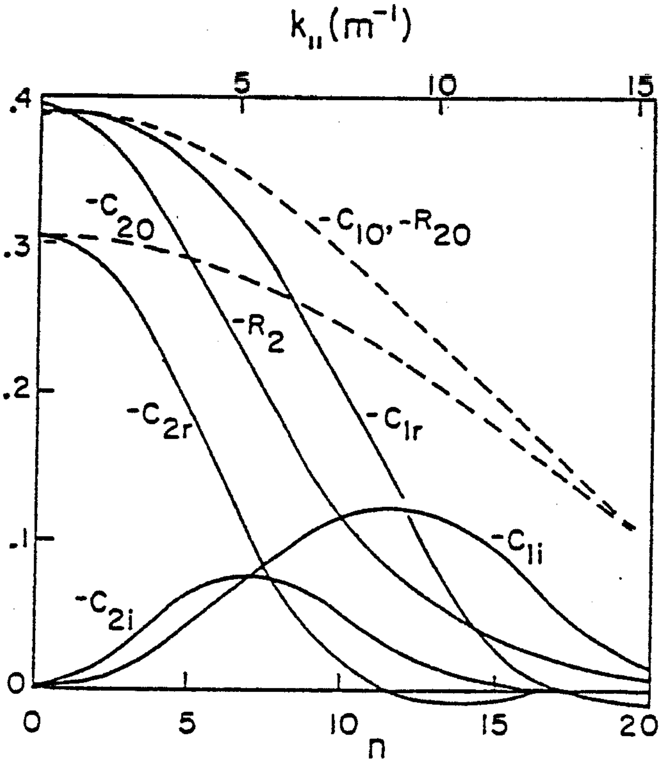

Reflection and conversion coefficients as a function of $k_{\parallel}$ (upper scale) or n (lower scale) for PLT parameters: $n_e = 6.2 \times 10^{19} m^3$, $R_o = 1.3m$, $B_o = 3.6W/m^2$ (f = 55MHz), $\beta_D = .01$, $n_p^- = 0$. Dashed lines show variation without absorption. Subscripts r and i denote real and imaginary parts of the conversion coefficients and, although some parts change sign, the magnitudes of C_1 and C_2 decrease monotonically with increasing n.

Fig. (5-3)

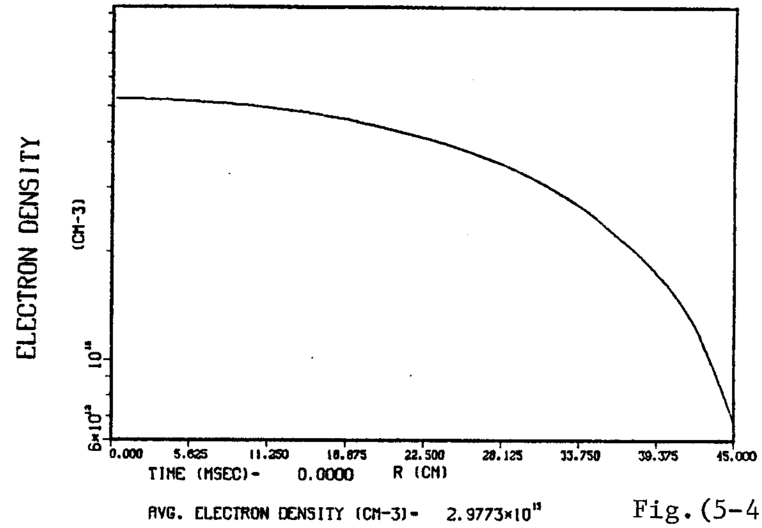

Fig.(5-4)

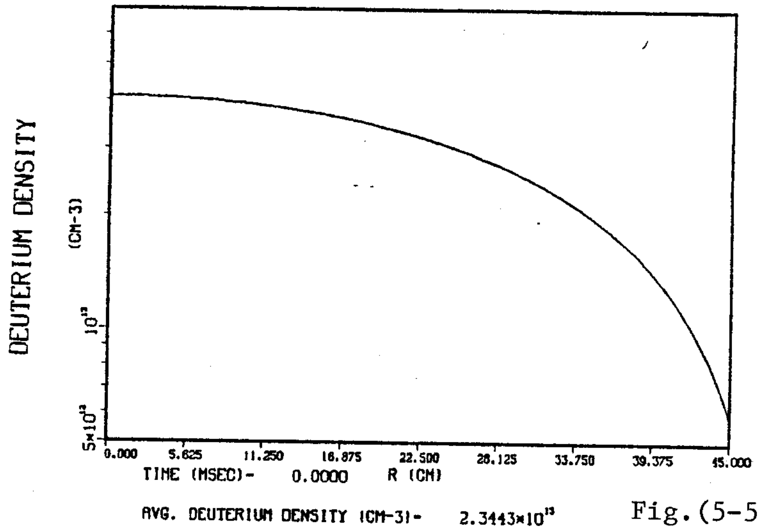

Fig.(5-5)

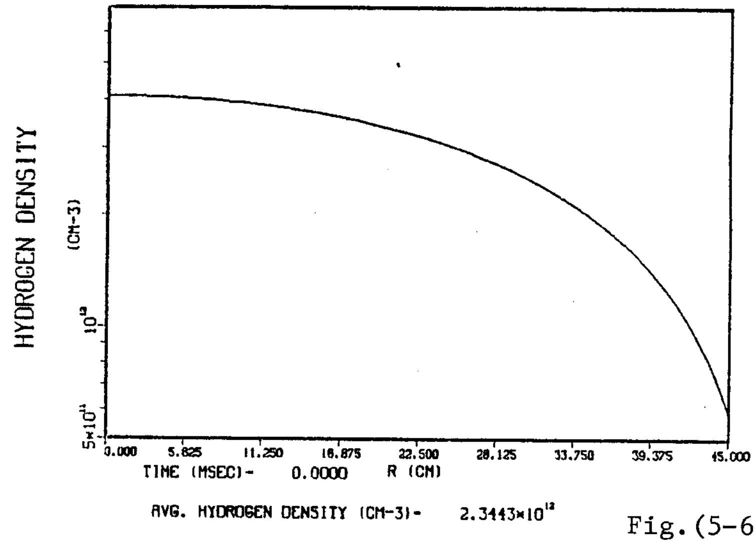

Fig.(5-6)

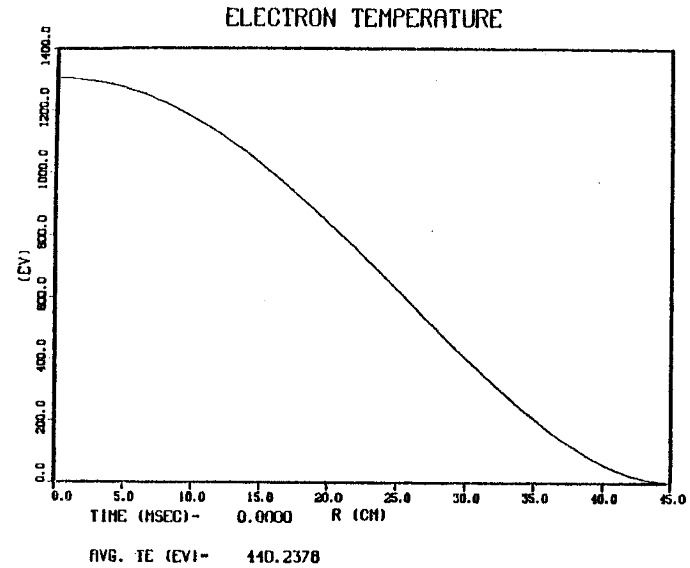

Fig.(5-7)

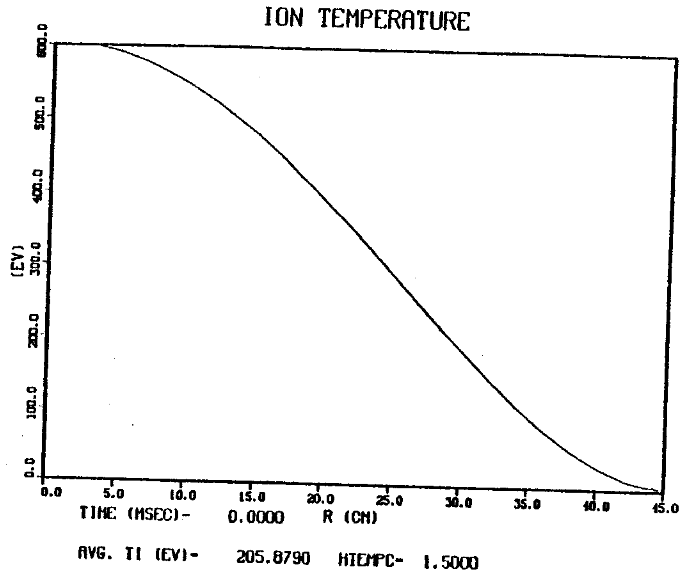

Fig.(5-8)

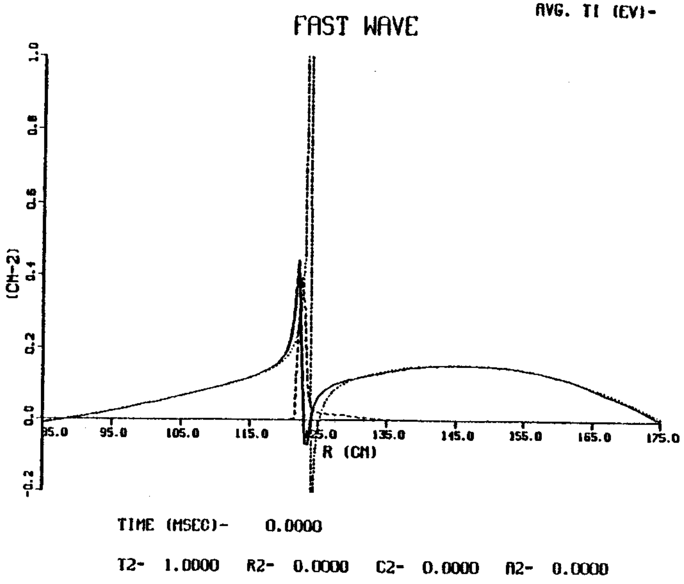

Fig.(5-9)

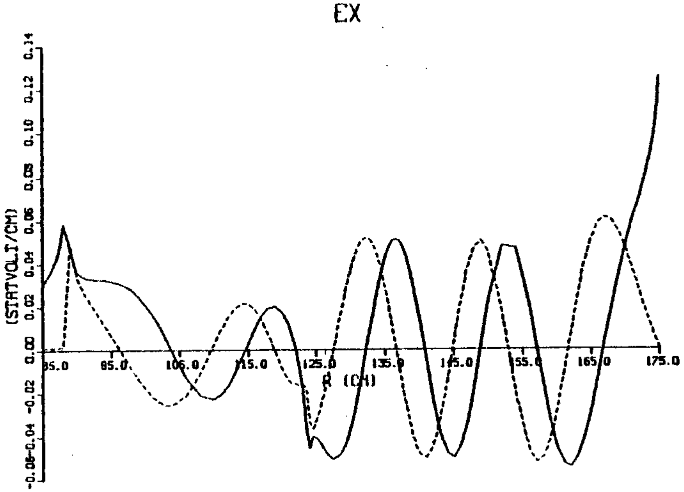

Fig.(5-10)

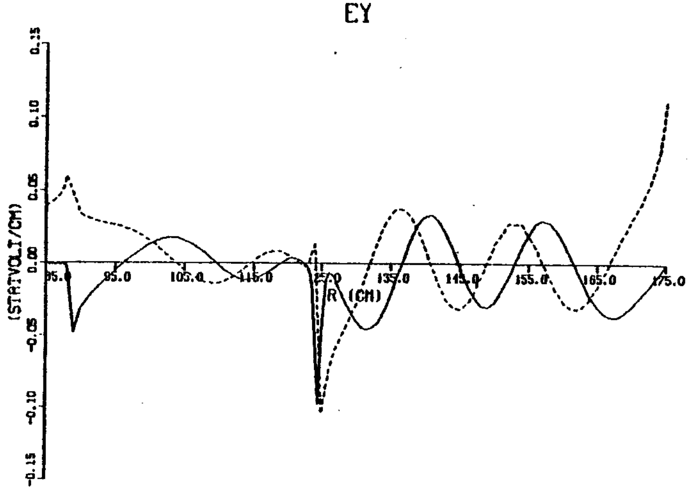

Fig.(5-11)

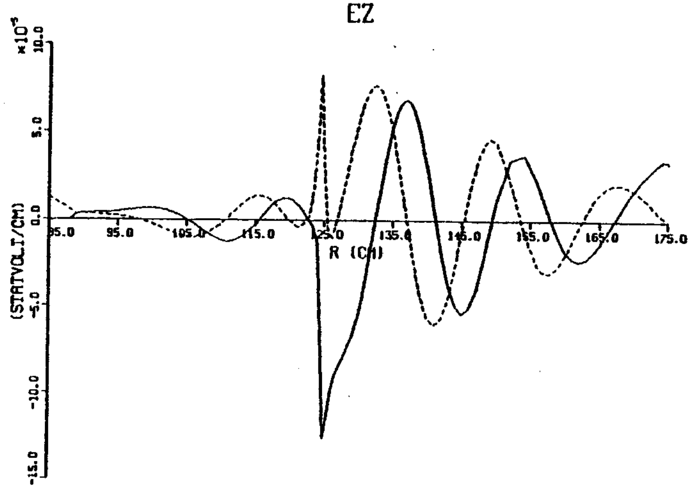

Fig.(5-12)

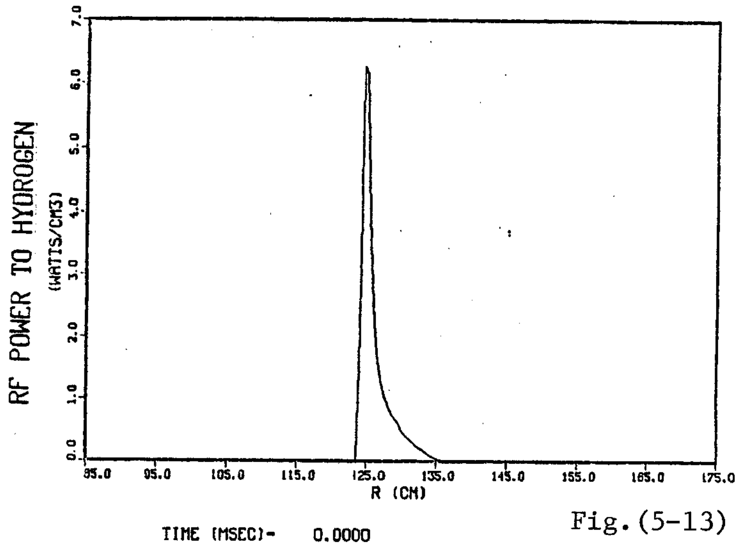

Fig.(5-13)

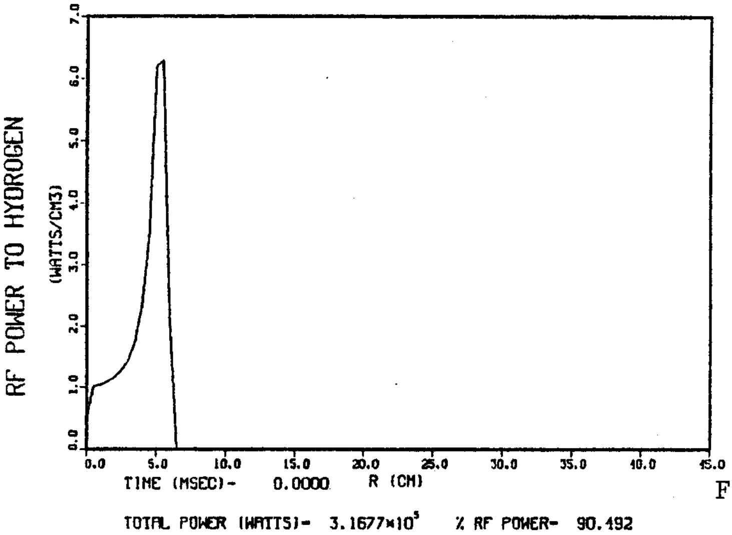

Fig.(5-14)

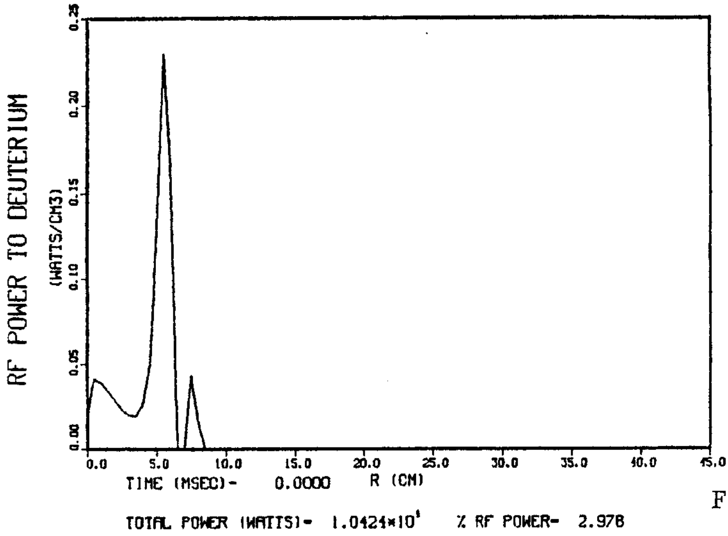

Fig.(5-15)

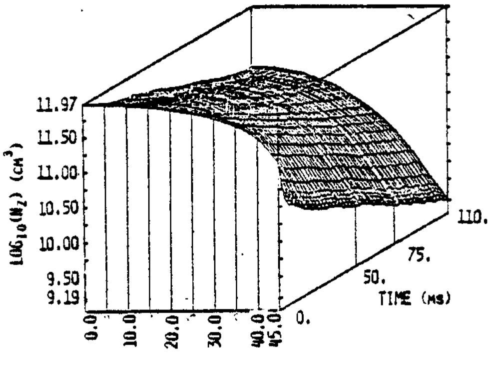

Fig.(5-16)

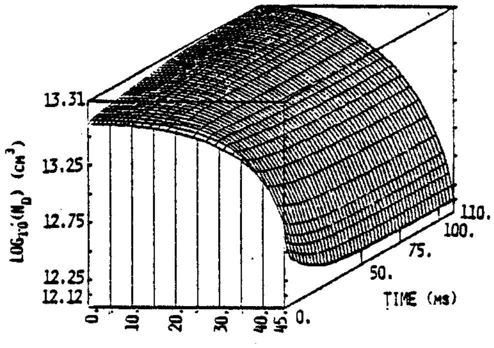

Fig.(5-17)

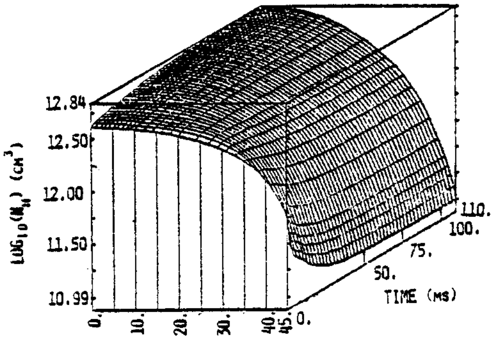

Fig.(5-18)

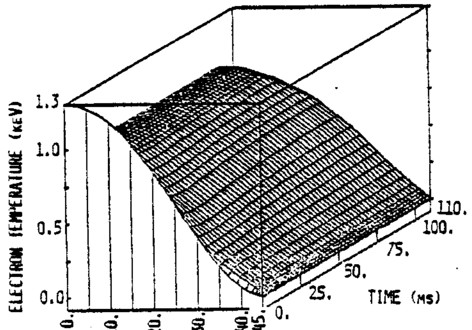

Fig.(5-19)

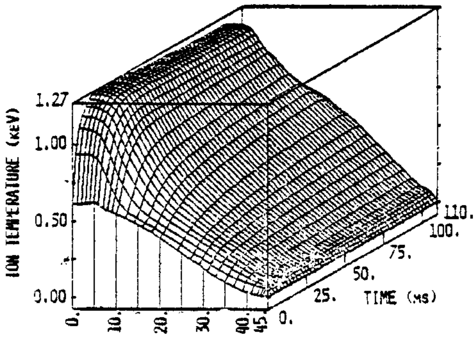

Fig.(5-20)

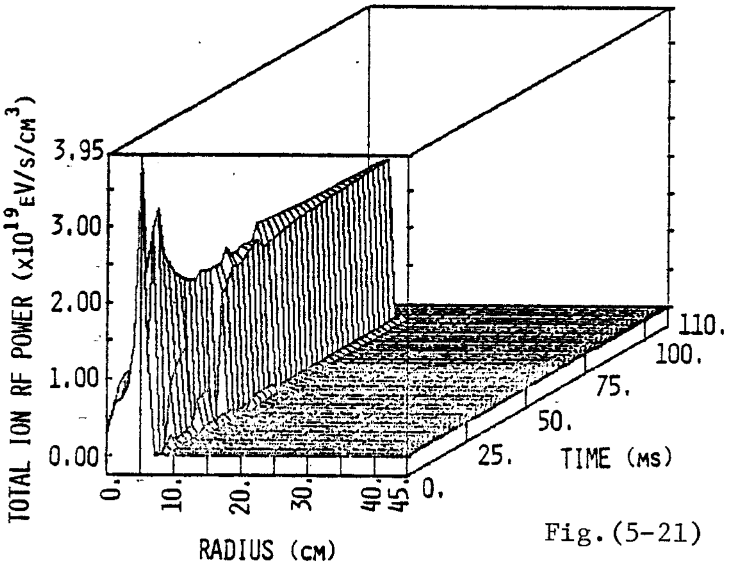

Fig.(5-21)

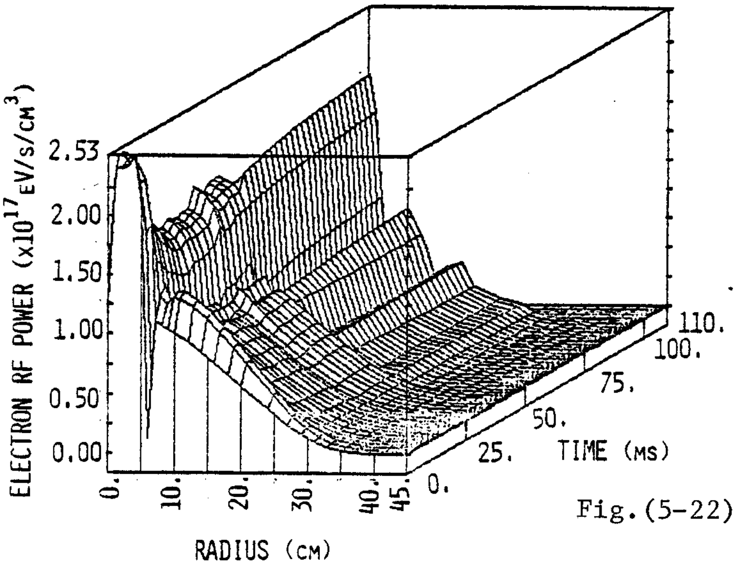

Fig.(5-22)

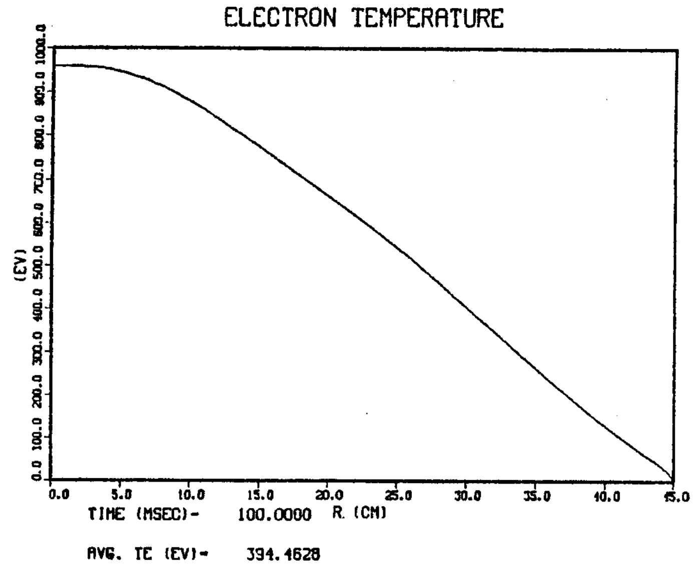

Fig.(5-23)

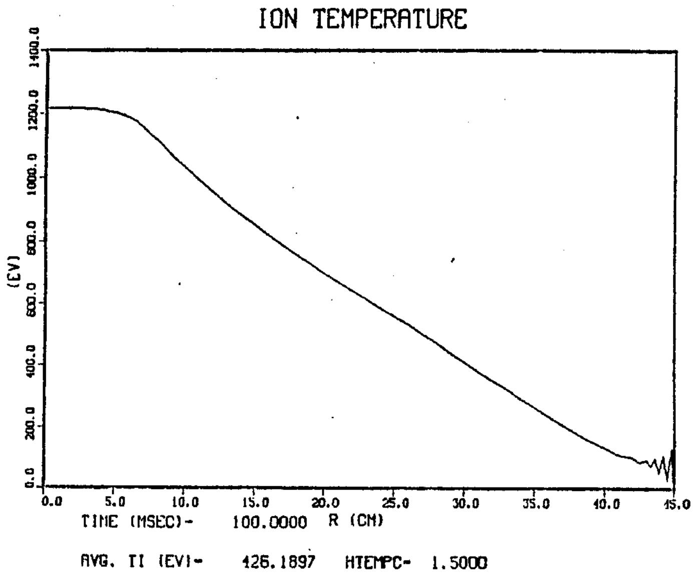

Fig.(5-24)

RF POWER TO HYDROGEN

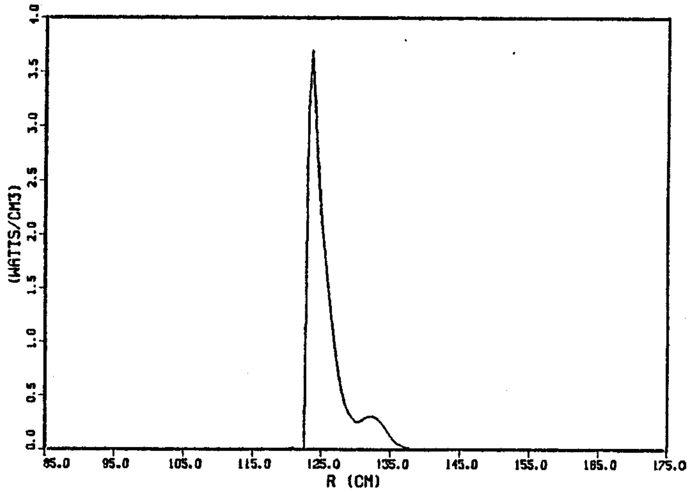

TIME (MSEC)- 100.0000

Fig. (5-25)

RF POWER TO HYDROGEN

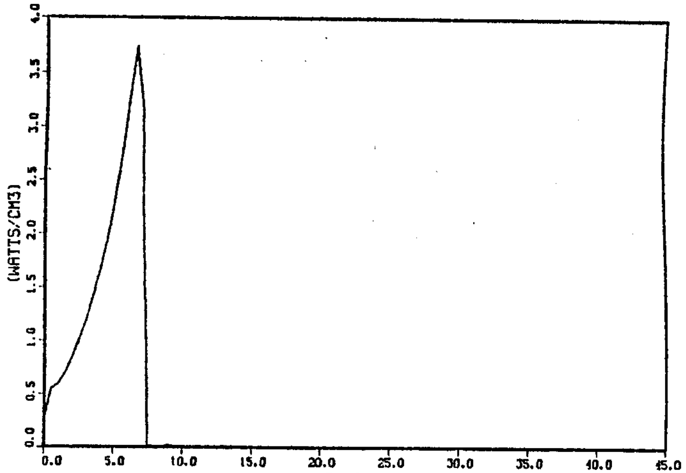

TIME (MSEC)- 100.0000

TOTAL POWER (WATTS)- 3.1593×10^5 % RF POWER- 90.239

Fig. (5-26)

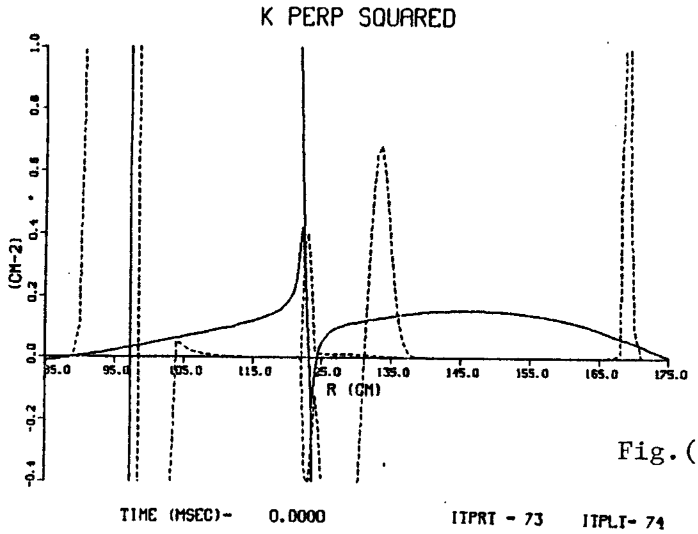

Fig.(5-27)

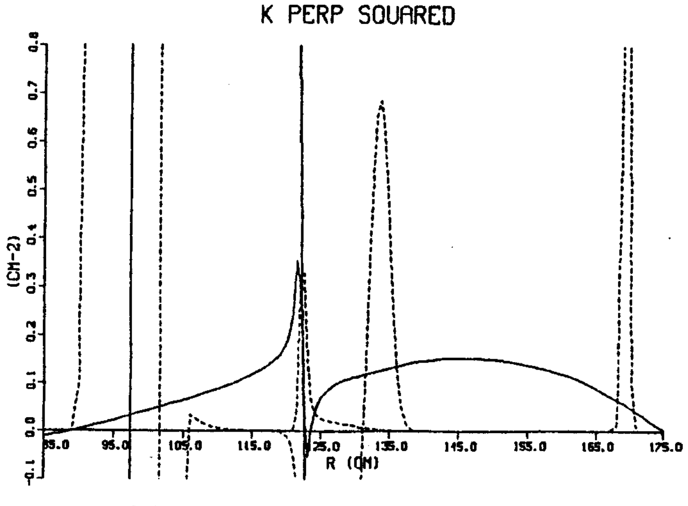

Fig.(5-28)

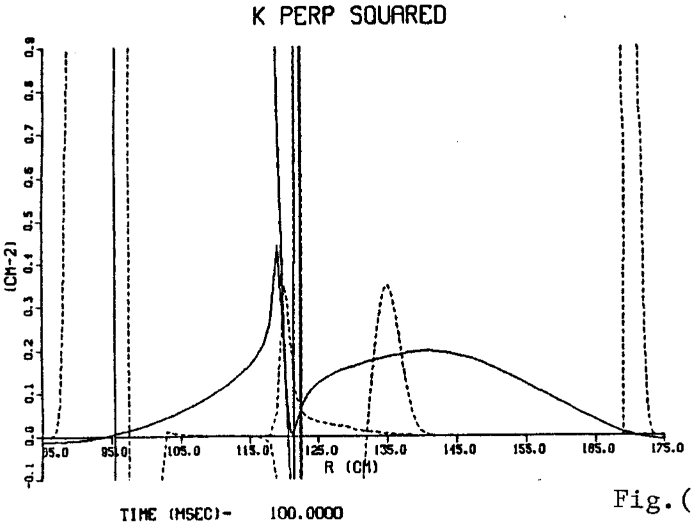

Fig.(5-29)

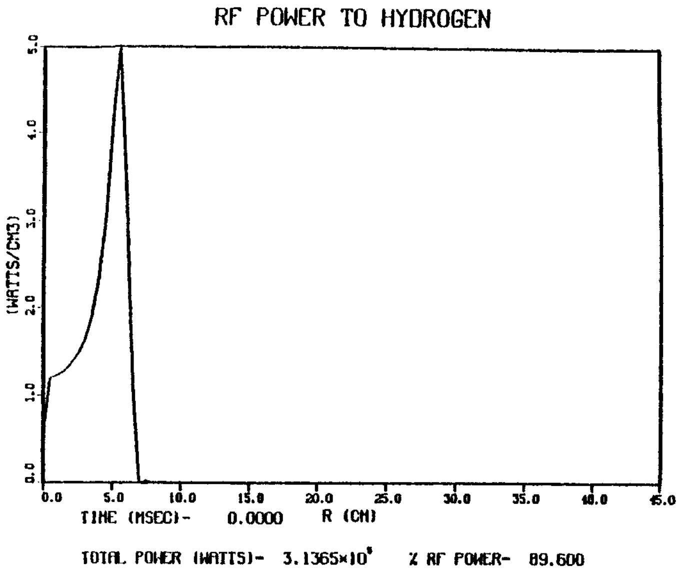

Fig.(5-30)

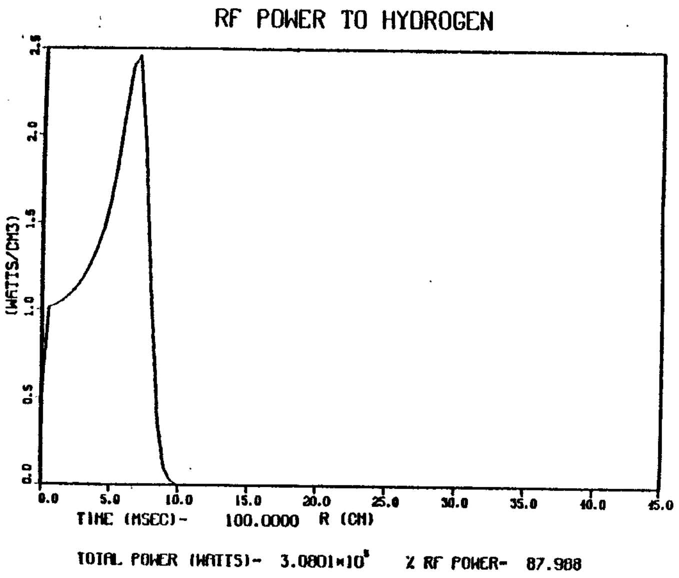

Fig.(5-31)

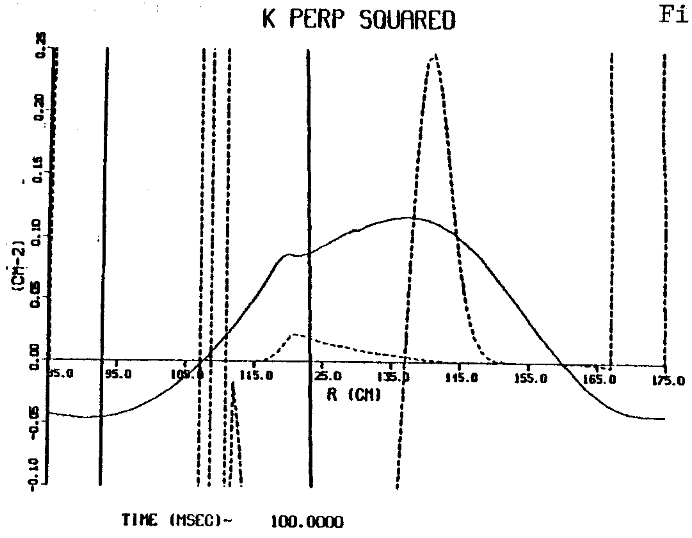

Fig.(5-32)

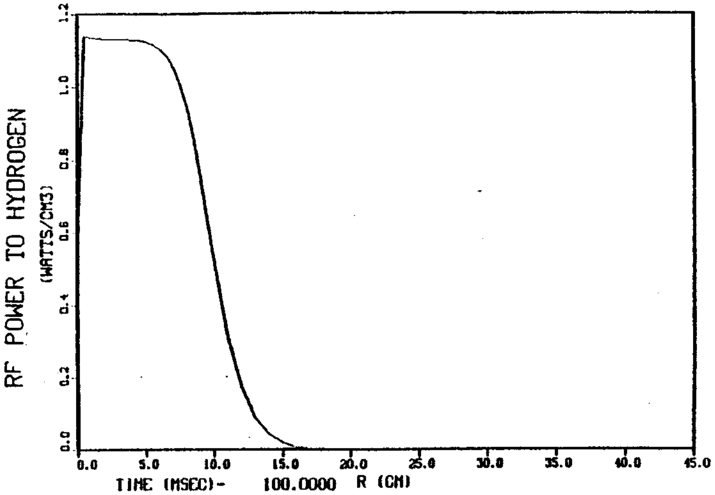

TIME (MSEC)- 100.0000 R (CM)

TOTAL POWER (WATTS)- 3.0174×10^{6} % RF POWER- 86.201

Fig.(5-33)

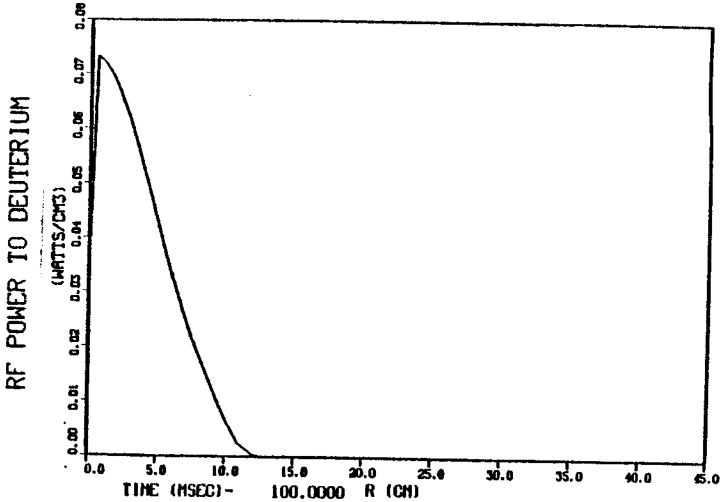

TIME (MSEC)- 100.0000 R (CM)

TOTAL POWER (WATTS)- 8.0624×10^{3} % RF POWER- 2.303

Fig.(5-34)

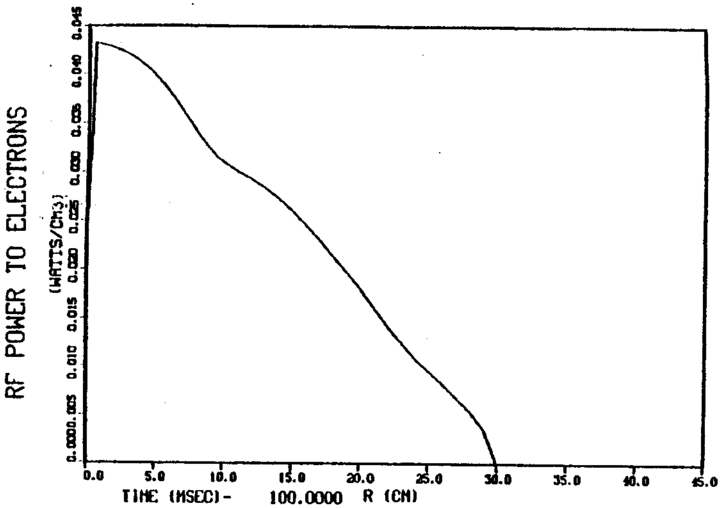

TIME (MSEC)- 100.0000 R (CM)

TOTAL POWER (WATTS)- 4.0232×10^{4} % RF POWER- 11.493

Fig.(5-35)

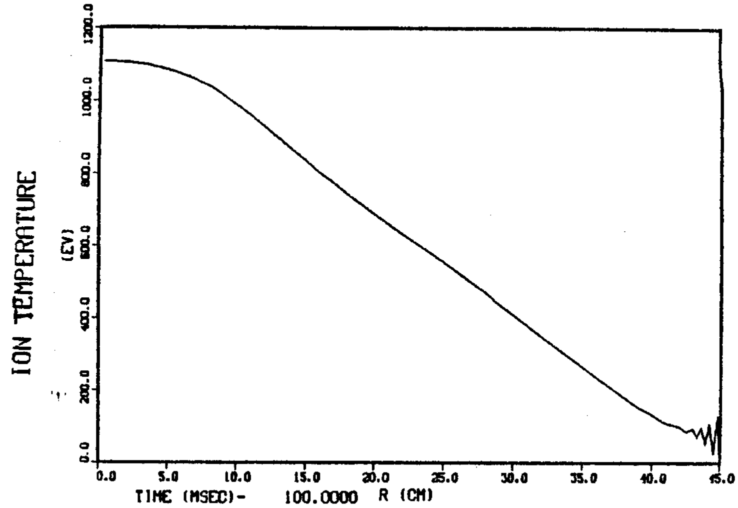

Fig.(5-36)

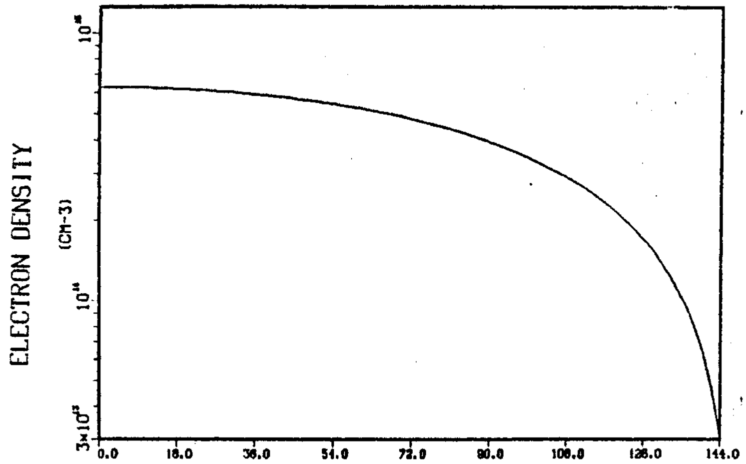

Fig.(5-37)

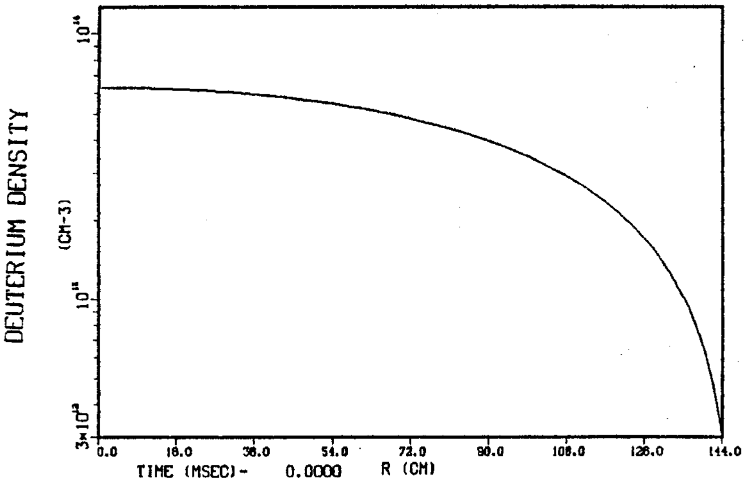

Fig.(5-38)

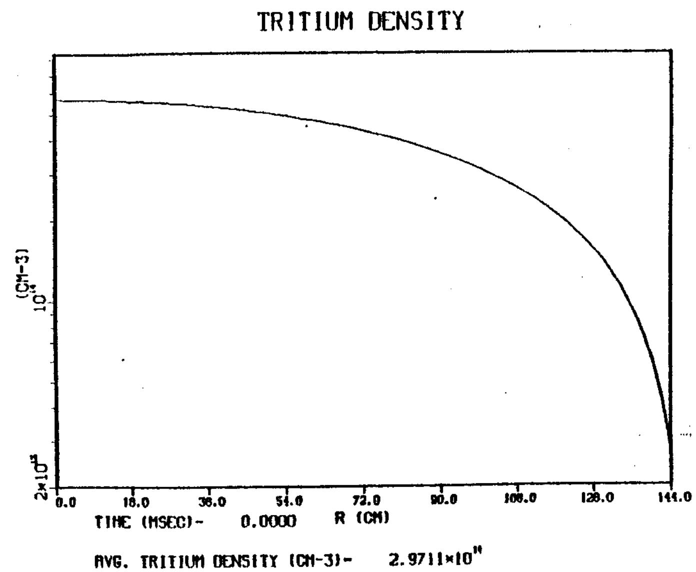

Fig.(5-39)

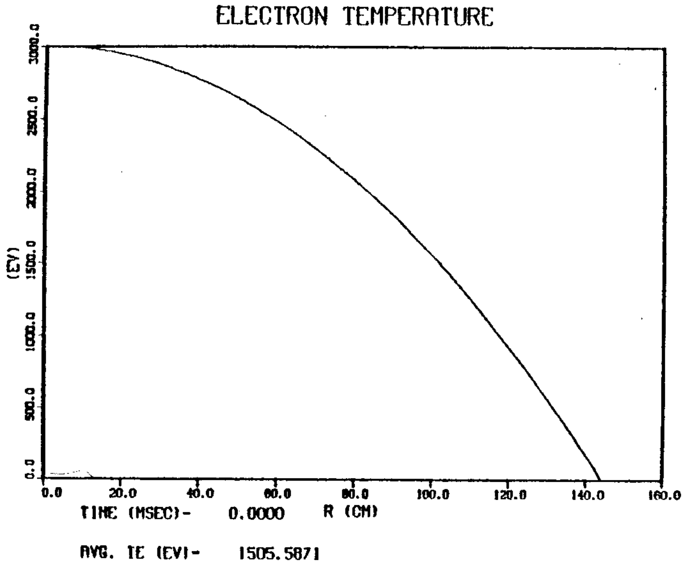

Fig.(5-40)

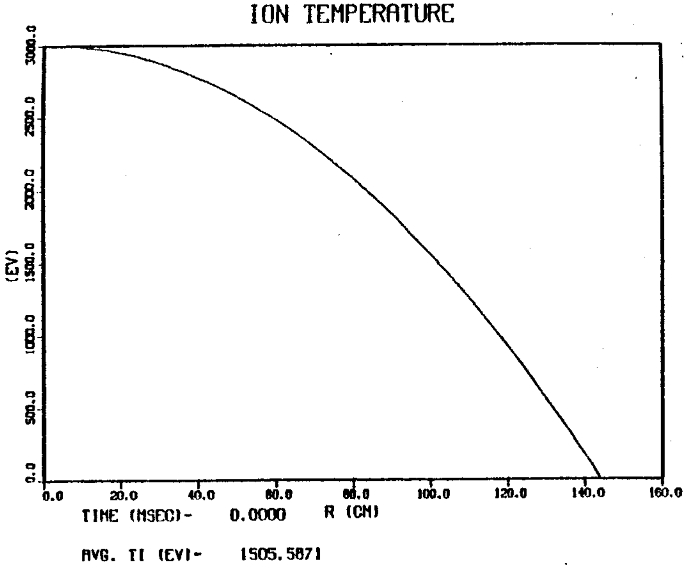

Fig.(5-41)

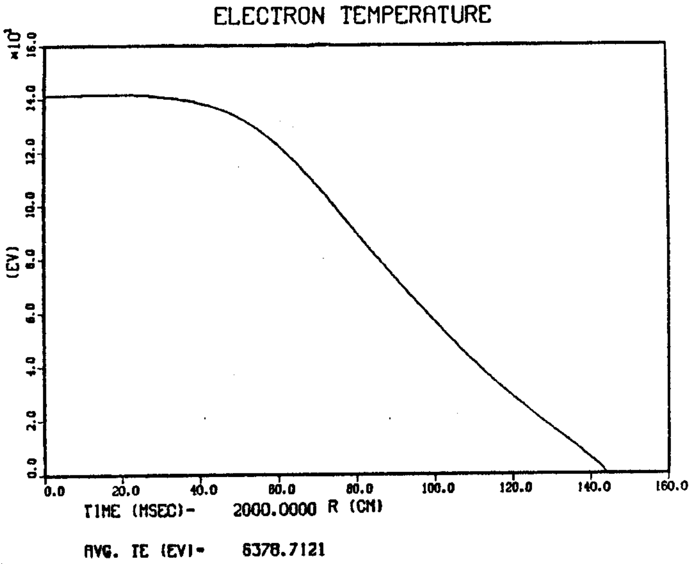

Fig.(5-42)

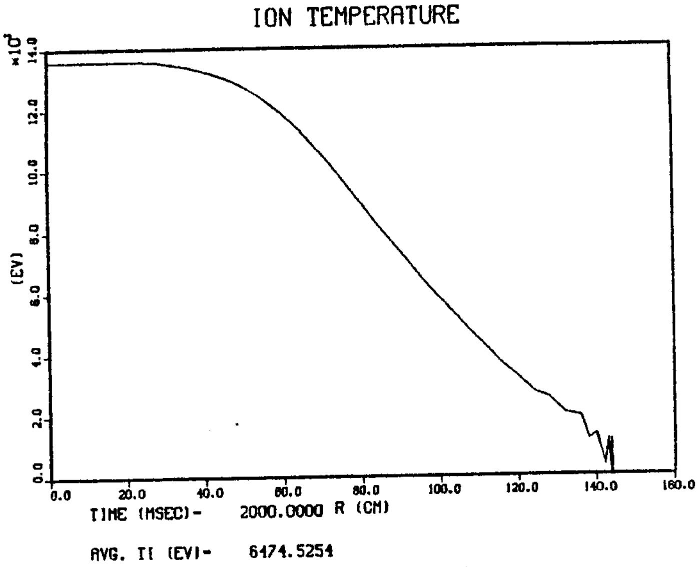

Fig.(5-43)

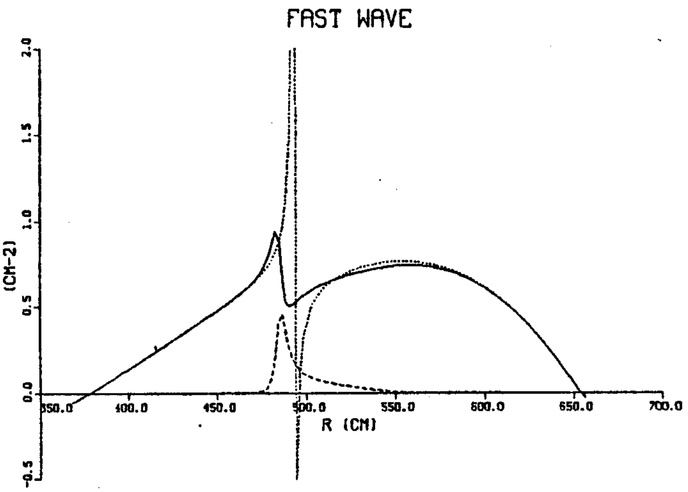

TIME (MSEC)- 0.0000

T2- 1.0000 R2- 0.0000 C2- 0.0000

Fig.(5-44)

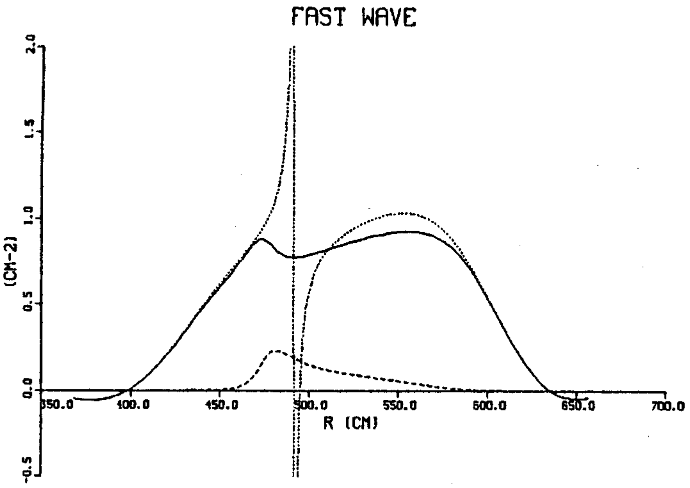

TIME (MSEC)- 1500.0000

T2- 1.0000 R2- 0.0000 C2- 0.0000

Fig.(5-45)

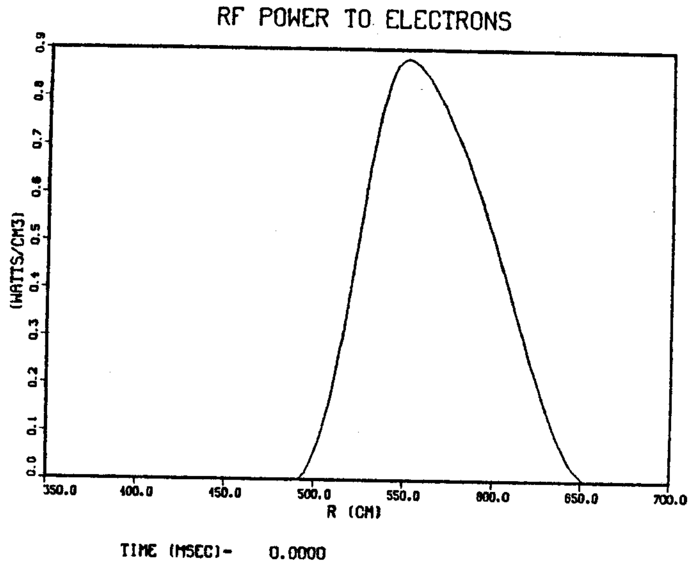

Fig.(5-46)

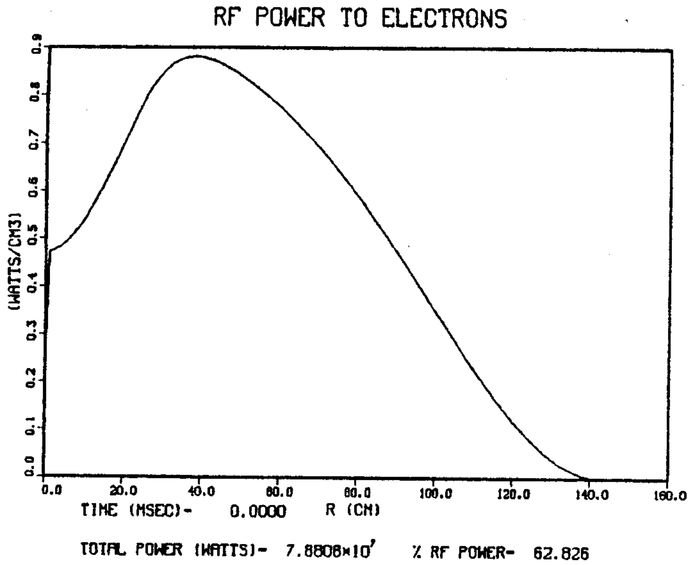

Fig.(5-47)

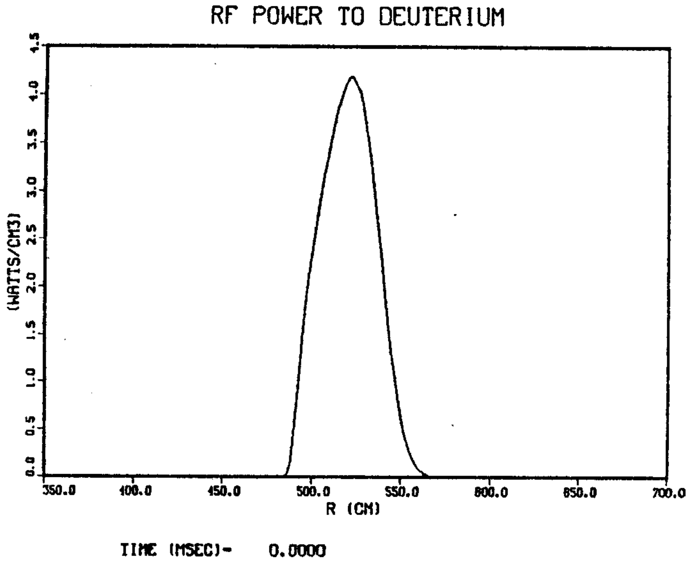

Fig.(5-48)

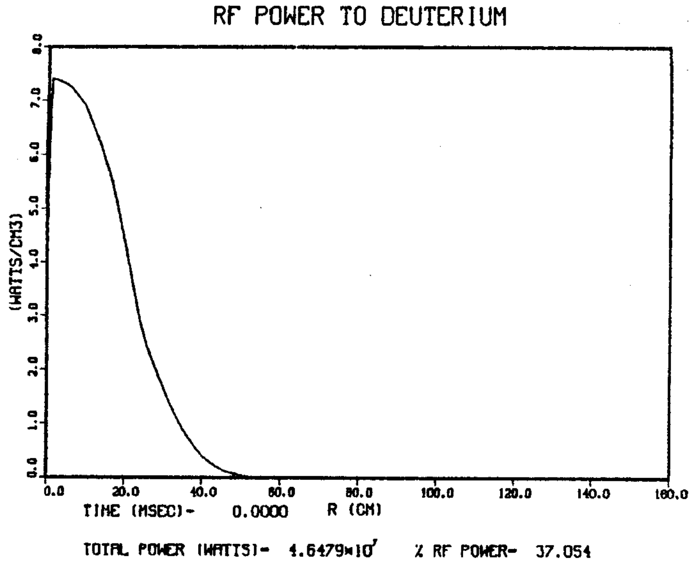

Fig.(5-49)

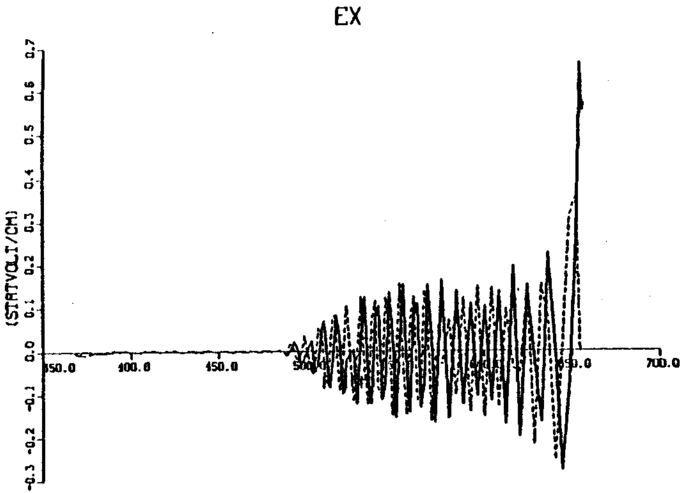

Fig.(5-50)

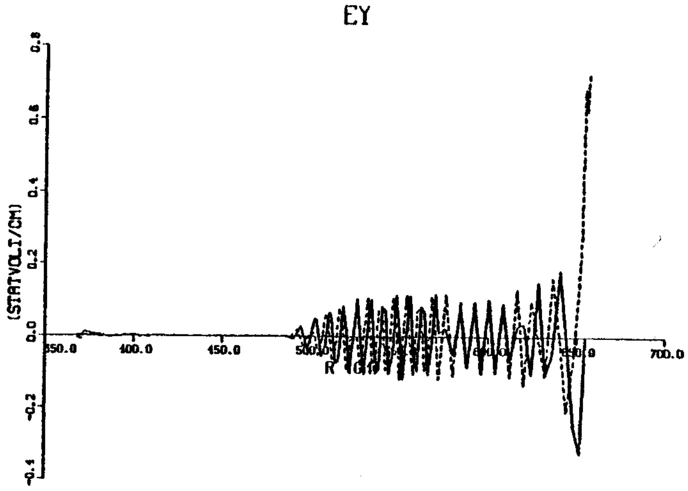

Fig.(5-51)

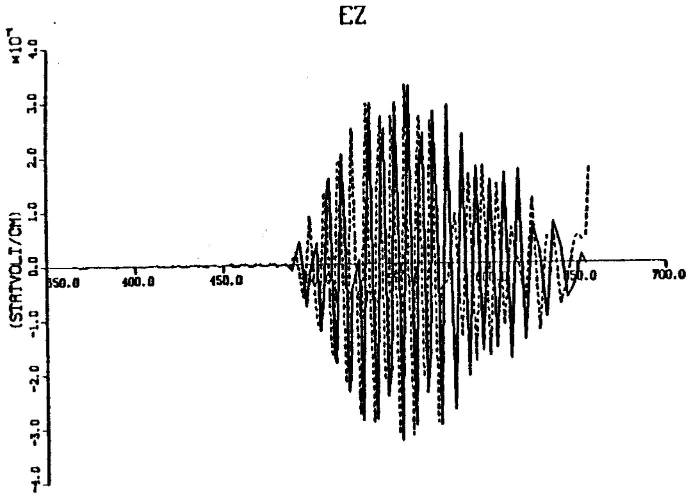

Fig.(5-52)

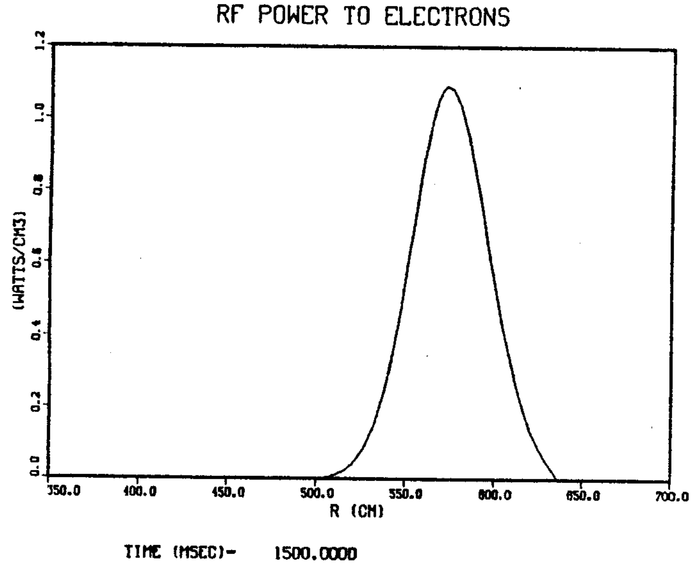

Fig.(5-53)

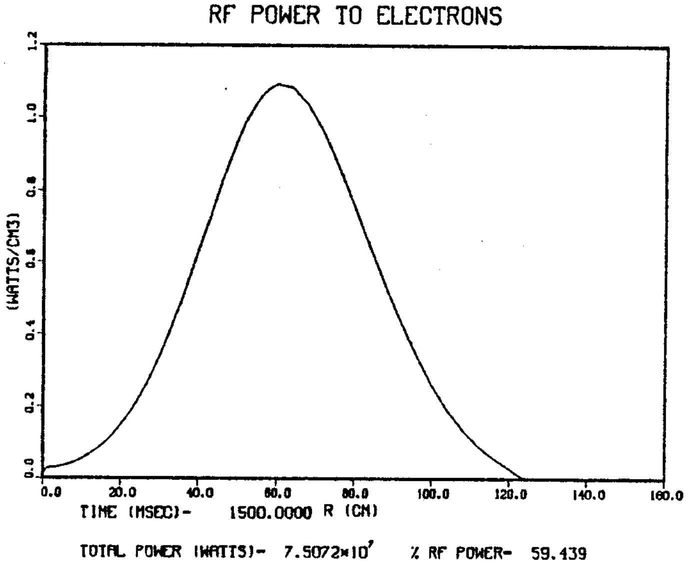

Fig.(5-54)

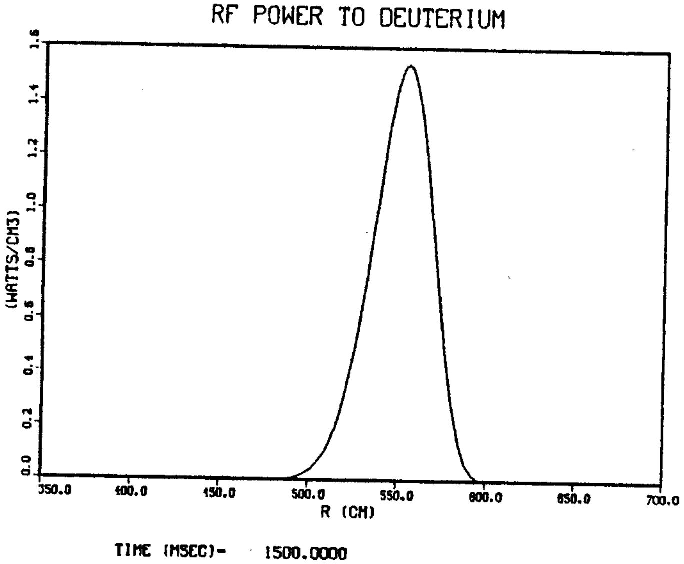

Fig.(5-55)

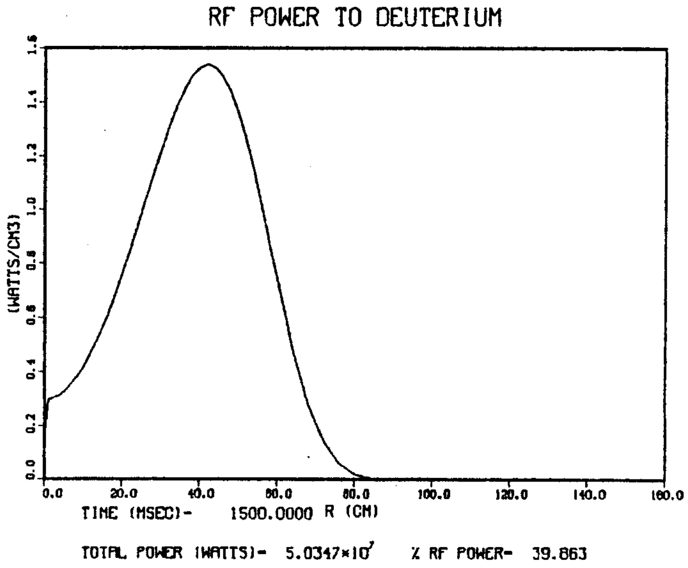

Fig.(5-56)

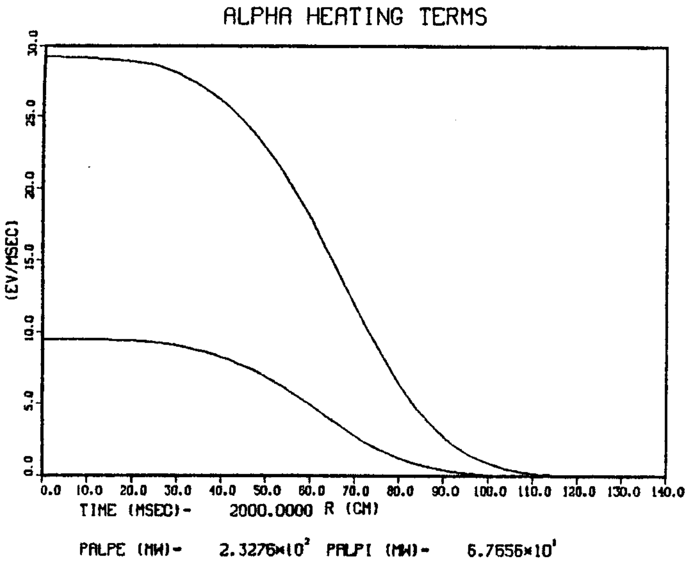

Fig.(5-57)

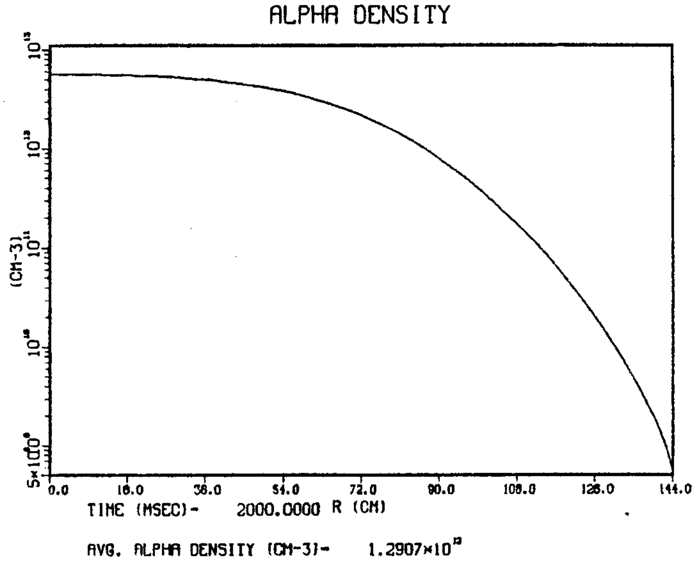

Fig.(5-58)

K PERP SQUARED

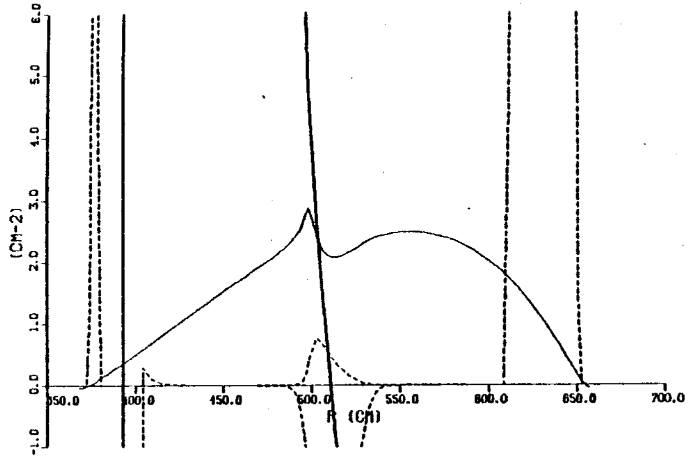

TIME (MSEC)- 0.0000

ITPRI- 65 ITPLT-66

Fig.(5-59)

RF POWER TO ELECTRONS

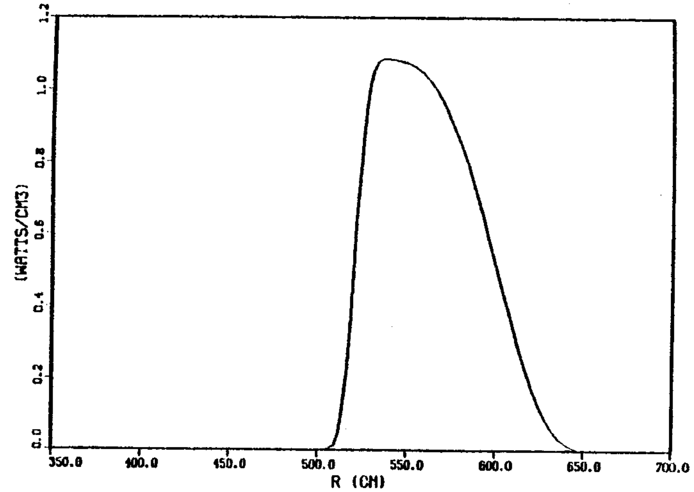

TIME (MSEC)- 0.0000

Fig.(5-60)

RF POWER TO DEUTERIUM

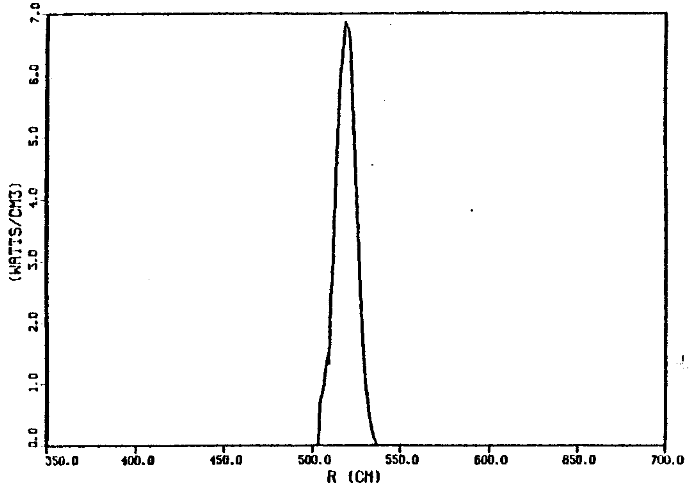

TIME (MSEC)- 0.0000

Fig.(5-61)

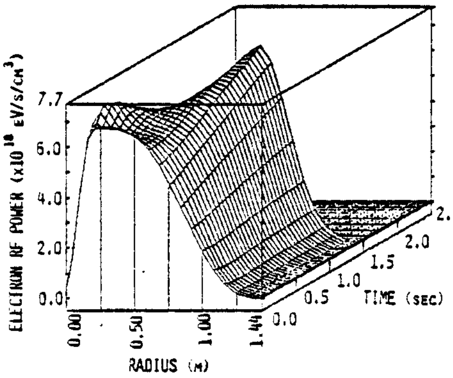

Fig.(5-62)

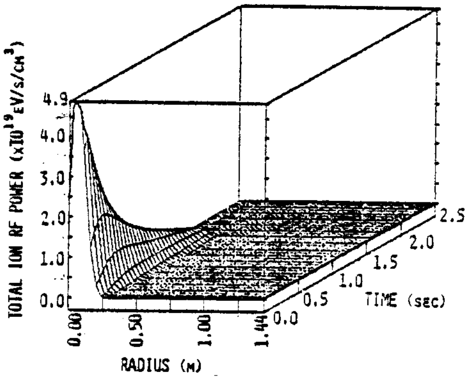

Fig.(5-63)

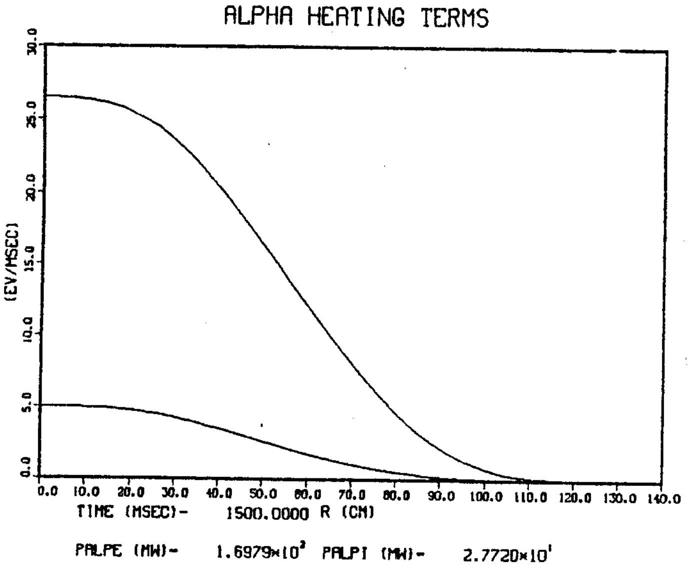

Fig.(5-64)

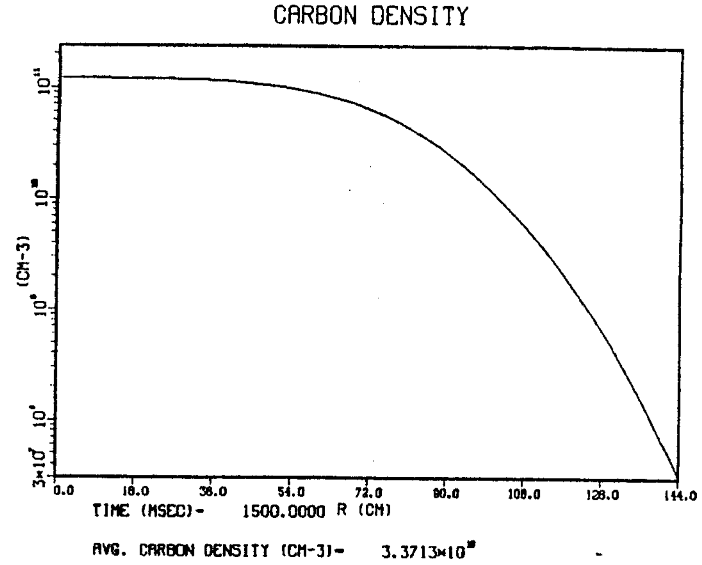

Fig.(5-65)

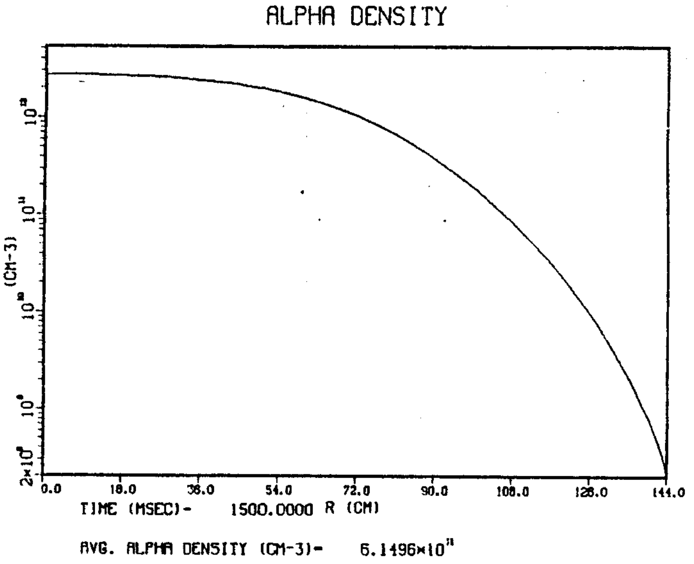

Fig.(5-66)

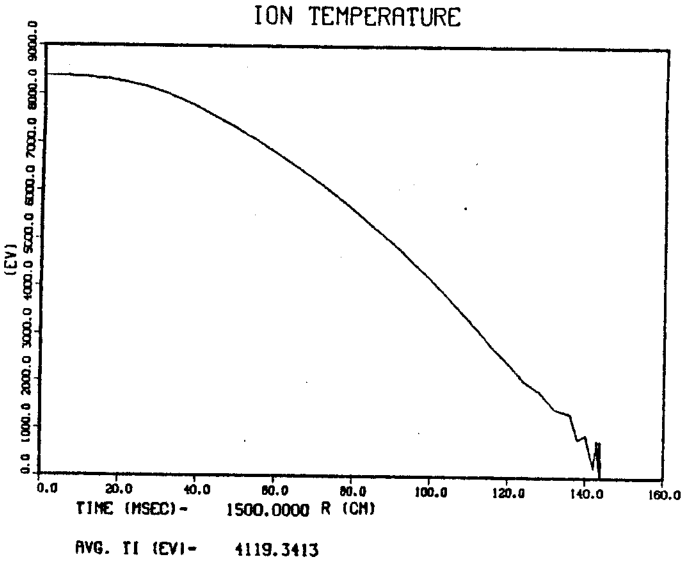
ION TEMPERATURE

Fig.(5-67)

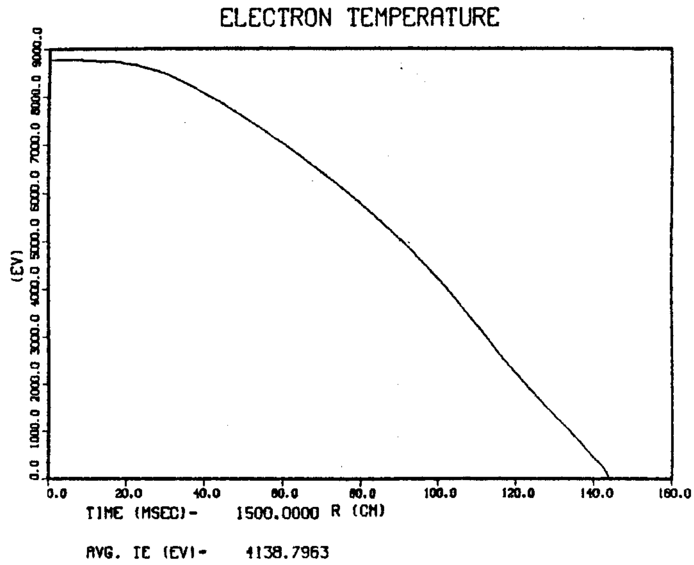
ELECTRON TEMPERATURE

Fig.(5-68)

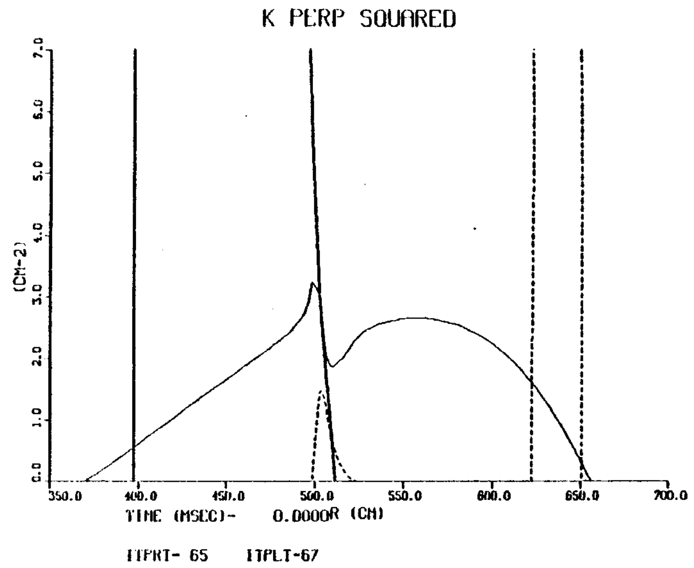

Fig.(5-69)

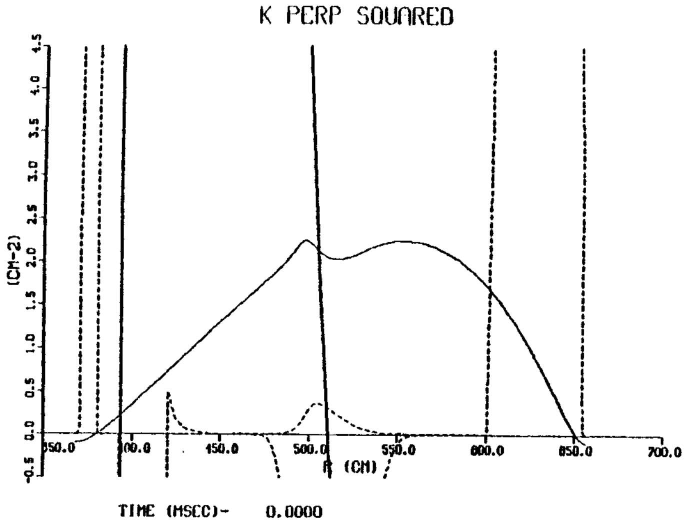

Fig.(5-70)

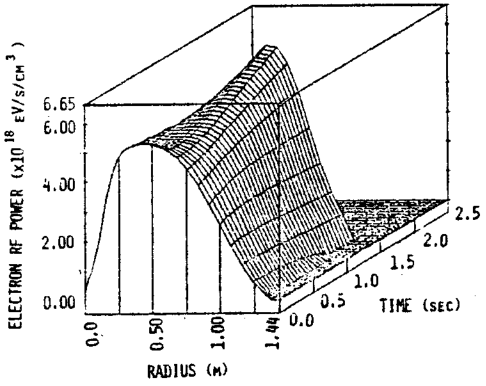

Fig.(5-71)

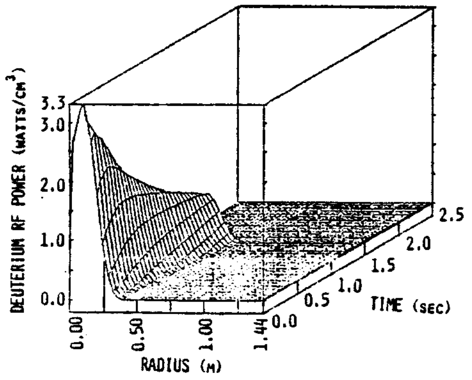

Fig.(5-72)

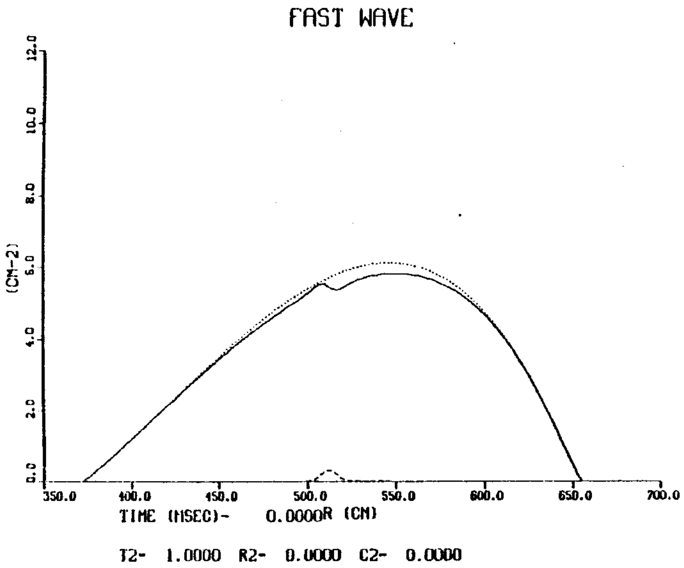

Fig.(5-73)

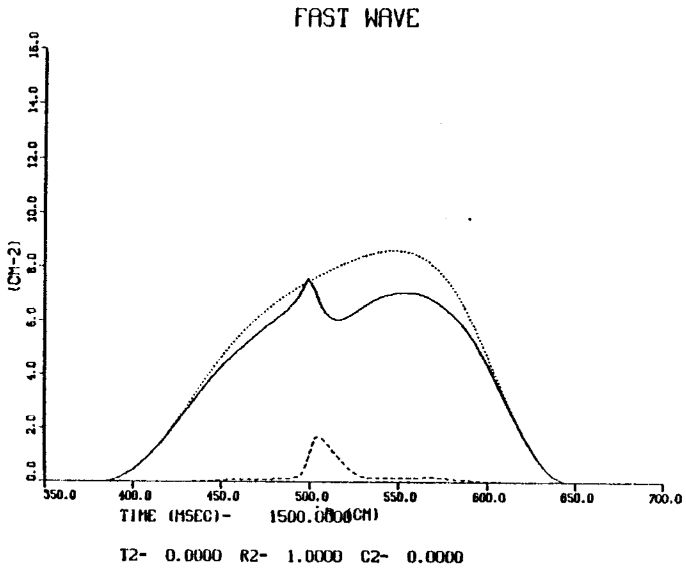

Fig.(5-74)

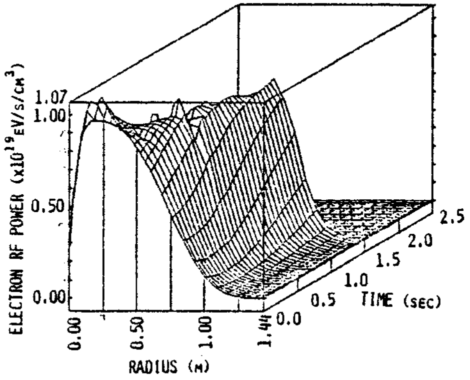

Fig.(5-75)

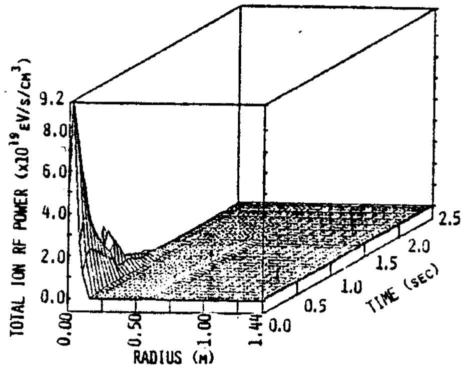

Fig.(5-76)

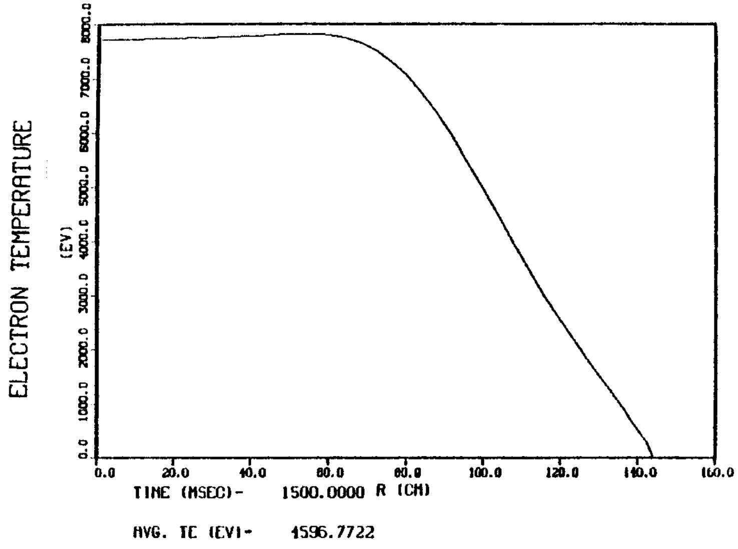

Fig.(5-77)

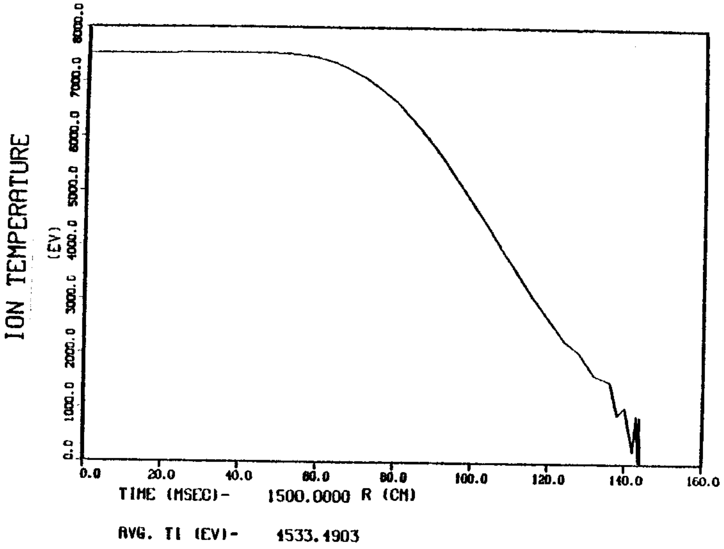

Fig.(5-78)

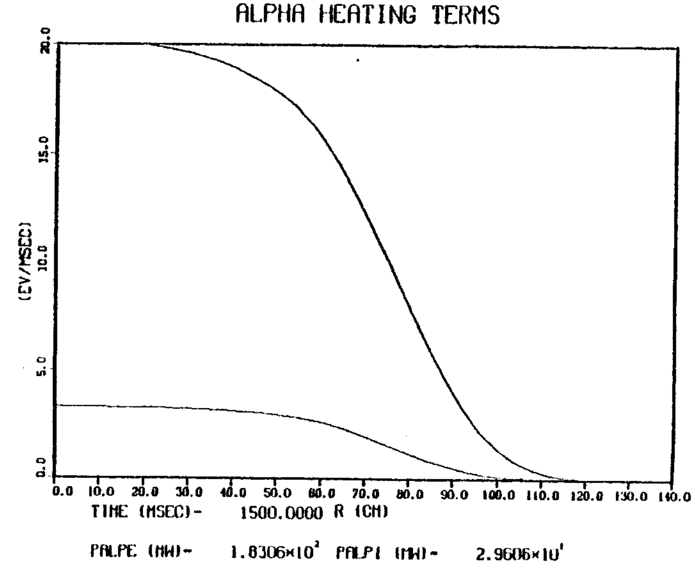

Fig.(5-79)

CHAPTER 5 REFERENCES

1. W. Houlberg, Ph.D. Thesis, Univ. of Wisconsin-Madison (1977).

2. S.I. Braginskii, Review of Plasma Physics 1 (1965) 205.

3. N.A. Krall, A.W. Trivelpiece, Principles of Plasma Physics, McGraw-Hill, N.Y. (1973).

4. D.T. Blackfield, UWFDM-278 (Jan. 1978).

5. J. Hosea, et al, PPL-1554 (July, 1979).

6. J. Hosea, et al, PPL-1588 (Oct.,1979).

7. S.O. Dean, et al, Atomic Energy Commission Report WASH-1295.

8. M.N. Rosenbluth, R.D. Hazeltine, F.L. Hinton, Phys. of Fluids 15 (1972) 116.

9. F.L. Hinton, T.B. Moore, Nuc. Fusion 14 (1974) 639.

10. F.L. Hinton, R.D. Hazeltine, Reviews of Modern Physics 48 (1976) 239.

11. B. Badger, et al, UWFDM-112 (Oct., 1975).

12. B. Badger, et al, UWFDM-191 (Dec., 1977).

13. B. Badger, et al, EPRI-ER-368 (July, 1976).

14. B. Badger, et al, UWFDM-330 (March, 1979).

15. M.R. Gordinier, Univ. of Wisconsin Report UWIFDM-12 (1978).

16. M.R. Gordinier, Univ. of Wisconsin Report UWIFDM 13 (1978).

17. W. Houlberg, UWFDM-103 (1974).

18. J.E. Scharer, D.T. Blackfield, J.B. Beyer, T.K. Mau, Nuc. Fusion 19 (1979) 1171.

19. D.E. Post, et al, INTOR Internal Report #19 (1979).

20. R.W. Conn, UWFDM-16 (July, 1972).

21. L. Spitzer, Jr., Physics of Fully Ionized Gases, Interscience Publs., Cambridge (1961) 233.

22. D.E. Post, et al, Atomic Data and Nuc. Data Tables 20 (1977) 397.

23. R.L. Freeman, E.M. Jones, CLM-R-137 (1974).

24. T.K. Mau, Ph.D. Thesis, Univ. of Wisconsin-Madison (1977).

25. T.H. Stix, MATT-1113 (Feb., 1975).

26. B. Bekefi, Radiation Processes in Plasmas, John Wiley and Sons, Inc., N.Y. (1966).

27. B. McVey, PLP 755 (May, 1978); Nuc. Fusion 19 (1979) 461.

28. D.G. Swanson, "The Effects of Localized Absorption on the Mode Conversion Process in the RF Heating of Plasmas," (1979) (unpublished).

29. J. Jacquinot, in Heating in Toroidal Plasmas (Proc. Joint Varenna-Grenoble Int'l. Symp. Grenoble, 1978) 127.

30. J. Mathews, R.L. Walker, Mathematical Methods of Physics, W.A. Benjamin, Inc., Mass. (1970).

31. TFR Group, in Controlled Fusion and Plasma Physics (Proc. 9th European Conf., Oxford, 1979) Invited Paper.

32. D.G. Swanson, Phys. Rev. Lett. 36 (1976) 316.

33. F.W. Perkins, Nuc. Fusion 17 (1977) 1197.

34. J. Kesner, R.W. Conn, Nuc. Fusion, 16 (1976) 397.

35. J.E. Scharer, D.T. Blackfield, Bull. Am. Phys. Soc., 21 (1976) 1158.

36. D.T. Blackfield, Bull. Am. Phys. Soc., 22 (1977) 1185.

CHAPTER 6

COMPARISON OF NUMERICAL RESULTS

6.A. PLT

In this section, the results for PLT obtained from the Fokker-Planck code, FORCE, and the space-time code, STICR-I are compared. The Fokker-Planck calculations revealed that only the proton distribution becomes nonMaxwellian in PLT. The protons become hotter than the deuterons, reaching an effective temperature of 1.7 x T_D at the time of the RF shutoff. Therefore, two ion energy balance equations should be solved when using a space-time transport code. STICR-I, however, uses only one.

Although the ratio of T_H to T_D is important in determining the mode conversion threshold, mode conversion itself leaves the density and temperature profiles unchanged. STICR-I neglects nonMaxwellian effects but does allow $T_H \neq T_D$ in the RF calculations. However, FORCE assumes that all of the wave energy is absorbed in the cyclotron layer near the plasma center. While these two codes examine the same experiment, they include different aspects. If the results obtained are different, it is necessary to understand why.

Figure (6-1) shows the change in the spatially averaged electron and ion temperatures with time. It appears that the initial temperatures do not agree between the two codes. This is because the average temperature is defined differently. In the space time code

$$\overline{T}_{i,e} \equiv \frac{\int_0^a T_{i,e}(r)rdr}{\int_0^a rdr} . \qquad (6\text{-}1)$$

In FORCE, the average ion temperature is a density weighted equivalent Maxwellian temperature

$$\overline{\overline{T}}_i = \frac{\frac{2}{3}\sum_\beta \int \frac{1}{2} m\ v^2 f\ (v)\ d^3v}{\sum_\beta \int f_\beta(v)\ d^3v} \qquad (6\text{-}2)$$

while the electron temperature is

$$\overline{T}_e = \frac{\frac{2}{3}\int \frac{1}{2} m_e v^2 f_e(v)\ d^3{}_v}{\int f_e(v)\ d^3v} . \qquad (6\text{-}3)$$

In STICR-I, this would be equivalent to defining the average temperature as

$$\overline{T} = \frac{\int_0^a n(r)\ T(r)\ rdr}{\int_0^a n(r)\ rdr} . \qquad (6\text{-}4)$$

If the density-weighted temperature was used in STICR-I, the two codes would agree. From the Fokker-Planck code, we find

$$\Delta \overline{T}_i \sim 150 \text{ eV} \tag{6-5}$$

while from the space-time code

$$\Delta \overline{T}_i \sim 220 \text{ eV}. \tag{6-6}$$

These results are comparable. Both codes show the average ion temperature doubling, in good agreement with the experiment. This results from the good agreement between charge exchange, radial losses and RF heating terms shown in Fig. (6-2). The slight difference between the two ion temperature increases may be a result of the more accurate treatment of Coulomb collisions in the Fokker-Planck calculations.

Figure (6-1) shows that T_e initially drops in the space-time code. This drop results from a difference in the value of the Ohmically heated T_e predicted by STICR-I, and the one which actually occurs. Upon using the experimental value, T_e drops. Figure (6-4) shows the mechanism which causes this decrease. Initially, the $\sim$20 kW of RF heating is more than offset by the $\sim$80 kW of power lost through radiation. The difference between the Ohmic heating ($\sim$500 kW) and the radial loss ($\sim$350 kW) together with the radiation results in $\sim$100 kW of net heating power. Since $T_e > T_i$, the electrons initially lose $\sim$600 kW to the ions. The net result is a loss of $\sim$500 kW of power from the electrons. Consequently, T_e drops. As T_e drops, both the radiation and rethermalization losses decrease. After 10 ms, $T_i > T_e$ in STICR-I. The electron-ion equilibration terms now become an energy source for the electrons. The electron temperature then begins to rise. The electron temperature in STICR-I reaches an equilibrium value near t = 60 ms, when the RF, Ohmic, and electron-ion equilibration heating terms equal the radial and radiation loss terms. After the initial drop in the electron temperature, $\Delta\overline{T}_e \sim 50$ eV, in agreement with both the experiment and FORCE.

On comparing Fig. (6-4) to Fig. (6-3), one can see the reason behind the initial discrepancy in $\Delta\overline{T}_e$ between the two codes. The radiation and RF heating values calculated by FORCE agree with the STICR-I results. However, the Ohmic heating term is larger while the radial loss term is smaller. These results, coupled with the more accurate Coulomb collisions calculations ($T_H \neq T_D$) enables the electron temperature to initially rise. Unlike STICR-I, if no RF was used, T_e would remain constant rather than fall. Unlike STICR-I, during the RF pulse, $T_e > T_D$, T_o during the RF pulse. There is always a net loss of energy from the electrons due to collisions, even though $T_H > T_e$ during most of the pulse. The electrons lose approximately 100 kW through collisions. This balances the net heating from Ohmic heating minus radial loss term. Therefore, the electron temperature increases less than 50 eV.

We find that STICR-I and FORCE agree with each other as well as with the actual PLT ICRF heating experiment. In PLT, the spatial effects of ICRF heating are small. Most of the heating occurs in the center, as assumed in FORCE. Mode conversion does not appear to affect either the RF power deposition or the density and temperature profiles. In addition, since $n_D > n_H$, the nonMaxwellian aspects of ICRF heating do not affect the overall ion temperature. The majority of the ions remain Maxwellian, as assumed in STICR-I. Even though $T_H \sim 1.5 \times T_D$, since $\frac{n_H}{n_D} = 0.1$, this effect is small on the ion energy balance. One can assume that $T_H = T_D = T_i$. In comparison, NUWMAK shows a great disagreement between codes.

6.B. NUWMAK

Chapter 4 showed that in both the fundamental and second harmonic heating cases, the deuterons and tritons were Maxwellian with $T_D \approx T_T$, even though most of the RF power was deposited in the deuterons. The only species found to be nonMaxwellian, excepting the alphas, was the carbon impurity in the fundamental heating case. Whereas FORCE assumes that all of the RF power is deposited at the center, STICR-II shows that this is not the case. Depending upon the ion harmonic and $k_{\parallel}$, from 40%-95% of the RF power is absorbed by the electrons before the plasma center is reached. We therefore expect the carbon impurity to remain Maxwellian when the cyclotron resonance is kept near the center.

There is not enough RF power available at the center to produce a nonMaxwellian impurity.

For this same reason, mode conversion effects should be small when the RF wave is launched from the low field side. In this case the wave, which is largely damped before the center is reached, must pass through the resonance zone to reach the mode conversion layer, which lies on the high field side.

Contrary to both the 0-D transport code, PORT, and the Fokker-Planck code, FORCE, the dominant RF heating mechanism, as one approaches reactor-like parameters, should be electron Landau and transit time damping. Although ion heating is dominant at the center, there is little wave energy reaching this region.

Both PORT and FORCE predict dominant ion heating in the second harmonic heating case. STICR-I does not. Therefore, we conclude that the predominance of electron heating is caused by spatial effects. The plasma should remain Maxwellian.

Comparing PORT and STICR-II for the same case, $\omega = 2\omega_{CD}$, we see that even though the plasma is larger and denser, STICR-II predicts that less auxiliary heating energy must be supplied. The 225 MJ calculated by PORT may actually be a lower bound since there are no impurities, $Z_{eff} = 1$. PORT neglects the profile effects which allow ignition to be achieved at the center before global ignition occurs. This can reduce the amount of heating power needed. In addition, PORT uses trapped particle scaling.

This scaling transports more energy radially than does "empirical PLT" scaling. Although the RF heating profiles do not change with scaling, the amount of auxiliary heating required to reach ignition is very sensitive to the scaling law. If STICR-II used trapped particle scaling, as much as 100 MJ of additional RF heating would be needed.

FORCE, which neglects charge exchange, radial, and radiation losses, and Ohmic heating, obtains $T_e \approx T_i$. Because of the high densities and temperatures in a reactor, the electron-ion equilibration time is quite short. Coupling this with the space-time results, we conclude that the requirement for auxiliary heating should be the same when either the ions or the electrons are heated, as long as the power is deposited near the plasma center. ICRF produced enhancement of the alpha power production should be minimal. Since electron heating is dominant higher ion harmonic heating, which heats electrons, may become more attractive from a technological standpoint. There appears to be no significant heating benefit in using fundamental or second harmonic heating over higher harmonics.

LIST OF FIGURES

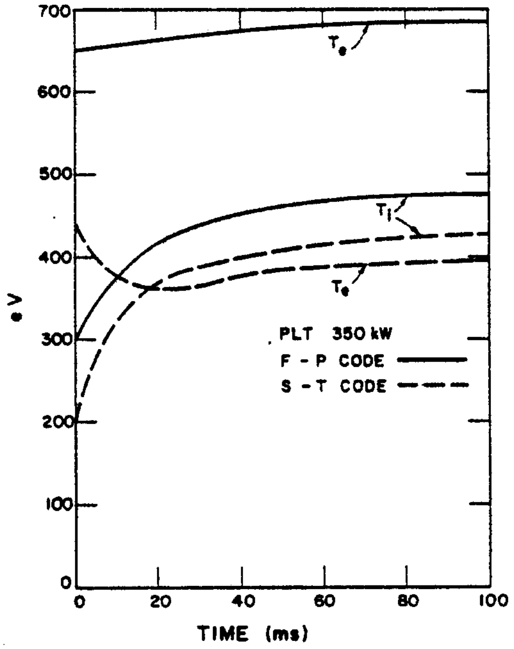

Fig.(6-1)

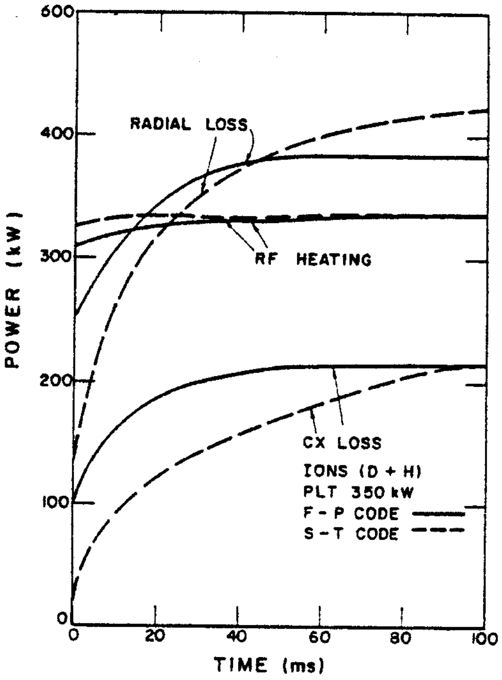

Fig.(6-2)

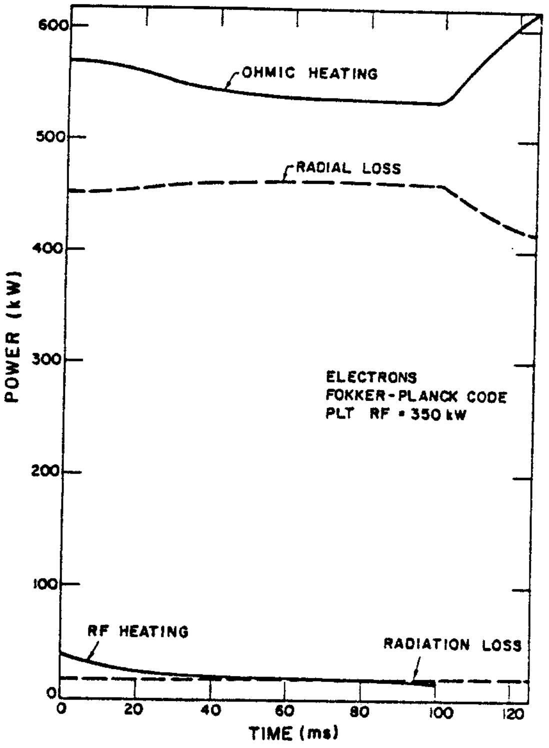

Fig.(6-3)

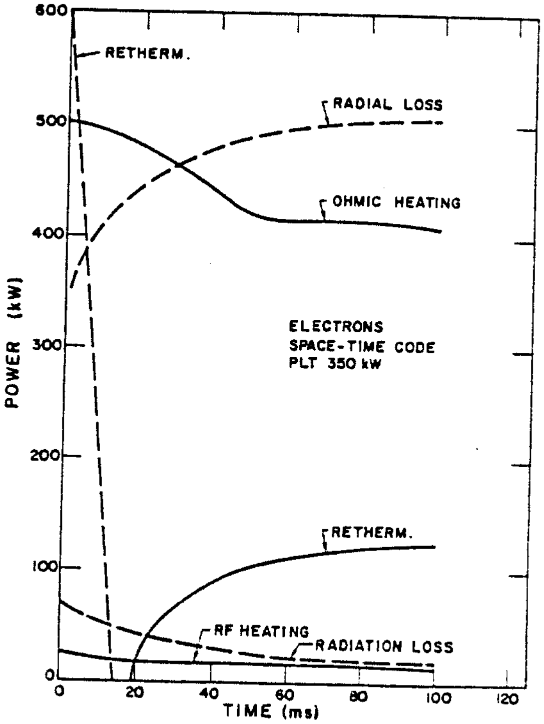

Fig.(6-4)

CHAPTER 7

SUMMARY AND CONCLUSIONS

In Chapter 1 we saw that ICRF was quite efficient in heating DIVA, TFR and PLT. The main body ion temperature doubled in several experiments and the overall heating efficiency was often greater than 80%, approaching that obtained by neutral beams.

The 0-D transport code with trapped particle scaling, discussed in Chapter 2, predicted that 175 MW for 1 second with $\omega = 2\omega_{cD}$ was enough power to ignite the NUWMAK conceptual reactor. In this scenario, the dominant heating mechanism was second harmonic damping by finite Larmour radius effects. The 0-D code neglects spatial effects which, as shown in Chapter 5, are very important.

The complete 3x3 hot plasma dispersion tensor, accurate for any temperature for ion harmonics up to five, was derived in Chapter 3. We have included impurities and, in the reactor cases, alphas. The complex value of $k_\perp$ obtained for a given real value of $k_\parallel$ and ω agrees well with the cold plasma value. The results compare quite favorably with those obtained by Stix in his reactor case.

In Chapter 4 we used a 0-D in real space, 2-D in velocity space, time-dependent, multi-species Fokker-Planck code to examine PLT and NUWMAK. In this chapter, as in Chapter 2, we have neglected spatial and any possible mode conversion effects. In PLT over 80% of the RF power was absorbed, by the presence of protons (~10%), through fundamental minority damping. The protons became non-Maxwellian with $T_H/T_D \sim 1.7$ and a high energy tail of 18 keV. The deuterium, electrons and oxygen species remained Maxwellian while the spatially-averaged deuterium temperature doubled. The electron temperature, as in the experiment, did not increase significantly. We were able to simulate the PLT experimental results when charge exchange, radial and radiation losses, and Ohmic heating were included.

The dispersion relation calculations assumed that each distribution could be represented by an "equivalent Maxwellian" distribution. As a possible improvement, one could represent the high energy proton tail in PLT as a sum of Maxwellian distributions.

In NUWMAK, the dominant heating was fundamental minority heating of deuterium, when $\omega = \omega_{cD}$, and second harmonic damping when $\omega = 2\omega_{cD}$. In either case, deuterium, tritium and electrons all remained Maxwellian with $T_D \simeq T_T \simeq T_e$. Little, if any, ICRF produced fusion reactor Q enhancement was found. If the electrons were heated directly by the RF, the amount of auxiliary power needed to reach ignition would remain the same.

In Chapter 5 we examined ICRF heating in PLT and NUWMAK using a WKB slab model coupled to a 1-D multi-species, time-dependent transport code. Using the slab model, we found that in PLT over 90% of the RF power is deposited in the protons at the plasma center over a width of 12-14 cm. We were able to numerically simulate both the ion temperature rise of 600 eV at the center, and the average ion temperature doubling using "PLT empirical" scaling. Again, the electron temperature did not rise.

The mode conversion threshold was calculated numerically. The incident fast wave could mode convert to an Ion Bernstein wave if the two dispersion relation roots coalesced over a finite grid mesh. This criterion appears to agree with the analytical expression obtained by Jacquinot. We found that PLT starts in the mode conversion regime. As the plasma heats, the mode conversion threshold rises so that over the final 40 ms of the RF pulse, no mode conversion occurs.

In NUWMAK, due to the higher densities and temperatures, the dominant heating mechanisms were electron Landau and transit time damping. In both NUWMAK and PLT, most of the RF power is absorbed by the plasma before the mode conversion layer is reached. The occurrence of mode conversion does not appear to change either the density or temperature profiles.

In both studies, we assumed that all ions had the same temperature. Although Chapter 4 showed this to be the case for NUWMAK, this does not hold for PLT. In our RF calculations, we found that the ratio T_H/T_D affects the mode conversion threshold. The threshold becomes higher when this ratio is increased. For a more accurate calculation for PLT, two energy balance equations should be used. In addition, we have neglected the possible effects of having a high energy proton tail on the dispersion properties. In PLT calculations, one should couple Fokker-Planck and transport calculations.

For PLT calculations, we used reflection, transmission and mode conversion coefficients for a slab model obtained by Swanson. For the NUWMAK cases these coefficients were obtained from work performed by McVey. In either case, electron effects were neglected and both formulisms break down at high temperatures ($\lambda \rightarrow 1$). In addition, since I_{02} and I_{22} represent complicated integral expressions which must be solved numerically, we have assumed that these values do not change significantly when PLT parameters change. Improvements in calculating the various reflection, transmission and mode conversion coefficients should also lead to more accurate results.

In addition, we have neglected any possible 2D and 3D effects. Although poloidal effects may be small, there appears to be a focusing effect when waves are launched from a coil with a finite length in the poloidal direction. We have also neglected all boundary effects and the possibility of eigenmode formation. The WKB slab model is more accurate when the wave is damped within one pass across the minor cross section. In PLT, this appears to be the case; we obtain good agreement with the experiment.

In Chapter 6, we find good agreement between the Fokker-Planck and 1-D transport codes in the PLT simulations. In the reactor cases, spatial effects are very important. These effects produce dominant electron absorption of the RF power which neither the 0-D transport nor the Fokker-Planck codes predict.

In both PLT and NUWMAK, we have neglected the ion-ion hybrid resonance layer. When the minority concentration becomes large (>10%), this layer can dominate the heating process when $\omega = \omega_{ci}$.

This has been observed in recent TFR experiments. We have examined cases where the minority concentration is low enough or the RF frequency is at an ion harmonic which minimizes this effect. Both the WKB and weak damping formulas break down in the vicinity of this resonance layer. When the ion-ion hybrid resonance layer is in the plasma and not in close proximity to the cyclotron resonance layer, different reflection, transmission and mode conversion coefficients must be used. Although we have not examined these cases, the formulism has been set up to do this. One needs only to determine the position of the ion-ion hybrid resonance layer and add the appropriate wave coefficients.

The following could improve the accuracy of our ICRF heating description:

(1) Add a second energy balance equation to the 1-D transport code;

(2) Couple the Fokker-Planck and transport codes in performing PLT calculations;

(3) Generalize the 3x3 dispersion tensor to include anisotropy and high energy tails;

(4) Add coefficients to examine ion-ion hybrid resonance effects;

(5) Include boundary effects to examine possible eigenmodes;

(6) Improve calculations of reflection, transmission and mode conversion coefficients; and

(7) Use ray tracing to examine 2D and 3D effects.

The above seven suggestions are nontrivial and will all involve much work. The codes which have been used are written in such a way that they can be easily updated.

There remains a large amount of work which needs to be done before we can say that we truly understand ICRF heating. We have provided a good start; other theses shall surely follow.

APPENDIX A

FLOW CHART OF RF DISPERSION RELATION USED IN THE FOKKER - PLANCK CODE.

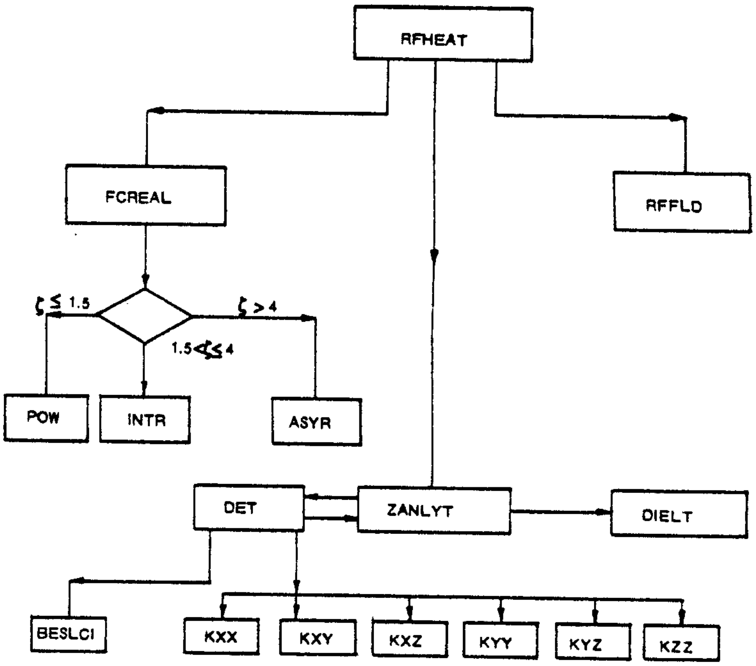

```
          subroutine rfheat
 *
 *
 cmt
 cmt      Refs. T.K. MAU, Ph.D. Thesis, Univ. of Wisconsin-Madison (1977)
 cmt            B. McVeu, Univ. of Wisconsin-Madison Report PLP 716 (Feb.,1977)
 cmt            B. McVeu, Univ. of Wisconsin-Madison Report 755 (May,1978)
 cmt
 cmt      THESE SUBROUTINES AND FUNCTIONS ARE USED IN THE FOKKER-PLANCK CODE FORCE
 cmt      THE RF DISPERSION RELATION ROUTINES IN THE SPACE-TIME CODES STICR-I AND
 cmt      STICR-II ARE SLIGHTLY DIFFERENT
 cmt
 cmt      SETS UP THE CALCULATION OF COMPLEX KPERP AND THE RF ELECTRIC FIELD
 cmt      det IS THE COMPLEX HOT PLASMA DISPERSION DETERMINANT SOLVED BY zanlut
 cmt      THE SMALLEST ROOT IS THE FAST WAVE ROOT
 cmt      THE NEXT LARGEST ROOT IS THE ION CYCLOTRON OR ION BERNSTEIN ROOT
 cmt      w = RF FREQUENCY (rad/sec)
 cmt      rrr = POSITION ALONG MINOR RADIUS (=0 in Fokker-Planck code)
 cmt      neq = NUMBER OF SPECIES
 cmt      i = 1 FOR ELECTRONS
 cmt        > 1 FOR IONS
 cmt      wc = CYCLOTRON FREQUENCY (rad/sec)
 cmt      reden = DENSITY (cm-3)
 cmt      eperp = PERPENDICULAR ENERGY (keV)
 cmt      epar = PARALLEL ENERGY (keV)
 cmt      vtx = PERPENDICULAR THERMAL VELOCITY (cm/sec)
 cmt      vtz = PARALLEL THERMAL VELOCITY (cm/sec)
 cmt      wp = PLASMA FREQUENCY (rad/sec)
 cmt      wp2 = wp*wp
 cmt      nn = HARMONIC NUMBER
 cmt      nhigh = HIGHEST HARMONIC NUMBER
 cmt      zeta = ARGUMENT OF FRIED-CONTE INTEGRAL
 cmt      zi = FRIED-CONTE INTEGRAL
 cmt      dzi = DERIVATIVE OF FRIED-CONTE INTEGRAL
 cmt      ftheta = theta (see T.K. Mau, Ph.D. Thesis, (1977))
 cmt      fphi = phi (see T.K. Mau, Ph.D. Thesis, (1977))
 cmt      xrcp = COLD PLASMA FAST WAVE KPERP**2 (see Brian McVeu, PLP 716 Feb.,1977)
 cmt             used in the initial guess for zanlut
 cmt      z(1) = FAST WAVE KPERP**2
 cmt      z(2) = ION BERNSTEIN KPERP**2
 cmt      xkperp = KPERP
 cmt      rffld CALCULATES THE RF ELECTRIC FIELD COMPONENTS FOR UNBOUNDED PLASMA
 *
 *

          external det
          complex det
          complex z(3),zi(11,5),dzi(11,5)
          common/mcon1/pi,twopi,fourpi,pio2,charge,time,dtr,dtn(15), nsotn(
        x      15),nstepu,n,nprint,nplot,nstop,nrstrt,nch,nchec, ium1,ium2,
        x      ium3, ixm1, ixm2, ixm3, ixim, ixim2, ixim3,ergtkev, potent,dpot,
        x              xmax,xmaxi,kbound,kgetafk,kambi, kqnande,mimax,bratio
        x       ,bratioi,pitang,ksinqui,vnorm,efusion(4), knprobs,nsl,beta0,
        x   fqmmesh,sbplo,ct,vef0,rdor, rhoo,nelio,elength,nsle,
        x              nsle2,rfudge,bdob,tfmax, rdora(5),rdorb(5),rdort(5),
        x      rdtchq(5),sfse,kbufin,kbufout, namebin,namebot,kbufu(5),kcsiq
        x       ,tauek(5), tauen(5),taupk(5),taupk1(5), taupor(5),kchnut,
        x    reacsl(5),fqtmesh,iqtmesh,ktpnut, ncutfe,potrat,npotz,fqbmesh,
        x      kinteg,kicca,tcv2, cmfp,tau1,tau2,tau3,lpek,lt,erot,twoth,
        x     taues(5),kspadi, evrat,endene,kmaxe,kvarte,kvarit,kczeff,zeffk
        x       , sqrt2,stopm,charge4,fourpi3,ergtkth,twopith,fstpi,clight
```

```
      common/mconlc/nimio,reden0,enerqu0,elecfld,aldol,mirmode,rvacu,
     c bvac0,betau,badob,Kbetdot,Kcuroff,Kpotsh,bado1,bado2,
     c elosr1,elosr2,eloseta,einjen,emulq,Kpotte,potte,Kflvp,
     c Kdlos,K011,K012,poten2,bratis,bratis1,Kdcle,elongt1,
     c sdlossp(2),sfdlosp(2),bratit,bratit1,bratiu,bratiu1,
     c brativ,brativ1,bf01,bf02,bfm1,bfm2,elongt2,em2sq,
     c v2ov1,elnrm2,tusap1,elnrm3,K2sor,sorqain(2),Kt2t1,
     c sortenq,Kpluqco,Kmco,ncrf,iiprt,imxwl,iplt,
     c Kdfix,delequ,mtabml,elmin,Kchxn,Klfix,Ketdi,Kcomod,
     c Kmskip,Kpast,efusinn(4),dprat,sinj,xrcp,
     c Kdlot,rcbc,Ktaul,Kinjhe3,etaul,Kbrem,Ksunc,Kfrar,Karwt,
     c wbrem,wsunc,einj1,Kbzd,poten3,istopqs,Kpot3,pot23,
     c e2as,e3as,Krel,eltemp,emc2,qehrate,spfrac,delrel,flavq,
     c Kmodfl,Kmplt,Kschex,Kpepap,Kelosp,Kcntplt,imsq(3)
c
      common/mslavr/slavh(4,2),fwc(5),sfeo(2),sfeo1(2),sfeo2(2),
     cefdd(2),efdn(2),pafeo(1000,2),pafeo11(1000),prfmw(5)
      common/mcon2/jo(20,4),io(71,4),jmin(4),imin(4), tnorm(5),ratiom(5,
     x      5),emass(5), anumb(5),anormK(5),dens(5),reden(5), enerqu(5),
     x      enqu(5),denstor(5), esor(1,5),xsor(1,5),usor(1,5), vsor(1,5)
     x      ,enit(5),xnit(5), unit(5),vnit(5),gam2(5,5), gamma(5,5),ratK
     x      (5,5),elons(5), tson(1,5),tsoff(1,5), abj1(1,5,5),abj2(1,5,5
     x      ), abj3(1,5,5),ccex(1,5,5), ratioz2(5,5),porpb(5),ensor(1,5)
     x      , ejsor(1,5),ensavq(5),ejstot(5), Kspec1(2,5),mxmax(5),
     x           etplos(5),dtplos(5), parmom(5),epar(5),eperp(5), disp(5
     x      ),denm(1),enqm(1), gam2ax(5,5),emasm(1),anumbm(1), entr(5,5)
     x      ,Kspecm(2,1),tauem(1), gammax(5,5),dennm(1),enqqm(1), abfac(
     x      5,5)
      common/mcont/iu,ix,jx1,neq,nmag,mmx,nonch,iz,nsor,nstep,nhigh,
     cnmaneq,Ksydm,iudm,mxdm,iup1jx,mx,iuh,iujn,iuhm1,iuhp1,mxp3m,
     cmxp4,mxp1,neap,mmxp,nmaqp,nmaneqp,mmx0,iup1,iup2,jxp1,iujx,
     cmtab,mmsv,msiq,mmsvp,jxis,neqm1
      complex fthet,fphi,besd,besl,xKperp,zlam,xKp2
      common/rfcm/wc(6),vtx(6),vtz(6),zx(6),fthet(11,6),fphi(11,6),freq,
     xbesa(7),zeta(11,6),zxm(6),besl(6,6),wp2(6),xKp2(2),wp(6),irr
     x ,xKperp(2),besd(6,6),cK(6),infer(2),besr(7),zlam(6),rrr,powrx
      complex efld,rfld,dielt,rffdn
      common/erfld/efld(3),rfld(2),dielt(6),xnpar,xnparz,xKpar,dbq(99)
     1,aprf(6,6),prfs(5),tprf(6,6),powerf,trfon,trfoff,rffdn(3),baxis
     c,rmaj,rmin,rminor,iwall(6),curr,dennd,dennt,dennh,ennd,ennt,ennh
      ncrfm=n-1
      if(ncrfm.gt.ncrf*(ncrfm/ncrf)) go to 999
c     rrr=rmin*float(71-irr)/70.
      w=2.*pi*freq
      r=0.
      s=0.
      el=0.
      do 1 i=1,neq
      go to 3333
 3333 wc(i)=charge*anumb(i)*baxis/emass(i)/clight
      if(i.eq.1) wc(1)=-wc(1)
c     reden(i)=reden0(i)*(1.-rrr*rrr/rmin/rmin)+.01*reden0(i)
c     eperp(i)=eperp0(i)*(1.-rrr*rrr/rmin/rmin)+.01*eperp0(i)
c     epar(i)=epar0(i)*(1.-rrr*rrr/rmin/rmin)+.01*epar0(i)
      go to 3334
 3334 vtx(i)=sqrt(2.*eperp(i)*ergtKev/emass(i))
      vtz(i)=sqrt(4.*epar(i)*ergtKev/emass(i))
      zx(i)=2.*epar(i)/eperp(i)
      if(i.eq.1) zx(i)=1.
      zxm(i)=1.-zx(i)
```

```
      if(i.eq.1) zxm(i)=0.
      wp2(i)=4.*pi*reden(i)*(charge*anumb(i))**2/emass(i)
      wp(i)=sqrt(wp2(i))
      do 4 nn=1,nhigh
      mn=nn+nhigh
      zeta(nn,i)=(w-nn*wc(i))/xKpar/vtz(i)
      go to 105
  105 zeta(mn,i)=(w+nn*wc(i))/xKpar/vtz(i)
      dbg(33)=zeta(nn,i)
      dbg(34)=zeta(mn,i)
      call  fcreal(zeta(nn,i),zr,zi,dzr,dzi,ntrm,rem,1.e-7)
      zl(nn,i)=cmplx(zr,0.)+cmplx(0.,1.)*zi
      go to 106
  106 dzl(nn,i)=cmplx(dzr,0.)+cmplx(0.,1.)*dzi
      call  fcreal(zeta(mn,i),zr1,zi1,dzr1,dzi1,ntm,rem,1.e-7)
      zl(mn,i)=cmplx(zr1,0.)+cmplx(0.,1.)*zi1
      dzl(mn,i)=cmplx(dzr1,0.)+cmplx(0.,1.)*dzi1
      fthet(nn,i)=2.*zx(i)*zl(nn,i)/vtz(i)-xKpar*zxm(i)*dzl(nn,i)/w
      fthet(mn,i)=2.*zx(i)*zl(mn,i)/vtz(i)-xKpar*zxm(i)*dzl(mn,i)/w
      fphi(nn,i)=(1.-nn*wc(i)*zxm(i)/w)*dzl(nn,i)
      go to 107
  107 fphi(mn,i)=(1.+nn*wc(i)*zxm(i)/w)*dzl(mn,i)
      dbg(35)=real(fthet(nn,i))
      dbg(36)=aimag(fthet(nn,i))
      dbg(37)=real(fthet(mn,i))
      dbg(38)=aimag(fthet(mn,i))
      dbg(39)=real(fphi(nn,i))
      dbg(40)=aimag(fphi(nn,i))
      dbg(41)=real(fphi(mn,i))
      dbg(42)=aimag(fphi(mn,i))
    4 continue
      go to 108
  108 zeta(ll,i)=w/xKpar/vtz(i)
      dbg(43)=zeta(ll,i)
      call  fcreal(zeta(ll,i),zr0,zi0,dzr0,dzi0,itm,rem,1.e-7)
      zl(ll,i)=cmplx(zr0,0.)+cmplx(0.,1.)*zi0
      dzl(ll,i)=cmplx(dzr0,0.)+cmplx(0.,1.)*dzi0
      fthet(ll,i)=2.*zx(i)*zl(ll,i)/vtz(i)-xKpar*zxm(i)*dzl(ll,i)/w
      fphi(ll,i)=dzl(ll,i)
      dbg(44)=real(fthet(ll,i))
      dbg(45)=aimag(fthet(ll,i))
      dbg(46)=real(fphi(ll,i))
      dbg(47)=aimag(fphi(ll,i))
      go to 109
  109 cK(i)=.5*wp2(i)/zx(i)/w/xKpar
cmnt    calculation cold plasma dispersion relation for (Kperp)**2
cmnt
      if(i.eq.1) go to 1
      r=r+wp2(i)/(wc(i)*(w+wc(i)))
      s=s+wp2(i)/(wc(i)*wc(i)-w*w)
      el=el-wp2(i)/(wc(i)*(w-wc(i)))
    1 continue
      rls=r*el/s
      xKs=xKpar**4/s
      aK=(w/clight)**2
      xrcp=(xKs-2.*aK*xKpar*xKpar+aK*aK*rls)/(aK-xKpar*xKpar/s)
      go to 110
  110 z(1)=cmplx(xrcp,0.)
      xr10=10.*xrcp
      z(2)=cmplx(xr10,xrcp)
```

```
      call zanlut(det,1.e-7,6,0,1,1,z,200,infer,ier)
      do 5 nn=1,2
      xKp2(nn)=z(nn)
      go to 111
  111 xKperp(nn)=csqrt(z(nn))
      dbg(48)=real(xKperp(1))
      go to 112
  112 dbg(49)=aimag(xKperp(1))
    5 continue
      dbg(65)=real(z(1))
      dbg(66)=aimag(z(1))
      dbg(67)=real(xKperp(1))
      dbg(68)=aimag(xKperp(1))
      call rffld
  999 call rfcoeff
      return
      end
      subroutine fcreal(ar,zr,zi,dzr,dzi,n,rem,tol)
*
*
cmt   WRITTEN BY BRIAN McVEY, Univ. of Wisconsin-Madison
cmt
cmt   CALCULATES FRIED-CONTE INTEGRALS FOR REAL ARGUMENTS
cmt
cmt   Refs. Brian McVey, Univ. of Wisc. Report PLP 755 (May,1978)
cmt         B. Fried, Conte, THE PLASMA DISPERSION FUNCTION (1961)
cmt
cmt   ar IS THE REAL ARGUMENT
cmt   zr IS THE REAL PART OF THE INTEGRAL
cmt   zi IS THE IMAGINARY PART OF THE INTEGRAL
cmt   dzr IS THE REAL PART OF THE DERIVATIVE OF THE INTEGRAL
cmt   dzi IS THE IMAGINARY PART OF THE DERIVATIVE OF THE INTEGRAL
cmt   n IS THE NUMBER OF ITERATIONS USED TO CALCULATE THE INTEGRAL
cmt   rem IS THE REMAINDER
cmt   tol IS THE TOLERANCE SPECIFIED TO CLACULATE THE INTEGRAL
*
*
      in=0
      sarpi=1.772454
      x=abs(ar)
      if(x.le.1.5) go to 11
      if(x.le.4.) go to 12
   14 call asur(x,zr,dzr,n,rem,tol)
      in=1
   31 asq=-x**2
      if(asq.lt.-8.e1) go to 81
      zi=sarpi*exp(asq)
      if(in.ne.1) go to 82
      dzi=-2.*x*zi
      go to 20
   82 dzr=-2.*(1.+x*zr)
      dzi=-2.*x*zi
      go to 20
   81 zi=0.
      dzi=0.
   20 if(ar.gt.0.) return
      zr=-zr
      dzi=-dzi
      return
   11 call powr(x,zr,n,rem,tol)
```

```
         go to 31
      12 call intr(x,zr,n,rem,tol)
         go to 31
         end
         subroutine asur(x,zr,dzr,n,rem,tol)
*
*
cmt      WRITTEN BY BRIAN McVEY, Univ. of Wisconsin-Madison
cmt
cmt      CALCULATES FRIED-CONTE INTEGRAL USING ASYMPTOTIC EXPANSION FOR LARGE ARGUMENTS
cmt      ZETA .gt. 4.
*
*
         rem1=1.
         s=1.
         dzr=0.
         b=1./x
         do 10 n=1,40
         x1=float(n)
         p=b**2*(2.*x1-1.)*.5
         if(n.eq.1) go to 11
         p1=p1*p
         go to 12
      11 p1=p
      12 rem=abs(p1)/abs(s)
         if(rem.lt.tol) go to 13
         if(rem1.lt.rem) go to 13
         rem1=rem
         dzr=dzr+p1
      10 s=s+p1
      13 zr=-b*s
         dzr=2.*(dzr+p1)
         return
         end
         subroutine intr(x,zr,n,rem,tol)
*
*
cmt      WRITTEN BY BRIAN McVEY, Univ. of Wisconsin-Madison
cmt
cmt      CALCULATES FRIED-CONTE INTEGRAL FOR 1.5 gt. ZETA .le. 4.
*
*
         dimension f(10)
         i1=0
         b=1.5
         call powr(b,f(1),n,rem,tol)
      35 n=0
      13 f(2)=-2.*(1.+b*f(1))
         do 10 i=1,7
         x1=float(i)
      10 f(i+2)=-2.*x1*f(i)-2.*b*f(i+1)
         h=(4.032e3*tol/abs(f(9)))**.125
         r=b+h
         if(r.lt.x) go to 19
         h=x-b
         i1=1
      19 b=b+h
         p=1.
         do 12 i=2,8
         x1=float(i-1)
```

```
      p=p*h/x1
   12 f(1)=f(1)+p*f(1)
      n=n+1
      if(i1.eq.0) go to 13
   14 zr=f(1)
      rem=.1*tol*float(n)+rem
      return
      end
      subroutine powr(x,zr,n,rem,tol)
*
*
cmt   WRITTEN BY BRIAN McVEY, Univ. of Wisconsin-Madison
cmt
cmt   CALCULATES POWER SERIES EXPANSION OF FRIED-CONTE INTEGRAL FOR SMALL ARGUMENTS
*
*
      s=1.
      do 10 n=1,40
      x1=float(n)
      p=-x**2*2./(2.*x1+1.)
      if(n.eq.1) go to 11
      p2=p2*p
      go to 12
   11 p2=p
   12 rem=abs(p2)/abs(s)
      if(rem.lt.tol) go to 13
   10 s=s+p2
   13 zr=-2.*x*s
      return
      end
      complex function Kxx(xx)
*
*
cmt   THIS FUNCTION IS THE Kxx ELEMENT OF THE HOT PLASMA DIELECTRIC TENSOR
cmt   Ref. T.K. MAU, Ph.D. Thesis, Univ. of Wisconsin-Madison (1977)
*
*
      complex xx
      common/mcont/iu, ix, ixi,neq,nmag,mmx,nonch,lz,nsor,nstep,nhigh,
     cnmaneq,Ksudm,iudm,mxdm,iuplix,mx,iuh,iuin,iuhm1,iuhp1,mxp3m,
     cmxp4,mxp1,neqp,mmxp,nmagp,nmaneqp,mmx8,iup1,iup2,ixp1,iuix,
     cmtab,mmsv,msig,mmsvp,ixis,neqm1
      complex fthet,fphi,besd,besi,xKperp,zlam,xKp2
      common/rfcm/wc(6),vtx(6),vtz(6),zx(6),fthet(11,6),fphi(11,6),freq,
     xbesa(7),zeta(11,6),zxm(6),besi(6,6),wp2(6),xKp2(2),wp(6),irr
     x ,xKperp(2),besd(6,6),cK(6),infer(2),besr(7),zlam(6),rrr,powrx
      complex efld,rfld,dielt,rffdn
      common/erfld/efld(3),rfld(2),dielt(6),xnpar,xnparz,xKpar,dbq(99)
     1,aprf(6,6),prfs(5),tprf(6,6),powerf,trfon,trfoff,rffdn(3),baxis
     c,rmaj,rmin,rminor,iwall(6),curr,dennd,dennt,dennh,ennd,ennt,ennh
      Kxx=cmplx(0.,0.)
      do 200 ii=1,neqp
      aprf(1,ii)=0.
  200 continue
      do 1 i=1,neq
      if(zlam(i).eq.cmplx(0.,0.)) go to 222
      do 2 m=1,nhigh
      mn=m+nhigh
      go to 101
  101 Kxx=Kxx+cK(i)*cexp(-zlam(i))*m*m*besi
```

```
     1(m,i)*(fthet(m,i)+fthet(mn,i))/zlam(i)
      dbg(29)=real(Kxx)
      go to 102
  102 dbg(30)=aimag(Kxx)
    2 continue
      go to 103
  222 Kxx=Kxx+.5*cK(i)*(fthet(1,i)+fthet(6,i))
  103 Kxx=Kxx+cmplx(1./neq,0.)
      dbg(31)=real(Kxx)
      go to 104
  104 dbg(32)=aimag(Kxx)
      aprf(1,i)=aimag(Kxx)-aprf(1,1)-aprf(1,2)-aprf(1,3)-aprf(1,4)
    1 continue
      return
      end
      complex function Kxy(xx)
*
*
cmt   THIS FUNCTION IS THE Kxy ELEMENT OF THE HOT PLASMA DIELECTRIC TENSOR
*
*
      complex xx
      common/mcont/iy, ix, ixl,neq,nmag,mmx,nonch,lz,nsor,nstep,nhigh,
     cnmaneq,Ksydm,iydm,mxdm,iyplix,mx,iyh,iyin,iyhml,iyhpl,mxp3m,
     cmxp4,mxpl,neqp,mmxp,nmagp,nmyneqp,mmx8,iypl,iyp2,ixpl,iyix,
     cmtab,mmsv,msig,mmsvp,ixls,neqml
      complex fthet,fphi,besd,besi,xKperp,zlam,xkp2
      common/rfcm/wc(6),vtx(6),vtz(6),zx(6),fthet(11,6),fphi(11,6),freq,
     xbesa(7),zeta(11,6),zxm(6),besi(6,6),wp2(6),xKp2(2),wp(6),irr
     x ,xKperp(2),besd(6,6),cK(6),infer(2),besr(7),zlam(6),rrr,powrx
      complex efld,rfld,dielt,rffdn
      common/erfld/efld(3),rfld(2),dielt(6),xnpar,xnparz,xKpar,dbg(99)
     1,aprf(6,6),prfs(5),tprf(6,6),powerf,trfon,trfoff,rffdn(3),baxis
     c,rmaj,rmin,rminor,iwall(6),curr,dennd,dennt,dennh,ennd,ennt,ennh
      Kxy=cmplx(0.,0.)
      do 200 ii=1,neqp
      aprf(2,ii)=0.
  200 continue
      do 1 i=1,neq
      do 2 m=1,nhigh
      mn=m+nhigh
      go to 101
  101 Kxy=Kxy+cmplx(0.,1.)*cK(i)*cexp(-zlam(i))*m*((besd(m,i)-
     1besi(m,i))*(fthet(m,i)-fthet(mn,i)))
    2 continue
      dbg(27)=real(Kxy)
      go to 102
  102 dbg(28)=aimag(Kxy)
      aprf(2,i)=real(Kxy)-aprf(2,1)-aprf(2,2)-aprf(2,3)-aprf(2,4)
    1 continue
      return
      end
      complex function Kxz(xx)
*
*
cmt   THIS FUNCTION IS THE Kxz ELEMENT OF THE HOT PLASMA DIELECTRIC TENSOR
*
*
      complex xx
      common/mcont/iy, ix, ixl,neq,nmag,mmx,nonch,lz,nsor,nstep,nhigh,
```

```
     cnmaneq,Ksudm,iudm,mxdm,iup1jx,mx,iuh,iujn,iuhm1,iuhp1,mxp3m,
     cmxp4,mxp1,neqp,mmxp,nmagp,nmaneqp,mmx8,iup1,iup2,jxp1,iujx,
     cmtab,mmsv,msig,mmsvp,jxis,neqm1
      complex fthet,fphi,besd,besi,xKperp,zlam,xKp2
      common/rfcm/wc(6),vtx(6),vtz(6),zx(6),fthet(11,6),fphi(11,6),freq,
     xbesa(7),zeta(11,6),zxm(6),besi(6,6),wp2(6),xKp2(2),wp(6),irr
     x ,xKperp(2),besd(6,6),cK(6),infer(2),besr(7),zlam(6),rrr,powrx
      complex efld,rfld,dielt,rffdn
      common/erfld/efld(3),rfld(2),dielt(6),xnpar,xnparz,xKpar,dbg(99)
     1,aprf(6,6),prfs(5),tprf(6,6),powerf,trfon,trfoff,rffdn(3),baxis
     c,rmaj,rmin,rminor,iwall(6),curr,dennd,dennt,dennh,ennd,ennt,ennh
      Kxz=cmplx(0.,0.)
      do 200 ii=1,neqp
      aprf(6,ii)=0.
  200 continue
      do 1 i=1,neq
      do 2 m=1,nhigh
      mn=m+nhigh
      go to 101
  101 if(zlam(i).ne.cmplx(0.,0.)) Kxz=Kxz-cK(i)*cexp(-zlam(i))*
     1csqrt(xx)*m*besi(m,i)*(fphi(m,i)-fphi(mn,i))/zlam(i)/wc(i)
      dbg(25)=real(Kxz)
      go to 102
  102 dbg(26)=aimag(Kxz)
    2 continue
      aprf(6,i)=aimag(Kxz)-aprf(6,1)-aprf(6,2)-aprf(6,3)-aprf(6,4)
    1 continue
      return
      end
      complex function Kuu(xx)
*
*
cmt   THIS FUNCTION IS THE Kuu ELEMENT OF THE HOT PLASMA DIELECTRIC TENSOR
*
*
      complex xx
      common/mcont/iu,jx,jx1,neq,nmag,mmx,nonch,lz,nsor,nstep,nhigh,
     cnmaneq,Ksudm,iudm,mxdm,iup1jx,mx,iuh,iujn,iuhm1,iuhp1,mxp3m,
     cmxp4,mxp1,neqp,mmxp,nmagp,nmaneqp,mmx8,iup1,iup2,jxp1,iujx,
     cmtab,mmsv,msig,mmsvp,jxis,neqm1
      complex fthet,fphi,besd,besi,xKperp,zlam,xKp2
      common/rfcm/wc(6),vtx(6),vtz(6),zx(6),fthet(11,6),fphi(11,6),freq,
     xbesa(7),zeta(11,6),zxm(6),besi(6,6),wp2(6),xKp2(2),wp(6),irr
     x ,xKperp(2),besd(6,6),cK(6),infer(2),besr(7),zlam(6),rrr,powrx
      complex efld,rfld,dielt,rffdn
      common/erfld/efld(3),rfld(2),dielt(6),xnpar,xnparz,xKpar,dbg(99)
     1,aprf(6,6),prfs(5),tprf(6,6),powerf,trfon,trfoff,rffdn(3),baxis
     c,rmaj,rmin,rminor,iwall(6),curr,dennd,dennt,dennh,ennd,ennt,ennh
      Kuu=cmplx(0.,0.)
      do 200 ii=1,neqp
      aprf(3,ii)=0.
  200 continue
      do 1 i=1,neq
      if(zlam(i).eq.cmplx(0.,0.)) go to 231
      go to 101
  101 Kuu=Kuu+cmplx(1./neq,0.)-2.*ck(i)*zlam(i)*cexp(-zlam(i))*
     1(besd(6,i)-besi(6,i))*fthet(11,i)
      dbg(21)=real(Kuu)
      go to 102
  102 dbg(22)=aimag(Kuu)
```

```
      do 2 m=1,nhigh
      mn=m+nhigh
      go to 103
  103 Kuu=Kuu+ck(i)*cexp(-zlam(i))*(m*m*besi
     1(m,i)/zlam(i)-2.*zlam(i)*(besd(m,i)-besi(m,i)))*(fthet(m,i)
     1+fthet(mn,i))
    2 continue
      go to 230
  231 Kuu=Kuu+cmplx(1./neq,0.)+.5*ck(i)*(fthet(1,i)+fthet(6,i))
  230 dbg(23)=real(Kuu)
      go to 104
  104 dbg(24)=aimag(Kuu)
      aprf(3,i)=aimag(Kuu)-aprf(3,1)-aprf(3,2)-aprf(3,3)-aprf(3,4)
    1 continue
      return
      end
      complex function Kuz(xx)
*
*
cmt   THIS FUNCTION IS THE Kuz ELEMENT OF THE HOT PLASMA DIELECTRIC TENSOR
*
*
      complex xx
      common/mcont/iu, jx, jxi,neq,nmag,mmx,nonch,iz,nsor,nstep,nhigh,
     cnmaneq,Ksudm,iudm,mxdm,iup1jx,mx,iuh,iujn,iuhm1,iuhp1,mxp3m,
     cmxp4,mxp1,neqp,mmxp,nmagp,nmaneqp,mmx8,iup1,iup2,jxp1,iujx,
     cmtab,mmsv,msig,mmsvp,jxis,neqm1
      complex fthet,fphi,besd,besi,xKperp,zlam,xKp2
      common/rfcm/wc(6),vtx(6),vtz(6),zx(6),fthet(11,6),fphi(11,6),freq,
     xbesa(7),zeta(11,6),zxm(6),besi(6,6),wp2(6),xKp2(2),wp(6),irr
     x ,xKperp(2),besd(6,6),cK(6),infer(2),besr(7),zlam(6),rrr,powrx
      complex efld,rfld,dielt,rffdn
      common/erfld/efld(3),rfld(2),dielt(6),xnpar,xnparz,xKpar,dbg(99)
     1,aprf(6,6),prfs(5),tprf(6,6),powerf,trfon,trfoff,rffdn(3),baxis
     c,rmaj,rmin,rminor,iwall(6),curr,dennd,dennt,dennh,ennd,ennt,ennh
      Kuz=cmplx(0.,0.)
      do 200 ii=1,neqp
      aprf(4,ii)=0.
  200 continue
      do 1 i=1,neq
      go to 101
  101 Kuz=Kuz+ck(i)*(cexp(-zlam(i))*csqrt(xx)*(besd(6,i)-besi(6,i))
     c*fphi(11,i)/wc(i))*cmplx(0.,1.)
      dbg(17)=real(Kuz)
      go to 102
  102 dbg(18)=aimag(Kuz)
      do 2 m=1,nhigh
      mn=m+nhigh
      go to 103
  103 Kuz=Kuz+ck(i)*(cexp(-zlam(i))*csqrt(xx)*(besd(m,i)-besi(m,i))
     1*(fphi(m,i)+fphi(mn,i))/wc(i))*cmplx(0.,1.)
      dbg(19)=real(Kuz)
      go to 104
  104 dbg(20)=aimag(Kuz)
    2 continue
      aprf(4,i)=real(Kuz)-aprf(4,1)-aprf(4,2)-aprf(4,3)-aprf(4,4)
    1 continue
      return
      end
      complex function Kzz(xx)
```

```
*
*
cmt   THIS FUNCTION IS THE Kzz ELEMENT OF THE HOT PLASMA DIELECTRIC TENSOR
*
*
       complex xx
       common/mcon1/pi,twopi,fourpi,pio2,charge,time,dtr,dtn(15), nsetn(
     x     15),nstepu,n,nprint,nplot,nstop,nrstrt,nch,nchec, ium1,ium2,
     x     ium3,ixm1,ixm2,ixm3,ixim,ixim2,ixim3,eratkev, potent,dpot,
     x               xmax,xmaxi,Kbound,KaetafK,Kambi, Kqnande,mimax,bratio
     x       ,bratio1,pltang,Ksinqul,vnorm,efusion(4), Knprobs,nsl,beta0,
     x  fammesh,sbple,ct,vef0,rdor, rhoo,nelio,elength,nsle,
     x               nsle2,rfudge,bdob,tfmax, rdora(5),rdorb(5),rdort(5),
     x      rdtcha(5),sfse,Kbufin,Kbufout, namebin,namebot,Kbufu(5),Kcsiq
     x       ,tauek(5), tauen(5),taupK(5),taupKi(5), taupr(5),Kchnut,
     x    reacsl(5),fatmesh,iatmesh,Ktpnut, ncutfe,potrat,npotz,fabmesh,
     x      Kintea,Kicca,tcv2, cmfp,tau1,tau2,tau3,ipeK,it,erot,twoth,
     x     taues(5),Kspadi, evrot,endene,Kmaxe,Kvarte,Kvarit,Kczeff,zeffk
     x       , sqrt2,stopm,charge4,fourpi3,eratKth,twopith,fstpi,clight
       common/mcont/iu,ix,ixi,neq,nmaq,mmx,nonch,iz,nsor,nstep,nhigh,
      cnmaneq,Ksudm,iudm,mxdm,iup1ix,mx,iuh,iuin,iuhm1,iuhp1,mxp3m,
      cmxp4,mxp1,neqp,mmxp,nmaqp,nmaneqp,mmx8,iup1,iup2,ixp1,iuix,
      cmtab,mmsv,msiq,mmsvp,ixis,neqm1
       complex fthet,fphi,besd,besi,xKperp,zlam,xKp2
       common/rfcm/wc(6),vtx(6),vtz(6),zx(6),fthet(11,6),fphi(11,6),freq,
      xbesa(7),zeta(11,6),zxm(6),besi(6,6),wp2(6),xKp2(2),wp(6),irr
      x ,xKperp(2),besd(6,6),ck(6),infer(2),besr(7),zlam(6),rrr,powrx
       complex efld,rfld,dielt,rffdn
       common/erfld/efld(3),rfld(2),dielt(6),xnpar,xnparz,xKpar,dbq(99)
      1,aprf(6,6),prfs(5),tprf(6,6),powerf,trfon,trfoff,rffdn(3),baxis
      c,rmai,rmin,rminor,iwall(6),curr,dennd,dennt,dennh,ennd,ennt,ennh
       Kzz=cmplx(0.,0.)
       do 200 ii=1,neqp
       aprf(5,ii)=0.
   200 continue
       do 1 i=1,neq
       go to 101
   101 Kzz=Kzz+cmplx(1./neq,0.)-wp2(i)*cexp(-zlam(i))*besi(6,i)*fphi
      1(11,i)/xKpar/xKpar/vtz(i)/vtz(i)
       dbq(13)=real(Kzz)
       go to 102
   102 dbq(14)=aimag(Kzz)
       do 2 m=1,nhigh
       mn=m+nhigh
       go to 103
   103 Kzz=Kzz-wp2(i)*cexp(-zlam(i))*besi(m,i)*(zeta(m,i)*fphi(m,i)
      1+zeta(mn,i)*fphi(mn,i))/(2.*pi*freq*xKpar*vtz(i))
       dbq(15)=real(Kzz)
       go to 104
   104 dbq(16)=aimag(Kzz)
     2 continue
       aprf(5,i)=aimag(kzz)-aprf(5,1)-aprf(5,2)-aprf(5,3)-aprf(5,4)
     1 continue
       return
       end
       complex function det(xx)
*
*
cmt   THIS FUNCTION IS THE DETERMINANT OF THE COMPLETE HOT PLASMA DISPERSION TENSOR
cmt   CALLS BESLCI WHICH CALCULATES COMPLEX MODIFIED BESSEL FUNCTIONS OF INTEGER
```

```
cmt    ORDER
cmt    zlam = ARGUMENT OF MODIFIED BESSEL FUNCTION
cmt    besi = MODIFIED BESSEL FUNCTION
cmt    besd = DERIVATIVE OF MODIFIED BESSEL FUNCTION
*
*
         complex xx,kxx,kxy,kxz,kyy,kyz,kzz
         common/mcon1/pi,twopi,fourpi,pio2,charge,time,dtr,dtn(15), nsetn(
       x      15),nstepu,n,nprint,nplot,nstop,nrstrt,nch,nchec, ium1,ium2,
       x      ium3, ixm1, ixm2, ixm3, ixim, ixim2, ixim3,ergtkev, potent,dpot,
       x                xmax,xmax1,kbound,kaetafk,kamb1, kanande,mimax,bratio
      .x       ,bratio1,pitang,ksinqul,vnorm,efusion(4), knprobs,nsl,beta0,
       x   fammesh,sbple,ct,vef0,rdor, rhoo,nellu,elength,nsle,
       x                nsle2,rfudge,bdob,tfmax, rdora(5),rdorb(5),rdort(5),
       x      rdtcha(5),sfse,kbufin,kbufout, namebin,namebot,kbufu(5),kcsig
       x       ,tauek(5), tauen(5),taupk(5),taupk1(5), taupr(5),kchnut,
       x    reacsl(5),fatmesh,latmesh,ktpnut, ncutfe,potrat,npotz,fabmesh,
       x      kinteg,kiccg,tcv2, cmfp,tau1,tau2,tau3,ipek,it,erot,twoth,
       x     taues(5),kspad1, evrot,endene,kmaxe,kvarte,kvarit,kczeff,zeffk
       x        , sqrt2,stopm,charge4,fourpi3,ergtkth,twopith,fstpi,clight
        common/mcont/iy, ix, ix1,neq,nmag,mmx,nonch,iz,nsor,nstep,nhigh,
       cnmaneq,ksydm,iydm,mxdm,iyp1ix,mx,iyh,iyin,iyhm1,iyhp1,mxp3m,
       cmxp4,mxp1,neap,mmxp,nmagp,nmaneqp,mmx8,iyp1,iyp2,ixp1,iyix,
       cmtab,mmsv,msig,mmsvp,ixis,neqm1
        complex fthet,fphi,besd,besi,xkperp,zlam,xkp2
       .common/rfcm/wc(6),vtx(6),vtz(6),zx(6),fthet(11,6),fphi(11,6),freq,
       xbesa(7),zeta(11,6),zxm(6),besi(6,6),wp2(6),xkp2(2),wp(6),irr
       x ,xkperp(2),besd(6,6),ck(6),infer(2),besr(7),zlam(6),rrr,powrx
        complex efld,rfld,dielt,rffdn
        common/erfld/efld(3),rfld(2),dielt(6),xnpar,xnparz,xkpar,dbg(99)
       1,apr(6,6),pris(5),tpr(6,6),powerf,trfon,trfoff,rffdn(3),baxis
       c,rmaj,rmin,rminor,iwall(6),curr,dennd,dennt,dennh,ennd,ennt,ennh
        det=cmplx(0.,0.)
        do 2220 ii=1,7
        besr(ii)=0.
        besa(ii)=0.
 2220   continue
        dbg(11)=real(xx)
  100   dbg(12)=aimag(xx)
        do 1 i=1,neq
        zlam(i)=.5*xx*(vtx(i)/wc(i))**2
        dbg(50)=real(xx)
        go to 121
  121   dbg(51)=aimag(xx)
        zlr=real(zlam(i))
        go to 101
  101   zli=aimag(zlam(i))
        if(zlam(i).eq.cmplx(0.,0.)) go to 223
        call beslci(zlr,zli,6,1,besr,besa,ncalc)
        besi(6,i)=cmplx(besr(1),0.)+cmplx(0.,1.)*besa(1)
        besd(6,i)=cmplx(besr(2),0.)+cmplx(0.,1.)*besa(2)
        dbg(1)=besr(1)
        dbg(2)=besa(1)
        dbg(3)=besr(2)
        go to 102
  102   dbg(4)=besa(2)
  223   continue
        do 2 mm=2,nhigh+1
        m=mm-1
        if(zlam(i).eq.cmplx(0.,0.)) go to 202
```

```
      besi(m,i)=cmplx(besr(mm),0.)+cmplx(0.,1.)*besa(mm)
      dbg(5)=besr(mm)
      go to 103
  103 dbg(6)=besa(mm)
      if(m.ne.1) besd(m,i)=besi(m-1,i)-m*besi(m,i)/zlam(i)
      if(m.eq.1) besd(1,i)=besi(6,i)-besi(1,i)/zlam(i)
      go to 201
  202 besd(m,i)=cmplx(0.,0.)
      besd(1,i)=cmplx(.5,0.)
      besd(6,i)=cmplx(0.,0.)
      besi(m,i)=cmplx(0.,0.)
      besi(6,i)=cmplx(1.,0.)
  201 continue
      dbg(7)=real(besd(m,i))
      go to 104
  104 dbg(8)=aimag(besd(m,i))
    2 continue
    1 continue
      xn=(clight/(2.*pi*freq))**2
      xnz=xKpar*xKpar*xn
      xnpar=xn
      xnparz=xnz
      go to 107
  107 det=((Kxx(xx)-xnz)*((Kyy(xx)-xnz-xx*xn)
     1*(Kzz(xx)-xx*xn)+Kyz(xx)*Kyz(xx))
     1+Kxy(xx)*(Kxy(xx)*(Kzz(xx)-xx*xn)
     1+Kyz(xx)*(Kxz(xx)+csqrt(xx)*xnz/xKpar))
     1+(Kxz(xx)+csqrt(xx)*xnz/xKpar)*(Kxy(xx)*Kyz(xx))
     1-(Kyy(xx)-xnz-xx*xn)*(Kxz(xx)+csqrt(xx)*xnz/xKpar))
      dbg(9)=real(det)
      go to 106
  106 dbg(10)=aimag(det)
      return
      end
      subroutine diel(rt)
*
*
cmt   CALCULATES DIELCTRIC ELEMENTS FOR FAST OR ION BERNSTEIN WAVE FOR GIVEN
cmt   KPERP**2
cmt   rt= KPERP**2 FOUND BY ZANLYT
cmt   THIS SUBROUTINE CALLED BY IMSL ROUTINE zanlyt
*
*
      complex efld,rfld,dielt,rffdn
      common/erfld/efld(3),rfld(2),dielt(6),xnpar,xnparz,xKpar,dbg(99)
     1,aprf(6,6),prfs(5),tprf(6,6),powerf,trfon,trfoff,rffdn(3),baxis
     c,rmaj,rmin,rminor,iwall(6),curr,dennd,dennt,dennh,ennd,ennt,ennh
      err1=real(rt)
      go to 108
  108 err2=aimag(rt)
      dielt(1)=cmplx(dbg(31),0.)+cmplx(0.,1.)*dbg(32)-cmplx(xnparz
     1,0.)
      dbg(71)=real(dielt(1))
      dbg(52)=aimag(dielt(1))
      dielt(2)=cmplx(dbg(27),0.)+cmplx(0.,1.)*dbg(28)
      dielt(3)=cmplx(dbg(25),0.)+cmplx(0.,1.)*dbg(26)+
     1csqrt(rt)*xnparz/xKpar
      dbg(55)=real(dielt(3))
      dbg(56)=aimag(dielt(3))
      dielt(4)=cmplx(dbg(23),0.)+cmplx(0.,1.)*dbg(24)-rt*xnpar-
```

```
     1cmplx(xnparz,0.)
      dbg(57)=real(dielt(4))
      dbg(58)=aimag(dielt(4))
      dielt(5)=cmplx(dbg(19),0.)+cmplx(0.,1.)*dbg(20)
      dielt(6)=cmplx(dbg(15),0.)+cmplx(0.,1.)*dbg(16)-rt*xnpar
      dbg(53)=real(dielt(6))
      dbg(54)=aimag(dielt(6))
      do 333 k=1,6
      do 334 i=1,5
      tprf(k,i)=aprf(k,i)
  334 continue
  333 continue
      return
      end
      subroutine rffld
*
*
cmt   CALCULATES THE UNNORMALIZED RF ELECTRIC FIELD COMPONENTS FOR THE FAST
cmt   AND/OR ION CYCLOTRON WAVES FOR AN INFINITE UNIFORM PLASMA USING WAVE EQUATION
cmt
cmt
cmt   efld(1) = Ex
cmt   efld(2) = Ey
cmt   efld(3) = Ez
cmt   rfld(1) = E+
cmt   rfld(2) = E-
cmt   prfs(i) IS THE RF POWER DEPOSITED IN SPECIES "i" USING WEAK DAMPING FORMULA
*
*
      complex ttem(3),tem(3,5)
      common/mcont/iu, ix, ix1,neq,nmag,mmx,nonch,iz,nsor,nstep,nhigh,
     cnmaneq,ksudm,iudm,mxdm,iup1ix,mx,iuh,iuin,iuhm1,iuhp1,mxp3m,
     cmxp4,mxp1,neqp,mmxp,nmagp,nmaneqp,mmx8,iup1,iup2,ixp1,iuix,
     cmtab,mmsv,msig,mmsvp,ixis,neqm1
      complex efld,rfld,dielt,rffdn
      common/erfld/efld(3),rfld(2),dielt(6),xnpar,xnparz,xkpar,dbg(99)
     1,aprf(6,6),prfs(5),tprf(6,6),powerf,trfon,trfoff,rffdn(3),baxis
     c,rmai,rmin,rminor,iwall(6),curr,dennd,dennt,dennh,ennd,ennt,ennh
      do 202 ii=1,neq
      prfs(ii)=0.
  202 continue
      cprf=0.
      efld(1)=cmplx(1.,0.)
      efld(2)=efld(1)*((dielt(3)+dielt(5))*dielt(3)/dielt(6)-dielt
     1(1)+dielt(2))/((dielt(3)+dielt(5))*dielt(5)/dielt(6)+dielt(2)
     1+dielt(4))
      dbg(59)=real(efld(2))'
      go to 110
  110 dbg(60)=aimag(efld(2))
      efld(3)=efld(1)*(dielt(2)-dielt(3)+(dielt(4)-
     1dielt(5))*dielt(1)/dielt(2))/(dielt(5)+dielt(6)
     1+(dielt(5)-dielt(4))*dielt(3)/dielt(2))
      ttem(1)=dielt(1)*efld(1)+dielt(2)*efld(2)+dielt(3)*efld(3)
      ttem(2)=-dielt(2)*efld(1)+dielt(4)*efld(2)+dielt(5)*efld(3)
      ttem(3)=dielt(3)*efld(1)-dielt(5)*efld(2)+dielt(6)*efld(3)
      dbg(61)=real(efld(3))
      go to 102
  102 dbg(62)=aimag(efld(3))
      rfld(1)=efld(1)+cmplx(0.,1.)*efld(2)
      rfld(2)=efld(1)-cmplx(0.,1.)*efld(2)
      do 331 i=1,neq
      tem(1,i)=2.*tprf(2,i)*efld(1)*(cmplx(dbg(59),0.)-cmplx(0.,1.)
     1*dbg(60))
      tem(2,i)=2.*tprf(4,i)*efld(2)*(cmplx(dbg(61),0.)-cmplx(0.,1.)
     1*dbg(62))
      tem(3,i)=2.*tprf(6,i)*efld(1)*(cmplx(dbg(61),0.)-cmplx(0.,1.)
     1*dbg(62))
      prfs(i)=tprf(1,i)*(cabs(efld(1)))**2+tprf(3,i)*(cabs(efld(2)))**2
     1+tprf(5,i)*(cabs(efld(3)))**2-aimag(tem(1,i))-aimag(tem(2,i))
     1+real(tem(3,i))
      cprf=cprf+prfs(i)
      go to 555
  555 cpn=powerf/cprf
  331 continue
      do 333 i=1,neq
      go to 556
  556 prfs(i)=cpn*prfs(i)
  333 continue
      return
      end
```

APPENDIX B

Kennel and Engelmann have assumed that a spectrum of randomly phased modes exist in order to justify the concept of particle diffusion caused by several random velocity displacements. A monochromatic, rather than a spectrum, of waves can be used if a plasma ion, having passed through the resonant heating zone, encounters many collisions so as to forget the phase of the cyclotron heating field before it passes through the heating zone again. The time between passes through this zone is(13)

$$\tau_p \simeq \pi R q / v_{\parallel} \qquad \text{(B-1)}$$

and the variation in τ_p is given by(4-13,16)

$$\Delta\tau_p \simeq \pi R q \Delta v_{\parallel} / v_{\parallel}^2 \; . \qquad \text{(B-2)}$$

After half a polodial rotation, Coulomb scattering causes an RMS deviation, $\Delta v_{\parallel}$, on the order of $(<\Delta v_{\parallel}>^2 \tau_p)^{1/2}$, where $<\Delta v_{\parallel}>^2$ is the diffusion coefficient(4-16,33). Ions "forget" the cyclotron phase between transists when $\omega_{ci}\Delta\tau_p >> 1$ or

$$\frac{<(\Delta v_{\parallel})^2>}{v_{\parallel}^2} >> \frac{1}{(\omega_{ci}\tau_p)^2} \frac{1}{\tau_p} \; , \qquad \text{(B-3)}$$

where the diffusion coefficient is(4-13,16)

$$<(\Delta v_{\parallel})^2> \;=\; \sum_f \frac{C_f}{v} G(\ell_f v)$$

$$C_f \equiv \frac{8\pi n_f Z_f^2 Z^2 e^4 \ln\Lambda}{m_f^2} \,, \quad \ell_f^2 \equiv m_f/2kT_f \tag{B-4}$$

$$G(x) \equiv \frac{\Phi(x) - x\Phi'(x)}{2x^2} \,, \quad \phi(x) \equiv \frac{2}{\pi^{\frac{1}{2}}} \int_0^x \exp(-y^2)dy .$$

From Table B-1, we see that Eq. (B-3) is valid for both PLT and NUWMAK.

Table B-1

	PLT	NUWMAK
R (cm)	130	512.5
q	~ 3	~ 3
T_f (keV)	1	10
$V_{\parallel} \tilde{\sim} v_{thi}$ (cm/s)	$2.2\text{x}10^7$	$6.2\text{x}10^7$
τ_p (ms)	0.056	0.078
ω_{ci} (r/s)	$1.57\text{x}10^8$	$2.9\text{x}10^8$
n_f (cm^{-3})	$3\text{x}10^{13}$	$3\text{x}10^{14}$
m_f/m_p	2.0	2.5
$\ell n\Omega$	~ 10	~ 10
$\dfrac{<(\Delta V_{\parallel})^2>}{V_{\parallel}^2}$ (sec^{-1})	340	96.5
$\dfrac{1}{(\omega_{ci}\tau_p)} = \dfrac{1}{\tau_p}$ (sec^{-1})	$2.3\text{x}10^{-4}$	$2.5\text{x}10^{-5}$

APPENDIX C

From Eq. (4-16), one term of C may be written as

$$C = \frac{|E_+|^2}{32Z^2e^2n_o}\,\delta(n\omega_{c\beta} - \omega + k_{\parallel}v_{\parallel})J^2_{n-1} \qquad (C\text{-}1)$$

where $J_n \equiv J_n(k_\perp v_\perp/\omega_{c\beta})$.

With

$$k_{\parallel} = (m - l)q/qR \qquad (C\text{-}2)$$

and with $m = 0$, $l = 100$ and $R \simeq R_0 \approx 500$ cm for NUWMAK or

$m = 0$, $l = 13$, $R \approx 130$ for PLT.

$k_{\parallel} = -.1\ \text{cm}^{-1} \equiv -k'_{\parallel}$ for PLT and

$k_{\parallel} = -.2\ \text{cm}^{-1} \equiv -k'_{\parallel}$ for NUWMAK (C-3)

so that

$$C = \frac{|E_+|^2}{32Z^2e^2n_o}\,\delta(n\omega_{c\beta} - \omega - k'_{\parallel}v_{\parallel})J^2_{n-1}\,. \qquad (C\text{-}4)$$

On averaging over θ

$$\langle C\rangle_\theta \simeq \frac{|E_+|^2}{32\pi Z^2e^2n_o}\,J^2_{n-1}\int_0^\pi \delta(n\omega_{c\beta} - \omega - k'_{\parallel}v_{\parallel})d\theta\,. \qquad (C\text{-}5)$$

Letting

$$x \equiv n\omega_{c\beta} = \frac{n\omega_{c\beta o}R_o}{R_o + a\sin\theta} \qquad (C\text{-}6)$$

then

$$dx = -\frac{n\omega_{c\beta o}R_o a\cos\theta}{(R_o + a\sin\theta)^2}\, d\theta = -\frac{a\cos\theta x^2}{R_o n\omega_{c\beta o}}\, d\theta . \tag{C-7}$$

Therefore

$$d\theta = -\frac{n\omega_{c\beta o}R_o}{ax^2\sin\theta}\, dx. \tag{C-8}$$

Since $\sin\theta = (R/a)\ (n\omega_{c\beta o}/x - 1)$

$$\cos\theta = (1 - (R/a)^2\ (n\omega_{c\beta o}/x - 1)^2)^{1/2} \equiv \xi(x). \tag{C-9}$$

Therefore

$$d\theta = -\frac{n\omega_{c\beta o}R_o}{ax^2\xi(x)}\, dx \tag{C-10}$$

and

$$\langle C\rangle_\theta = -\frac{|E_+|^2 J_{n-1}^2 R_o n\omega_{c\beta o}}{32\pi Z^2 e^2 n_o a}\int_0^\pi \frac{\delta(x - k_\parallel' v_\parallel - \omega)}{x^2\xi(x)}\, dx \tag{C-11}$$

$$= \frac{|E_+|^2 J_{n-1}^2 R_o n\omega_{c\beta o}}{32\pi Z^2 e^2 n_o a(\omega + k_\parallel' v_\parallel)^2 \xi(x_o)} \tag{C-12}$$

where

$$\xi(x_o) \equiv \left\{1 - \left(\frac{R}{a}\right)^2 \left(\frac{n\omega_{c\beta o}}{\omega + k_\parallel' v_\parallel} - 1\right)^2\right\}^{\frac{1}{2}} . \tag{C-13}$$

Since $\omega + k'_{\parallel} v_{\parallel} = n\omega_{c\beta o}$,

$$\langle C \rangle_{\theta} = \frac{|E_{+}|^2 J^2_{n-1} R_o \ \omega_{c\beta o}}{32 \ Z^2 e^2 n_o a \pi n \omega^2_{c\beta} \xi(x_o)} \simeq \frac{|E_{+}|^2 J^2_{n-1} R}{32 \ Z^2 e^2 n_o a n \omega_{c\beta o} \xi(x_o)} \qquad \text{(C-14)}$$

with $\omega_{c\beta} \simeq \omega_{c\beta o}$.

A similar procedure may be used to derive the other two terms of the expression for C given in Eq. (4-17).

APPENDIX D

The first approximation used in the ICRF model is the weak damping formula

$$P = \frac{\omega}{2} \bar{E}^* \cdot \bar{\bar{K}}^a \cdot \bar{E} \qquad \text{(D-1)}$$

which determines the RF power deposition. Equation (D-1) holds when

$$\frac{\mathrm{Im} k_\perp}{\mathrm{Re} k_\perp} << 1. \qquad \text{(D-2)}$$

Since there is little energy in the Ion Bernstein branch, the first approximation used is

$$\varepsilon \equiv \frac{\mathrm{Im} k_{\perp f}}{\mathrm{Re} k_{\perp f}} << 1. \qquad \text{(D-3)}$$

The remaining approximations are in the WKB method used to find the RF electric field. Again, since there is little energy in the Ion Bernstein mode, we calculate epsilons for the fast wave only. The WKB approximations should be better for the Ion Bernstein wave(5-27). To obtain the fast wave electric field for Eq. (D-1), we use the following WKB type equation

$$\frac{d^2 E^f}{dr^2} + k_{\perp f}^2(r) E^f = 0. \qquad \text{(D-4)}$$

There are several approximations used in obtaining the solution for Eq. (D-4)

$$E \propto \frac{1}{k_{\perp f}^{1/2}} e^{i\int k_{\perp f} \cdot dr} . \qquad \text{(D-5)}$$

To find the solution we assume that

$$E \propto e^{i\phi}. \qquad \text{(D-6)}$$

Equation (D-4) becomes

$$-(\phi')^2 + i\phi'' + k_{\perp f}^2 = 0. \qquad \text{(D-7)}$$

If we assume that

$$|\phi''| \ll k_{\perp f}^2 \qquad \text{(D-8)}$$

then we have

$$\phi' = \pm k_{\perp f} \qquad \text{(D-9)}$$

or

$$\phi = \pm \int k_{\perp f} \cdot dr. \qquad \text{(D-10)}$$

For $|\phi''|$ to be small

$$\frac{|\phi''|}{|k_{\perp f}^2|} \simeq \left| \frac{k'_{\perp f}}{k_{\perp f}^2} \right| \equiv \varepsilon_1 \ll 1. \qquad \text{(D-11)}$$

For a higher order approximation to Eq. (D-4), from Eq. (D-9)

$$\phi'' \approx \pm k'_{\perp f} \tag{D-12}$$

Therefore

$$-(\phi')^2 \pm ik'_{\perp f} + k^2_{\perp f} = 0 \tag{D-13}$$

$$(\phi')^2 \simeq k^2_{\perp f} \pm i\, k'_{\perp f} \tag{D-14}$$

$$\phi \simeq \pm \int k_{\perp f} \cdot dr \pm \frac{i}{4} \ln k^2_{\perp f} \tag{D-15}$$

which yields the solution

$$E^f(r) \simeq \frac{C_+}{k_{\perp f}^{1/2}}\, e^{i\int k_{\perp f} \cdot dr} + \frac{C_-}{k_{\perp f}^{1/2}}\, e^{-i\int k_{\perp f} \cdot dr}. \tag{D-16}$$

For a wave traveling from the low field side $C_- = 0$ so

$$E^f(r) = \frac{C_+}{k_{\perp f}^{1/2}}\, e^{i\int k_{\perp f} \cdot dr} \tag{D-17}$$

For Eq. (D-16) to hold

$$\frac{|\phi''|}{|k^2_{\perp f}|} \ll 1 \tag{D-18}$$

From Eq. (D-14)

$$\phi' \simeq k_{\perp f} + i \frac{k'_{\perp f}}{2k_{\perp f}} \tag{D-19}$$

therefore

$$\phi'' \simeq k'_{\perp f} + i \frac{k''_{\perp f}}{2k_{\perp f}} - i \frac{(k'_{\perp f})^2}{2k^2_{\perp f}} \tag{D-20}$$

so that

$$\varepsilon_2 \equiv \left| \frac{k'_{\perp f}}{k^2_{\perp f}} + i \frac{k''_{\perp f}}{2k^3_{\perp f}} - i \frac{(k'_{\perp f})^2}{2k^4_{\perp f}} \right| << 1. \tag{D-21}$$

By inserting Eq. (D-17) into Eq. (D-4) a similar approximation is obtained

$$\varepsilon_3 \equiv \left| \frac{3}{4} \frac{(k'_{\perp f})^2}{k^4_{\perp f}} - \frac{k''_{\perp f}}{2k^3_{\perp f}} \right| << 1. \tag{D-22}$$

Since $k_{\perp f}$ is a complicated function of r, we have fitted both $\mathrm{Re}k_{\perp f}(r)$ and $\mathrm{Im}k_{\perp f}(r)$ to polynomials. Both $\mathrm{Re}k_{\perp f}(r)$ and $\mathrm{Im}k_{\perp f}(r)$ are divided into 12 intervals, 11 having 10 points while the region on the inside plasma edge has 7 points. In each interval $\mathrm{Re}k_{\perp f}$ and $\mathrm{Im}k_{\perp f}$ is approximated by a fifth order polynomial so that

$\left| \sum_{i=0}^{5} A_i r^i - \mathrm{Re}k_{\perp f} \right|$ and $\left| \sum_{i=0}^{5} B_i r^i - \mathrm{Im}k_{\perp f} \right|$ are minimized in each of the 12 regions. By using a polynomial fit in each zone, ε_1, ε_2, and ε_3 can be calculated. In the $\text{Re}k_{\perp f}$ and the $\text{Im}k_{\perp f}$ plots, the solid curve is the actual value while the dashed line represents the polynomial approximation. In the epsilon plots, ε_2 is the solid curve, the dashed line is ε, the dotted line is ε_1, while the chaindot line plots ε_3. In all the epsilon figures $\varepsilon_1 \approx \varepsilon_2 \approx \varepsilon_3$.

Figures (D-1-2) show the real and imaginary parts of $k_{\perp f}$ for PLT at $t = 0$ with $C_H = 1.5$. The mode conversion layer near $r = 125$ cm can be seen. The polynomial fit is accurate except near the mode conversion layer. $\text{Im}k_{\perp f}$ is nonzero at the inner edge where the wave does not penetrate and in the cyclotron layer. We see that $\text{Im}k_{\perp f}$ is large in a region between the mode conversion layer and the launching structure at $r = 175$ cm. The sharp rise in $\text{Im}k_{\perp f}$ due to the presence of the ion-ion hybrid resonance can be seen. In Fig. (D-3) we see there are three regions where both the weak damping and WKB formulations breakdown. The region at the outer edge does not affect the calculations. This region is an evanescence zone and also appears in the NUWMAK calculations. In PLT, little power is absorbed in this region(34) so we assume that the wave is launched inside of this zone. The inner edge also is an evanescence region. In both PLT and NUWMAK, little, if any energy reaches the inner surface. Therefore, this inner zone does not affect the calculations.

The important region is near the center 120 cm $\leq r \leq$ 130 cm where mode conversion may occur. In this thin layer, most of the RF is deposited. Both the WKB and weak damping formulas break down in this region. In comparison to the experiment, the RF heating width predicted by STICR-I seems to be correct. The actual deposition within this 10 cm needs a more accurate description. The effect of a more complete calculation on either the density or temperature profiles should be minimal.

When C_H = 1.0 or 2.0, the areas where both the WKB and weak damping formulations are valid remain the same. Mode conversion does not appear to affect the results, the RF power deposition should be unaffected by the presence of mode conversion in our model.

In PLT, where $k_\parallel = 0.2$ cm^{-1}, the sharp change in $\text{Re}k_{\perp f}$ and $\text{Im}k_{\perp f}$ over the plasma center is eliminated as shown in Figs. (D-4-5). There are wide evanescence regions on both sides of the plasma. Since the wave is assumed to penetrate the outside evanescence region without absorption and does not reach the inner edge with much energy, these regions can be neglected in Fig. (D-6). Both the WKB and weak damping formulations are valid over the entire resonance layer at the center. There is a region on the high field side (98 cm $\leq r \leq$ 115 cm) where the WKB theory is not valid. However, the RF wave is damped before this region is reached. In addition, the polynomial approximation of $\text{Im}k_{\perp f}$ is not too accurate in this zone and may contribute to making ε_1, ε_2 and ε_3 too large. The exact expression, becomes large over a very small width in this interval, when $\mathrm{Re}k_{\perp f} \to 0$.

We next proceed to examine the WKB and weak damping approximations in the conceptual reactor NUWMAK. In the fundamental heating case, we find that $\mathrm{Re}k_{\perp f}$ and $\mathrm{Im}k_{\perp f}$ are more accurately approximated by polynomials (Fig. (D-7-8)). In Fig. (D-9), we see there are again edge regions where both formulations break down. Again, by assuming that the incoming wave can propagate through the outer evanescence zone, this region can be ignored. The wave is damped before the inner edge is reached so this region can also be neglected. Unlike PLT, both formulations are valid over the plasma center. As the plasma temperature increases, $\mathrm{Re}k_{\perp f}$ becomes smoother (Fig. (D-10)). The damping zone spreads and $\mathrm{Im}k_{\perp f}$ becomes smoother at the plasma center (Fig. (D-11)). Figure (D-12) shows the WKB and weak damping formulas improving as the temperature increases.

Figures (D-13-21) pertain to second harmonic heating in NUWMAK. On compaing Figs. (D-13-15) where mode conversion occurs to Figs. (16-21) where mode conversion is absent, we find little change. In second harmonic heating the zones of validity are unaffected by temperature. Both the WKB and weak damping formulas are valid over a wider region in comparison to fundamental heating.

Figures (D-22-24) deal with third harmonic heating in NUWMAK. $\mathrm{Re}k_{\perp f}$ and $\mathrm{Im}k_{\perp f}$ are very smooth over the resonance zone and are accurately approximated by polynomials. Both formulas hold well over the central regions and break down near the plasma edges. As the plasma temperature increases the epsilons increase, although both formulations appear to remain valid.

In conclusion, for PLT, mode conversion does not appear to influence the areas of validity. There are regions at both edges where the formulas break down. Little power is deposited in these regions so their effects on the RF depositions should be minimal. Near the plasma center, where most of the power is deposited, both formulas break down. However, the heating width which is predicted agrees well with the experiment. The ratio $\frac{T_H}{T_D}$ does not affect the widths of the regions of validity.

For NUWMAK, both approximations become good over the resonance zone. There is still an inner and outer edge region where the approximations break down. However, when mode conversion is present, the inner edge cannot be reached, the wave being reflected at the mode conversion layer. When mode conversion is absent, the wave is damped before the inner edge is reached. The assumption of no power being absorbed in the outer evanescence zone allows us to ignore this region as well. Mode conversion does not appear to affect the validity of either formulation.

As the RF frequency increases, both WKB and weak damping approximations become better. As the plasma temperature increases, the approximations used in the calculations of fundamental heating improve. For second and third harmonic heating, the epsilon values increase slightly. On the whole, both approximations appear to hold over the entire region of NUWMAK where heating, either ion or electron, occur. Our conclusions should be more accurate in NUWMAK than in PLT. The slab model should be more accurate in large devices such as a reactor.

LIST OF FIGURES

(D-13) $\mathrm{Re}k_{\perp}$ (solid line) and the fifth order polynomial fit (dashed line) for NUWMAK, $f = 2f_{cD}$, $k_{\parallel} = 0.1\ \mathrm{cm}^{-1}$, $t = 0$ sec.

(D-14) $\mathrm{Im}k_{\perp}$ (solid line) and the fifth order polynomial fit (dashed line) for NUWMAK, $f = 2f_{cD}$, $k_{\parallel} = 0.1\ \mathrm{cm}^{-1}$, $t = 0$ sec.

(D-15) ε (dashed line), ε_1 (dotted line), ε_2 (solid line), ε_3 (chaindot line) for NUWMAK, $f = 2f_{cD}$, $k_{\parallel} = 0.1\ \mathrm{cm}^{-1}$, $t = 0$ sec.

(D-16) $\mathrm{Re}k_{\perp}$ (solid line) and the fifth order polynomial fit (dashed line) for NUWMAK, $f = 2f_{cD}$, $k_{\parallel} = 0.2\ \mathrm{cm}^{-1}$, $t = 0$ sec.

(D-17) $\mathrm{Im}k_{\perp}$ (solid line) and the fifth order polynomial fit (dashed line) for NUWMAK, $f = 2f_{cD}$, $k_{\parallel} = 0.2\ \mathrm{cm}^{-1}$, $t = 0$ sec.

(D-18) ε (dashed line), ε_1 (dotted line), ε_2 (solid line), ε_3 $f = 2f_{cD}$, $k_{\parallel} = 0.2\ \mathrm{cm}^{-1}$, $t = 0$ sec.

(D-19) $\mathrm{Re}k_{\perp}$ (solid line) and the fifth order polynomial fit (dashed line) for NUWMAK, $f = 2f_{cD}$, $k_{\parallel} = 0.3\ \mathrm{cm}^{-1}$, $t = 0$ sec.

(D-20) $\mathrm{Im}k_{\perp}$ (solid line) and the fifth order polynomial fit (dashed line) for NUWMAK, $f = 2f_{cD}$, $k_{\parallel} = 0.3\ \mathrm{cm}^{-1}$, $t = 0$ sec.

(D-21) ε (dashed line), ε_1 (dotted line), ε_2 (solid line), ε_3 (chaindot line) for NUWMAK, $f = 2f_{cD}$, $k_{\parallel} = 0.3\ \mathrm{cm}^{-1}$, $t = 0$ sec.

(D-22) $\mathrm{Re}k_{\perp}$ (solid line) and the fifth order polynomial fit (dashed line) for NUWMAK, $f = 3f_{cD}$, $k_{\parallel} = 0.2\ \mathrm{cm}^{-1}$, $t = 0$ sec.

(D-23) Im$k_\perp$ (solid line) and the fifth order polynomial fit (dashed line) for NUWMAK, $f = 3f_{cD}$, $k_\parallel = 0.2$ cm^{-1}, $t = 0$ sec.

(D-24) ε (dashed line), ε_1 (dotted line), ε_2 (solid line), ε_3 (chaindot line) for NUWMAK, $f = 3f_{cD}$, $k_\parallel = 0.2$ cm^{-1}, $t = 0$ sec.

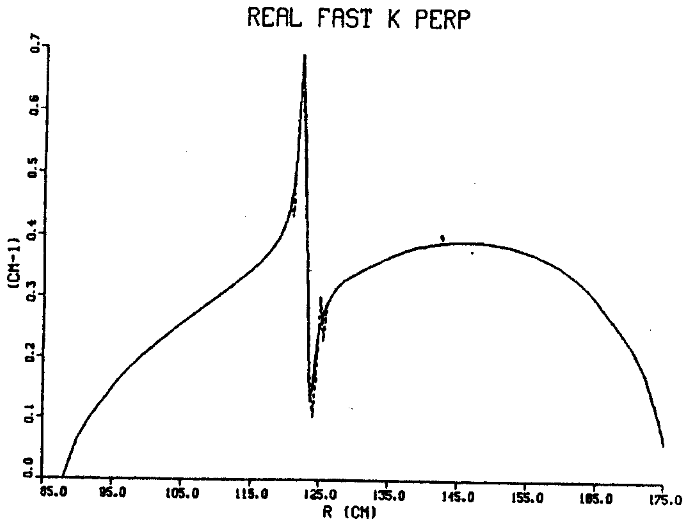

TIME (MSEC)= 0.0000 NPOLY= 5

Fig.(D-1)

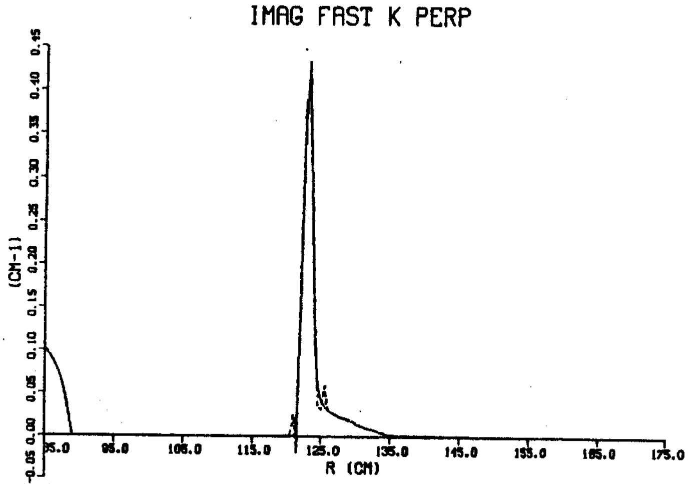

Fig.(D-2)

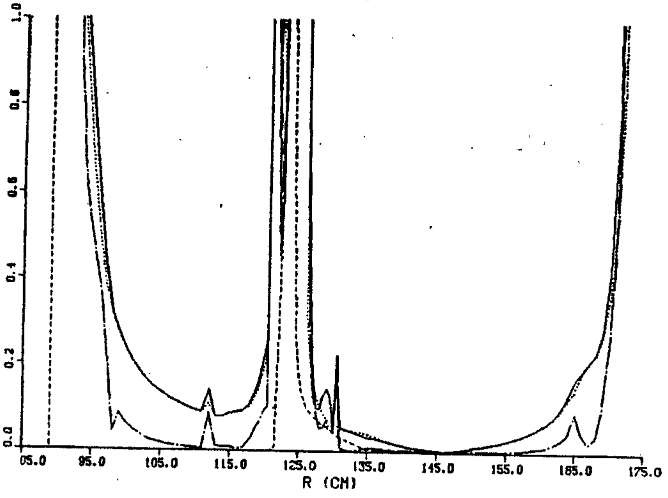

Fig.(D-3)

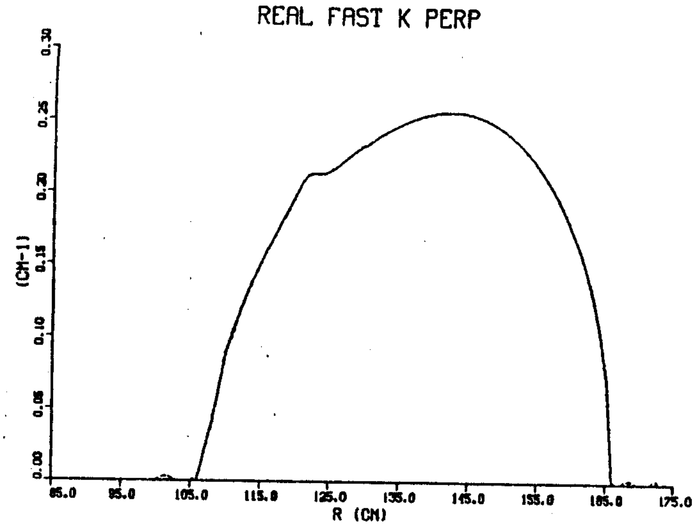

TIME (MSEC)= 0.0000 NPOLY= 5

Fig.(D-4)

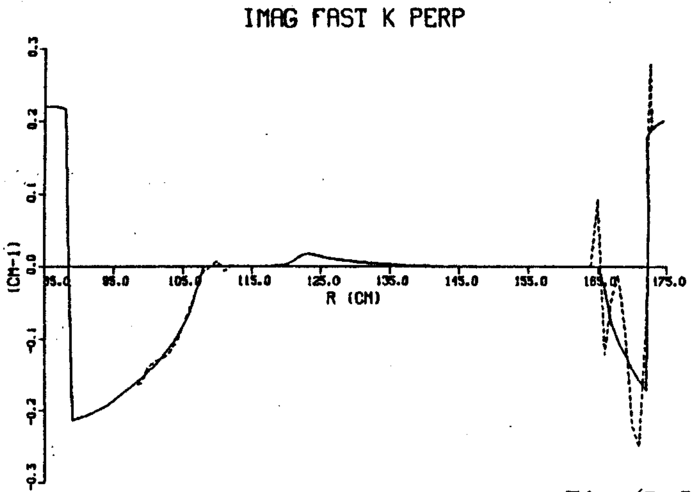

Fig.(D-5)

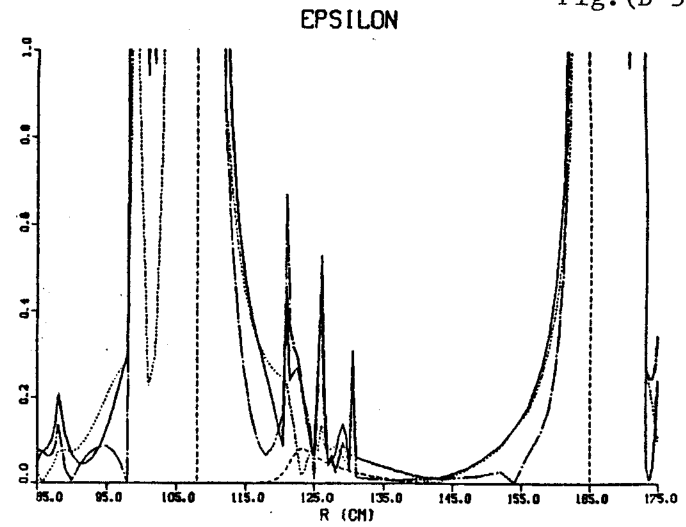

Fig.(D-6)

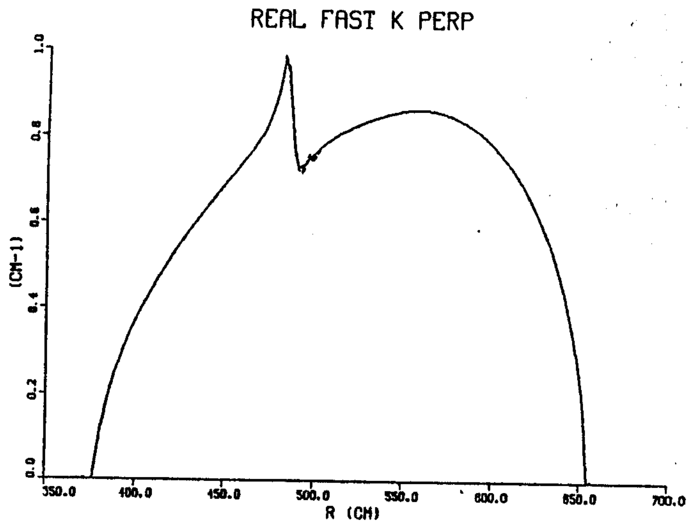

Fig.(D-7)

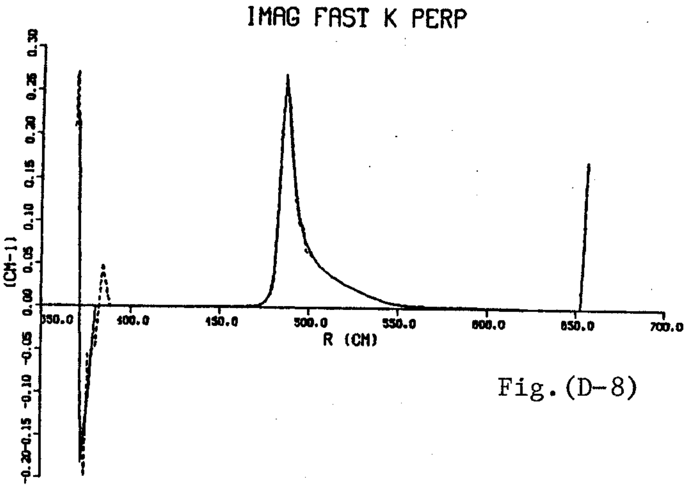

Fig.(D-8)

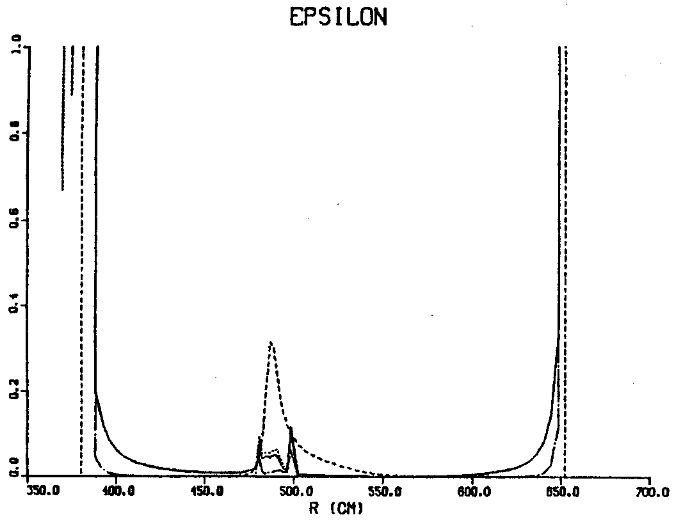

Fig.(D-9)

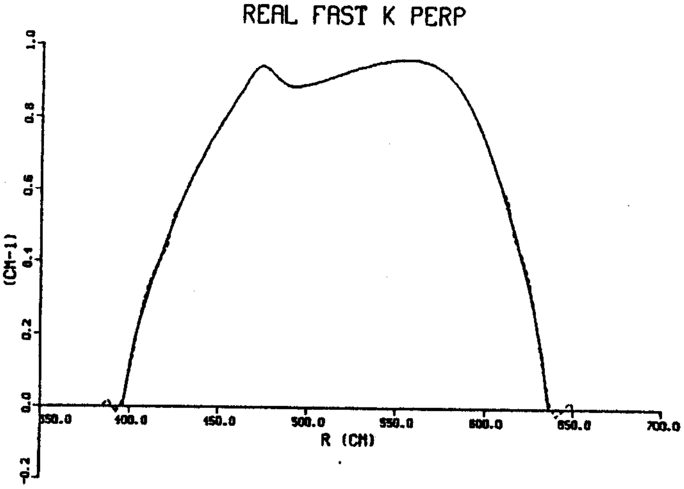

TIME (MSEC)= 1500.0000 NPOLY= 5

Fig.(D-10)

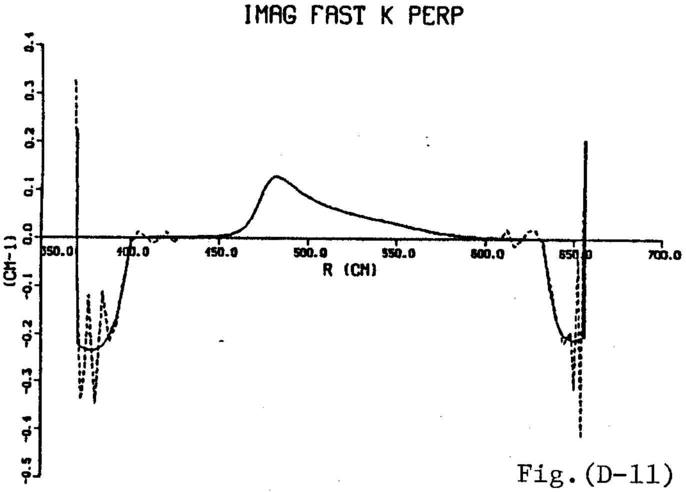

Fig.(D-11)

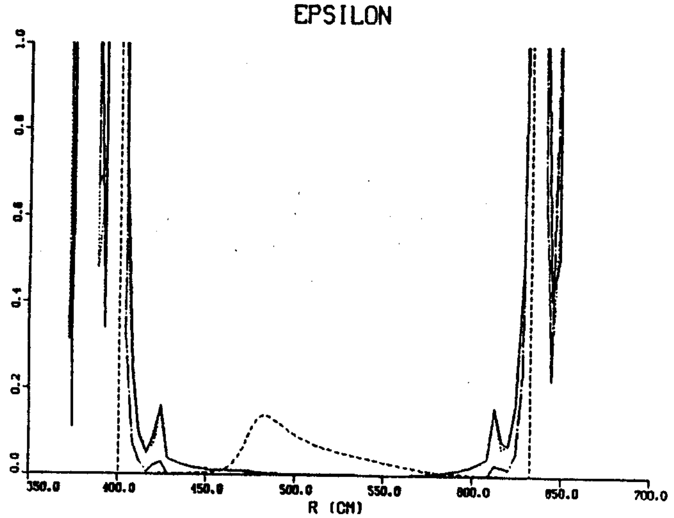

Fig.(D-12)

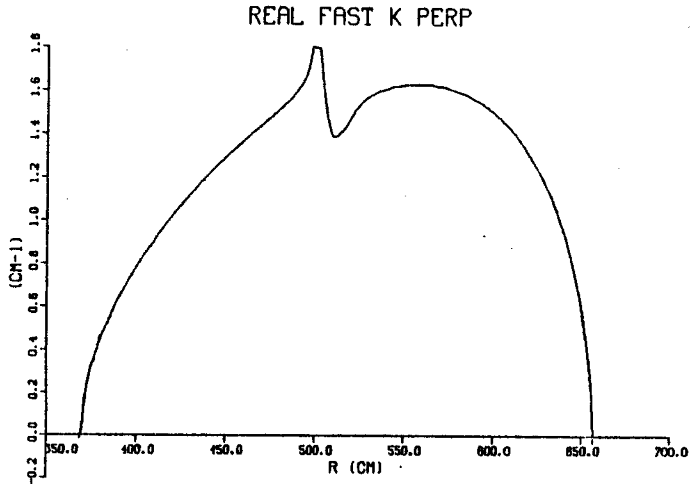

TIME (MSEC)= 0.0000 NPOLY= 5

Fig.(D-13)

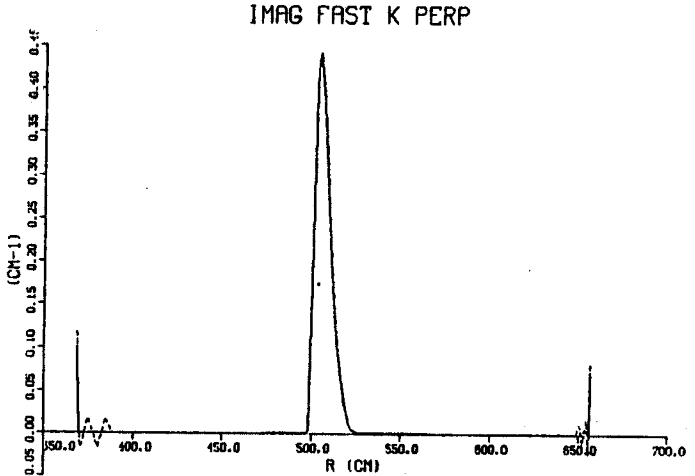

Fig.(D-14)

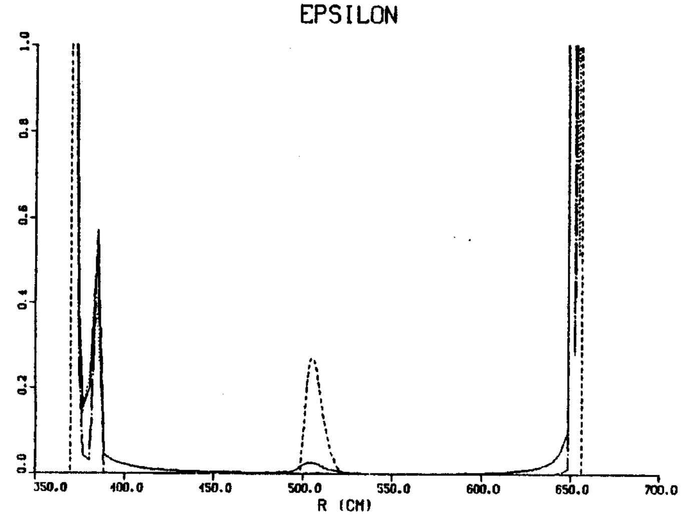

Fig.(D-15)

REAL FAST K PERP

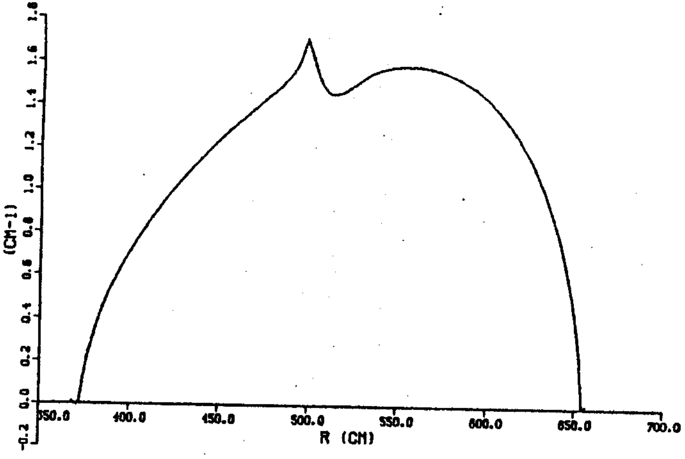

TIME (MSEC)- 0.0000 NPOLY- 5

Fig.(D-16)

IMAG FAST K PERP

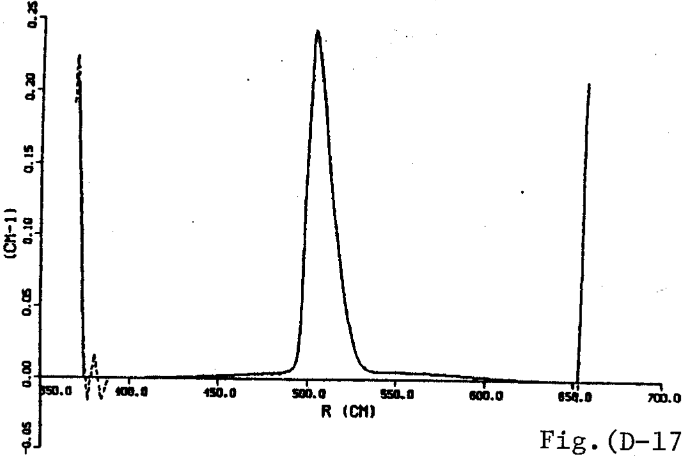

Fig.(D-17)

EPSILON

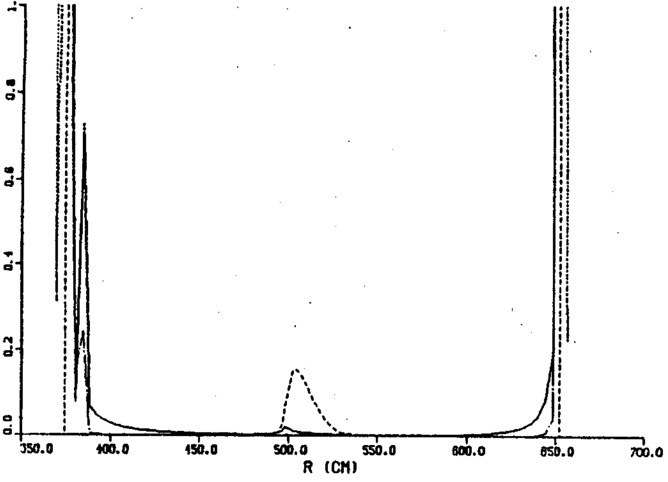

Fig.(D-18)

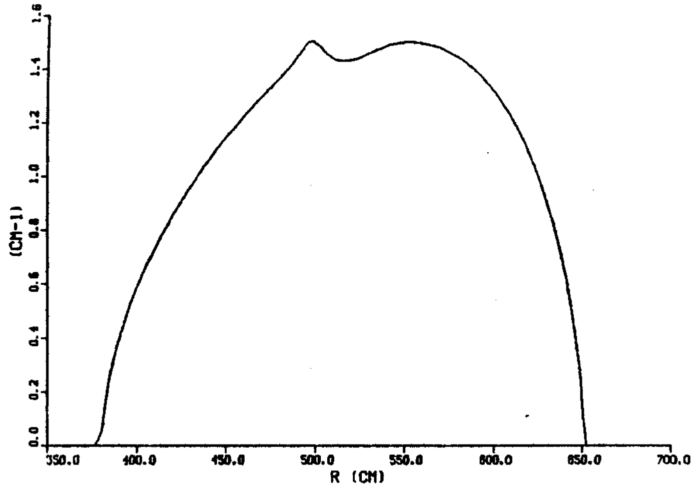

REAL FAST K PERP

TIME (MSEC)- 0.0000 NPOLY- 5

Fig.(D-19)

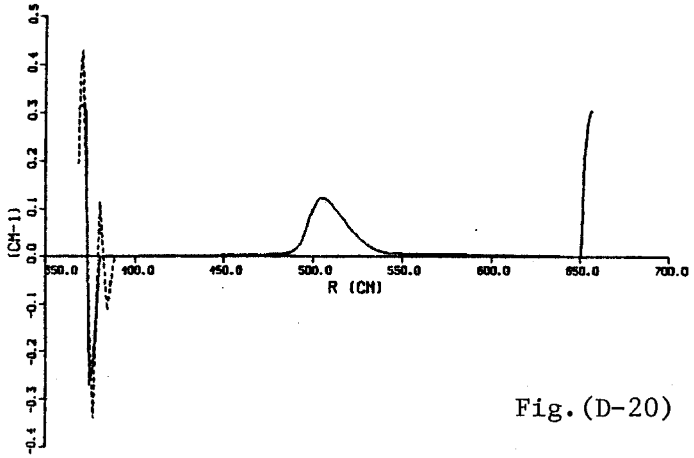

IMAG FAST K PERP

Fig.(D-20)

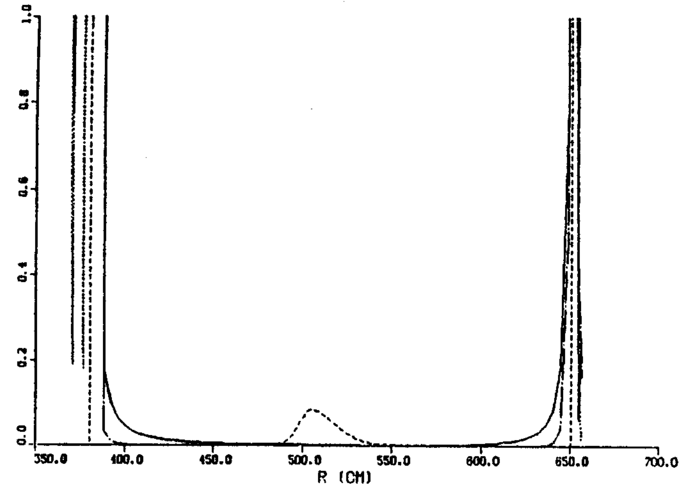

EPSILON

Fig.(D-21)

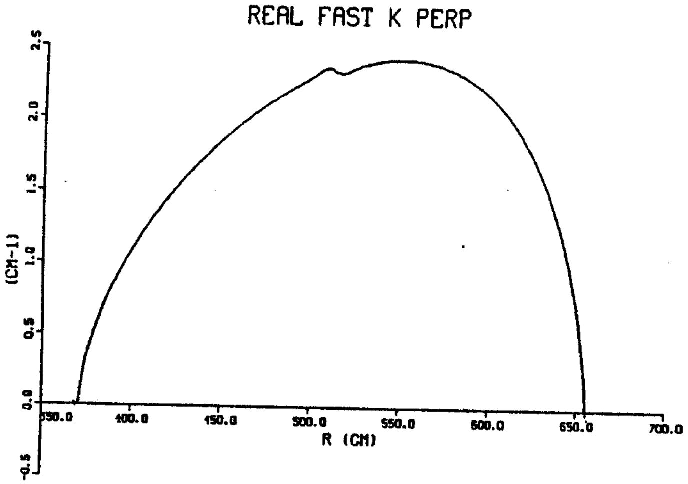

REAL FAST K PERP

TIME (MSEC)= 0.0000 NPOLY= 5

Fig.(D-22)

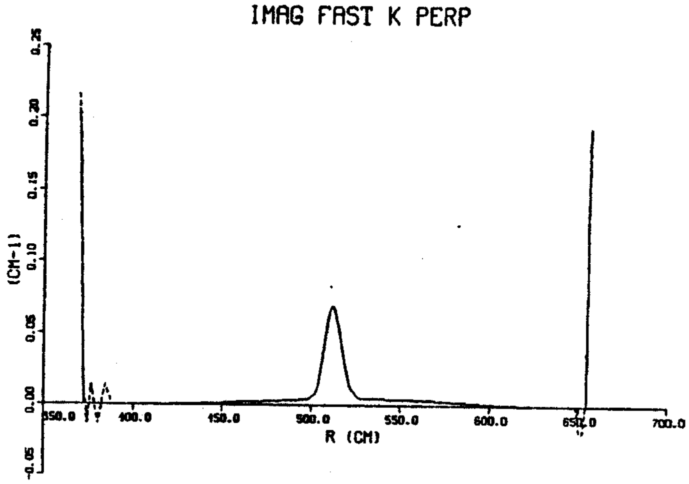

IMAG FAST K PERP

Fig.(D-23)

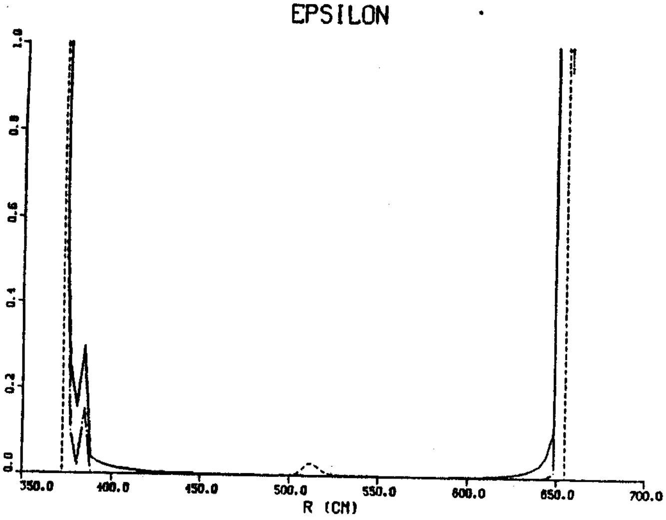

EPSILON

Fig.(D-24)